PhD Thesis

Institute of Physical Chemistry
Polish Academy of Sciences
Kasprzaka 44/52
01-224 Warsaw, Poland

PhD Thesis

Preparation and applications of platforms based on gold nanoparticles and graphene

Izabela Kamińska

Supervisor:
Prof. dr. hab. Marcin Opałło
Institite of Physical Chemistry, PAS
Poland

Co-supervisor:
Dr. Rabah Boukherroub
Interdisciplinary Research Institute
France

This dissertation was prepared within the International PhD in Chemistry Studies at the Institute of Physical Chemistry of the Polish Academy of Sciences in Warsaw.
Programme co-financed by the European Regional Development Fund, Operational Program Innovative Economy 2007-2013.
The dissertation was prepared within the co-tutorial agreement between the Institute of Physical Chemistry of the Polish Academy of Sciences in Poland and Lille1 University in France.

INNOVATIVE ECONOMY
NATIONAL COHESION STRATEGY

FNP
Foundation for Polish Science

EUROPEAN UNION
EUROPEAN REGIONAL DEVELOPMENT FUND

Warsaw, October 2013

I am very grateful to Dr. Joanna Niedziółka-Jönsson for introducing me to the work in the laboratory, many interesting discussions and her great support. I would like to thank my supervisor Prof. dr. Marcin Opałło for his guidance and kindness during my PhD studies.

I would like to express my gratitude to Prof. Sabine Szunerits and Dr. Rabah Boukherroub who helped me a lot during my visit in France. Thank to their enthusiasm and friendliness it was easier to stay so long far from home. I would like to thank all members of the Nanobiointerfaces Group for a good atmosphere in the laboratory.

I would like to thank all members of the Department of Electrode Processes, expecially the Surface Nanoengineering Group for their cooperation and friendly atmosphere. I would like to express my gratitude to Dr. Martin Jönsson-Niedziółka, Dr. Wojciech Nogala and Dr. Wojciech Adamiak, for their help in the laboratory, fruitful discussions and for sharing with me many interesting ideas.

I would like to thank the coordinator of the International PhD Projects Programme Prof. dr. Alina Ciach.

I would like to thank Dr. Adam Presz (Institute of High Pressure Physics PAS) for SEM micrographs, Dr. Janusz Sobczak and Dr. Wojciech Lisowski for XPS analysis, Dr. Adam Łaszcz and Prof. dr. Andrzej Czerwiński (Institute of Electron Technology) for TEM analysis, Dr. Janusz Stafiej for preparing cellular automaton model, Dr. Yannick Coffinier (Interdisciplinary Research Institute, France) for SEM micrographs, Dr. Agnieszka Kamińska and Dr. Sylwester Gawinkowski for SERS measurements, Dr. Marcin Pisarek for AES analysis, Justyna Jędraszko for SECM measurements, and one more time Dr. Martin Jönsson-Niedziółka for SEM and AFM micrographs, and photographs.

I would like to thank Prof. dr. Sebastian Maćkowski (Nicolaus Copernicus University) for giving me an opportunity to do measurements in his laboratory. I would like to thank the Optics of Hybrid Nanomaterials Group, especially Magdalena Twardowska, Kamil Wiwatowski and Bartosz Krajnik for introducing me to the wide-field fluorescence and confocal microscopy, and their help with all measurements.

I would like to thank my Family and Friends who always believe in me and support all my decisions.

Finally, many grateful thanks to My Paweł who is inexhaustible source of support, patience and love.

To the memory of my beloved Mom

I would like to acknowledge financial support from:

The Institute of Physical Chemistry, Polish Academy of Sciences

The Foundation for Polish Science

Project operated within the Foundation for Polish Science International PhD Projects Programme co-financed by the European Regional Development Fund, Operational Program Innovative Economy 2007-2013.

The Foundation for Polish Science

FOCUS Programme No. 3/2010

Abstract

In this thesis, new methods for the preparation of interfaces covered with gold nanoparticles (AuNPs) and/or reduced graphene oxide (rGO) based materials are introduced. An electrode|aqueous electrolyte|gold precursor solution in toluene three-phase junction was applied for AuNPs electrodeposition. Nanoparticles obtained in various conditions, with cyclic voltammetry or chronoamperometry, were investigated to find optimal conditions for their electrodeposition. To characterize the properties of AuNPs deposited at the electrode surface, electrochemical, spectroscopic and microscopic methods were employed. These modified surfaces were applied as a new catalytic and bioelectrocatalytic material, as well as sensing platform for surface-enhanced Raman spectroscopy (SERS) and fluorescence microscopy. This allowed to demonstrate some potential applications of AuNPs deposited at the three-phase junction.

In the following part, a new and simple method for graphene oxide (GO) reduction and simultaneous functionalization was proposed. Selected aromatic molecules were employed as reducing agents in reactions carried out under mild conditions. To characterize the new composites, electrochemical, spectroscopic and microscopic techniques were used. These composites were also investigated as potential substrates for sensors and (electro)chemical switches.

Finally, both materials, AuNPs and/or reduced GO, were applied as new sensors in fluorescence microscopy. Using these materials separately and afterwards hybrid coatings containing both structures, allowed exploring interactions between them. This strategy was also applied to explore fluorescence properties of a selected biomolecule and the influence of both materials on it.

Streszczenie

W niniejszej pracy zostały przedstawione nowe metody otrzymywania podłoży pokrytych nanocząstkami złota i/lub materiałami zawierającymi zredukowany tlenek grafenu (rGO). Złącze trzech faz electroda|elektrolit wodny|roztwór prekursora złota w toluenie zostało wykorzystane do elektroosadzania nanocząstek złota. Nanocząstki otrzymane w różnych warunkach, przy pomocy woltamperometrii cyklicznej lub chronoamperometrii, zostały zbadane w celu określenia optymalnych warunków ich electroosadzania. Aby scharakteryzować właściwości nanocząstek złota osadzonych na powierzchni elektrody wykorzystano metody elektrochemiczne, spektroskopowe i mikroskopowe. Tak modyfikowane powierzchnie zostały zastosowane jako nowy materiał katalityczny i bioelektrokatalityczny, jak również jako platforma do powierzchniowo wzmocnionej spektroskopii Ramana (SERS) i mikroskopii fluorescencyjnej. Eksperymenty te pozwoliły zademonstrować pewne potencjalne zastosowania nanocząstek złota otrzymanych na granicy trzech faz.

W kolejnej części, zaproponowano nową i nieskomplikowaną metodę redukcji tlenku grafenu (GO) i jego jednoczesnej funkcjonalizacji. Wybrane cząsteczki z grupy związków aromatycznych zostały użyte jako reduktory w reakcjach prowadzonych w łagodnych warunkach. Aby scharakteryzować nowe kompozyty zastosowano szereg metod elektrochemicznych, spektroskopowych i mikroskopowych. Zostały one również wykorzystane jako potencjalne podłoża do czujników oraz (elektro)chemicznych przełączników.

W końcu oba materiały, nanocząstki złota i/lub zredukowany GO, osadzone na powierzchni zostały zastosowane jako nowe czujniki w mikroskopii fluorescencyjnej. Wykorzystanie tych materiałów osobno, a następnie hybrydowych warstw zawierających obie struktury pozwoliło badać ich wzajemne oddziaływania. Ta strategia została również zastosowana do poznania właściwości fluorescencyjnych wybranej biocząsteczki oraz wpływu jaki mają na nią oba materiały.

TABLE OF CONTENTS

Acknowledgements…… i

Abstract…… v

Streszczenie…… vi

Major abbreviations..…… 1

Introduction…… 3

Literature review…… 4

1. Gold nanoparticles ……..…… 4

1.1. Introduction……... 4

1.2. Synthesis…… 5

1.3. Physico-chemical properties…… 7

1.3.1. Surface plasmon resonance (SPR)…… 7

1.3.2. Fluorescence…… 10

1.3.3. Catalysis…… 13

1.4. Applications..…… 15

2. Electrochemistry at a three-phase junction…… 22

2.1. Introduction……... 22

2.2. Droplets immobilized on the electrode surface..…… 23

2.3. Flat or cylindrical electrode immersed in two immiscible liquids…….. 26

3. Graphene and graphene-based materials…… 30

3.1. Introduction……... 30

3.2. Properties……... 31

3.3. Synthesis…… 32

3.4. Applications……... 39

4. Indium tin oxide nanoparticles…… 47

4.1. Introduction……... 47

4.2. Preparation methods and properties…… 47

4.3. Applications……... 50

Goal…… 54

Results and discussion…… 55

5. Techniques…….. 55

5.1. Cyclic voltammetry.....……..... ***55***

5.2. Chronoamperometry…… 56

5.3. Scanning electrochemical microscopy…… 57

5.4. Atomic force microscopy…… 59

5.5. Scanning electron microscopy…… 60

5.6. Transmission electron microscopy…… 62

5.7. UV-vis spectroscopy…….. 63

5.8. Surface-enhanced Raman spectroscopy…..…… 64

5.9. Wide-field fluorescence microscopy…… 65

5.10. Confocal microscopy…… 66

5.11. X-ray photoelectron spectroscopy and Auger electron spectroscopy….. 68

5.12. Contact angle measurements…….. 69

6. Chemicals, materials and biomolecules…… 71

7. Instrumentation…… 73

8. Electrodeposition of gold nanoparticles at a three-phase junction…… 75

8.1. Preparation of the electrochemical cell and electrodeposition protocol… 75

8.2. The mechanism of the reaction and modeling…… 78

8.3. Characterization…… 84

8.3.1. Voltammetry…… 84

8.3.2. Optical, SEM and AFM imaging…… 85

8.3.3. Auger Electron Spectroscopy…… 90

8.3.4. UV-vis spectroscopy…… 91

9. Catalytic properties of gold nanoparticles…… 94

9.1. Glucose electrooxidation…… 94

9.2. Dioxygen reduction…… 95

10. Indium tin oxide and gold nanoparticles hybrid material.…… 100

10.1. Layer by layer deposition of ITO nanoparticles…… 100

10.1.1. Deposition protocol…… 100

10.1.2. SEM and AFM characterization…… 101

10.2. Electrodeposition of gold nanoparticles on ITO nanoparticulate film… 103

10.2.1. (Electro)deposition protocol…… 103

10.2.2. Electrochemical and microscopic characterization…… 103

10.3. Catalytic properties of gold nanoparticles and ITO nanoparticulate film hybrid material ***107***

10.3.1. Glucose electrooxidation *107*

10.3.2. Dioxygen reduction *109*

10.3.3. Mediatorless bioeletrocatalysis with immobilized enzyme *112*

11. Graphene oxide and reduced graphene oxide based composites **115**

11.1. Graphene oxide and reduced graphene oxide ***115***

11.2. Reduced graphene oxide composites with dopamine and its derivatives ***117***

11.2.1. Characterization *118*

11.2.2. Modification *122*

11.3. Reduced graphene oxide composites with tetrathiafulvalene and its derivatives ***126***

11.3.1. Characterization *127*

11.3.2. Modification *130*

12. Surface-enhanced Raman spectroscopy **134**

12.1. Preliminary experiments with dyes ***134***

12.1.1. Malachite green isothiocyanate *134*

12.1.2. Rhodamine 6G, 1,4–mercaptobenzoic acid and porphycene *137*

12.2. Biomolecules sensing ***142***

12.2.1. L-alanine *142*

12.2.2. Choline *143*

13. Fluorescence microscopy **145**

13.1. Introduction ***145***

13.2. Preparation protocol and SEM characterization ***146***

13.3. Wide-field fluorescence microscopy. ***147***

13.4. Confocal microscopy ***150***

Summary and conclusions **155**

References **157**

Published papers **171**

Major abbreviations

ACN	acetonitrile
AES	Auger electron spectroscopy
AFM	atomic force microscopy
AuNPs	gold nanoparticles
Bchl-*a*	bacteriochlorophyll-*a*
BOx	bilirubin oxidase
CA	chronoamperometry
$CBPQT^{4+}$	cyclophane cyclobis(paraquat-p-phenylene)
CE	counter electrode
CNTs	carbon nanotubes
CV	cyclic voltammetry
CVD	chemical vapor deposition
DA	dopamine
DA≡	alkynyl-terminated dopamine
DA-N_3	azide-terminated dopamine
DLA	diffusion limited aggregation
EDC	ethyl(dimethylaminopropyl) carbodiimide
EF	enhancement factor
Fc	ferrocene
FET	field-effect transistor
FIB	focused ion beam
FMO	Fenna-Matthews-Olson
FRET	fluorescence resonance energy transfer
FTO	fluorine doped tin oxide
Fwhm	full width at half maximum
GC	glassy carbon
GNRs	graphene nanoribbons
GO	graphene oxide
HAADF	high angle annular dark field
HS-PF	*1H,1H,2H,2H*-perfluorodecanethiol
IR	infrared
ITO	tin doped indium oxide
ITO_{NP}	tin doped indium oxide nanoparticles

LED	light emitting diode
LIBs	lithium ion batteries
LoD	limit of detection
LSPR	localized surface plasmon resonance
MBA	*1,4*-mercaptobenzoic acid
MGITC	malachite green isothiocyanate
n-BuFc	*n*-butylferrocene
NHS	*n*-hydroxysuccinimide
NOP	*N*-octyl-2-pyrrolidone
NR	normal Raman
ORR	oxygen reduction reaction
PC	porphycene
PPC	pigment-protein complex
R6G	rhodamine 6G
RE	reference electrode
rGO	reduced graphene oxide
SECM	scanning electrochemical microscopy
SEM	scanning electron microscopy
SERS	surface-enhanced Raman spectroscopy
SPM	scanning probe microscopy
SPR	surface plasmon resonance
STEM	scanning transmission electron microscopy
TE	transparent electrode
TEM	transmission electron microscopy
THF	tetrahydrofuran
TOA($AuCl_4$)	tetraoctylammonium tetrachloroaurate
TOABr	tetraoctylammonium bromide
TTF	tetrathiafulvalene
TTF-N_3	azide-terminated tetrathiafulvalene
UME	ultramicroelectrode
WE	working electrode
XEDS	energy dispersive X-ray spectroscopy
XPS	X-ray photoelectron spectroscopy

Introduction

Gold nanoparticles have been widely used for centuries, in chemistry and electrochemistry, materials science or biology and medicine. At that time, a significant number of preparation methods that allow obtaining nanoparticles with different properties were introduced and developed. Although this field is intensively explored, there is still a space for novelty in the formation of gold nanoparticles with appropriate characteristics. Multifarious nanoparticles are of great interest *e.g.* as a catalyst in electrochemistry, but also in various spectroscopic techniques as a platform for imaging and sensing.

Recently, graphene and graphene-based materials are intensively explored due to their interesting and attractive properties. These materials found applications in many fields of science, ranging from electronics and photonics to supercapacitors, solar cells, biodevices and sensing platforms. For this reason, graphene and graphene-based materials have become a serious competitor to metallic nanoparticles. More and more often these new, pristine and hybrid, materials are introduced as a better and more efficient replacement for gold nanoparticles.

This thesis is a result of the research on surfaces modified with gold nanoparticles and/or graphene-based materials provided since 2009 until 2013 at the Institute of Physical Chemistry in Poland and at the Interdisciplinary Research Institute in France. Electrodeposition at a three-phase junction is presented as a new method for the formation of flower-like, stable and well-adhered gold nanoparticles. Due to their properties, multifarious gold nanoparticles found applications in (bio)catalysis and optical sensing. In other part of this work, a simple method for graphene-based materials formation is introduced. After functionalization, the resulting structures are studied as prospective materials for (bio)sensing and (electro)chemical switches.

In the final part, hybrid materials of gold nanoparticles and reduced graphene oxide are used as complex platforms for investigating photosynthetic pigment-protein (the Fenna-Matthews-Olson (FMO)) complex. For a better understanding of the photosynthesis, it is important to explore the adjustement of the energy sites by the protein and photon conversion. Fluorescence properties of the FMO, *i.e.* fluorescence transients, were investigated on both materials, separately and together. Although the described experiments are at the preliminary stage and results are not easily explainable, they are very promising and further research may result in valuable information about photosynthetic complexes.

LITERATURE REVIEW

1. Gold nanoparticles

1.1. Introduction

Gold nanoparticles (AuNPs) have been well-known and utilized for centuries, mostly by artists, for coloring stained glass, ceramics, or even huge statues. The reason for such a great interest is due to remarkable colorful visual effects. However, when the historical aspect of gold is discussed, one should rather use the term a "colloidal gold", since this noble metal was used in the form of a suspension, usually in water. In the Middle-Ages, colloidal gold found another application in medicine [1]. It was called "an elixir of life", and was broadly utilized as a cure for various ailments, even melancholy. Talismans in the form of small objects or powders were very eagerly used as an amulet against evil spirits. In the 17th and 18th centuries more detailed information about healing properties of gold were provided by alchemists [1]. It was believed to have a soothing and salutary effect on the heart and was used against fainting and fevers, as a drug on blistered skin or the gums and tongue, as well as a treatment of syphilis, goiter and scrofula [1]. Although with time, the attitude towards therapeutic properties of gold had changed, and negative effects on the body were noticed, the colloidal gold was still used in medical diagnostics up to the 20th century [2].

More scientific studies on the properties of colloidal gold have been carried out for the first time at the end of the 19th century by Michael Faraday [3]. In his work, he described optical properties of gold that strongly depended on the experimental conditions such as the gold film thickness, the concentrations of the suspension or the applied mechanical compression. In the second half of the 20th century, not only diverse new methods of preparation were presented [4–10], but also much more detailed investigations of physic-chemical properties. The size and shape dependent optical, electronic and magnetic properties were intensively studied and reported (quantum size effect). Thanks to the better understanding of the nature of gold nanostructures, but also their stability and biocompatibility, they found applications in many fields of science: chemistry, electronics, electrochemistry, materials science, but also in biology and medicine, as therapeutic, imaging or sensing agents.

Although nowadays scientists acquire in-depth knowledge about gold nanostructures, there is still an unfilled space for novel procedures of preparation, and even more importantly there is a great need for nanomaterials which could be used in "real life" devices.

1.2. Synthesis

Research on nanomaterials requires the selection of an appropriate method of their preparation. In the case of nanoparticles, well-defined dimensions as well as monodispersity are crucial. This is one of the reasons for the development of various synthetic methods [11].

The first, widely explored group, are "liquid chemical methods". The most conventional version, known today as a classical one was introduced in 1951 by Turkevich *et al.* [4]. Au nanoparticles of a round shape, with the size *ca.* 10-20 nm, were prepared by the reduction of $HAuCl_4$ in water by sodium citrate (Figure 1.1). Although, in 1970s Frens *et al.* obtained Au nanoparticles with a wider range of diameters, between 10 and 147 nm, there was a problem to keep a small size distribution for larger nanoparticles, and avoid the formation of aggregates [5,6].

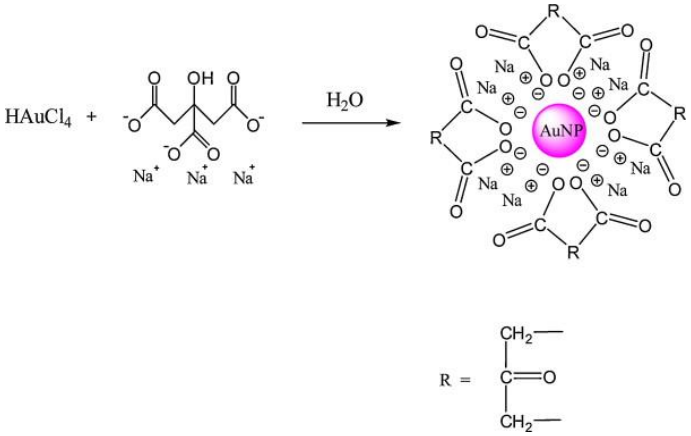

Figure 1.1. AuNPs synthesis using the Turkevich method [11].

A two-phase system pioneered by Faraday in the 19th century [3], was an inspiration for Brust and Schiffrin to grow gold clusters in a liquid-liquid (water-toluene) system [7,12] (Figure 1.2). In their case, gold precursor was dissolved in an aqueous phase and tetraoctylammonium bromide, which was both a stabilizing agent and a phase transfer reagent, was in toluene. By a vigorous stirring, tetrachloroaurate was transferred into the organic phase. At the end, a binding agent (dodecanethiol) and a reducing agent (sodium borohydride) were added one after another. This idea had a great impact on the development of novel methods for nanoparticles preparation, because it overcame many drawbacks and difficulties that appeared before. First of all, the obtained gold clusters were stable, could be prepared in organic solvents, but also precipitated and re-dissolved. Additionally they might be functionalized in a

controlled manner with self-assembled monolayer of interest. Analogous system was used by Sastry *et al.*, however as an organic phase they employed hexadecylaniline (HDA) in chloroform [13]. The size of the nanoparticles was easily controlled by $AuCl_4^-$:HDA molar ratio.

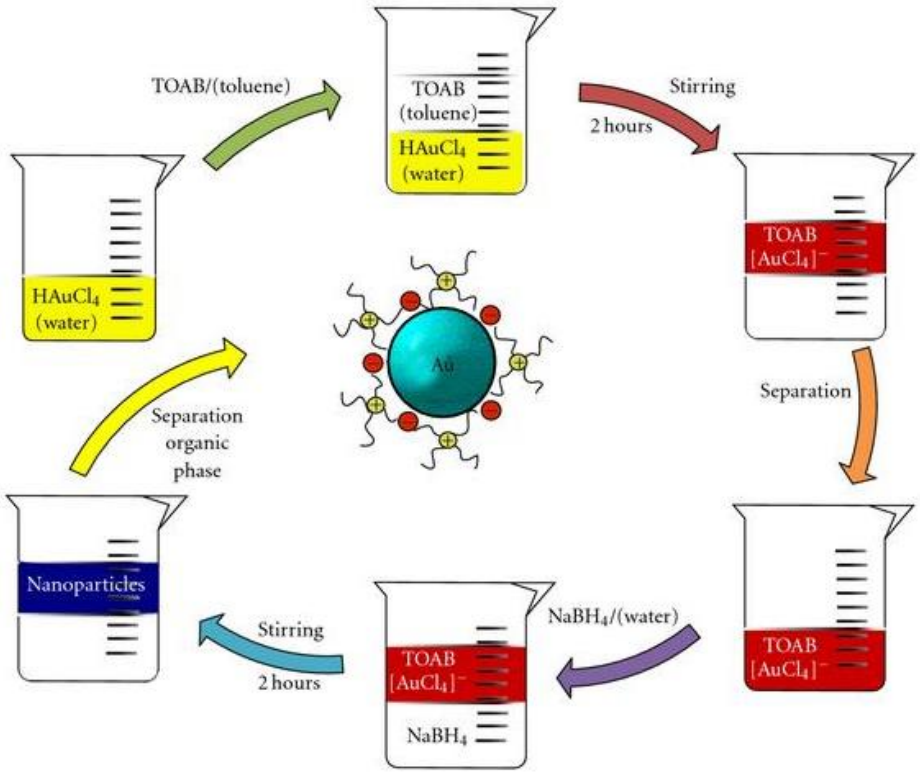

Figure 1.2. Scheme of the Brust and Schiffrin synthesis of gold nanoparticles [12].

An electron transfer across the liquid-liquid interface induced the possibility for the utilization of an electrochemical control over this process. Initially the idea was realized by the application of an appropriate potential that drives the reduction process of $AuCl_4^-$ ions in the organic phase using potassium hexacyanoferrate (II) $[K_4Fe(CN)_6]$ in water as the electron transfer agent [8]. This reaction resulted in the formation and growth of gold nanoparticles at the interface and not in the bulk solution. In another approach, with organic solvent as a source of gold precursor, a water soluble monomer, like tyramine, was involved [14–16]. In that case, gold ions were reduced by the monomer and then the electropolymerization proceeded. Finally, AuNPs were formed and stabilized by the polymer matrix. It was also shown that by adjustment of the Galvani potential difference the size of the nanoparticles can be altered in a controlled manner [16].

Contrary to the presented examples, the two-phase systems of an aqueous solution with Au ions and an organic solvent with hydrophobic electron transfer agent, was also

successfully applied and explored [17–20]. In the first case, in-depth analysis of aggregation processes was presented, in both qualitative and quantitative manners, using decamethylferrocene in *1,2*-dichloroethane as a lipophilic electron donor [17]. Dryfe *et al.* also utilized liquid-liquid interface to analyze the parallel routes for gold nanoparticles formation *via* interfacial reaction and bulk reaction followed by self-assembly [18]. In the latter one, tyrosine is used as a multifunctional agent (phase transfer, reducing and capping agent). In this system, a highly stable AuNPs can be formed both at liquid-liquid and air-water interfaces, and their morphology in these two situations are completely different [19].

By broadening the perspectives for new applications of gold nanoparticles, such as sensors and catalysts, there was a need to prepare suitable substrates or electrodes coated with nanoparticles. In most works, in order to modify the surface with gold nanoparticles, the electrodeposition from a single, aqueous or organic, phase was employed. The oldest methods require the electrodeposition of gold nanoparticles in a template, namely porous alumina membranes with a well-defined pore size [9,10,21]. In another protocol, prior functionalization of the gold nanoparticles with redox active molecules is necessary. These redox species are electrooxidized and consequently the assembly of metal clusters is formed on the surface [22]. Other methods involve the deposition of nanoparticles at an electrode surface through the electrochemical formation of a sol-gel film with previously mixed AuNPs [23] or layer-by-layer deposition of oppositely charged AuNPs [24]. Many works have been devoted to the direct reduction of gold-containing ions (Au^{3+} or $AuCl_4^-$) at the electrode, for example: indium tin oxide (ITO) [25–27], fluorine doped tin oxide (FTO) [28], or glassy carbon (GC) [29,30]. The latter case is an example of gold nanoparticles electrodeposition from a microemulsion system [30].

1.3. Physico-chemical properties

1.3.1. Surface plasmon resonance

Gold nanoparticles exhibit many interesting optical and electrical properties, which make them a promising material in a great number of branches of science. One of the feature that brought gold to the forefront of research is surface plasmon resonance (SPR) [31–34]. This phenomenon is strictly connected to the existence of the valence electrons. It means that the oscillating electromagnetic field of the incident light can cause the collective oscillations of the conductive electrons. When the frequency of the photons of incident light is adjusted, then the amplitude of the oscillations reaches maximum value and the resonance is observed. When the incident light interacts with gold nanoparticles instead of gold film, the localized

surface plasmon resonance (LSPR) might be generated [35–40]. For LSPR, incident light induces a strong absorption for the particles much smaller that the incident wavelength [35]. For both SPR and LSPR there is a strong dependence of the resonance position on the changes in a local dielectric environment. LSPR is additionally sensitive to the particles' properties, like size, shape, composition or structure. The difference between the propagation of plasmons in both cases is schematically presented in the Figure 1.3.

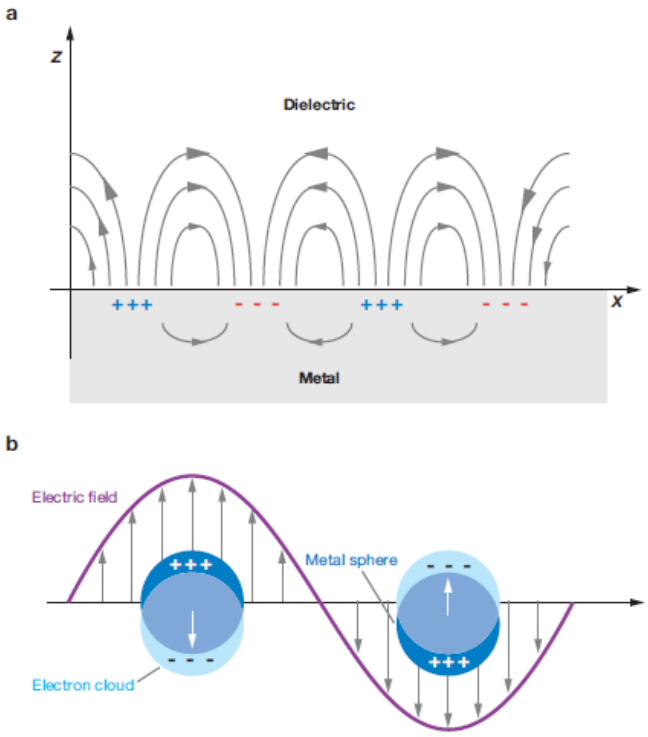

Figure 1.3. Schematic diagram illustrating (a) a propagating plasmon and (b) a localized surface plasmon [35].

The nature of surface plasmons was explained for the first time by Mie in 1908 [41]. His solution to Maxwell's equations describes extinction spectra of spherical particles of arbitrary size. The entire cross section of extinction (absorption + scattering) is given as total electromagnetic radiation. For smaller particles (< 20 nm) the solution can be given by taking into account only dipole oscillations of the conductive electrons. However for bigger particles, higher multipoles (especially quadrupole) become meaningful [36,42,43]. For the first case, the extinction cross section (C_{ext}) for isolated, round shape nanoparticles (dipole approximation) can be calculated using equation 1.1:

$$C_{ext} = \frac{24\pi^2 R^3 \varepsilon_m^{3/2}}{\lambda} \frac{\varepsilon_i}{(\varepsilon_r + 2\varepsilon_m)^2 + \varepsilon_i^2} \qquad \textbf{(1.1)}$$

where $\varepsilon = \varepsilon_r(\omega) + i\varepsilon_i(\omega)$ is the complex dielectric permittivity of the metal, $\varepsilon_r(\omega)$ is the real part and $\varepsilon_i(\omega)$ is the imaginary part of the dielectric function of the metal, ε_m is the dielectric constant of the surrounding medium, which is related to the refractive index of the medium by $\varepsilon_m = n_m^2$. SPR position and bandwidth are determined by $\varepsilon_r(\omega)$ and $\varepsilon_i(\omega)$, respectively [36,43].

There are many reports about the factors that influence the position and intensity of surface plasmons that are in agreement with Mie's solution, like AuNPs structure and morphology, temperature or dielectric constant of the closest surrounding [31,35–40,43–47]. One of the factors that was calculated from the Mie's solution is the influence of the thickness of the shell on the SPR for gold nanoshells [31,45,46]. This is another feature of nanostructure that can be used for tuning the position of the resonance band. For silica core of 60 nm in diameter, different thin shells were prepared, with the thickness 5 – 20 nm. This leads to the shift of SPR band of about 300 nm, and gives very promising perspectives for biomedical imaging and therapeutic applications (Figure 1.4) [45].

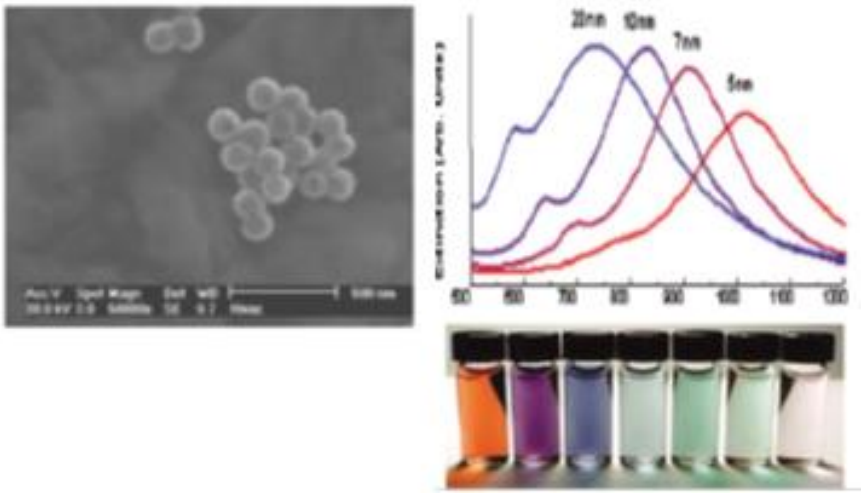

Figure 1.4. Tunable optical properties of gold nanoshells by changing the shell thickness [45].

Mie's solution was expanded for elongated nanoparticles by Gans in 1912 [48]. He explained the appearance of two plasmon resonance absorption bands, which correspond to the electron oscillations along two axes: transverse and longitudinal (Figure 1.5). The latter one, which is the consequence of the electron oscillations along the long axis, is shifted to the

near infrared range, according to the transverse one, and can be tuned by changing length/width ratio of the nanorod [31,36,43,47].

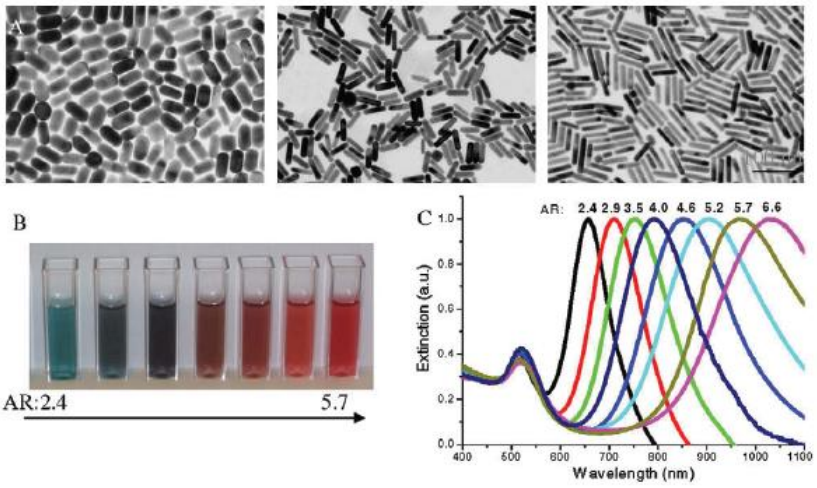

Figure 1.5. Tunable optical properties of gold nanorods by changing the aspect ratios. Gold nanorods of different aspect ratios exhibit different dimensions as seen by TEM (A), in different color (B) and different SPR wavelength (C) [43].

Although Mie's solution gives valuable information about dipole and multipole oscillations which can be applied to a great number of systems for modeling their optical properties, there are still systems than need more complex treatment. In order to take into account additional factors, like a presence of a layer deposited on particles, a substrate, eventual interactions between nanostructures, or heterogeneous environment, computational electrodynamics methods need to be applied [42,49,50].

1.3.2. Fluorescence

The first observation of photoluminescence in bulk gold, in the visible range of electromagnetic spectrum, was described in 1969, and its quantum efficiency was very low (10^{-10}) [51]. Later, when more researches were devoted to nanometer-dimensional samples, it was shown that Au nanostructures have significantly enhanced fluorescence, compared to the bulk gold, up to 6-7 orders of magnitude [52–54]. Fluorescence studies of Au nanoparticles [44,52–57], nanoclusters [53,58–62] and nanorods [53,63–65] have been carried out in a number of different systems and immediate environment conditions. These reports mostly concentrate on size and aspect ratio dependent properties (Figure 1.6) [55,56,58,63–65], but also on a crucial influence of the closest surrounding, like capping agents (Figure 1.7) [54,57,59–62] or employed matrices [58]. For

Au nanoclusters it was shown that emission spectrum can be tuned from UV to near-IR, when the number of atoms in the cluster is changed, between 5 and 31. Additionally the selection of an appropriate matrix, which influences Au quantum dots formation, can increase the fluorescence quantum yield [58]. In the case of Au nanorods the influence of aspect ratio was investigated to find optimum properties for creating new applications, for example in biosensing. Generally speaking, an increase of length with constant width red-shifts the emission wavelength maximum and increases the quantum yield [63,64].

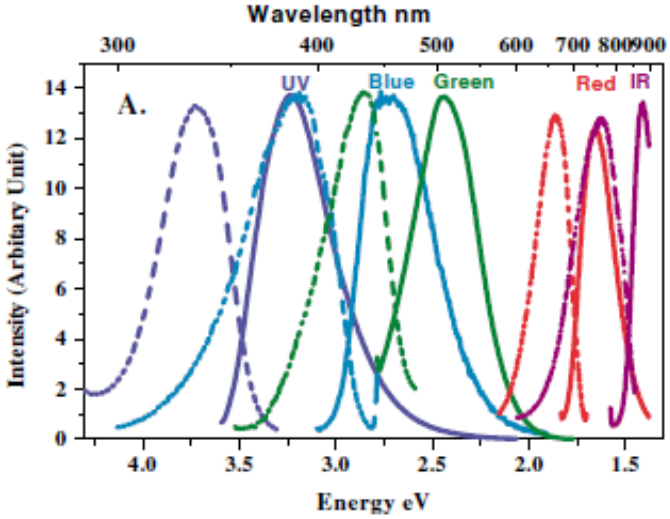

Figure 1.6. Excitation (dashed) and emission (solid) spectra of differently sized gold nanoclusters [58].

There have been many attempts to explain the mechanism of this phenomenon [51,54,57,61,62]. One of the commonly used models, employed in theoretical studies, involves an interband radiative transition between the conductive band and *d* bands[51]. In other works, the photoluminescence was assigned to recombination of electrons between the ground state and two different excited states [62] or to ligand to metal charge transfer transition [57]. Another attempt to model the relation between the surface modification of gold and its emission spectra was presented by Goldys and Sobhan [54]. They showed that the shift of emission energy may have electrostatic origins what was proved by using differently charged surface adsorbates. The appearance of ligands induces a shift of energy levels inside and outside the nanoparticles (the relative shift between Fermi energy level in the metal and highest occupied molecular orbital in the ligand), which consequently influences the fluorescence band position. Still none of the described models fully explains the impact of gold properties or the engaged ligands on the spectral shift or variations in quantum yield of the fluorescence.

Summarizing, it has to be emphasized that the lack of general model causes that still more effort is put into optimizing the experimental conditions in order to increase the quantum yield of fluorescence, than in-depth understanding the mechanism of the process.

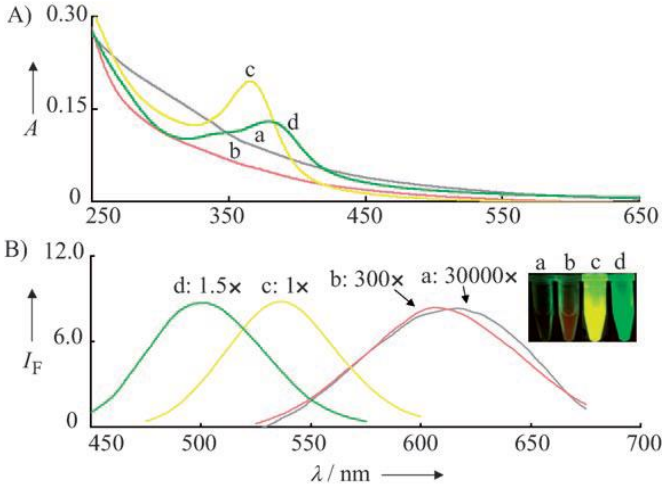

Figure 1.7. A) UV/Vis absorbance spectra and B) normalized fluorescence spectra of AuNPs (a), 2-mercaptoethanol-Au NPs (b), 6-mercaptohexanol-AuNPs (c), and 11-mercaptoundecanol-AuNPs (d) [57].

Fluorescence is studied not only as a native property of AuNPs but gold nanoparticles-based fluorescence sensors are also widely investigated. Several techniques, especially fluorescence microscopy, take advantage of the fluorescence measurements of investigated (bio)molecules in close proximity to metallic nanoparticles [53,66]. Depending on the distance between the probe and AuNPs, the fluorescence may be quenched or enhanced (Figure 1.8) [66]. When the molecule is close enough, its fluorescence is quenched due to non-radiative processes *e.g.* charge transfer to metallic structure. At a higher distance, it may still "feel" a very strong electromagnetic field from gold, while being far enough to donate an electron and its fluorescence can be significantly enhanced. When the distance is even bigger, molecules do not "feel" metallic nanostructures.

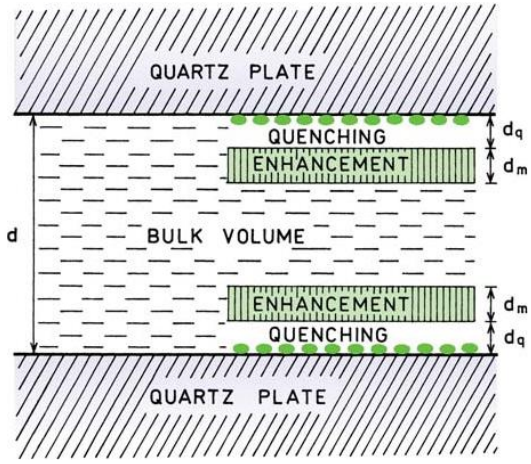

Figure 1.8. Schematic illustration for a fluorophore solution between two metallic island (green ellipsoids) films [66].

1.3.3. Catalysis

Although gold has been known since ancient times, and its nanostructured nature since the end of the 19th century [3], only in the 70's and 80's of the 20th century, Haruta [67,68], Hutchings [69] and Bond [70] recognized its unique catalytic activity. The first published reports presented gold nanoparticles supported on metal oxides which showed catalytic activity towards low-temperature oxidation of carbon monoxide and hydrogen [67,68], hydrogenation of mono-olefins [70] and hydrochlorination of acetylene [69]. Before these breakthrough discoveries, gold was considered as an inert metal which has a limited surface chemistry. Nonetheless during passing decades this unexplored field was greatly developed and nowadays an impressive number of reactions, which are catalyzed by (supported) gold nanostructures, can be demonstrated. These days great efforts are devoted in order to explain the nature of this phenomenon, the influence of the support [71–73], the properties of gold nanoparticles [71–73], and the existence of active sites (Figure 1.8) [74,75]. This is the reason why surface science, nanoscience and computational modeling have also been involved in this area.

The gold-based catalysts can be analyzed from different points of view. One can focus on preparation and characterization aspect [71,74], application in different reactions, structural sensitivity, or presence of active sites and the mechanism of the reactions [74–77]. It is not possible to include in one subchapter all important and valuable achievements and developments in the subject of gold-based catalysts. This is the reason why only a small and very condensed part of the total accomplishment with a couple of examples is presented here.

From a material perspective, a number of gold-containing structures used as catalysts can be mentioned. The simplest and most straightforward are single crystalline gold surfaces

[71,74,76], another ones are: so-called gold-single-crystal-based inverse model catalysts (single crystal of gold decorated with different metal compounds like oxides, nitrides or sulfides) [76], bimetallic systems (Pt, Pd, Ni, Ag or Cu used as the second metal) [74,76], and gold nanoparticles unsupported or supported on metal oxides (eg. TiO_2, MgO or FeO_x), which are probably the most commonly used [44,71–76,78].

The list of reactions which are catalyzed by gold-based catalysts is remarkably long. The first one, which is often used as a probe reaction to test the catalytic activity of the surface of interest is CO oxidation at low temperatures [44,67,68,71–75,78–80]. Gold-containing materials are also used to catalyze: selective oxidation of hydrocarbons, ketones, or aldehydes [73,76,81], carbohydrates (*e.g.* glucose) [24,73,82] or alcohols [44,73,76,80,81], C-C bond formation [76,79,81], hydrogenation reactions [44,71,73,76,81], reactions involving nitrogen oxides [71,73,83], cyclization reactions [81], formation of hydrogen peroxide [81,83], and others. It appeared that biocompatibility might also have an important influence on catalysis properties of gold-based catalysts. An important example that needs to be mentioned here are gold nanoparticles with additionally immobilized enzymes (eg. bilirubin oxidase [84], glucose oxidase [82], laccase [85] or horseradish peroxidase [86,87]) which were proved to provide suitable and favourable conditions for bioelectrocatalysis.

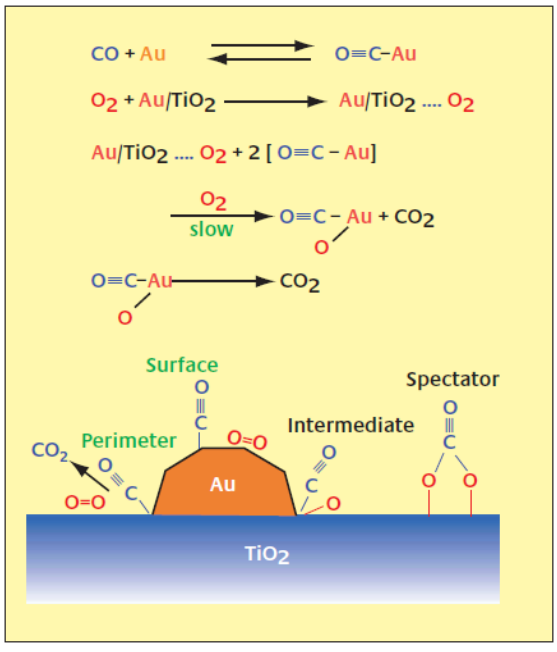

Figure 1.8. Schematic representation for CO oxidation pathways over Au/TiO_2 and possible existence of active sites [74].

More and more often, for deeper understanding of the mechanisms of different reactions, various computational models and theoretical analysis are involved. Also in the case of unique catalytic properties of gold these approaches are employed, in order to enrich or clarify experimental results [74,76,88]. Nevertheless there are still undeveloped areas in this subject, just like preparation of new catalytic materials, their application in potentially interesting reactions, and explanation for reactions mechanisms. For this reason, there is still much space for new opportunities and future studies.

1.4. Applications

There is a number of reasons for such a widespread use of gold nanoparticles and continued interest in this subject for such a long time but most likely biocompatibility, well-controlled synthesis and functionalization, as well as size- and shape-dependent properties are of crucial importance. In this subchapter, an outline of the possibilities offered by nanoparticles in biology, medicine and other related fields is presented. Although applications might be classified in many different ways, here they are shared into three sections: labelling (and imaging), sensing (and detection) and delivery (and therapy) (Figure 1.9).

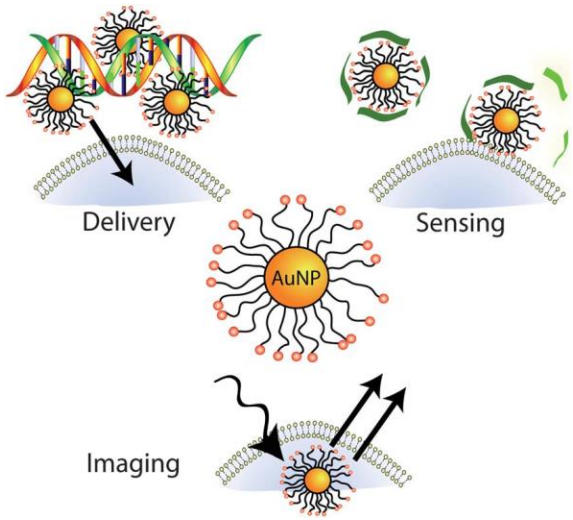

Figure 1.9. Applications of gold nanoparticles in bionanotechnology [89].

A wide spectrum of applications is accessible, *e.g.* through a broad spectrum of functionalization methods. Apart from the specific shape or size of gold nanomaterials, in most cases, additional elements or compounds need to be applied, for further use. Three main strategies for attachment can be mentioned: covalent bonding *via* gold-thiol groups [90],

physisorption [36], as well as noncovalent bonding thanks to the electrostatic interactions *via* charged particles and oppositely charged (bio)molecules. The first one is possible due to an affinity of sulfur to gold surfaces which is well-known however yet not fully explained [90,91]. It is worth to mention that these methods are well established however not trivial, since aggregation and unspecific binding have to be ruled-out. In some cases, bioconjugate chemistry with the most common crosslink ethyl(dimethylaminopropyl) carbodiimide/*N*-hydroxysuccinimide (EDC/NHS) method can be applied as the second step [92].

Gold nanoparticles have been used for a long time for imaging biological structures and have been also utilized as a contrast agent for labelling biomolecules or selected structures in living cells and organisms [31,43,45,52,93–97]. In this case, two issues need to be described: interactions between labelled element and specific region of interest which needs to be visualized, as well as applied imaging methods. Modified gold nanoparticles which are used for labelling were named by Parak and co-workers as "passive" reporters [98] because, unlike those used in sensors, their properties are not changed. The main techniques that are used for visualizing take advantage of the recognition between antibody- or ligand-conjugated gold nanoparticles and specific molecules or region of interest (antigens or receptors or regions containing them). While there are not so many ways for targeting gold nanoparticles, there is a wide range of methods used for imaging and most of them are based on photoexcitation. Some particles can be directly imaged with optical microscopy (in phase contrast or differential interface contrast) [45,93], dark field microscopy which can be used as a "colourful" method by applying nanoparticles of different size and shape [31,43,93,96], confocal microscopy [45,52,62,93,97], and fluorescence microscopy since gold is not so strongly affected by photobleaching like organic fluorophores [55,59,65,97]. The interaction between light and particles might also cause the local heating and consequently density fluctuations or liquid expansion. In the first case photothermal imaging is possible while sound wave that is created in the second case can be visualized with photoacoustic measurement. Apart from interactions with visible light, gold nanoparticles can be affected by electrons or X-rays. Thanks to the high molecular weight, (high-resolution) transmission electron microscopy (TEM), which gives the highest lateral resolution among all mentioned methods, can be successfully applied and even a single particle track can be followed, while for observing whole structures or even entire organs, X-ray computer tomography is one of the best choice.

(Bio)sensors and medical diagnosis devices are related to both identifying and determining the concentration of the analytes. During these analysis or measurements, properties of gold nanoparticles that are changing indicate the presence of the analyte or/and

additionally allow for its quantification. Sensors which are known and available nowadays can be divided into few groups depending on the properties of particles which are involved in its functioning. The first kind can be called optical biosensors or surface plasmon-based sensors. As the name suggests size- and shape-dependent optical properties of gold nanomaterials, but even more importantly the aggregation aspects are engaged. This method was pioneered by Leuvering [99], who used sol particles immunoassays which consisted of 40 nm gold particles and specific antibody in order to determine human chorionic gonadotropin hormone in urine (chromatographic immunoassays are used up to these days in pregnancy tests). This and other sensors of that type take advantage of plasmon band sensitivity towards creation of small aggregates or even slight distance changes between two single nanoparticles, which shift the resonance band and in consequence change the color of the solution. The subject of colorimetric detection of analytes was substantially developed by Mirkin and co-workers [100], presented for the first time with DNA hybridization; it opened new opportunities for novel types of biosensors and sequencing schemes for DNA. Such investigations allow for single base pair mismatch detection during hybridization [93,97,101] or the presence of genetic mutations [93,95]. Similar concept was demonstrated for monitoring enzyme activity, using streptavidin-biotin interactions, depending on the presence of enzyme inhibitor, aggregation and color change occurred or not [34,89,98,102]. There are a lot of other possibilities, like "nanometer ruler" used for measuring distances between molecules with high precision [103], sensors used for detection of heavy metals, toxins or other environmental pollutions [57,89,97,104].

Fluorescence quenching effect in close proximity to gold nanoctructures is another strategy engaged in sensor devices. They are widely used for DNA hybridization studies [65,66,97,101]. Generally two concepts are used, in the first one, specific binding of receptor-conjugated gold particles with analyte results in the quenching effect and the decrease of fluorescence is observed [65,66,97,101]. However the opposite situation is also possible, addition of a spacer (DNA, metal ions or others) may cause receding of the analyte and recovery of the fluorescence [57,66,97]. Due to non-bleaching nature of gold nanoparticles and easy photobleaching of cellular native fluorescence, cell imaging is also possible [45,55,59,94,97]. Ahn *et al.* have shown that fluorescence-quenched AuNPs imaging allows for drug screening as well as rapid and efficient visual monitoring of enzyme activity [105]. Rotello *et al.* reported that sensor system with functionalized AuNPs can be utilized to differentiate various species of bacteria, but also to distinguish between normal, cancerous and metastatic cells [94]. The same group demonstrated the recognition of proteins by recording their fingerprint with "chemical

nose" sensor arrays (Figure 1.10) [89]. Although in most cases Au nanostructures are used to quench the fluorescence of biomolecules in close proximity, in recent years more and more efforts are devoted to study metal-enhanced fluorescence [36,66] *e.g.* for detection of heavy ions *e.g.* lead [106] or drugs *e.g.* cocaine [107].

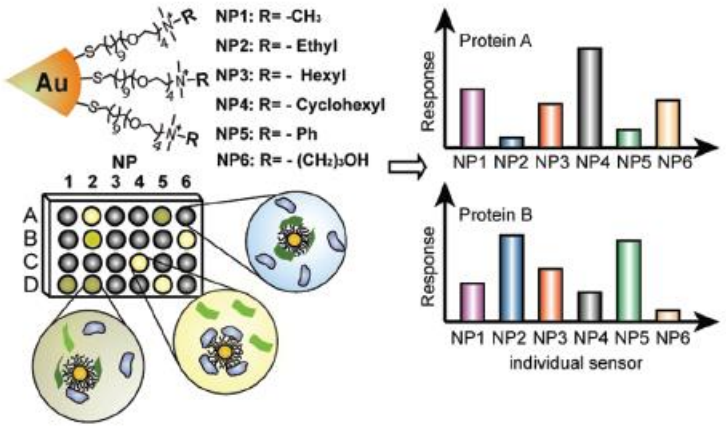

Figure 1.10. The combination of an array of sensors generates fingerprint response patterns for individual proteins [89].

Surface-enhanced Raman spectroscopy (SERS) is an extremely powerful tool used for imaging and sensing. However this section is mostly devoted to detection application of SERS platforms. In this technique, rough gold surface or nanoparticles are necessary to enhance Raman scattering that normally is very weak or even undetectable, because of its low probability (Chapter 5.9). Efficiently working, optimized platform can provide dramatic increase of the signal up to 10-11 orders of magnitude [108], what is the consequence of the strong enhancement of electric field close to the surface. Although it is not so trivial to prepare reproducible and stable SERS sensors, there is a long list of advantages which make it worth. First of all, every individual compound gives a characteristic signal (a fingerprint) and can be recognized also in more complex systems. Trace amounts of chemicals or even single molecules can be detected, as well as quantified, even in mixtures [108,109]. Finally, recorded signal is sensitive towards: orientation and symmetry of molecules, presence of specific functional group and their oxidation states, intermolecular interactions and deformations [108]. Qualitative and quantitative determination of proteins [110] or DNA can be performed. This technique has been also used in order to identify the composition of living cells or even whole organisms, as well as *in vitro* sensing [111]. Thanks to a very accurate and detailed information that can be obtained, SERS is also involved in a more advanced medical diagnosis of various diseases: cancer, diabetes, Alzheimer and Parkinson [108,110,112].

The last, but not least group of sensors employs electron transfer process. In this case, gold nanoparticle are used to amplify the signal by catalyzing the reaction and/or providing the extended active surface area, or simply ensure the connection between biomolecules and electrode surface [93,98,113]. Particles can be conjugated with an enzyme which specifically reduces or oxidizes an analyte, gold plays a role of a connector or a tunnel for electrons between electrode surface and redox centers of an enzyme [93]. The presence of the analyte and the efficiency of redox reaction can be analyzed by measuring an electric current using *e.g.* cyclic voltammetry. Genosensors (DNA sensors) can be prepared using various strategies, for example by direct detection of gold nanoparticles anchored on DNA sensor surface by *e.g.* stripping voltammetry or by monitoring resistance changes after hybridization with high sensitivity towards point mutations of mismatches [114]; this gives a direct response about conductivity of DNA double helix.

There is a strong need for new therapeutical technologies, the development of novel delivery and therapy agents [93–95,97,115–117]. Gold nanoparticles stand on the forefront among already tested elements because of their outstanding physico-chemical properties, abundant surface chemistry and biocompatibility. The delivery applications are generally divided into two categories: drug or gene delivery and photothermal or photodynamic therapy [94,95,97]. For the first group there is a number of therapeutics already tested *in vitro, in vivo*, or sometimes even in clinical trials [115], *e.g.* anticancer agents, antibiotics, or other antibacterial agents, and anothers used for the treatment of gene and acquired diseases. There are few extremely important factors that need to be taken into account when planning new therapeutics: the choice of optimal properties of gold nanostructure (size, shape, stability and possible aggregations) and all conjugated elements or cargos, targeting strategy in order to maximize their accumulation in the place of interest (tumor cells in case of oncotherapy, or nucleus for genetic regulations) and lowering the potential toxicity in healthy tissues of the organism, as well as interactions with immune system, period of circulation in blood and methodology for removing them from the body (excretion) (Figure 1.11). Except the main component – gold nanoparticles (nanorods, nanoshells, nanocages, etc.), therapeutic agents consist of: therapeutic cargo with or without drug-host molecule, antibody or other specific targeting receptor ("active" delivery system), protective ligand, and sometimes additional molecules for *e.g.* fluorescence imaging (by this, the therapy is connected with diagnosis and it allows for theranostics) (Figure 1.11) [94,95,97,117]. There are a couple of intracellular delivery strategies which are based on either physical strategies, like microinjection or electroporation, and biochemical ones, using cationic coating, cell penetrating peptides, ligand-mediated

internalization, or sub-cellular targeting with biodegradable carriers [116]. Drug releasing method is not less important, one can use light- or pH-controlled release, as well as "cutting" bonds by reduction [94]. Gold nanoparticles are also widely tested in photothermal and photodynamic therapy (PDT). The first one is based on the ability of particles to convert absorbed energy through irradiation with light into thermal energy, this induce the local growth of the temperature and is utilized for denaturation of "sick" biomolecules or demaging of cancerous cells [95,97]. The methodology of PDT is slightly different, additional light-sensitive compounds, so called photosensitizers, need to be engaged. This compound is excited with light and reactive singlet oxygen species are generated, which consequently destroy cancerous cells and other targets, *e.g.* microbial or viral species [95,97]. For both phototherapies, similar like for drug delivery, very precise targeting and selectivity are crucial. The fact that some of those curing agents or therapies are used on patients should make us realize that it is a real chance for the application of bionanotechnology (based on gold nanostructres) in medicine, however all serious drawbacks, especially targeting and toxicity, cause that unfortunately only a very small part of the invented therapeutic strategies are in use, in a real life [115].

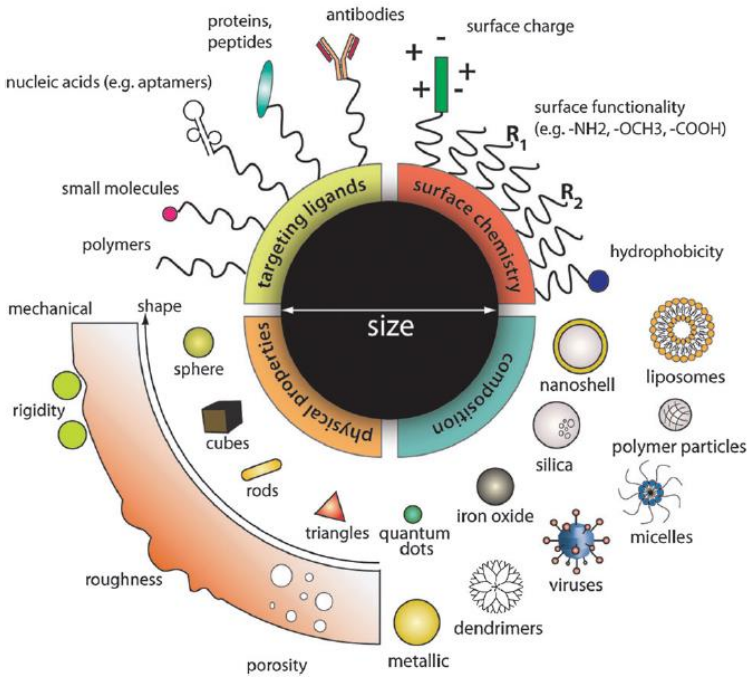

Figure 1.11. Designing nanoparticles for intercellular applications [116].

This chapter surely does not fulfill the entire potential of gold nanomaterials. However it presents an outline of a very broad area in science and real-life technologies where they are employed and a rough of a wide range of opportunities which they provide.

In this thesis, gold nanoparticles electrodeposited at a three-phase junction are investigated and characterized. At first, their properties are analyzed in detail with electrochemical, spectroscopic and microscopic analysis. Then AuNPs are used as a catalyst in reactions of glucose oxidation and dioxygen reduction. Finally, their prospective application as a biosensing platform is studied with surface-enhanced Raman spectroscopy and fluorescence microscopy.

2. Electrochemistry at a three-phase junction

2.1. Introduction

In this chapter, different types of electrified interfaces are discussed. An interface might be defined as an ideal plane, which determines the boundary between two phases. When two phases come to contact, the rearrangement of charges (electrons, ions or dipoles) close to the interface is observed. Consequently a potential difference across the boundary may be generated. This system is defined as an electrified interface.

In the first case, only one liquid phase, which needs to contain an electrolyte to provide an ion flow, is employed. The interface is created between a working electrode and a bulk solution, and applied potential (electrons flow) is used to drive a chemical process (ions flow). Afterwards, a conventional liquid-liquid interface can be engaged to measure ion transfer or to conduct the chemical process at the interface of two immiscible liquids boundary. Except charge transfer reactions across liquid-liquid interface [118–120], this system can be also used for *e.g.* investigating particles dynamics and separation [121], deposition of metallic clusters [8,122,123], or generating nanocrystalline films [18,20].

Instead of two components (electrode-liquid or liquid-liquid), three phases in various configurations can be also used to provide triple interface systems. A thin film of a liquid can be immobilized on the electrode interface which is immersed in the other liquid phase [124,125]. In contrast to a conventional liquid-liquid interface, the interfacial ion transfer can be driven by the process placed on the electrode. An idea of a three-phase boundary can be also realized by the array of droplets immobilized on the electrode which is immersed in the second liquid phase, and a triple interface is formed on the circumference of the droplets [126–141]. On the other hand, in a more straightforward arrangement, the cylindrical or flat electrode can be immersed perpendicularly in two immiscible liquids, and a three-phase junction has a form of a belt or a stripe, which is created on a small zone where all three phases are in close contact with each other [142–149].

All mentioned systems and configurations need to be analyzed individually since they exhibit peculiar properties. In this chapter, two configurations which involve a three-phase junction are discussed: droplets immobilized on the electrode surface immersed in the second liquid phase and an electrode perpendicularly immersed in two immiscible liquids. This systems are widely used for investigating charge transfer reactions across two liquid phases and determining the Gibbs free energy of ion transfer [126–129,134–136,138,139,141–144], testing

catalytic [130] and photochemical [131] processes, depositing different materials [135,140,143–146], as well as they can be employed as a sensor for a certain type of ions [132].

2.2. Droplets immobilized on the electrode surface

The first strategy for creating triple phase interface consists of single or multiple droplet(s) (phase I) immobilized on an electrode surface (phase II), which is then immersed in another liquid (phase III) (Figure 2.1). In most cases droplet(s) of an organic phase are attached on a solid surface dipped in an aqueous phase. Most of all, this approach has been employed to estimate the Gibbs energy of ions transfer, for simple organic and inorganic cations [128,135,141] or anions [126,131–136,138,139,141,150,151], but also for more complicated systems, like ionic forms of small peptides and amino acids [128,129] or drugs [127]. Beneficially, experiments with this system might be carried out to study biphasic systems with no need to employ four-electrode setup, which allows to avoid serious problems, such as: (1) a required presence of two supporting electrolyte in both solutions, what can narrow the potential window, (2) rather high volume of both solvents, (3) limited number of suitable supporting electrolyte that can be used in organic solvents, (4) a relatively complicated handling of the cell. By using three electrode cell, no supporting electrolyte is necessary in the organic phase, its volume can be very small, but also no reference electrode for the organic solvent is needful.

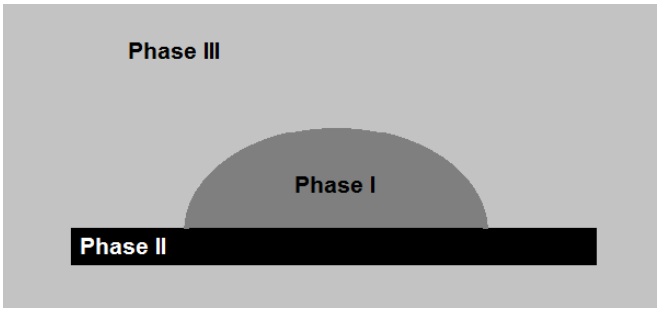

Figure 2.1. Schematic illustration of a droplet (phase I) deposited on the electrode surface (phase II) and immersed in another liquid phase (phase III).

A triple interface systems together with a three-electrode cell configuration give the possibility to work with a wide variety of both organic solvents with redox probes [126–129,133–135,140,141,150,151] and pure redox liquids [131,132,136–139]. No necessity for a supporting electrolyte in the water immiscible phase even broadens the group of prospective and suitable organic

liquids. Both polar (acetone [140], nitrobenzene [126,128,129,133,134,141], *n*-octanol [127,141] or *1,2*-dichlotoethene [127,135]) and non-polar (toluene [151], decane [150] or hexane [150]) solvents can be employed in the experiments with the three-phase junction. For experiments utilizing organic solvents with redox probes, various species like ferrocene [133,134], decamethylferrocene [126,127,129,134,141,150,151], potassium hexacyanoferrate [135], hexaammineruthenium (III) chloride [135], Fe(III) tetraphenylporphyrine chloride [141] have been tested.

Depending on whether the redox species or liquid is electrooxidizable or electroreducible, either anion (Figure 2.2 a) or cation (Figure 2.2 b) transfer can be observed across the liquid-liquid interface, respectively. In the first case, the oxidation of the compound in the organic phase is accompanied by the anion transfer from the aqueous phase inside the organic droplet, what can be written as:

$$Red_{(org)} + An^-_{(aq)} \rightleftarrows Ox^+_{(org)} + An^-_{(org)} + e^- \quad \textbf{(2.1)}$$

However, the opposite situation with anion transfer from organic to aqueous phase is also possible. It depends on the Gibbs energy transfer of both anions. The one that is more easily transferable will leave its initial liquid phase and diffuse into the bulk of another phase.

Analogously, if the compound in the organic phase is electroreducible, its reduction will cause the transfer of the cation from the aqueous to the organic phase:

$$Ox_{(org)} + Cat^+_{(aq)} + e^- \rightleftarrows Red^-_{(org)} + Cat^+_{(org)} \quad \textbf{(2.2)}$$

Similarly like for anions, the opposite situation with cation transfer from aqueous into organic phase is possible. All described cases are determined by the Gibbs energy transfer of ions present in both liquid phases.

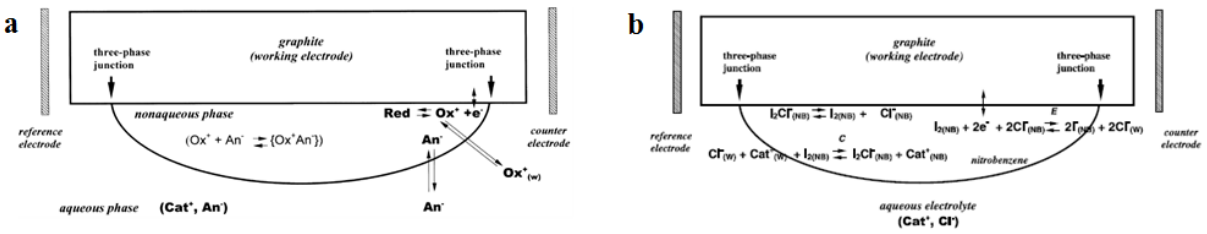

Figure 2.2. Schematic representation of the situation in which an organic droplet contains an electroactive species, which oxidation (a) / reduction (b) is accompanied by anions (a) / cations (b) transfer from the aqueous to the organic phase [128,134].

Although much effort was devoted to study the described type of setup, a methodology with aqueous droplets on an electrode surface was also performed by Compton and co-workers [135]. Conversely like with oil droplet(s), in this example, water droplet(s) attached to graphite electrode were immersed in organic phase (1,2-dichloroethane) with a supporting electrolyte (tetrabutylammonium perchlorate). Several types of systems were examined, with two redox species, potassium hexacyanoferrate and hexaammineruthenium (III) chloride, in supported and unsupported aqueous droplets. It was shown with cyclic voltammetry that for the unsupported system, while the reaction starts at a three-phase junction, the process is "easier" than when it takes place at the whole interface between a droplet and the working electrode. This means that the Gibbs free energy for $Fe(CN)_6^{4-}$ and $Fe(CN)_6^{3-}$ as well as $Ru(NH_3)_6^{3+}$ and $Ru(NH_3)_6^{2+}$ in unsupported droplets ($\Delta G^{unsupported}$) is lower than in supported droplets ($\Delta G^{supported}$). What is more, for $Fe(CN)_6^{4-}/Fe(CN)_6^{3-}$ couple the difference $\Delta G^{unsupported} - \Delta G^{unsupported}$ is higher than for $Ru(NH_3)_6^{3+}/Ru(NH_3)_6^{2+}$ couple, which is attributed to differently charges species and consequently various ionic strengths.

Despite the fact that a triple interface with immobilized droplet(s) has been generally used to study ion transfer across the liquid-liquid interface, it is worth to mention that there have been some attempts to utilize this setup as a microreactor for electrodeposition of metallic structures on the electrode surface at a three-phase junction [135]. Water droplets containing copper salt (with or without supporting electrolyte) were attached to the graphite electrode, which was then immersed in *1,2*-dichloroethane containing supporting electrolyte, and by applying potential for 20 s, the deposition was performed [135]. A comparison of a scanning confocal microscope images and profiles for unsupported and supported droplets revealed that in the first case, copper was present only at the circumference of the droplets, which proved that in that case the reaction took place only at a three-phase junction (Figure 2.3). This researches showed that in the inverse system, where aqueous droplets on the electrode are immersed in an organic electrolyte, provides favourable conditions for determining activity coefficients, but also takes advantage of the possibility to dissolve different metal salts in water and carry out electrodeposition, giving the evidence that the reaction takes place at a three-phase junction.

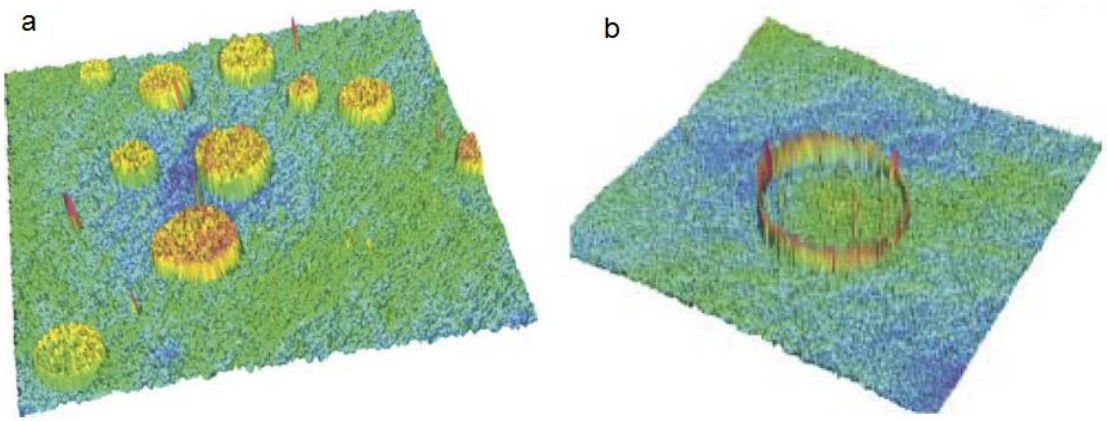

Figure 2.3. 3-dimensional images obtained with scanning confocal microscopy, for copper deposited in supported (a) and unsupported (b) droplets [135].

2.3. Flat or cylindrical electrode immersed in two immiscible liquids

In 2005, Stojek and co-workers introduced a novel methodology for obtaining and investigating a three-phase junction [142]. In this approach, a cylindrical electrode was perpendicularly immersed into two immiscible liquids, the organic solvent with a redox species and aqueous electrolyte with various inorganic salts (Figure 2.4 a). This was considered to be advantageous over microdroplets array, because of greater simplicity of preparation procedure and also reproducibility, since, it was much easier to repeat experiment, than preparing a number of times the same array of droplets. However it has to be noted, that the volume of both liquid phases is substantial, and this can be considered as a serious drawback, especially in the case of organic solvents. Generally, this approach where a wire or plate electrode is immersed in a biphasic system of two immiscible liquids (two bulk liquids phases), with one phase containing redox probe and the other a supporting electrolyte [142–149] was intensively explored not only for investigating ion transfer, but also electrogeneration of different structures at a three-phase junction. In this case, a position and a well-defined length of a boundary can be controlled by the dimensions of the electrode. There is a strong analogy with the droplet(s) system, because in order to maintain the electroneutrality both, charge and ion transfer, reactions have to occur simultaneously. If the organic phase does not contain initially a foreign electrolyte, the reaction can start only at a triple interface, where ions (from aqueous electrolyte) are available.

This setup has been applied in a number of reactions, where various materials were deposited: polymer layer on a platinum or gold cylindrical rod [143,144], silicate stripe [145] or film [146]. In the primary experiment [142] gold or platinum cylinders were used as a working

electrode, nitrobenzene as an organic solvent containing ferrocene or decamethylferrocene, and aqueous solution contained various organic salts. The formal potentials were determined from the standard potentials of transfer of anions across liquid-liquid interface for different diameters of the working electrodes. To prove in a more direct way that the process starts at a triple interface, a deposition of a polymer was utilized [143]. The monomer of *n*-vinylcarbazole was dissolved in nitrobenzene, and by applying a potential the monomer was oxidized and deposited in the form of a belt, in the place where both liquids were in contact. The thickness of the belt depends on the deposition time (Figure 2.4 b-d) and the kind of ions present in the aqueous solution. This experiment clearly confirms the contribution of a three-phase junction. The triple interface was also employed to deposit a silicate stripe with a sol-gel process [145]. In this approach, an ITO flat electrode was used as a working electrode, nitrobenzene as an organic solvent which contained a sol-gel precursor, *n*-octyltriethoxysilane, and aqueous electrolyte contained sodium sulphite [145]. The electrochemical oxidation of the sulphite anions resulted in protons formation, which then catalyzed the sol-gel process and the hydrophobic silicate stripe was formed. The similar strategy was used to obtain a thin functionalized silica film [146]. However, additional ionic liquid precursor was used and the electrode was slowly withdrawn in order to obtain a wider functionalized deposit.

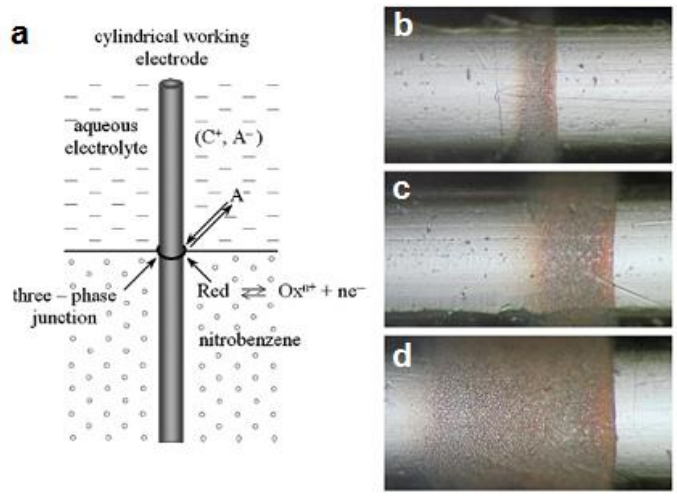

Figure 2.4. Schematic drawing of the formation of a three-phase junction at the cylindrical electrode immersed into two immiscible liquids (a), and optical microscope images of polymer deposited at a triple boundary during 50 s (b), 100 s (c) and 500 s (d) [143].

Marken and coworkers combined an idea of a three-phase junction with a microfluidic device [147]. In contrast with a traditional interface, both immiscible liquid phases, *N*-octyl-2-pyrrolidone (NOP) and aqueous electrolyte, flowed in the channels and gold

working electrode was immovable (Figure 2.5 a). This novel hydrodynamic system was used to investigate the oxidation of *n*-butylferrocene (*n*-BuFc) coupled with the transfer of anions from an aqueous to organic phase, and compared with a traditional one-phase flow system [147]. The reaction zone can be controlled by the flow rate and the size of the working electrode, however "undercutting" of the organic phase under the aqueous phase and the expansion of a three phase boundary was observed (Figure 2.5 b). The "flowing" three-phase junction was also investigated in different systems, where gold electrode was exchanged with boron-doped diamond [149] or platinised Teflon electrode [148]. In the first case, the problem of "undercutting" was solved by replacing NOP with acetonitrile, which not only stabilized the triple interface but also enhanced mass transport and rate of conversion [149]. In the following studies, *tert*-butylferrocene in acetonitrile was used instead of *n*-BuFc [148] and the system was investigated as a potential tool for new electrosynthesis with a limited use of the organic solution, electrolyte and purification processes.

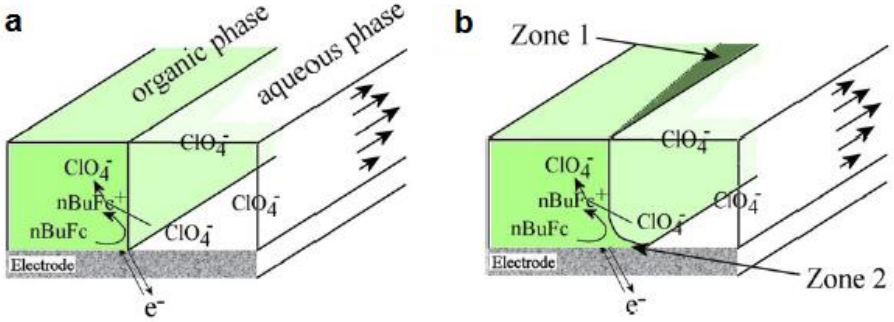

Figure 2.5. Schematic illustration of the coupled electron transfer (electrooxidation of *n*-BuFc in the organic phase) and anions transfer across liquid-liquid interface in the flow cell system (a) and the reaction zone (the expansion of a three phase boundary – zone 1 and "undercutting of the aqueous phase under the organic phase – zone 2) (b) [147].

All systems which involve a solid|liquid|liquid boundary with different configurations, various redox active species and electrolytes can be employed, among others, for investigating the transfer of cations and anions across liquid-liquid interface, as well as for electrodepositing different structures. In both cases, a simultaneous ion and charge transfer reactions are crucial and strongly dependent on each other. Introducing a triple interface provided the possibility to work in a three-electrode system and a great contribution into phase boundary studies has been given. Consequently, by determining the Gibbs transfer energy of particular ionic species, the knowledge about crucial biological and physiological processes between aqueous and organic domains has been deepened. Additionally, this kind

of system offers a better control over the process of electrogeneration, where the position and dimensions of the deposit can be imposed.

In this work, an electrode|liquid|liquid three-phase junction was employed for gold nanoparticles electrodeposition. Toluene was used as an organic phase which contains gold precursor and aqueous electrolyte was used as a source of counterions. Detailed analysis of the role of a triple phase in gold generation is presented and described in the Chapter 8.

3. Graphene and graphene-based materials

3.1. Introduction

Graphene is a two-dimensional (2D) one-atom thick honeycomb carbon lattice with remarkable electronic, mechanical, thermal and optical properties. It can be "wrapped up into fullerence, rolled into nanotube or stacked into graphite" (Figure 3.1) [152]. In the last couple of years graphene has become widely popular and eagerly explored worldwide thanks to achievements of Geim, Novoselov and co-workers from the University of Manchester in the UK and the Institute for Microelectronics Technology in Russia, who, in 2004, for the first time obtained and examined a single graphene layer [153].

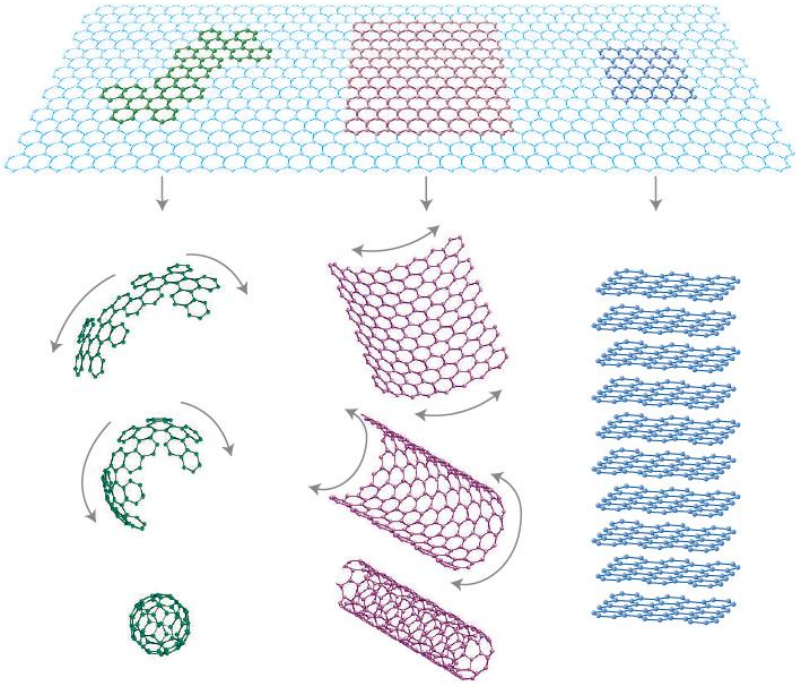

Figure 3.1. Graphene (on the top) presented as a material from which other structures like fullerenes (on the left), nanotubes (in the middle) and graphite (on the right) can be built up [152].

Nonetheless a story of graphene is much older than 9 years and theoretically it has been studied for more than six decades. In 1947 Phillip Wallace published his work "The band theory of graphite", in which he used an approximation and assumed that for his calculations interactions between planes in graphite can be neglected and each single hexagonal layer can be treated individually [154]. In 1984 Semenoff presented his considerations and calculations about electronic properties of graphite monolayer using dynamic model [155] and made very important conclusion about the presence of massless charge carriers (Dirac

fermions). The name "graphene" was used for the first time by Mouras and coworkers in 1987, and described co-called "Graphite Intercalation Compounds" which means materials with different elements or molecules inserted between graphite layers [156]. Contrary to reported theoretical predictions [154,155], at that time and also many years later, it was stated that this 2D material cannot exist individually in isolated form because it would be unstable [157] or immediately scroll on the periphery and buckle [158]. However since 2004 it was proved by many research groups that these issues do not preclude obtaining single graphene sheet.
Nowadays it is clear that graphene and graphene-based materials offer many interesting and attractive opportunities. The number of works devoted to them and quantity of created novel devices is already significant and still growing. They found applications in (flexible) electronics, transistors, energy storage devices, solar cells, or biodevices. In each case fabrication method plays a key role, for example for electronic devices, a high-quality and pure structure without defects must be utilized [152,153,159–173], while for biodevices usually graphene-based composites that are definitely not one-atom thick [12,108,173–288] can be applied.

In this chapter, the properties of graphene and graphene-based composites are presented and discussed. Preparation methods are of crucial interest in this work and for this reason most of the attention is devoted to this aspect. Finally, application opportunities are briefly described.

3.2. Properties

Graphene shows a great promise for applications in many fields of science and technology due to its remarkable properties that often exceed those of other materials. Its characteristics strongly depend on the production process (section 3.3). In this part, only the best properties ever reported for graphene prepared with various methods are collected.

One of the most important issues that makes graphene so attractive and progressive material is a very high electrical conductivity. Mayorov *et al.* showed that the device made of mechanically exfoliated graphene sandwiched between hexagonal boron-nitride crystals exhibits ballistic transport in micrometer scale at room temperature [289]. Charge transfer mobility calculated for low carrier concentration ($n \sim 10^{11}$ cm^{-2}) equals > 100 000 cm^2 V^{-1} s^{-1}, what grows even up to 500 000 cm^2 V^{-1} s^{-1} for $n \sim 10^{12}$ cm^{-2} and low temperature, that is one order of magnitude higher than graphene deposited on oxidized Si wafer [289].

For electronic and photonic industry not only electrical but also thermal conductivity is of crucial importance. That raises from the need for materials that can easily and efficiently

dissipate heat to keep the right temperature of the electronic systems. Carbon materials are especially interesting thermal conductors and recently it was shown that graphene reveals up to 5000 W m^{-1} K^{-1} , which is comparable or higher than differently prepared carbon nanotubes, but *ca.* 5 times higher than diamond and 5 orders of magnitude higher than amorphous carbon [290].

Optical transmittance of graphene was theoretically predicted and experimentally measured (with specially prepared graphene crystals) to be strongly influenced by its unusual electronic structure [291,292]. It was shown that one-atom thick single graphene layer absorbs $\pi\alpha$ = 2.3% of white light, where $\alpha = e^2/\hbar c$ is the fine structure constant. This result and the fact that each additional graphene layer (shown for 5 layers) increases opacity of exactly $\pi\alpha$ = 2.3% illustrates strong relation with quantum electrodynamics and the model of non-interacting massless Dirac fermions [292]. Light transmittance measurements also revealed that opacity in the visible range is practically independent on wavelength. In consequence, these excellent optoelectronic properties give real chances for wide range of new applications in photochemistry, photocatalysis and development of devices for energy conversion and storage [222,223].

Hone and coworkers presented measurements of elasticity and instrinsic breaking strength for a single graphene monolayer used as a membrane in atomic force microscopy measurements [293]. Results of their experiments proved that graphene is the strongest material ever measured, with the breaking strength of 42 N m^{-1}, Young's modulus of 1 terapascal (TPa) and intrinsic strength equals 130 GPa. To make these numbers more real and readable one can compare graphene with other materials that are the best in their "disciplines". Ultimate tensile strength which is the maximum stress that the materials can withstand, obtained for silicon or silicon carbide fibre was up to 7 GPa [294,295], for boron nitride nanotube it is up to 33 GPa [296] and for multi-walled carbon nanotube 11-63 GPa [297]. In the case of Young's modulus, a measure of stiffness, values characteristic for graphene are comparable with the highest classified diamond and single-walled carbon nanotube [297,298].

3.3. Synthesis

There are two important issues that need to be taken into account in order to choose the most appropriate method to prepare graphene, first is the quality of the material that one wants to obtain, the latter one is the production cost [173] (Figure 3.2). The most popular and

widely used techniques are: mechanical exfoliation, epitaxial method, chemical vapor deposition, graphene oxide reduction, and others less frequently utilized like pyrolysis of sodium ethoxide or unzipping nanotubes.

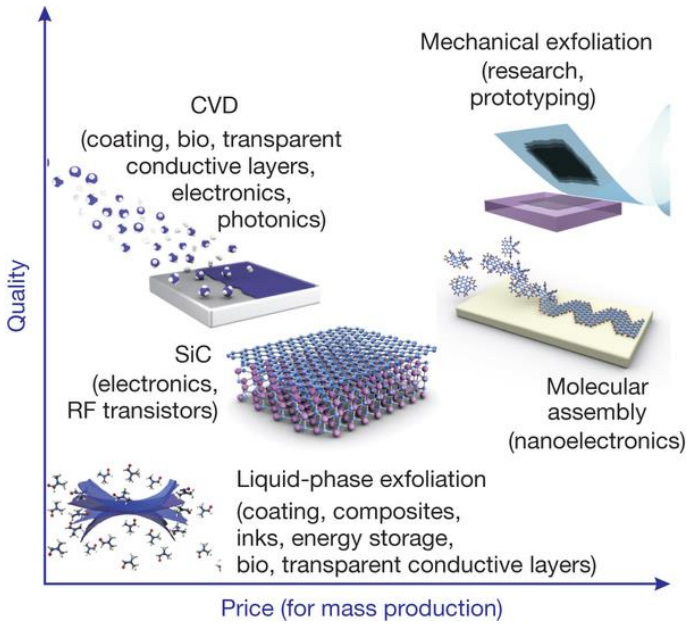

Figure 3.2. Various methods of graphene production in terms of quality and price as well as potential applications [173].

Mechanical cleavage allowed for the first time to obtain single graphene layer and more importantly to study its properties [153]. Researchers from Manchester group used adhesive tape to peel off repeatedly thinner and thinner graphite layers from highly oriented pyrolytic graphite, down to single graphene layer (Figure 3.3 c). Afterwards they employed multiterminal Hall bar devices in order to test electronic properties of the exfoliated flakes (Figure 3.3 d-e). Experimental values of charge carrier mobility exceed 15000 $cm^2 V^{-1} s^{-1}$, mean free path ~0.4 μm (defined as a ballistic transport of charges) and huge sustainable current (> 10^8 A/cm) was recorded. Graphene also exhibits pronounced ambipolar field effect which means that in the transistor charge carriers can be tuned from electrons to holes and back continuously by changing the gate voltage [152,153,159]. The band overlap was estimated down to 4 meV which is in agreement with theory that a single graphene layer is a zero-gap semiconductor. Although this method is not very productive and definitely not suitable for mass-production, nowadays it allows obtaining graphene flakes of the highest quality without defects, perfect for scientific purposes.

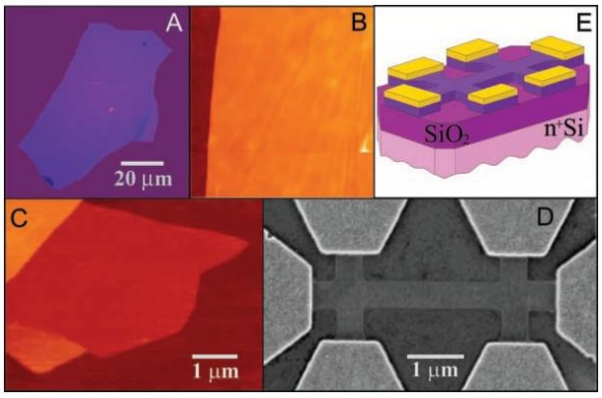

Figure 3.3. (A) Photograph of a relatively large multilayer graphene flake with thickness ~3 nm on the top of an oxidized Si wafer. (B) AFM image of 2 μm by 2 μm area of this flake near its edge. Colors: dark brown, SiO_2 surface; orange, 3 nm height above the SiO_2 surface. (C) AFM image of single-layer graphene. Colors: dark brown, SiO_2 surface; brown-red (central area), 0.8 nm height; yellow-brown (bottom left), 1.2 nm; orange (top left), 2.5 nm. (D) SEM image of one of our experimental devices prepared from few-layer graphene. (E) Schematic view of the device in (D) [153].

Another possibility for obtaining graphene is epitaxial synthesis on silicon carbide (SiC) [160–163]. First the surface is purified by etching in hydrogen, then the process occurs at high temperatures (>1200°C) in vacuum; under these conditions, silicon sublimates and graphene or thin graphite films are formed. Materials prepared with epitaxial growth are of rather high quality and were used by many researchers to characterize their physical properties. This method was used for the first time in 2004 and although authors did not produce single graphene flakes, they showed interesting results prepared with 3-layers ultrathin graphite [162]. Using magnetoconductance measurements high mobility and charge carrier density ~10^{12} cm^{-2} was determined. A thin film was also applied in a top-gate electrode and its conductance could be tuned by gate voltage. In another example, angle-resolved photoemmision spectroscopy was employed to determine the shape of π energy bands for one up to four graphene layers [160]. They also showed that due to interactions between layers the charge carrier concentration decreased for each additional layer of about one order of magnitude [160]. In contrast to mechanical exfoliation, epitaxial synthesis already found an application in transistor prototypes with 100 GHz speed, that one day might be commercially available (Figure 3.4) [163]. Compared to the most widely used silicon the cutoff frequency of the novel device is 2.5-10 times higher, showing a great promise for new electronic systems.

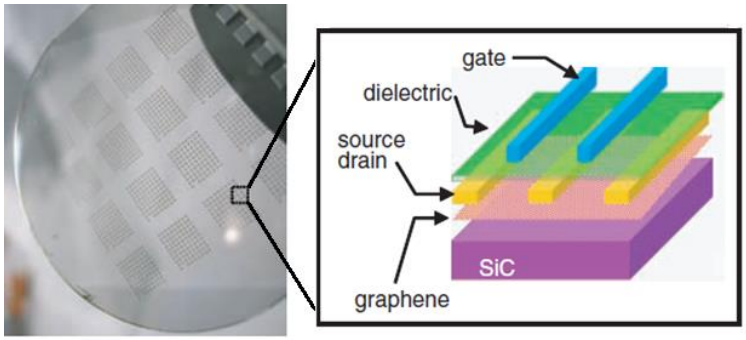

Figure 3.4. Image of devices fabricated on a 2-inch graphene wafer and schematic cross-sectional view of a top-gated graphene field-effect transistor [163].

Chemical vapor deposition (CVD) is the next competitive method which actually combine advantages of both previously describes techniques [164–169]. On the one hand, it is possible to obtain rather large size of continuous single graphene sheets like with epitaxial synthesis or even bigger. On the other hand, the initial surface materials that are employed are cheaper compared to SiC and the quality of the material is similarly high as obtained with mechanical cleavage [173]. In a CVD process the substrate and volatile precursor are placed in the chamber, and by applying high temperature the precursor decomposes on the surface and graphene growth process proceeds. The reaction might be provided in atmospheric pressure [166], low pressure [165–167] or vacuum [168] and the most popular surfaces used for CVD are copper [165–168] and nickel [164,167] foils or films. Afterwards, an ultrathin film can be transferred onto target substrate. Usually the charge carrier density is in the order of 10^3 cm^2 V^{-1} s^{-1} [164–166], and not more than 10^4 cm^2 V^{-1} s^{-1}, which is smaller than obtained for mechanically exfoliated graphene. There might be a couple of factors that influence electronic properties just like presence of grain boundaries and doping effect. Nonetheless, these values are still impressive and graphene obtainted with CVD is competitive. An improved roll-to-roll technique was presented in order to facilitate the production of large (30-inch) films for transparent electrodes (Figure 3.5) [165]. This method consists of three steps: polymer adhesion, copper etching and transfer of graphene into substrate of interest with polymer release. By combining optical transmittance up to 97.4%, resistance ~30 Ω sq^{-1}, high electron mobility of 7350 cm^2 V^{-1} s^{-1} and huge mechanical stability, it shows promises for replacing indium tin oxide electrodes [165]. Losurdo and coworkers also showed that for CVD method, the presence of hydrogen in the reaction is crucial but different for copper and nickel substrates [167]. Manipulation of hydrogen content may influence the deposition and growth process of graphene on the surface, as well as its quality, which means that it can be used to optimize experimental conditions.

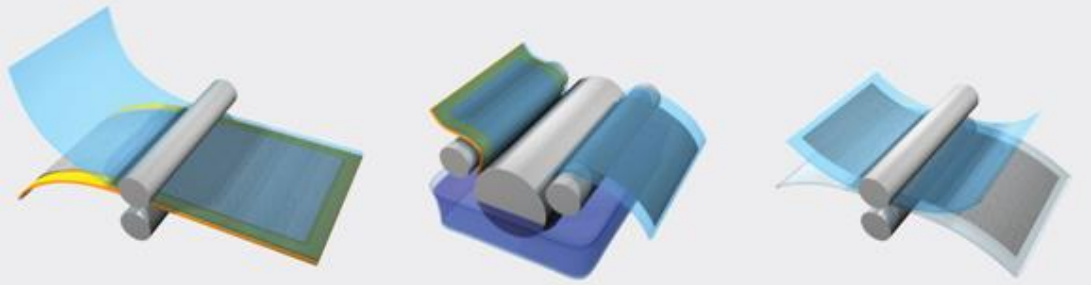

Figure 3.5. Schematic of the roll-based production of graphene films grown on a copper foil. The process includes adhesion of polymer supports, copper etching (rinsing) and dry transfer-printing on a target substrate [165].

Graphene nanoribbons (GNRs) obtained by unzipping carbon nanotubes (CTNs) have a form of rather narrow, elongated graphene stripes. This method offers some important advantages since it is possible to control their parameters and to some extent also their morphology by choosing CNTs with well-defined suitable size and chirality. There are several options to produce GNRs like oxidative splitting (Figure 3.6) [299], plasma etching [300,301], reductive splitting [302], sonochemical reaction [303] and sputter-etching [171]. Nanoribbons prepared using solution-based oxidative processes with a help of $KMnO_4$ were easily soluble in water because of a large amount of oxygen species similarly like graphene oxide [299]. Although this reaction is rather simple, additional reduction was necessary to restore sp^2 carbon lattice to improve poor conductivity, although it was impossible to obtain comparable results like with previously described techniques. The same group solved this problem by changing the oxidation agent into reducing one, namely they employed potassium vapor followed by sonication in chlorosulfonic acid [302]. This allowed to produce GNRs with greatly improved conductivity and reduced amount of defects when compared to oxidative splitting. One of the newest and interesting results published by Wei and coworkers present intramolecular junctions consisting of GNR prepared from partially unzipped CNT and the part that was not treated (Figure 3.7) [171]. Splitting is made by sputter-etching with zinc/acid and the rest part of CNT is covered with protective polymer, which is removed at the end. This GNR/SWCNT junction was successfully tested as a photodetector with high photocurrent and photovoltage.

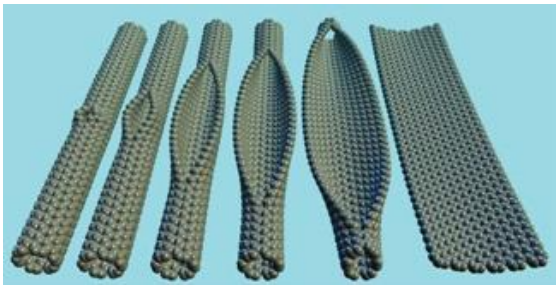

Figure 3.6. Schematic illustration of the gradual unzipping of one wall of a carbon nanotube to form a nanoribbon [299].

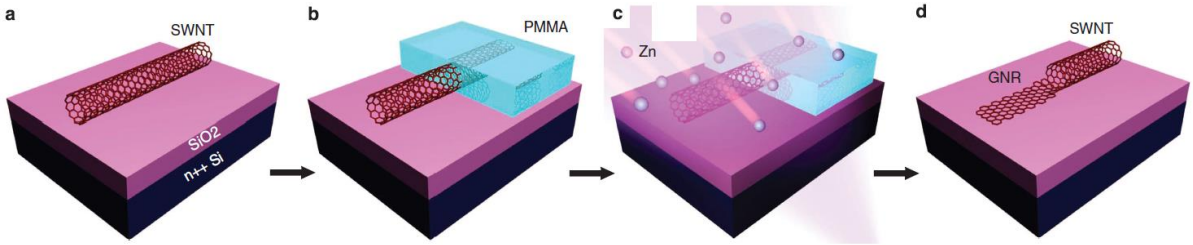

Figure 3.7. Schematic illustration of the patterned unzipping of a single-walled CNT (SWCNT) for producing SWCNT/CNR intramolecular junction [171].

Liquid phase exfoliation based on graphene oxide reduction gained a lot of attention during previous years as it offers an impressive spectrum of possible strategies. The main reason for this state is high accessibility of these methods, since most of them can be utilized in almost every laboratory with no need for sophisticated equipment, high temperature or very low pressure/vacuum. Additionally, these techniques show real chance for inexpensive mass production. In all methods graphite is used as a starting material which is then oxidized to graphite oxide, using one of the most popular oxidation methods: Brodie [304], Staudenmaier [305] or Hummers [306] methods. Afterwards graphite oxide is easily exfoliated, usually by ultrasonication, and the final product, graphene oxide (GO), is ready for further functionalization [230]. GO is extremely rich with oxygen containing functional groups, mainly hydroxyls (-OH), carbonyls (-C=O), oxygen epoxides and carboxyls, which disrupt sp^2 carbon network and influence the insulating character of GO in contrast with highly conductive graphene (Figure 3.8) [174]. There are several strategies to reduce GO: chemical reduction [174–187], thermal reduction [174,188–190], covalent or noncovalent functionalization [191–213], and less commonly used, electrochemical [214,215], photocatalytic [216,217] and photothermal reduction [218–220].

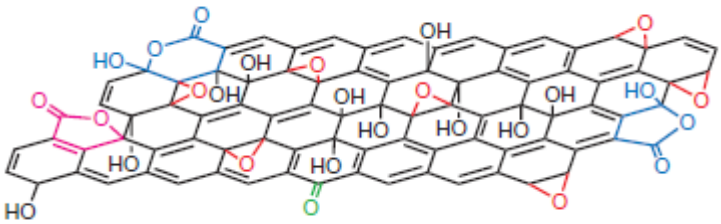

Figure 3.8. One of the possible structural models of GO [174].

In the first case there is a need for efficiently working reducing agent and for a long time the best results were obtained with anhydrous hydrazine (N_2H_4). For the first time this method was introduced by Stankovich *et al.* and measured C/O ratio changed from 2.7 for GO to 10.3 for reduced GO (rGO) and electrical conductivity up to 2620 S m^{-1} which is five orders of magniture higher that GO. However, under these conditions, there is still a significant amount of oxygen species left on the rGO surface [177]. There were also some attempts to solve this problem but the mechanism of this reaction is still not fully explained [175]. To overcome the hazardous character of hydrazine and limit the presence of nitrogen impurities, different reducing agents were investigated. Chemical reduction can be also carried out with sodium borohydride ($NaBH_4$) [174,178], hydroquinone [179] or lithium aluminum hydride [180] and regarded as more environmentally friendly "green" reducing agents like alcohols [184,185], sugars [186], vitamin C [176,181], acetic acids [187] or strong alkali solutions [182,183]. For vitamin C results also look promising with C/O ratio ~12.5 and electrical conductivity up to 7700 S m^{-1} for the final reduced material [176], compared to 0.05 S m^{-1} for GO [307], while for GO reduction using hydriodic acid/acetic acid, the conductivity is ~7850 S m^{-1}, C/O ratio is 15.27 and sheet resistivity is 19.6 Ω sq^{-1} [187].

Next approach to produce rGO is thermal reduction where high temperatures (> 550°C) are applied and no reducing agents are necessary [174,188–190]. McAllister and coworkers presented the possible mechanism for the thermal exfoliation of GO [188]. They explained that under the heating process oxygen species are decomposed and CO_2 which is one of the product is expanding during reaction, and when the pressure is growing rGO flakes are separated [188]. It was shown by Ajayan *et al.* [174] and Gilje *et al.* [190] that when both chemical and thermal exfoliation methods are combined the reduction process is even more efficient and obtained rGO of higher quality. Electrical conductivity measured for these samples reached 2.02×10^4 S m^{-1} [174] with extremely high C/O ratio > 246 and 5.73×10^4 S m^{-1} [190], although C/O ratio in this case did not change compared to other methods.

Another strategy to change in a controlled way the optoelectronic properties of GO is covalent [191–200] and non-covalent functionalization [194,201–212]. Covalent functionalization takes advantages of the reactivity of oxygen species in GO which can specifically bond with target molecules. There are plenty of chemical compounds that were employed in this method like: porphyrin [196], fullerene [196], poly(vinylalcohol) [197], amine-terminated ionic liquid [198], 3-aminopropyltriethoxysilane [199], boronic acid [200], perfluorophenyl azide [192], aryldiazonium salts [193], phenylacetylene moieties [194], ferrocene [195], and more. In case of non-covalent functionalization, strong π -π stacking interactions between GO carbon network and aromatic compounds or biological molecules play a key role. The number of possibilities is also impressive, for example one can use: single-strand DNA [208,209], doxorubicin hydrochloride [211], pyrene [201,202,206], dopamine [203], tetrathiafulvalene (TTF) [204,205,207], tetracyanoethylene [205], aptamer with fluoresceine [212], perfluorophenyl azides [192] and many more [210]. Except changing optoelectronic properties, covalent and non-covalent functionalization were also used: to control the solubility of graphene [192,197,198], to investigate nonlinear optical properties and photonic applications [196], to test mechanical properties [199], to create gas storage device [200], for detection of proteins [202,209] and DNA [209], for DNA analysis [208] and to prepare biosensing platforms [210] and conducting paper for flexible devices [187].

A short comparison of the properties of graphene and graphene-based materials obtained with different methods is presented in the Table 3.1. However, it to be emphasized that this is a very sketchy description because even within each method materials with different characteristics can be prepared, what was described in this section.

Table 3.1. Properties of graphene obtained with different methods [173].

Method	Crystallite size (μm)	Sample size (mm)	Charge carrier mobility (at ambient temperature) ($cm^2 V^{-1} s^{-1}$)	Applications
Mechanical exfoliation	>1,000	>1	$>2 \times 10^5$ and $> 10^6$ (at low temperature)	Research
Chemical exfoliation	≤0.1	Infinite as a layer of overlapping flakes	100 (for a layer of overlapping flakes)	Coatings, paint/ink, composites, transparent conductive layers, energy storage, bioapplications
Chemical exfoliation via graphene oxide	~100	Infinite as a layer of overlapping flakes	1 (for a layer of overlapping flakes)	Coatings, paint/ink, composites, transparent conductive layers, energy storage, bioapplications
CVD	1,000	~1,000	10,000	Photonics, nanoelectronics, transparent conductive layers, sensors, bioapplications
SiC	50	100	10,000	High-frequency transistors and other electronic devices

3.4. Applications

In recent years graphene began to occupy increasingly important place in many fields of science, what has a direct impact on a growing number of applications from electronics and

photonics to supercapacitors, solar cells, biodevices and sensing platforms [12,108,153,163,165,169–173,187,200,202,208–210,212,221–288,308–338]. There are many promising results, however in most cases the creation of such devices is in the preliminary stage and additional modifications and optimizations are essential.

When a single graphene layer was obtained for the first time it was clear that due to its remarkable optoelectronic properties one day it will be employed in building up new devices like transistors, flexible electronics, photonics, etc [153]. Nowadays this idea seems to be more and more realistic and the preliminary attempts were made. However, preparing a high-quality graphene with sufficient size is still a big challenge, and for these purposes only epitaxially grown [160–163] and CVD [164–169] graphene are applicable. Although graphene gives so many opportunities, its applications develop rather slowly. Novoselov *et al.* [173] in one of their review articles make some predictions about the time when graphene-based electronics and photonics will appear, at least in the form of prototypes, that is now – 20 years. Except field-effect transistors, which are described in the following sections of this chapter, researchers presented graphene-based: flexible transparent electrode which can be the main compartment of touch screens [165], organic light-emitting diodes (OLED) [170], high-frequency transistors [163,169], photodetectors [171], and optical polarizers [172]. Although in some cases the researchers are not very far from their main goal, further improvement and optimization of most mentioned devices as well as better control over materials preparation are necessary. For the nearest future there are some predictions for creating graphene-based logic transistors, THz wave detectors and generators, mode-locked lasers, etc [173].

One of the challenging issue of the modern world is energy, its conversion and storage [12,173,221–235]. In the first case, photovoltaic devices, fuel cells and (photo)catalysts are widely developed and explored. Equally crucial are efficient energy storage devices *e.g.* lithium ion batteries, supercapacitors or hydrogen storage systems which nowadays are of great importance. Graphene has been already employed in many kinds of energy-related materials, usually as a part of more complex composites. The first step to utilize natural sources of energy is its efficient conversion into usable forms; one group of tools enabling to do it are solar cells [12,190,222]. In this kind of device, graphene can be used in (1) thin film solar cells as a transparent electrode (TE), (2) in dye-sensitized solar cells [12] as a TE, counter electrode, electron/hole acceptor/transporter and light absorber, as well as (3) in heterojunction solar cells as electron/hole acceptor/transporter [222]. In the case of TE, graphene shows promises to replace ITO or FTO in the future while it has suitable properties and additionally can be flexible in contrast with stiff surfaces. Nonetheless, solar cells performance based on

graphene still need to be improved [223]. Fuel cell is the next device for energy conversion which is based on fuel oxidation, where the catalyst plays a key role [225,226]. Up to date, platinum performs the best results but the most serious drawback is the high price of this material. It was proved that the amount of platinum can be decreased, however additional support surface is crucial [225,226]. Graphene and nitrogen doped graphene appeared to be very efficiently working supporting materials and additional improvement was achieved by creating 3D nanostructures with graphene and platinum nanoparticles *e.g.* with layer-by-layer technique [226]. One of the most environmentally friendly and clean fuel is hydrogen, and the most common method to gain it is direct water splitting with photocatalyst [223,339]. Graphene and graphene-based materials were successfully added as an additional compartment into already existing photocatalysts to improve their efficiency, but were also tested separately as an individual catalytic materials [222–224,229]. There is a strong need for energy storage materials with very high capacitance and long cycling life. The first example which is described to be the most promising but still far from mass production is hydrogen energy storage [221]. Graphene platelet nanofibers are one of the candidates. However, it was also shown that well-defined distance between layers or nanofibers controlled by carbon nanotubes or fullerenes is crucial and can increase the capacitance [221,227]. Also in this case, graphene or its composites comply with the conditions for supporting materials for metal or metal oxide nanopartciles which can bind hydrogen molecules. There are also already commercially available and widely used lithium ion batteries (LIBs). LIBs are optimized and well-suited for small portable devices. However, a continuously growing demand for higher power and longer cycling life causes the need for improved batteries. Graphene and its composites were employed in different building blocks of LIBs, alone or together with metals, metal oxides (Figure 3.9) or silicon [173,221,222,224,228–231]. Graphene and graphene composites were used both as an anode and cathode materials in LIBs. All of these hybrid materials show increased capacitance and/or cycling life of batteries, what shows real chances for LIBs with much better performance. Very promising and fast-growing group of energy storage devices are supercapacitors, both electrical double-layer capacitors and pseudo-capacitors [229,231–235]. Supercapacitors are based on the electrostatic storage of a charge at the electrode and electrolyte interface. Pseudo-capacitors are connected with energy storage due to redox reactions or adsorption, generally faradaic processes. There are several strategies introduced to employ graphene-based materials, like conductive polymer/graphene [232], metal oxides/graphene [234] and metal hydroxides/graphene [233] composites. One of the best results in terms of capacitance were obtained for polyaniline/graphene based nanosheets up to 1046 F/g

[232] with energy density ~39 W h kg^{-1} at a power density of 70 kW kg^{-1} and for $Ni(OH)_2$ nanoplates on graphene sheets ~1335 F g^{-1} [233] with energy density ~37 W h kg^{-1} at a power density of 10 kW kg^{-1}. This is in agreement with results obtained for a well-known pseudocapacitive material, RuO_2 [234,235], however much cheaper and less toxic, which makes graphene-based supercapacitors very attractive for further investigations.

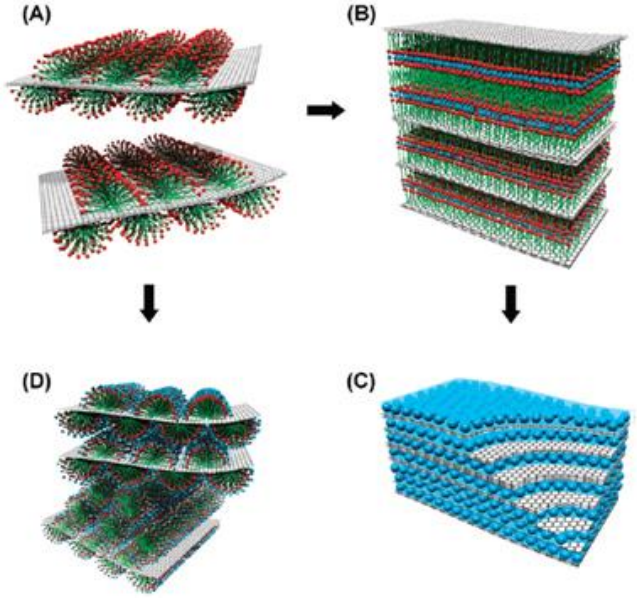

Figure 3.9. Schematic illustrations of the self-assembly approach to ordered metal oxide/graphene nanocomposites. (A) Graphene or graphene stacks used as the substrate. Adsorption of surfactant hemimicelles on the surfaces of graphene or graphene stacks causes its dispersion in surfactant micelles in an aqueous solution. (B) The self-assembly of anionic sulfonate surfactant on the graphene surface with oppositely charged metal cation (*e.g.* Sn_2) species and the transition into the lamella mesophase toward the formation of SnO_2/graphene nanocomposites, where hydrophobic graphenes are sandwiched in the hydrophobic domains of the anionic surfactant. (C) Metal oxide/graphene layered nanocomposites composed of alternating layers of metal oxide nanocrystals and graphene/ graphene stacks after crystallization of metal oxide and removal of the surfactant. (D) Self-assembled hexagonal nanostructure of metal oxide precursor (*e.g.*, silicate) with nonionic surfactants (*e.g.*, Pluronic P123) on graphene stacks [228].

Chemical and biological sensing and recognition are next research fields where graphene has been investigated as a potentially perspective material. For sensing platforms which can be shared into field-effect transistors (FET) [308–327], electrochemical sensors [225,257–270,328–338] and optical/fluorescence sensors [212,236–247,252–254], the most important properties of graphene are conductivity and chemical inertness. In the case of electrical sensors, graphene or graphene-based materials are used as conductive channels between two metal electrodes, source and drain electrodes (Figure 3.10) [308]. Due to their extremely high active surface area

and high surface-to-volume ratio, the sensitivity of such a device can be greatly increased. This kind of sensing platform is based on the monitoring of conductivity changes under the absorption of the investigated molecule or due to variations of the closest surrounding like pH changes [309]. Graphene-based FET sensors were successfully used to record the presence of gas molecules like NO_2 [310,311], NO [312], Cl_2 [310], NH_3 [311,313], H_2 [314], H_2S [315] or dinitrotoluene [316]. It was also shown that FET sensors can work in aqueous environment which is especially important for biosensing. They were used for sensing DNA [317–319] working in a non-real-time with a LoD down to pM level [317] and in a real-time mode with a LoD ~nM [319], glucose [320], proteins [321–325], bacteria [326] and even for sensing and measuring dynamic activity of living cells [327]. Li and coworkers showed that by using CVD graphene it is possible to detect DNA hybridization with LoD ~pM and even a single-base mismatch [317]. Chen *et al.* employed rGO modified with gold nanoparticles-antibody conjugate for a specific recognition of Immunoglobulin G with LoD ~ng mL^{-1} [321]. Other groups showed that graphene-based FET can be utilized to record bioelectrical signals from living cells namely to monitor hormonal catecholamine molecules, what was allowed due to proceeding PC12 neutron cell growth directly on poly-L-lysine modified rGO (Figure 3.11) [327].

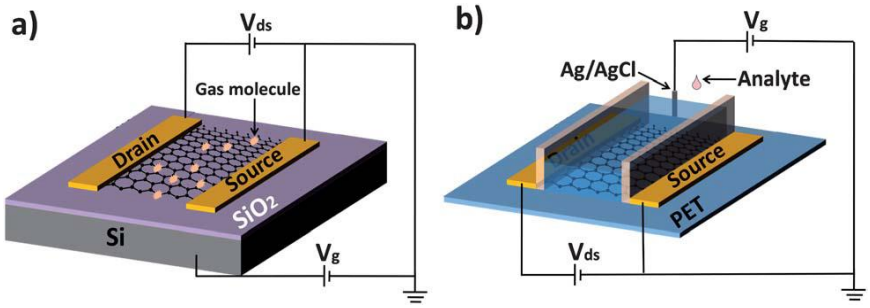

Figure 3.10. (a) Typical back-gate GFET on Si/SiO_2 substrate used as gas sensor. (b) Typical solution-gate GFET on flexible polyethylene terephthalate (PET) substrate used as chemical and biological sensor in aqueous solution [308].

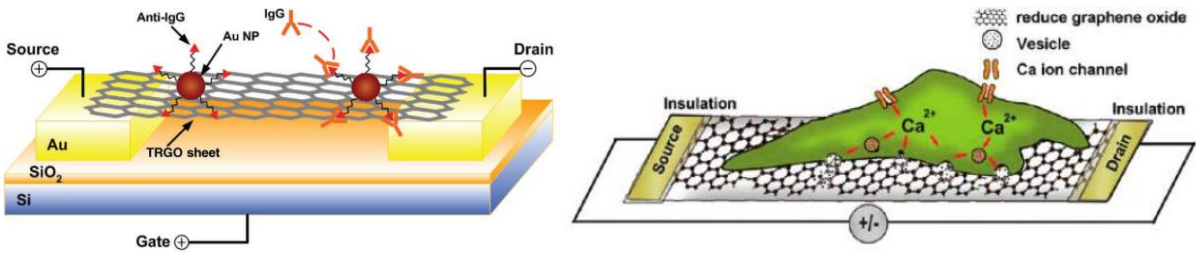

Figure 3.11. Schematic illustration of thermally rGO decorated with gold nanoparticles-antibody conjugate FET used for recognition of Immunoglobulin G [321] and rGO FET with PC12 cells [327].

Electrochemical sensing which is exceptionally suitable for electroactive molecules can employ graphene either as a working electrode or as a component which can be used to functionalize various electrodes. There are many compounds already detected or recognized by such devices like: hydrogen peroxide [225,257,258,328,329], glucose [259,260,267,330], antigens [268,331–333], enzymes [334], nucleotides and nucleic acids [261–263,335,336], dopamine [264,265,269,270,337] or pesticides [266,338]. In most cases composite materials contained reduced GO prepared with a help of hydrazine [257–266] or $NaBH_4$ [267–270], but GO reduction was also provided by thermal exfoliation [330,333], arc discharge [335], electrochemical reduction [336] and with the help of various reducing agents like ethylene glycol [225] or polyethyleneimine [328]. Other forms of graphene, like functionalized GO [332,334], as well as pristine graphene obtained with microwave plasma CVD [337] were also employed in sensing platforms. GO- and rGO-based composites contain gold nanoparticles [257,267,268], platinum nanoparticles [225,269,330], Prussian Blue nanocubes [328], conductive polymer [262], β-cyclodextrin [270] or enzymes like horseradish peroxidase [258,332,333] and glucose oxidase [259,261]. Some of graphene-based materials were additionally silanized [265,336], functionalized with hydroxylic acid [263] or doped with nitrogen [260].

Sensors based on fluorescence process are highly sensitive, selective and fast. They take advantage of either fluorescence quenching due to the presence of graphene-based materials or their own fluorescence. Fluorescence quenching is brought about by energy transfer (FRET, fluorescence resonance energy transfer) between sensor compounds and tag/recognition molecule coupled with fluorophore and when this molecule interacts with a target, its fluorescence is restored. This kind of sensing platforms were used to detect DNA or visualize hybridization [236–240], to detect proteins [240–242], intracellular ATP molecules [212] or metal ions [243,244]. Graphene-based sensors were used not only as a fluorescence quencher but also as a fluorescent label [245,246]. This methodology was employed by Jung *et al.* in order to detect rotavirus which was captured by antibody immobilized on the sensor surface [245]. After the target was captured, antibodies modified with gold nanoparticles were applied. Upon interaction with attached rotavirus, the fluorescence of graphene material was quenched (Figure 3.12). Except fluorescence, graphene-based materials are also utilized in sensors based on SPR [247–251] and SERS [108,252–256] techniques. As it was described in Chapter 1, SPR platforms which contain a thin gold film as a main component are well-known and widely used (bio)sensors. In 2010, Wu and coworkers published their calculations about sensitivity improvement due to the presence of graphene on the SPR gold surface [250]. They implied that increased efficiency may be due to stable adsorption of investigated molecules *via* strong π-π

stacking interactions with graphene lattice and also high surface-to-volume ratio of graphene which facilitates adsorption. Optical properties of graphene influence the sensitivity to refractive index changes. This value also depends on the number of graphene layer, so it can be controlled. Szunerits, Boukherroub and co-workers showed through the measurements of a real-time kinetic of biotin-streptavidin that the response in the presence of graphene layer is 1.63 times higher [248]. They also reported SPR-based enzyme detector [251] with lowered LoD (0.5 nM) and improved selectivity. Although graphene modified SPR substrates hold promises, this area is still not deeply investigated and there is much space for novel biosensors. With SERS substrates which contain graphene, the situation is similar. Although Raman spectroscopy is widely used for graphene, GO and graphene-based materials characterization, there is still much unfilled space for their application in SERS as a sensing platform or its building block [255]. Zhang *et al.* reported a new efficient SERS substrate which consists of rGO decorated with gold or silver nanoparticles. They demonstrated that it is applicable for aromatic molecule detection at nanomolar level [252]. In another example GO/Ag nanoparticles hybrid was used for folic acid detection. Detection in nanomolar range in both water and diluted human serum shows promises for application in medicine and biotechnology [253].

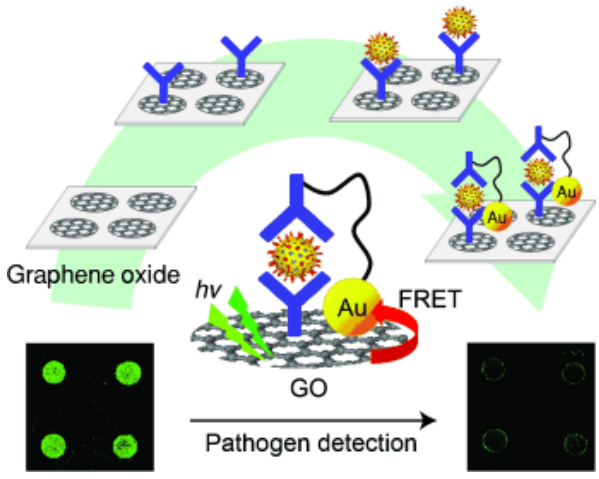

Figure 3.12. Schematic illustration of immune-fluorescence-biosensor [245].

Another area which takes advantage of interesting properties of graphene-based materials is nanomedicine [271–288]. Except of biosensing applications described in this section, there were also some attempts to introduce graphene into imaging, therapy and diagnostic investigations. Zhao *et al.* [271] and Zhou *et al.* [272] stated that like with all nanomaterials engaged in biomedical applications, also in the case of graphene the discussion about its

biocompatibility, cytotoxicity and influence on natural environment need to be raised. It was shown that due to easy and accessible functionalization of graphene, GO and rGO the character of these materials can be changed in wide spectrum, from toxic and dangerous to suitable for medical applications [271]. Their effect on living organisms is strongly dependent on size, shape, dose, functional groups, surface charge as well as number of layers [273]. Graphene-based hybrid structures as well as pristine graphene have already been investigated as an antibacterial agent [275–277], for bioimaging [271,278–283], genetic engineering [284–287], drug delivery [274,283,286,288] and phototherapy [271,288]. Important information about recent advances in biomedical applications of graphene and graphene-based materials are described in detail in a number of review articles [271–274]. It needs to be emphasized that the rapid progress in developing graphene-based materials makes a great impression, however a lot much effort need to be put in this subject in order to optimize many of this new structures or devices as well as to make them commercially available.

In this thesis, GO and rGO-based composites are introduced and described. For the reduction process various aromatic molecules and their derivatives were utilized. All these reaction were performed in mild conditions with the help of sonication. This simple approach allowed preparing efficiently reduced and simultaneously functionalized stable composites which were then applied as sensing platforms.

4. Indium tin oxide nanoparticles

4.1. Introduction

Indium tin oxide (ITO) in the form of thin layers belongs to the group of transparent conductive oxides which interestingly displays coupled properties of optical transparency and high electrical conductivity [340]. ITO is a *n*-doped semiconductor material with a large band gap up to 4.3 eV [341]. It consists of solid solution of indium oxide (In_2O_3) and tin oxide (SnO_2), with usually < 10% of the second one. Its energy band structure makes it highly transparent to the visible light (> 80%), but at the same time it can "block" the UV and near-IR light, either by absorption or reflection [342–345]. The presence of the dopant (tin) but also impurities greatly improves the conductivity of ITO (~10^4 Ω^{-1} cm^{-1}, with sheet resistance ~10 Ω sq^{-1}) when compared with undoped In_2O_3 (~10^{-2} Ω^{-1} cm^{-1} at 1000 K)[340,346]. This is realized by the presence of extra valence electrons of the dopant, in this case 4 valence electrons in tin atom, in contrast to host which is indium with 3 valence electrons. These dopants introduced additional allowed energy states, a new "dopant band" close to the conductive band and more carriers are available for conduction [340].

An attractive combination of optical and electronic properties, together with stability makes ITO suitable as a transparent electrode in a number of optoelectronic devices, just like photodiodes [347,348], solar cells [349,350], e-papers [351], flat panel displays [352,353], light emitting diode [354] or UV/IR shielding windows [342]. Although ITO thin films deposited on glass are commercially available, the cost of preparation is still relatively high. Methods such as chemical vapor deposition, physical vapor deposition or electron beam evaporation are complicated, and sophisticated equipment is necessary. What is more important, these methods are limited to rigid materials and require high temperatures. Those issues were partially solved by preparing ITO nanoparticles with various liquid phase chemical methods, which then could be used as thin coating films.

4.2. Preparation methods and properties

There is an impressive number of articles devoted to the new preparation methods of ITO nanoparticles [339,341–344,347,355–365]. This is connected with the strong relationship between optoelectronic properties and the size of particles, their crystalline structure as well as possible aggregates. In this section, wet chemical methods are described, since more and more

often they are employed to prepare ITO nanoparticles with well-defined morphological and optoelectronic properties, with no need to engage complicated and expensive equipment. The most popular are thermal decomposition [342,355–358], hydrothermal synthesis [358,359], colloidal chemistry approach (with a sol-gel process) [358,360,361], liquid phase precipitation [339,341,344,362,366,367], solvothermal synthesis [343,363,364], and also less explored strategy like mineralization in templates [365].

In the first case, acetate of both indium and tin were used together with oleic acid and oleylamine as capping agents, and prepared nanoparticles could be dispersed in nonpolar solvents [342]. Additionally, it was shown that oleic acid can be exchanged with azido-terminated phosphate ligands giving an opportunity to apply "click" chemistry. The final nanocomposite was deposited on glass or plastic surfaces which were almost transparent in visible light (> 90%), absorb UV light in the range of 300 – 400 nm and depending on the content of dopant showed various transmittance in near-IR region [342]. Fang and coworkers used analogous methodology to prepare quasi-spherical and monodisperse particles. Additionally they showed that ITO photoluminescence is influenced by the contribution of tin oxide [356]. Another group which utilized thermal decomposition presented that surface plasmon resonance can be tuned between ~1600 nm to more than 2200 nm by manipulating indium/tin ratio (Figure 4.1) [357].

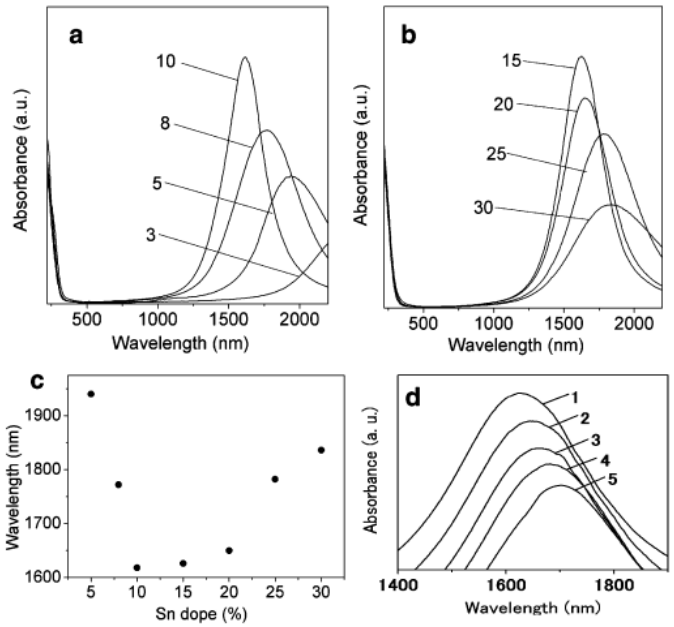

Figure 4.1. (a, b) UV – vis – NIR spectra of ITO NPs doped with (a) 3 – 10 % and (b) 15 – 30 % Sn. (c) Dependence of the SPR peaks of ITO NPs on the doped % Sn. (d) NIR spectra of 8 % Sn-doped ITO NPs in (1) hexane, (2) cyclohexane, (3) decahydronaphtalene, (4) o-dichlorobenzene and (5) nitrobenzene [357].

Summers and coworkers combined two methods to prepare ITO nanoparticles, in order to improve their properties [360]. By using simultaneously nucleophilic attack and hydrolysis reaction, not agglomerated and highly crystalline nanoparticles were formed. In a different approach involving sol-gel process, obtained ITO and FTO (fluorine-doped tin oxide) nanoparticles were employed together with TiO_2 electrode in dye-sensitized solar cell [361]. Addition of ITO nanoparticles improved the efficiency and current density by 20 %.

Moghaddam *et al.* presented a comparison of ITO nanoparticles prepared with three different methods: thermal decomposition, hydrothermal synthesis and sol-gel process (Figure 4.2) [358]. They combined experimental results with the Rietveld profile refinement method [368] and Popa's model [369] in order to calculate structural parameters and model crystallites. They showed that nanoparticles obtained with sol-gel combustion reveal the highest conductivity, crystallinity and low-energy photoluminescence band intensity, however at the same time they present low compactness and mechanical stability. In contrast, nanostructures formed using hydrothermal synthesis exhibited low conductivity, maximum micro-strain and the highest anisotropy in crystalline. For the last analyzed case (decomposition), ITO nanoparticles revealed high strength, low crystalline and high micro-strain.

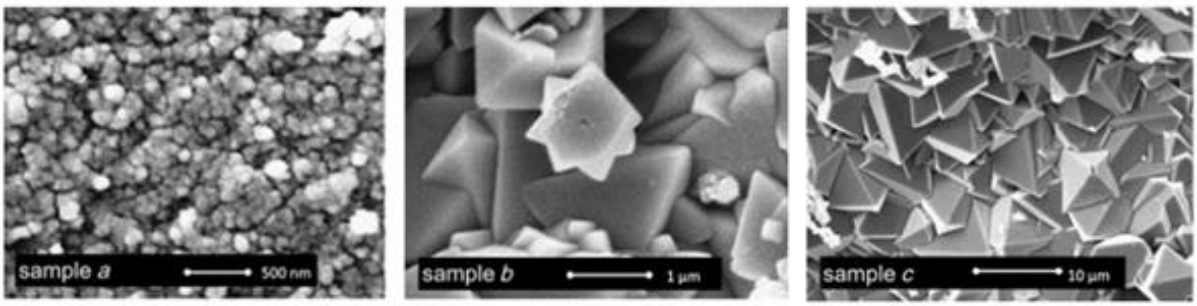

Figure 4.2. SEM images of sample obtained with thermal decomposition (a), hydrothermal synthesis (b) and sol-gel process (c) [358].

In the last example ring-shaped self-assembly of peptide-based biomimetic molecules with catalytic activity were used as a template to grow ITO nanoparticles (Figure 4.3) [365]. Authors took advantage of a natural affinity of some specific peptides, in this case bolaamphiphilic peptide-derivatives, to inorganic materials, here indium tin oxide. The resulting nanoparticles were much bigger (~150 nm) than those prepared with co-precipitation method (9–30 nm) [339,344,362,366,367] or colloidal chemistry approach (5–15 nm) [360,361] and in contrast to hexagonal structure, they have fluorite structure. Using biomimetic templates it

was possible to control the shape of nanoparticles, crystalline structure and their conductivity was improved [365].

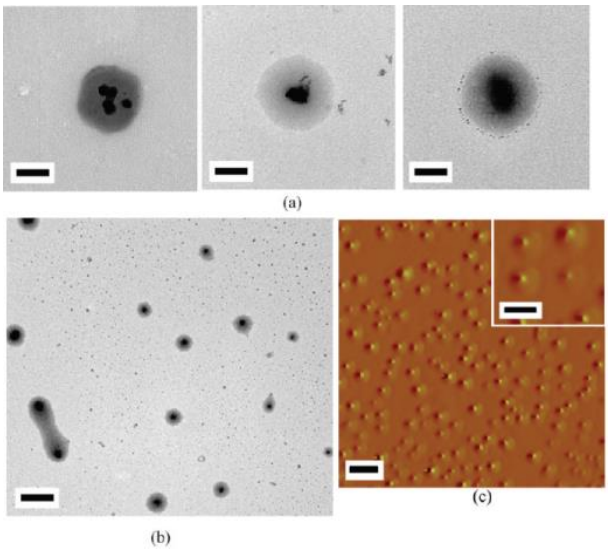

Figure 4.3. ITO nanoparticles formation inside a peptide assembly. (a) Growth of ITO nanoparticles inside of the assembly over time. TEM images of ITO nanoparticles grown for one, three, and five weeks (left to right, scale bar: 100 nm), (b) ITO nanoparticles grown in the peptide assembly after a four-week incubation (scale bar: 500 nm), (c) phase images of the ITO nanoparticles surrounded by the peptide assembly (scale bar: 500 nm) Inset: magnified AFM image (scale bar: 200 nm) [365].

4.3. Applications

In addition to the examples described in the section 4.2, there is a substantial number of works where authors utilize commercially available ITO nanoparticles for many interesting applications. They can be used directly in a pristine form [370–373] or might be incorporated (unmodified [352,374,375] or functionalized [376–378]) into complex materials.

Although most of the already presented works focused on optoelectronic applications of ITO nanoparticles, it has to be mentioned that they were also tested as an electrochemically active material [370,373]. In both cases, subsequent immersion and withdrawal in the suspension of ITO nanoparticles in methanol was used to deposit single layer of ITO nanoparticles (~20 nm) on ITO electrode. This step was repeated to deposit next layers and the method allowed to obtain densely packed porous material with a thickness ~60 nm per each layer [370]. A capacitive current increases with a growing number of layers due to a larger active surface area. Further experiment performed with a small droplet of redox liquid deposited on ITO nanoparticles modified electrode (Figure 4.4) proved that the whole porous film is

electrochemically active. Analogously prepared modified surfaces with additionally adsorbed bilirubin oxidase were used as a bioelectrocatalyst in dioxygen reduction reaction [373]. AFM and SEM analysis showed that the enzyme is present in the form of bigger aggregates, and electrochemical measurements confirmed the stability of bilirubin oxidase adsorbed on ITO nanoparticles. This system facilitated mediatorless bioelectrocatalysis of dioxygen reduction and first tests with zinc-dioxygen were also presented.

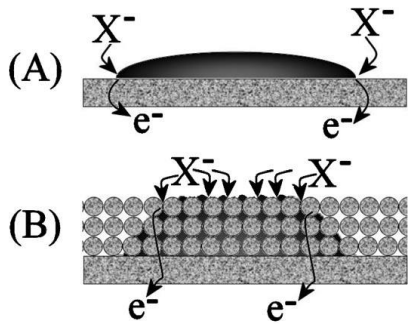

Figure 4.4. Schematic illustration of a bare ITO electrode (A) and an ITO electrode covered with ITO nanoparticles (B) with redox liquid deposit [370].

Commercially available ITO nanoparticles were successfully tested as components in optoelectronic devices [375], fuel cells [376] or smart materials *e.g.* conductive paper [377]. In the first device, ITO nanoparticles were applied for preparing an anode for light-emitting diodes (LEDs) [375]. The surface was prepared by spin coating and annealing at 600°C in vacuum. Afterwards, the mixture of two ionomers was deposited and the resulting layer of conductive polymer was coated with chloroform. All was covered with a calcium cathode and aluminum as a protective layer. Polymer LED (PLED) with ITO nanoparticles performed similar characteristics like PLED with control ITO film, and even higher luminescence efficiency [375]. In another example, ITO nanoparticles were used as a support for Pt nanoparticles and together with multi-walled carbon nanotubes (MWCNT) coated with Nafion they formed cathode for polymer electrolyte membrane fuel cell (Figure 4.5) [376]. ITO nanoparticles were used as a substitute for carbon materials which are exposed to corrosion [379], and showed in real environments similar performance. What is more important, the amount of MWCNT could be sufficiently reduced.

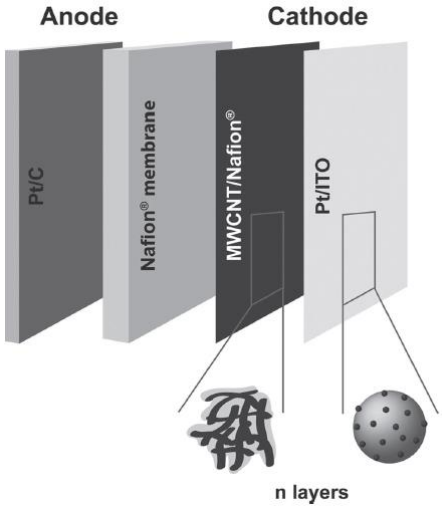

Figure 4.5. Schematic view of the multilayer membrane electrode assembly with Pt/ITO-MWCNT/Nafion cathode [376].

Interesting properties of ITO nanoparticles and their biocompatibility encouraged scientists to employ them in bioelectronic systems [374,378]. In the first example ITO nanoparticles were combined with chitosan with encapsulated isoform of cytochrome P450 (cyt P450) and cytochrome P450 reductase, and deposited on glassy carbon electrode [374]. This system can find many applications since this form of cyt P450 is involved in metabolism of ~16% of therapeutically important drugs. ITO nanoparticles provided extended scaffold for immobilized biomolecules and also facilitated direct electron transfer between proteins and electrode [374]. In another approach, ITO nanoparticles were used as tags for direct detection of nucleic acids [378]. At first the surface was modified with peptide nucleic acid, then the examined sample of nucleic acid was applied and heteroduplex was formed. Finally, ITO nanoparticles functionalized with zirconium were provided and conductive network was created by anchoring tags on phosphates (Figure 4.6) [378]. Conductance measurements ensure a great distinction between fully complementary and even a one-base mismatched oligonucleotide, showing a drop of a signal of ~95%. Described biosensor reveals fast response, high sensitivity and excellent selectivity.

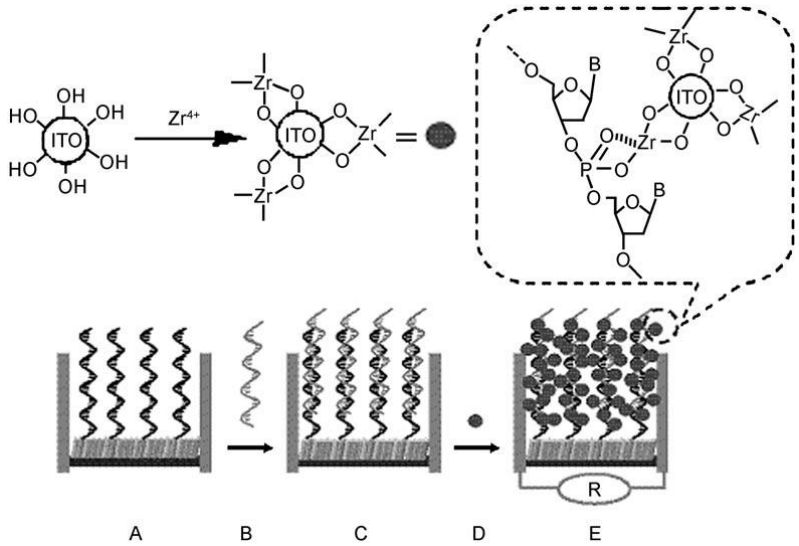

Figure 4.6. Schematic representation of the nucleic acid biosensor based on direct tagging of the hybridized target nucleic acid with ITO nanoparticles and electrical detection [378].

In this thesis, the application of ITO nanoparticles film as a platform for further modification with gold nanoparticles is demonstrated. Only commercially available nanoparticles were used. Deposition was realized by subsequent immersions and withdrawals of an electrode surface into the ITO nanoparticles suspension solution. These film electrodes were used for catalytic oxidation of glucose and dioxygen reduction. In the latter case, such prepared platforms with or without gold nanoparticles, after further modification with bilirubin oxidase, were tested as bioelectrocatalyst.

Goal

The main goal of this thesis was to develop new methods of the preparation of gold nanoparticles and graphene-based materials. At first, solid|liquid|liquid three-phase junction was studied as a novel system for metallic nanoparticles electrodeposition. After detailed characterization, these deposits were applied as catalytic and biocatalytic materials as well as sensing platforms for surface-enhanced Raman spectroscopy. Another point of this work was to design a new and simple method for graphene oxide reduction and simultaneous functionalization. These materials were characterized and further modified. Both materials, gold nanoparticles and/or reduced graphene oxide, were also applied as sensing platforms for fluorescence microscopy.

RESULTS AND DISCUSSION

5. Techniques

5.1. Cyclic voltammetry

Cyclic voltammetry (CV) is one of the potential sweep methods in which applied potential is varied linearly with time. The resulting current plotted versus potential is called cyclic voltammogram. CV is frequently used as an electroanalytical tool for investigating electrode reactions and determining thermodynamics, kinetics or mechanisms. It is also possible to identify electron transfer or adsorption processes with this method.

In a three-electrode system the voltage is applied between a working electrode (WE) and a counter electrode (CE) and the potential of the WE is monitored with respect to the a reference electrode (RE). During the measurement, when the potential reaches the value of the switching potential E_λ, it is reversed towards initial value (Figure 5.1). Measurements are carried out in a constant scan rate, which is usually changed from single microvolts per second to hundreds of volts per second.

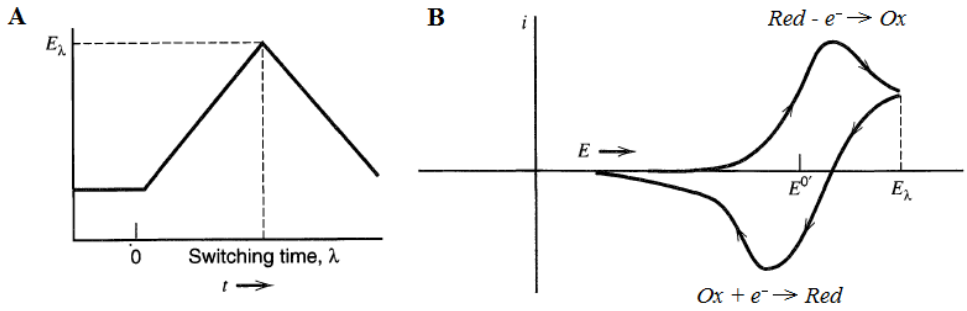

Figure 5.1. Potential sweep in CV (A) and resulting cyclic votlammogram (B) [380].

There are many factors which can influence the shape of a cyclic voltammogram like reversibility, diffusion, adsorption, reaction mechanism or kinetics. For the first case usually three processes are possible: electrochemically reversible, quasi-reversible or irreversible. This feature is determined by the magnitude of $|E_{pc} - E_{pa}|$. If the difference between cathodic and anodic peak current ($|E_{pc} - E_{pa}|$) equals $57/n$ *mV*, where n is a number of electrons transferred in the reaction, then the reaction is reversible. For quasi-reversible reactions peaks separation is larger and for irreversible processes one of a peak might not be observed at all.

Manipulating the scan rate υ may provide information about the nature (*e.g.* kinetics) of the electrode reactions. For reversible and diffusion controlled process, the peak current i_p is proportional to $\upsilon^{1/2}$ by the relation:

$$i(t) = 2.69 \cdot 10^5 n^{3/2} A D^{1/2} C^0 \vartheta^{1/2} \qquad \textbf{(5.1)}$$

where A is area of an electrode, D is diffusion coefficient, C^0 is a concentration of a redox species [380]. For a surface controlled (adsorbed substrate or restricted diffusion rate) process i_p is proportional to υ.

In this work CV was used to characterize new materials: gold nanoparticles electrodeposited at a three-phase junction and graphene-based composites. It was also employed for investigating catalytic and bioelectrocatalytic properties of gold deposits.

5.2. Chronoamperometry

Chronoamperometry (CA) belongs to the family of potential step methods. Experiment is performed for a constant potential and the current is measured as a function of time. This is a single potential step *CA.* For double-pulse measurements, two values of potential are applied one after another. Schematic illustration of this situation with a potential program and a current response is shown in Figure 5.2.

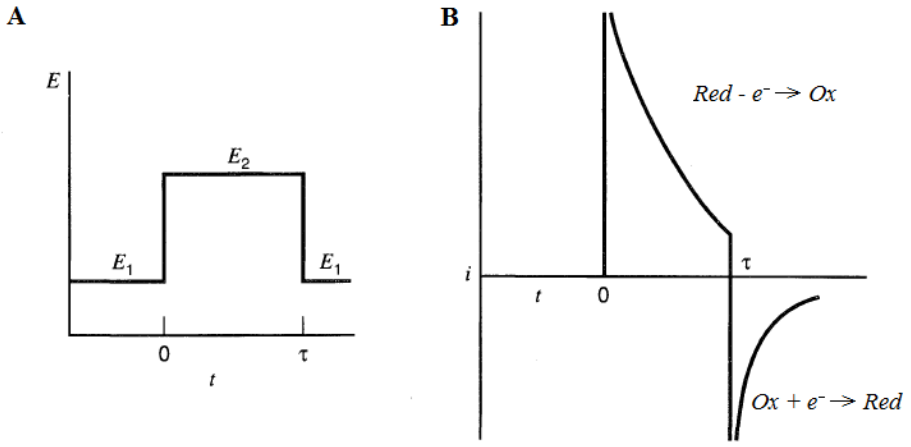

Figure 5.2. Double potential step CA with a potential program and a current response [380].

Figure 5.2 represents the situation when at the beginning the solution contains an electroactive species and no current flow is recorded. Then the potential is shifted to E_2 at t = 0 and when

the potential value is high enough, the oxidation occurs. Shifting the potential back to E_1 at $t = \tau$ results in re-reduction of the species and cathodic current flow is observed.

Electric current recorded as a function of time for a controlled potential program is described by the Cottrell equation:

$$i(t) = \frac{nFAD^{1/2}C^0}{\pi^{1/2}t^{1/2}} \qquad \textbf{(5.2)}$$

where n is a number of transferred electrons, F is Faraday's constant, A is area of a (planar) electrode, D is diffusion coefficient, C^0 is a concentration of a redox species, t is time [380]. This equation describes diffusion controlled process in unstirred electrolyte at a planar electrode.

CA is mainly used for investigating electrode stability or enzyme activity as well as determination of diffusion coefficient. It can be also employed for metallic nanoparticles electrodeposition [381–383]. In this case, two analogous single and double potential step programs are used. In this case, instead of a redox probe, a solution contains metal (*e.g.* gold or silver) precursors. For a double-pulse method the first potential is applied for nucleation at a very short time. The second one, relatively much longer pulse is applied to grow nuclei that were formed during the first step. In a single potential program, only the growth pulse is applied. Double potential CA allows to control size, shape and density of electrogenerated structures.

In this work double-potential step CA was used for gold electrodeposition at a three-phase junction.

5.3. Scanning electrochemical microscopy

Scanning electrochemical microscopy belongs to the group of scanning probe microscopies (SPM). It allows to investigate the local (electro)chemical behavior of the sample, to probe liquid|liquid, solid|liquid or gas|liquid interfaces, to create image of an interface, a membrane or a living cell and for micro- or nanopatterning [384,385].

The key part of the setup is an ultramicroelectrode (UME) which is moved by positioning system. Together with a RE and a CE it forms three-electrode cell. However, it is possible to work in a four-electrode cell when the sample is connected as the second WE. They are all connected to the potentiostat or bipotentiostat controlled by the PC.

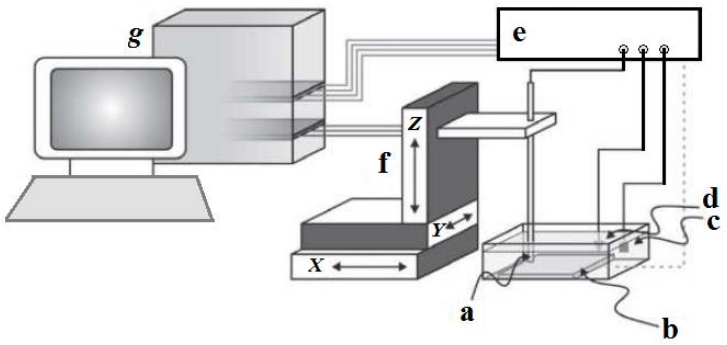

Figure 5.3. Schematic illustration of SECM setup: (a) microelectrode, (b) sample, (c) counter electrode, (d) reference electrode, (e) (bio)potentiostat, (f) positioning system and (g) PC [385].

Generally SECM experiments are performed in feedback (FB) and generation-collection (GC) modes [385]. In the first case, supporting electrolyte has to contain one redox form of a quesi-reversible redox couple. If a reduced form R is present in a bulk solution (Figure 5.4 A) and high enough potential is applied at the UME, it can be oxidized to the form O. During this process a steady-state current is recorded. When the UME is approached to the insulating substrate (Figure 5.4 B), O form cannot be reduced. Consequently, R form is not regenerated and its diffusion towards UME is hindered (negative FB). When the substrate is conductive (Figure 5.4 C), after oxidation at the UME, O species can be reduced at the substrate surface and R species are regenerated (positive FB).

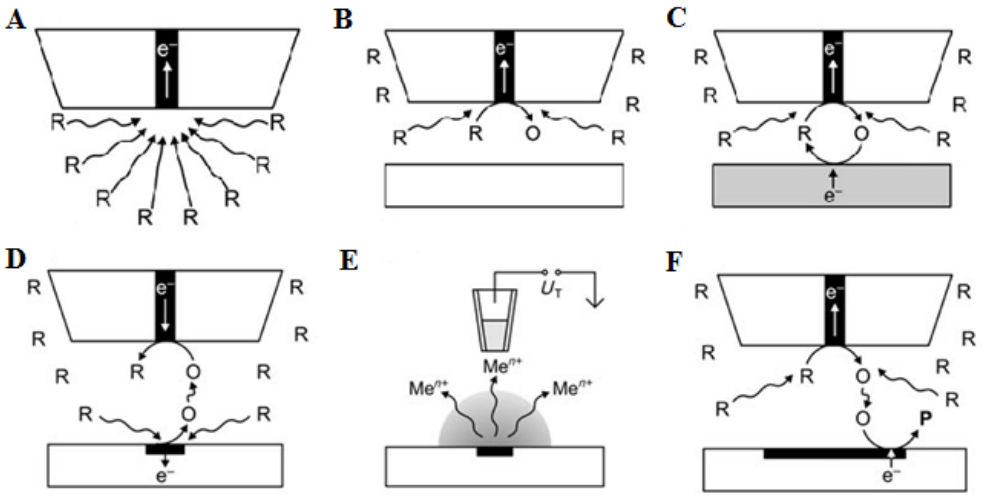

Figure 5.4. Principle of the feedback mode (A-C) and generation-collection mode (D-F); A – steady-state diffusion limited current in the bulk solution, B – hindered diffusion when the UME approaches the sample (negative feedback), C – mediator regeneration by a heterogeneous reaction at the sample (positive feedback), D – SG/TC mode with an amperometric UME, E – SG/TC mode with a potentiometric microelectrode (*e.g.* ion-selective electrodes), F – TG/SC mode [385].

In GC mode, contrary to FB mode, the solution initially does not contain any substance which can be converted at the UME at the electrode potential. In substrate generation/tip collection (SG/TC) mode, measurements can be carried out with amperometric (Figure 5.4 D) or potentiometric (Figure 5.4 E) UME. The sample is used as a generator of an oxidizable or reducible species which can be subsequently detected at the UME, if it approaches close enough to the active site. In tip generation/substrate collection (TG/SC) mode, the potential applied to UME allows for product generation, that is collected at the sample surface (Figure 5.4 F) [385].

In this work SECM was utilized to determine products of dioxygen reduction reaction performed at various surfaces: ITO with AuNPs, ITO with ITO nanoparticles (ITO_{NP}) and ITO covered with both gold and ITO_{NP}.

5.4. Atomic force microscopy

Atomic force microscopy (AFM) is another SPM technique. This high-resolution method is widely used for topography investigations (imaging and measuring) and patterning [386–389]. The most important components are: AFM fine tip attached to the cantilever, piezoelectric element, laser, photodiode, detector and PC. Depending on the goal of experiment, it is used in contact and tapping modes (Figure 5.5).

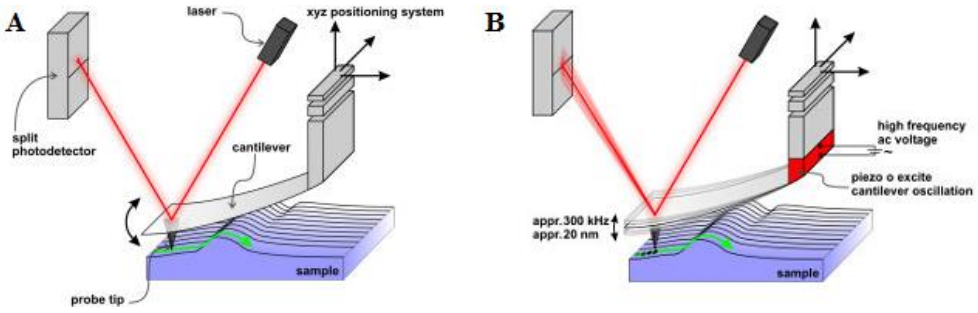

Figure 5.5. Schematic illustration of AFM static contact (A) and dynamic tapping (B) modes [390].

In the contact mode the force that is used as an imaging signal translates into cantilever deflection. In this mode relatively soft cantilevers compared to the tip and sample materials should be used. This means that rather stiff and hard surfaces can be studied. During scanning the tip is in contact with the sample and the repulsive force is measured. In a dynamic mode, piezoelectric element is additionally engaged. The cantilever is vibrating in a

controlled manner at or close to the resonance frequency. Interactions between the tip and the sample result in changes of the oscillations amplitude. This value can be kept constant by changing *z* position using feedback loop. This allows to investigate topography even if the probed sample is soft.

In this thesis, AFM was used to measure the height of gold nanoparticles electrodeposited at the ITO electrode surface. The thickness of ITO_{NP} film deposited at the ITO electrode was estimated from AFM cross section profile measurement.

5.5. Scanning electron microscopy

Scanning electron microscopy (SEM) is a very powerful imaging tool commonly used to visualize nano- and microstructures [391–393]. The difference between optical microscopy and SEM is the way how an image is "produced". In the first case the sample is probed with photons while in SEM focused electron beam is transmitted from electron gun (Figure 5.6). The resolution of SEM images is so greatly improved when compared with optical ones due to *ca.* 10^5 times shorter wavelength of electrons than photons.

Electrons generated in electron gun are accelerated in an electric field. Then the beam is focused by condenser lenses, passes though deflection coils and when it is properly oriented it finally scans the sample [391]. There are many possible ways for loosing energy by electrons interacting with the sample. It can be emitted as low-energy secondary electrons (SE), high-energy backscattered electrons, characteristic X-rays, transmitted electrons or heat. Usually a detector that collects SE electrons is utilized. Obtained SEM images are characterized with a very high quality and resolution [393]. However, in some cases, it is more intentional to use a detector that collects backscattered electrons. It allows to record images with high compositional contrast of different components present in the sample [393].

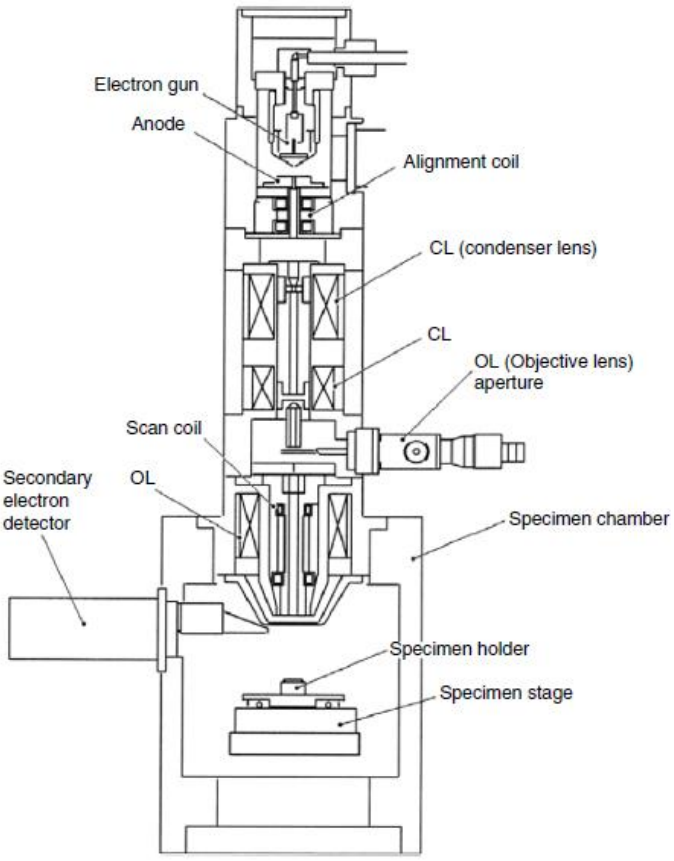

Figure 5.6. Schematic illustration of SEM setup [391].

One of the crucial issues to be considered is the preparation of a sample. Conductive substrates do not need a special treatment; they only have to be electrically grounded. This is also applicable for substrates which only a top layer is conductive (*e.g.* ITO electrode). However, when the sample is insulating, an ultrathin conductive film has to be deposited, usually by sputtering. Metallic (*e.g.* gold or platinum) thin films are commonly used. Nonetheless, there is an exception from these methodologies when non-conductive samples are analyzed in low-voltage mode of SEM or environmental SEM. Last but not least, the sample has to fit the holder that is placed in the chamber.

In this work SEM was widely used for imaging nano- and submicrometer nanoparticles. It was mainly used to characterize gold electrodeposited at a three-phase junction but also to visualize ITO_{NP}|AuNPs hybrid material. Finally SEM images were used to estimate the thickness of graphene-based composites deposited by drop-casting on the electrode surface.

5.6. Transmission electron microscopy

In transmission electron microscope (TEM), similarly like in SEM, electrons are used to screen the sample and produce an image [394–396]. However, there are several significant differences between them. First of all, in TEM, electron beam is partially transmitted through the sample and then it is collected on the fluorescent screen (Figure 5.7). Another issue is how strongly the beam is accelerated by an anode. For TEM it is usually 100 keV (40 – 400 keV), while for SEM it ranges between 0.2 and 40 keV. The last point is the specimen preparation. Since the beam has to penetrate the sample, the specimen has to be thin enough, in the order of hundreds of nanometers. Otherwise the electron beam might be scattered. Required sample can be prepared by etching or with focused ion beam cross section technique.

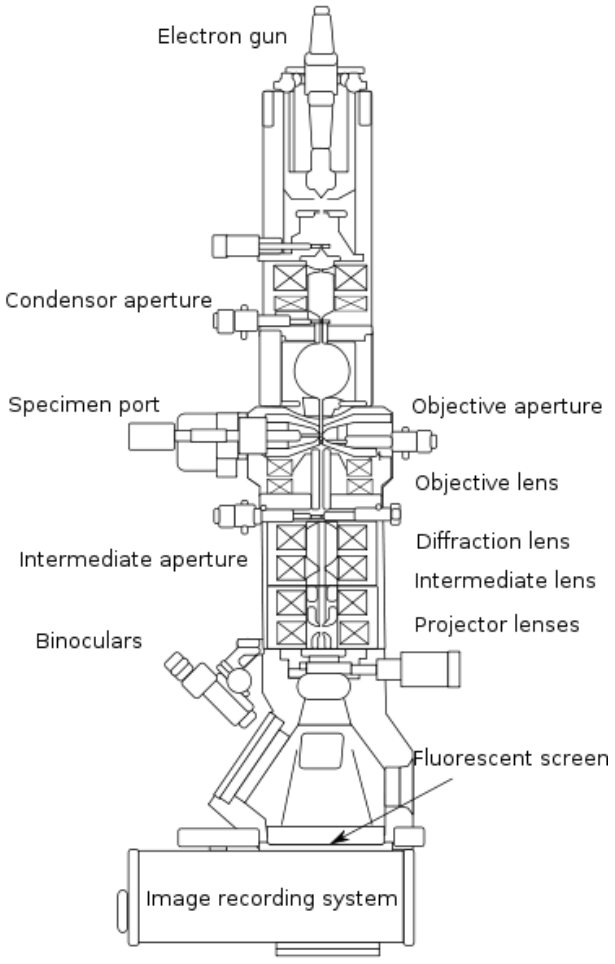

Figure 5.7. Schematic illustration of TEM setup [397].

Although TEM has drawbacks *e.g.* due to complicated sample preparation protocol, it is extremely powerful imaging tool. The highest reported resolution was in the sub-Ångström

range [395,396]. The most suitable samples for TEM analysis are thin foils, nanostructures and powders.

In this work TEM was used for imaging a cross section of ITO electrode modified with ITO and gold nanoparticles. Namely, it was utilized to characterize ITO_{NP} porous film as a 3D scaffold for AuNPs electrodeposition. Additionally, it was coupled with energy dispersive X-ray spectroscopy (XEDS) technique which was used for compositional analysis.

5.7. UV-vis spectroscopy

UV-vis spectroscopy is widely used as an analytical tool for quantitative determination of various chemical compounds [398,399]. Typically measurements are performed in solutions although solids and gases may also be investigated. This technique is used either for absorption or reflectance measurements in visible and near-ultraviolet light. Depending on the need this range can be extended up to near-infrared (UV-vis-IR) by using additional source of light *e.g.* tungsten-halogen lamp [400]. A spectrum that is recorded reflects the energy that is absorbed by the electrons of the molecule which are in consequence transitioned from the ground state into excited state. "Portion" of energy that can be absorbed is quantified and connected with a recorded wavelength by the relation, $E = h\,\lambda^{-1}$, where h is a Planck constant [399].

A physical quantity that is measured by the spectrophotometer as a function of wavelength λ is an absorbance A, which is defined by transmittance T:

$$A(\lambda) = \log(1/T(\lambda)) \qquad \textbf{(5.3)}$$

while T is expressed by the intensity of light that is transmitted I_T and the intensity of the incident light I_0 by $T = I_T/I_0$. So finally absorbance $A(\lambda)$ measured for each wavelength λ equals to $\log(I_0/I_T)$ [399].

From analytical point of view, there is an important relation between the measured absorbance A, also known as an optical density, and the concentration c of the investigated chemical compound. This is known as a Lambert-Beer law:

$$A = \varepsilon\, c\, L \qquad \textbf{(5.4)}$$

where ε is an extinction coefficient and L is a length of the light path through the sample [399]. ε is also known as molar absorptivity and defines the ability of chemical compound to absorb the light and is characteristic for each species.

Although in many cases a concentration can be estimated from this equation, there are some deviations that need further analysis. Lambert-Beer law is not suitable for samples of too high concentration, which causes the saturation of the absorption band. It also cannot be applied when the chemical compound that is investigated changes color with the concentration. The last example concerns inhomogeneous samples in the form of suspension because local concentration may change in time.

In this work, UV-vis spectroscopy was used to define sensitivity of multifarious gold particles by performing measurements in different solvents. It was engaged for absorption measurements of graphene oxide and reduced graphene oxide. This technique was also applied for colorimetric determination of mannose released from graphene-based composite.

5.8. Surface-enhanced Raman spectroscopy

Raman scattering is a kind of inelastic scattering of incident photons by atoms or molecules. In contrast with elastic Rayleigh scattering, it is characterized with a very low probability of occurrence. Approximately, only 1 per 10^7 of scattered photons and scattered inelastically [399]. For this reason, although Raman spectroscopy provides valuable information, it is not a very sensitive method. To eliminate this serious drawback, metallic rough surfaces or nanostructures (mainly silver, gold and copper) are employed. This technique is called surface-enhanced Raman scattering (SERS). SERS is a very powerful and sensitive tool for imaging and detection. The presence of an appropriate and highly optimizes metallic substrate allows to enhance Raman signal up to 13-14 orders of magnitude (Figure 5.7).

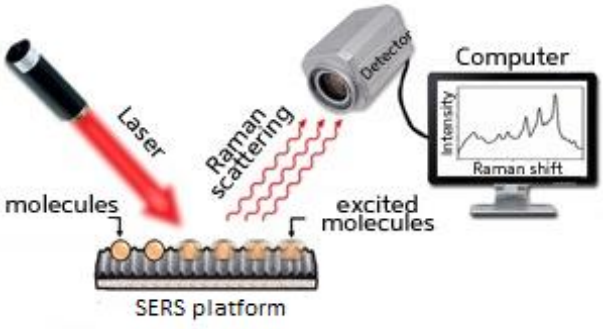

Figure 5.8. Schematic illustration of SERS setup [401].

There are two mechanisms which are used to explain the nature of this significant enhancement, electromagnetic and chemical [108]. The first one corresponds to the enhancement of an electric field through resonant excitation of localized surface plasmons. The latter one is due to charge transfer between investigated molecules and metallic surface. This is related to changes in electronic states of absorbed molecules [108]. Usually both mechanisms are taken into account because enhancement of a molecular polarizability α as well as enhancement of an electric field E can enlarge induced dipole μ of the molecule and consequently the intensity of scattering [399]:

$$\mu = \alpha E \qquad \textbf{(5.5)}$$

From SERS spectra one can obtain information about chemical composition and chemical state of functional groups, concentration, intermolecular interactions, symmetry as well as quality and deformation of the investigated material. Since vibration modes normal to the surface are most strongly enhanced (surface selection rules) the orientation of molecules can be also analyzed. This technique gives very detailed information about mixtures, composites, complex materials and also allows for single molecule detection (Chapter 1.4). However, there are several rules that need to be fulfilled to prepare appropriate experiment and make correct conclusions. First of all, SERS platforms have to be reproducible and stable to ensure repeatability of results. The wavelength of a laser has to be chosen individually, not only in terms of different metallic structures used as a SERS platform, but also their size and shape. There are many factors which influence the shape of SERS spectra and final results need to be interpreted very carefully.

In this thesis SERS spectroscopy was used to investigate the ability of flower-like AuNPs to enhance Raman scattering. Analysis was prepared with various dyes and biomolecules.

5.9. Wide-field fluorescence microscopy

Wide-field fluorescence microscope is an optical microscope, which uses fluorescence or phosphorescence to create an image of the sample [402]. White light emitted from the source passes through the first, excitation filter to produce a beam with well-defined wavelength (Figure 5.9). Then it is reflected by a dichroic filter and focused by the objective on the

sample. If the illuminated sample contains the specimen *e.g.* the fluorophore which can fluoresce, the light that it is emitted goes through dichroic and emission filters and is recorded by a detector or camera.

As a kind of an optical microscope its spatial resolution is limited due to the wavelength of electromagnetic wave that is used to excite the sample (diffraction limit) [66]. Another limitation is due to the photobleaching. This is a process of irreversible degradation of fluorescent molecules which takes place when it is exposed to the excitation light.

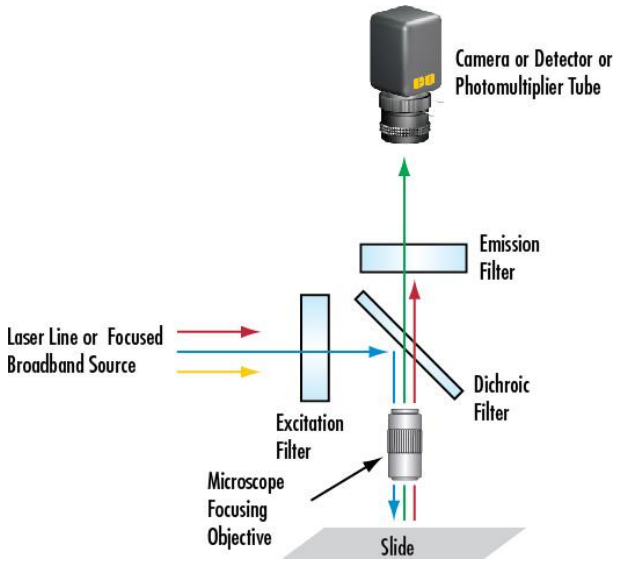

Figure 5.9. Schematic illustration of fluorescence microscope setup [402].

In this work, epifluorescence microscope was used to record images of surfaces with the deposited Fenna-Matthews-Olson (FMO) complex in transmission and emission modes. In that kind of system excitation of the specimen and detection of its fluorescence are realized with the same objective (the same path of light). Parameters that were used are the following: illumination light 365 nm, dichroic filter 650 nm, filter 800/10 nm, gain 300, oil immersion objective 100x, acquisition time 0.5 s and EMCCD (electron multiplying CCD) camera as a detector.

5.10. Confocal microscopy

Confocal microscopy is another optical technique for examining the optical properties of nanostructures. In contrast to the wide-field fluorescence microscopy, background and out-

of-focus light are both eliminated by point illumination and application of pinholes to allow measuring weak signals.

Schematic illustration of the confocal microscope setup is presented in Figure 5.10. In this work, Fianium supercontinuum laser source was used with a chosen wavelength 590 nm as an excitation light. The excitation beam passes through a number of optical elements. It is reflected by the mirror M1, passes through the lens system and pinhole, which expands its diameter. Then the beam passes through the grey filter (not used in this work) and dichroic mirror, where the light with a wavelength shorter than 650 nm is reflected and light with longer wavelengths is transmitted. Then the laser beam is focused by the objective (LM Plan x50 Olympus) on the sample. The sample is placed on a Table, which can be moved along three orthogonal axes (xyz). Fluorescence emitted from the sample is collected by the same objective. Afterwards, emitted light passes through the system of optical filters, whose cut off the light with wavelengths shorter than 665 nm (for spectral detection using a CCD camera) and pass the spectral band of 820-840 nm (for fluorescence transient detection using an avalanche photodiode). It allows collecting only the fluorescence emission associated with the FMO protein. In this work, fluorescence spectra were recorded with a CCD camera, and photodiode was used for fluorescence decay time measurements.

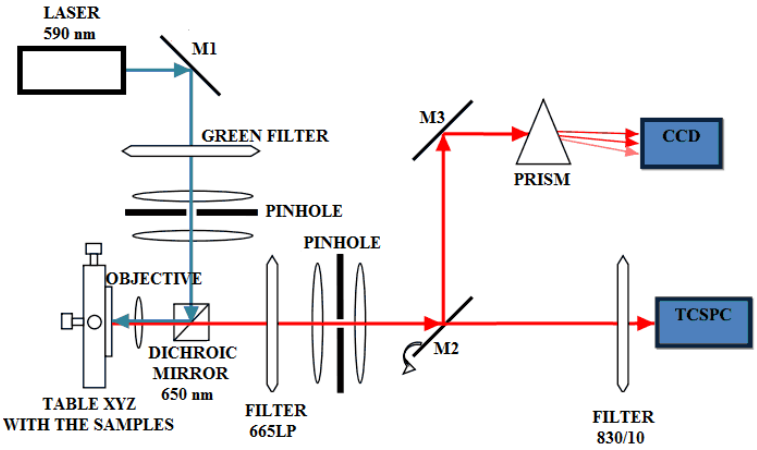

Figure 5.10. Schematic illustration of confocal microscope setup [403].

In this thesis, the confocal microscope was used for fluorescence intensity and decay time measurements of FMO deposited on a bare ITO and ITO covered with gold nanoparticles and/or rGO.

5.11. X-ray photoelectron spectroscopy and Auger electron spectroscopy

X-ray photoelectron spectroscopy (XPS) and Auger electron spectroscopy (AES) are used to identify elemental composition of investigated materials [394,398,404]. In XPS, electrons are released from the sample due to X-ray irradiation. Their binding energy E_B, that is measured, depends on the energy of photons of X-ray beam $h\nu$, kinetic energy of emitted photoelectron E_K, and work function characteristic to spectrometer W:

$$E_B = h\nu - (E_K + W) \qquad \textbf{(5.6)}$$

A schematic illustration of the mechanism of XPS and a system used for measurements are shown in Figure 5.11.

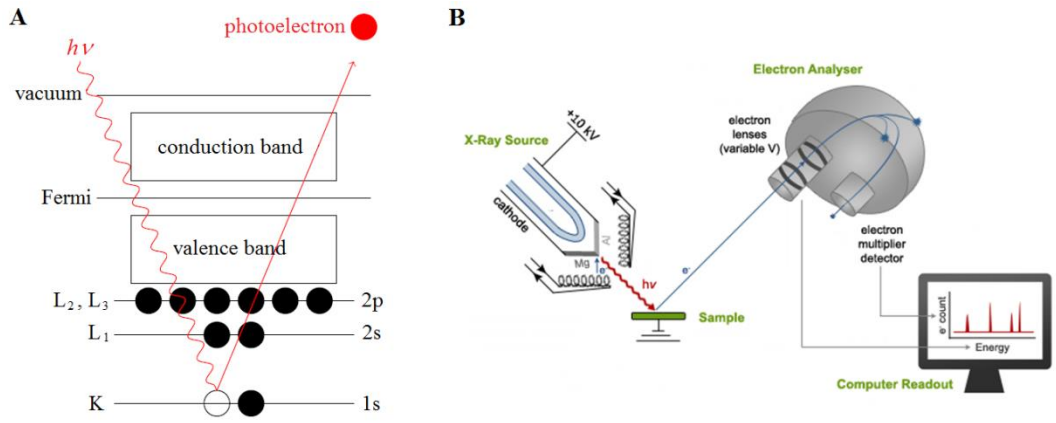

Figure 5.11. Schematic illustration of the mechanism of XPS (A) and setup (B) [405].

There are two main issues which distinguish AES from XPS. First of all, instead of X-ray source, a beam of electrons is used during measurement. Secondly, Auger effect consists of two processes (Figure 5.12). At first, a core electron is removed, then created hole is filled with electron from higher energy level and finally the energy difference is released. Consequently, measured kinetic energy E_K that is released is a function of binding energy E_B^1 of primarily removed electron, energy of the electron E' which fill the gap after the first electron and binding energy E_B^2 of the electron that is removed from atom (Auger electron):

$$E_K = E_B^1 - E' - E_B^2 \qquad \textbf{(5.7)}$$

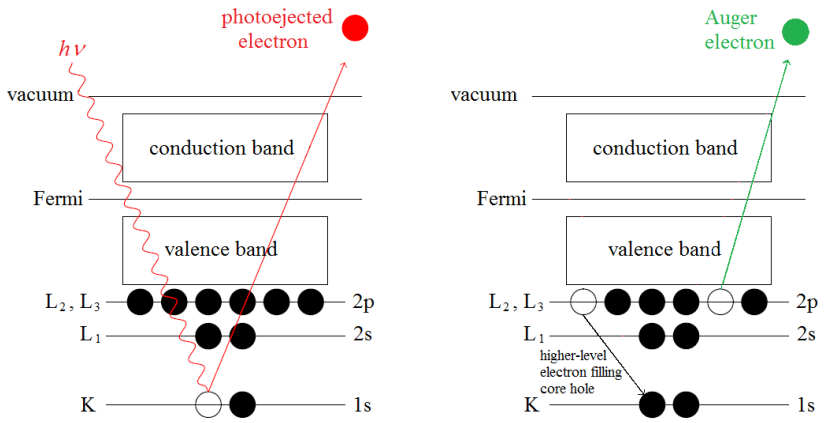

Figure 5.12. Schematic illustration of the mechanism of AES.

There are several main differences between both methods that need to be taken into account to choose appropriate technique. Except the source of excitation beam that was described, the first difference is connected with lateral resolution, for AES it is down to tens of nm, while for XPS it is in the order of micrometers. Furthermore, AES can be coupled with SEM for simultaneous imaging. While conductive substrate can be analyzed by both techniques, for insulating surfaces XPS is much more suitable because of charging effects which disrupt Auger electrons. For identifying and quantifying the contribution of elements present in the sample, XPS is more powerful tool. High-resolution core level spectra allows to distinguish between different species of the same element *e.g.* in C1s core level spectrum one can see bands from C-H/C-C, C-O or C=O groups (chapter 11). This is more difficult with AES, mostly because this method involves three electrons which influence the final measured value of E_K, while for XPS released photoelectrons are directly measured.

Both methods were used in this thesis to identify different materials. XPS was applied for graphene-based materials characterization where detailed information about chemical state of species was necessary. AES was engaged in AuNPs analysis, since high lateral resolution was important.

5.12. Contact angle measurements

Contact angle measurements are employed to investigate wettability of a solid surface, surface energy and liquid|liquid or solid|liquid solubility [406]. Experiments can be carried out using a simple sessile drop technique with goniometer method. The contact angle θ that is measured is formed between solid|liquid and liquid|gas interfaces (Figure 5.13). It can be

measured using Young equation (Figure 5.13*). Goniometer allows for a visual measurement of the contact angle from the captured image.

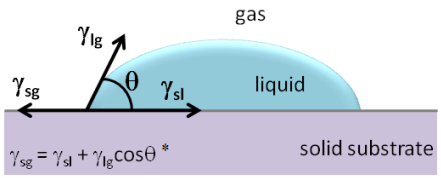

Figure 5.13. Schematic illustration of contact angle (θ) measurement and Young equation*.

In this work, 5 μL droplet of deionized water was placed with the syringe on the investigated solid substrate. Optical system was used to record a profile of this droplet and calculate contact angle.

6. Chemicals, materials and biomolecules

Tin-doped indium oxide coated glass (ITO) (sheet resistivity 8−12 Ω sq^{-1}) was obtained from Delta Technologies Ltd. ITO nanoparticles (ITO_{NP}) (average diameter *ca.* 20 nm, dispersion in water, Nanophase Technologies Corp., USA) were dried and re-dispersed by ultrasonication in methanol (3 wt.%).

$HAuCl_4 \cdot 3H_2O$, tetraoctylammonium bromide (TOABr), KPF_6, $NaClO_4$, KCl, NaOH and H_2SO_4 were obtained from Sigma-Aldrich. Tetraoctylammonium tetrachloroaurate ($TOA(AuCl_4)$), 15 mM solution, was obtained by anion exchange from TOABr and $HAuCl_4 \cdot 3H_2O$ aqueous solutions as described elsewhere [7]. D-(+)-Glucose (99.5%) was obtained from Sigma–Aldrich. Methanol, ethanol, toluene, citric acid and sulfuric acid (all analytically pure) were from Chempur. Na_2HPO_4 (analytically pure) was purchased from POCh. Bilirubin oxidase (BOx) was donated by Amano Enzyme Inc.

Malachite green isothiocyanate (MGITC) was from Invitrogen. Rhodamine 6G (R6G), 1,4-mercaptobenzoic acid (MBA), choline and alanine were obtained from Sigma-Aldrich. Porphycene was synthesized and purified according to literature procedure [407,408].

Graphite powder (<20 μm), H_2O_2, $KMnO_4$, $Ru(NH_3)_6Cl_3$, phosphate buffered saline (PBS), tetrathiafulvalene (TTF), dopamine (DA), acetonitrile (ACN), tetrahydrofuran (THF), *1H,1H,2H,2H*-perfluorodecanethiol (HS-PF), ethynylferrocene (EFc), CuI, triethylamine (TEA), $CuSO_4 \cdot 5H_2O$, L-ascorbic acid, $FeClO_4$ and ethylenediaminetetraacetic acid (EDTA) were purchased from Sigma-Aldrich. The azide-terminated (DA-N_3) and alkynyl-terminated (DA≡) dopamine anchors were prepared as previously described [409]. Cyclophane cyclobis(paraquat-p-phenylene) ($CBPQT^{4+}$) was synthesized as reported previously [410]. The formation of α-propargyl mannopyranoside (alkanyl-terminated mannose) was achieved according to reports by Roy *et al.* [411] and Yeoh *et al.* [412]. The azide-terminated tetrathiafulvalene (TTF-N_3) anchor was prepared from 2-(hydroxymethyl)tetrathiafulvalene, using a previously described protocol [413].

Fenna-Matthews-Olson (FMO) complex was obtained from prof. Richard Cogdell (University of Glasgow).

Graphene oxide (GO) was synthesized from graphite powder by a modified Hummers method [306,414]. Typically, 1 g of graphite powder was added to 23 mL of concentrated H_2SO_4 in an ice bath. $KMnO_4$ (3 g) was then added slowly with stirring and cooling to keep the temperature of the reaction mixture below 20°C. The temperature of the reaction mixture was increased and maintained at 35°C for 30 min. When 46 mL of deionized water was added slowly to this mixture temperature was increased to 98°C. After 15 minutes, 140 mL of deionized water was added followed by 10 mL of 30% H_2O_2 solution. The solid product was separated by centrifugation. It was washed repeatedly with 5% HCl solution until the sulfate ions are removed and then washed with distilled water repeatedly until it becomes free of chloride ions. The product was then filtered and washed 3–4 times with acetone to make it moisture free and the residue thus obtained was dried in an air-oven at 65°C overnight. A total of 0.5 g of the synthesized graphite oxide was dispersed in 100 mL of water, exfoliated through ultrasonication for 3 h, and used as a stock of GO−water suspension.

7. Instrumentation

Cyclic voltammetry (CV) and chronoamperometry (CA) were performed with an Autolab PGSTAT30 (Metrohm Autolab) electrochemical system with GPES software.

SECM measurements were carried out with CHI900B SECM workstation (CH Instruments) by Justyna Jędraszko. Pt microelectrodes for SECM experiments were made by sealing a Pt wire (25 μm diameter, Goodfellow, England) using PC-10 micropipette puller (Narishige) into borosilicate glass capillaries and polished.

Atomic force microscopy (AFM) was performed with a multimode scanning probe microscope (Bruker) using the ScanAsyst mode by Dr. Martin Jönsson-Niedziółka.

Scanning electron microscopy (SEM) images were obtained with a Zeiss Supra Field and FEI Nova NanoSEM 450 scanning electron microscope with FEG (field emission gun, Schottky type) systems by Dr. Adam Presz and Dr. Martin Jonssön-Niedziółka. Images presented in the chapter 11 were obtained with an electron microscope ULTRA 55 (Zeiss) by Dr. Yannick Coffinier.

Transmission electron microscopy (TEM) specimens were prepared by the focused ion beam (FIB) cross-section method in a FEI Helios NanoLab system. The cross-sections for TEM observations and analyses were cut from the region of the three-phase junction using a focused beam of Ga^+ ions. The specimens were characterized in scanning transmission electron microscopy (STEM) mode in a JEOL JEM-2100 TEM microscope. Elemental mapping was performed using energy-dispersive X-ray spectroscopy (XEDS) with high angle annular dark field (HAADF) imaging of the analyzed area in STEM mode. Analysis was performed by Dr. Adam Łaszcz and Prof. Andrzej Czerwiński.

UV-vis spectra were recorded with using double beam Nicolet Evolution 300 spectrophotometer (Thermo) (Chapter 8 and 12) and Perkin−Elmer Lambda UV/vis 950 spectrophotometer (Chapter 11).

SERS measurements were performed using a Renishaw InVia Raman system equipped with a He−Ne laser emitting a 632.5 nm line used as the excitation source by Dr. Agnieszka Kamińska and Dr. Sylwester Gawinkowski.

X-ray photoelectron spectroscopy (XPS) experiments were performed in a PHl 5000 VersaProbe-Scanning ESCA Microprobe (ULVAC-PHI, Japan/USA) instrument at a base pressure below 5×10^{-9} mbar by Dr. Janusz Sobczak and Dr. Wojciech Lisowski.

A high resolution Auger microprobe, Microlab 350 (Thermo Electron), was used to determine the chemical composition of the deposited Au particles, utilizing high resolution SEM and Auger electron spectroscopy (AES) by Dr. Marcin Pisarek.

Water contact angles were measured using deionized water with a remote-computer controlled goniometer system (DIGIDROP by GBX, France). The precision is ±1°.

Fluorescence measurements were performed in the Optics of Hybrid Nanostructures group headed by Prof. Sebastian Maćkowski. Wide-field fluorescence microscope Nikon Eclipse Ti-U with EMCCD Andor iXon Du-888 detector and confocal microscope constructed by Bartosz Krajnik, described in detail in the section 5.10, were utilized. Experiments were carried out by Magdalena Twardowska and Kamil Wiwatowski, with a great help of Bartosz Krajnik. Computer program used for analysis of fluorescence maps was written in LabView by Nikodem Czechowski. Fluorescence maps, profile lines and enhancement factors were provided by Magdalena Twardowska, correlations by Kamil Wiwatowski.

8. Electrodeposition of gold nanoparticles at a three-phase junction

In this chapter, electrodeposition of gold nanoparticles and submicrometer particles at a three-phase junction electrode|liquid|liquid is introduced and described. At the beginning the electrochemical cell used for deposition and the experimental protocol are presented. Then preliminary studies about the mechanism of gold particles formation using two models are discussed. Finally, spectroscopic, electrochemical and microscopic characterization of formed gold deposit is presented and described.

8.1. Preparation of the electrochemical cell and electrodeposition protocol

In the first part of experimental work, an electrochemical cell (Figure 8.1) was prepared from a simple vial. In its lower part, two wires, platinum (Pt) and silver (Ag), were pressed across the cell wall and protected with silicone glue. They play a role of counter and pseudo-reference electrode, respectively. After the cell was cleaned and dried, the first liquid phase was added. In most experiments, an aqueous solution of KPF_6 was used, but in some experiments it was exchanged with other electrolytes, $KClO_4$ or KCl. Toluene solution, a second liquid phase, with a gold precursor was prepared as described before [7]. Namely, toluene solution of tetraoctylammonium bromide (TOABr) which plays a role of phase-transfer compound was mixed with aqueous solution of tetrachloroaurate acid ($HAuCl_4$) and by anion exchange a toluene solution of TOA($AuCl_4$) was obtained. To avoid a disruption of the liquid|liquid phase, a flat ITO working electrode was first immersed in the cell filled only with aqueous solution and then toluene solution with gold precursor was added (Figure 8.1).

Instead of a single liquid phase [29,415,416] a system of the three-phase junction was employed, mainly to control the properties of the deposit (obtained in the form of stripe at the junction – pink line in Figure 8.1_A), its density but also to have a better control over nanoparticles properties and improve their stability. Additionally, instead of nanoparticles in a bulk solution or at a liquid|liquid interface, it was possible to obtain the deposit at the electrode surface [7,8,16–18]. It is the first example when electrode|liquid|liquid interface is utilized for metallic nanoparticles deposition.

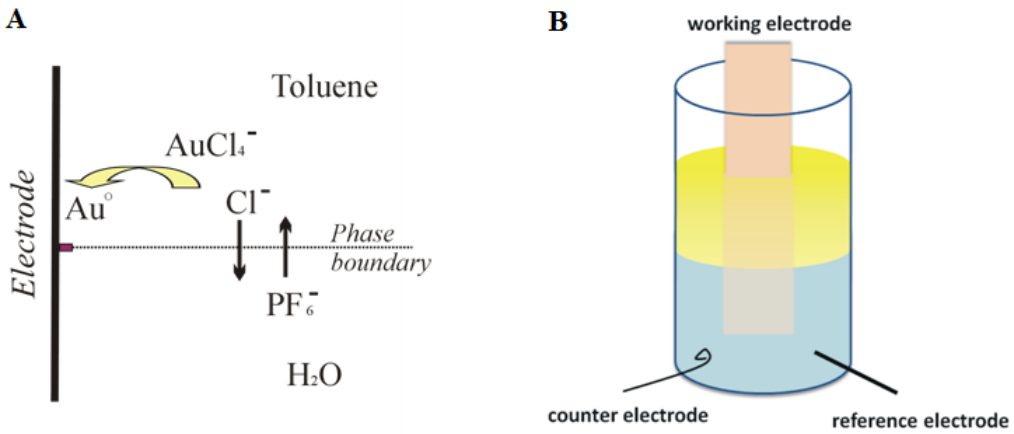

Figure 8.1. 2D (A) and 3D (B) schematic illustration of the electrochemical cell used for electrodeposition of AuNPs at the three-phase junction.

One can choose two strategies for metallic nanoparticles electrodeposition either by cyclic voltammetry (CV) or chronoamperometry (CA). Both of them were tested in this work. At first, applying CV technique, a hundred subsequent scans were recorded in the potential range +0.5 V to -0.35 V at a scan rate 10 mV s^{-1}. From SEM image and statistical analysis it was noticed that the deposit is rather inhomogeneous and the size distribution is pretty wide (Figure 8.2).

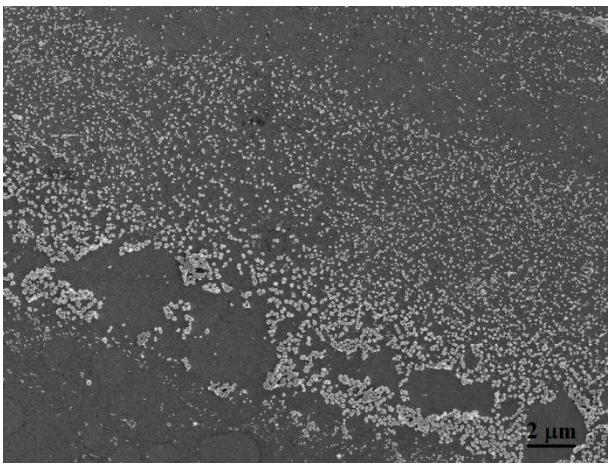

Figure 8.2. SEM image of gold deposit on ITO electrode obtained by cyclic voltammetry (from +0.5 V to -0.35 V during 100 subsequent scans).

To refine this methodology and to improve the features of AuNPs deposit, CA was employed. There are basically two possibilities, one-pulse and double-pulse deposition. As the names suggest in the first case only a single value of the potential is applied for a defined time, while in the second case the first very short pulse is applied for nucleation and then it is switched for the second one for growth (Figure 8.3_C). It was shown earlier that the double-

pulse CA provides much better control over nanoparticles' properties than single step CA [29,381–383,416]. However, in this work both methods were investigated and compared. For a double-pulse technique, first a more negative potential E_1 (-1.0, -0.7 or -0.5 V) was applied with the nucleation time of 10, 20, 50 and 200 ms. The second pulse V_2 was applied at 0 or -0.1 V for 10, 50, 100, 500, 1500, or 2500 s. SEM and AFM images show that the best results in terms of homogeneity in size and density are obtained for E_1 = -0.7 V during 50 ms and E_2 = 0 V. For the second pulse different durations were carefully tested and results are presented in the following sections of this chapter. Interestingly, the elimination of the first step did not influence the properties of the deposit as it could be expected. The shape and size of gold particles are comparable to those obtained with a double-pulse technique (Figure 8.3). What is even more surprising, after changing the sequence of the pulses, the obtained deposit is similar to the one prepared with previously described single- and double-pulse techniques.

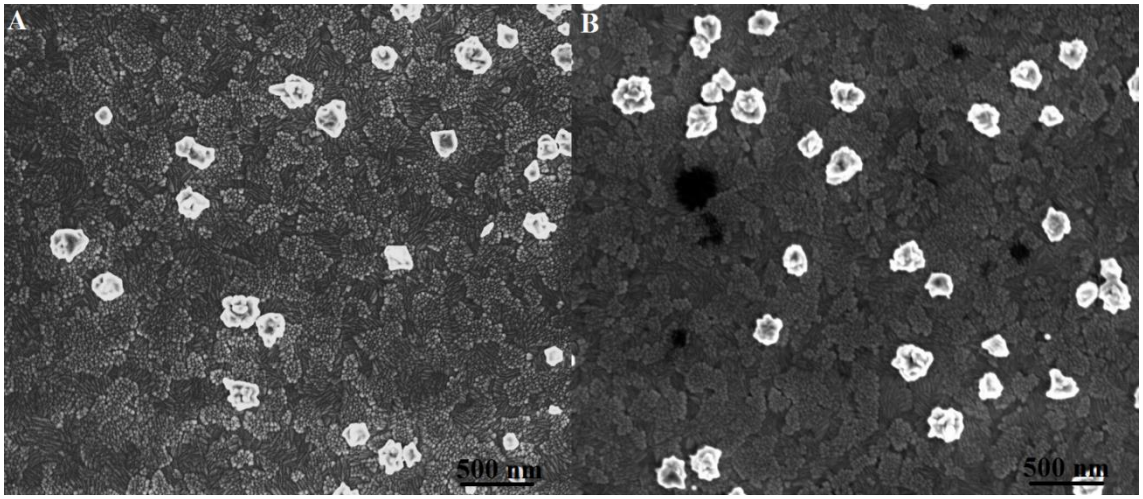

Figure 8.3. SEM images of gold deposit on ITO electrode obtained by (A) double-potential-step CA (V_1 = −0.7 V for 50 ms and V_2 = 0 V for 100 s) and (B) single-potential-step CA (at 0 V for 100 s).

Such test experiments proved that the presence of a triple boundary between two liquids and an electrode influence strongly the properties of nanoparticles as compared to a single-liquid-phase system. The electrogeneration is greatly influenced by the geometry of the cell and the properties of both liquid phases and to a lesser extent by the sequence of potentials. This was confirmed by experiments with different aqueous electrolytes. As it was mentioned above in most experiment KPF_6 was used (standard transfer potential from water into the organic phase, $\Delta_{aq}^{org}\varphi_{PF_6^-}^0$ = 0 V). However to show the influence of the electrolyte, the experiments with aqueous solution of $KClO_4$ ($\Delta_{aq}^{org}\varphi_{ClO_4^-}^0$ = 0.083 V) or

KCl ($\Delta_{aq}^{org}\varphi_{Cl^-}^{0}$ = 0.324 V) [138,141,417] were performed. According to SEM images (Figure 8.4), it is concluded that the more hydrophilic anion in the aqueous solution the smaller and less dense deposition is. This gives the next clue about the mechanism of the reaction at a triple interface and suggests that anions are strongly involved. In order to characterize gold deposit obtained with a double-pulse technique and make some conclusions about the process of electrogeneration, the properties of gold particles are described in details in the next parts of this chapter.

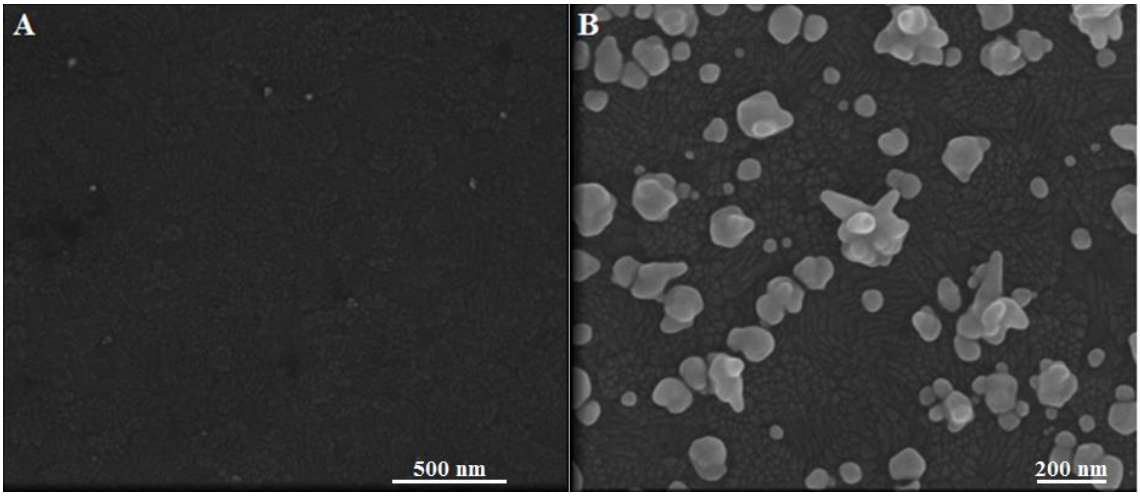

Figure 8.4. SEM images of gold deposit on ITO electrode obtained by double-potential-step CA with the first potential step at −0.7 V for 50 ms and the second one shifted to 0 V for 2500 s obtained for KCl (A) and $NaClO_4$ (B) as a supporting electrolyte.

8.2. The mechanism of the reaction and modeling

There are two processes at a three-phase junction: reactions at a liquid-liquid interface and gold deposition at a solid substrate. From already described experiments it is concluded that the reaction is controlled by the presence of a triple boundary. The main drawback is that it is not possible to look inside the cell and make direct observations of the surface during the reaction, with a microscope. However, from optical and SEM images it is assumed that the stripe with gold particles is formed on the electrode surface, in the place where both liquids are in contact.

To explain what happens at a three-phase junction, additional investigations and computer modeling were necessary. At first, two-liquid system was analyzed to explain whether and how toluene containing gold precursor interacts with aqueous electrolyte. Two glass tubes were filled similarly like an electrochemical cell, with aqueous electrolyte at the

bottom and toluene/TOA($AuCl_4$) at the top (Figure 8.5). On the left, in both photos one can see freshly prepared solutions which are transparent and clear. On the right, there is a vial left for 24 h and both lower and upper phase became cloudy. What was also visible but hard to see on the photos is an emulsion or a kind of sludge formed at the liquid-liquid interface. This experiment shows that although the solubility of toluene in water is very low (0.563 mL in 1000 mL H_2O at 25°C) this system is not infinitely sustainable and an emulsion zone that is formed can expand with time [418,419].

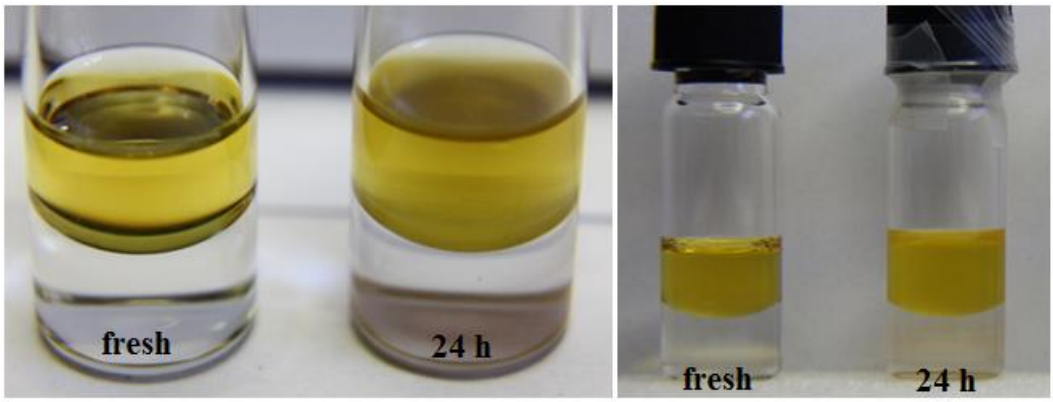

Figure 8.5. Optical images of glass vials filled with aqueous electrolyte and toluene with gold precursor, on the left, freshly prepared and on the right, left for 24 h (both images show the same pair of vials but with different magnification).

In the next experiment, the formation of the emulsion was shown in a more direct way. Two droplets, of an aqueous electrolyte and toluene with gold precursor, were deposited on a glass substrate and covered with a glass slide (Figure 8.6_A). Under the optical microscope, it was noticed that when both liquids got into contact, immediately the emulsion was formed (Figure 8.6_B). The width of the emulsion zone extended with time, during tens of seconds (Figure 8.6_C). Longer observations were not possible due to liquid evaporation.

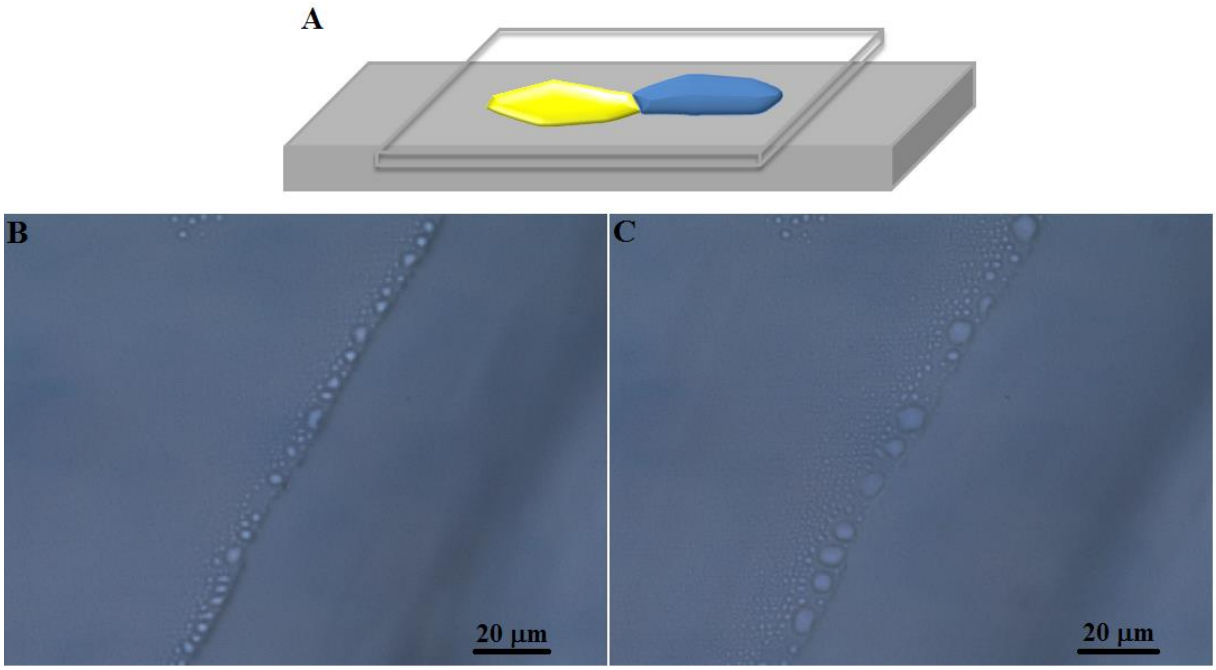

Figure 8.6. Schematic illustration of a simple system with two droplets (aqueous electrolyte and organic solvent) employed for the investigation of an emulsion formation (A); two optical images of the emulsion formed at a liquid|liquid interface (B) immediately after the droplets came into contact and (C) after *ca.* 50 s.

Next, a resistivity of utilized solutions and the system of two-liquids was measured. From impedance spectroscopy data it was calculated that for 0.1 M KCl, 0.1 M KPF_6 and 1mM $TOA(AuCl_4)$(toluene) | 0.1 M KPF_6 (1:1 ratio), the resistivity is in the same order of magnitude ~1 Ω m (table 8.1). However for 1mM $TOA(AuCl_4)$ in toluene, the resistivity was so high that it was difficult to measure it in a traditional cell that was used in all experiments. To solve this problem, the cell was changed for two parallel electrodes (1.9 cm × 0.75 cm) separated at 0.1 cm distance. The resistivity of a toluene solution with gold precursor equals $1.32 \cdot 10^6$ Ω m, which is three orders of magnitude lower than that of pure toluene. Nonetheless it is still very high, ~10^6 more than for liquid|liquid system. This clearly indicates that dissolution of the gold precursor salt in toluene is negligible and the presence of an aqueous electrolyte which serves counterions is necessary.

Table 8.1. Values of resistivity measured with impedance spectroscopy.

Solution	Resistivity (Ω m)
0.1 M KCl	0.79
0.1 M KPF_6	0.92
1mM $TOAAuCl_4$(toluene) | 0.1 M KPF_6	1.01
1mM $TOAAuCl_4$(toluene)	1.32×10^6
Toluene	1.34×10^9

The last part of this section is devoted to modeling of gold nanoparticles formation to show possible scenario of their growth. There are two models which can be used to describe a growth process of both deposited and electrodeposited layers and particle clusters. In DLA (diffusion limited aggregation) model, it is assumed that these processes are connected with Brownian motions of diffusing reagents and clusters aggregation is limited by diffusion [420]. The algorithm describes a randomly walking molecule which sticks to the previously created cluster. The concentration of molecules is relatively low. Growing cluster follows towards random concentration gradient, creating tree-like structures that are called Brownian trees [420]. In Eden model it is assumed that in conditions controlled by reaction, a small probability for sticking and/or an excess of the substrate demonstrate a conversion into another type of morphology – much more compact without branching [421,422].

The multifarious shape of electrodeposited nanoparticles indicates that the intermediate process between DLA deposition model (developed Brownian trees) and Eden model (compact clusters) is responsible for growing process. Moreover, it can be influenced by diffusion of gold atoms to the spots with the lowest energy where the neighboring places are most frequently filled with gold atoms. A simple model of cellular automaton was created to visualize the growth of electrodeposited particles and to check the role of both diffusion and reaction limited mechanism. Gold electrodeposition occurs from anionic form of gold precursor dissolved only in organic phase in a strong anodic polarization of an electrode. In these conditions an electrowetting of an electrode surface with an aqueous phase is observed. It was assumed that the deposition takes place in organic droplets, which can adhere to the electrode only in one point and they cannot wet the substrate.

In a designed cellular automaton model the system has a discrete form of cubes (Figure 8.7) [423]. They have different chemical composition. At the beginning there are three types of cubes representing an aqueous electrolyte (AQU), organic solvent with gold

precursor (ORG) and an electrode (MET) (Figure 8.7). ORG cell which sticks to the electrode surface is changed into AUM cell representing the first nuclei of a metallic gold. ORG cell adjacent to the AQU cell is signed as ORS and it defines a surface of a droplet. ORS cells which are adjacent to AUM cells are named ORR and they are "reactive". In such system there are random "migrants" which represent a gold precursor. If the "migrant", during its random walk, goes into ORR cell, than it is changed into AUM, and ORS cells adjacent to it become new ORR cells.

There are two parameters that were considered, P_{agr} which is a probability that "the migrant" goes into ORR cell and P_{surf} which describes the adsorption of "migrants" on the surface. There are also additional conditions: 1) "migrants" are present only in ORG and ORS cells, 2) the probability of a transfer from ORG to ORS cell equals P_{surf}, 3) the probability of a transfer from ORG and ORS cells into ORR equals P_{agr}, 4) "the migrant" stops to exist when it enters ORR cell which is then changed into AUM cell.

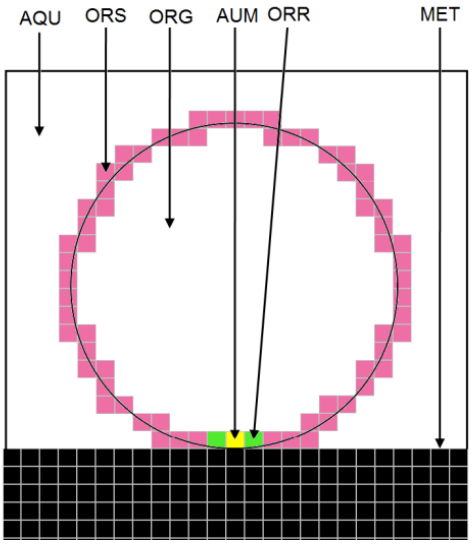

Figure 8.7. Schematic illustration of the cellular automaton model.

Using the cellular automaton model [423] with different values of both probabilities (0.01, 0.1 and 1), nine examples of various cluster shapes are created (Figure 8.8). It is noteworthy that both probabilities are related to different processes and they are not correlated. While P_{surf} describes a tendency of gold precursor for adsorbing on the surface (P_{surf} = 1 means there is no tendency for adsorption, P_{surf} = 0 means that molecules which appeared on the surface will never leave it), P_{agr} indicates a tendency for aggregation that is probability that when a gold compound appeared in a reactive place (a boundary between

already created cluster and both aqueous and organic phase), then it reacts and connects with gold cluster. In situation when both probabilities equal 1, obtained structures are branched and loose, which is not the case of electrodeposited AuNPs. Particles obtained at the three-phase junction are more compact than branched, so for modeling it means low values for P_{agr}.

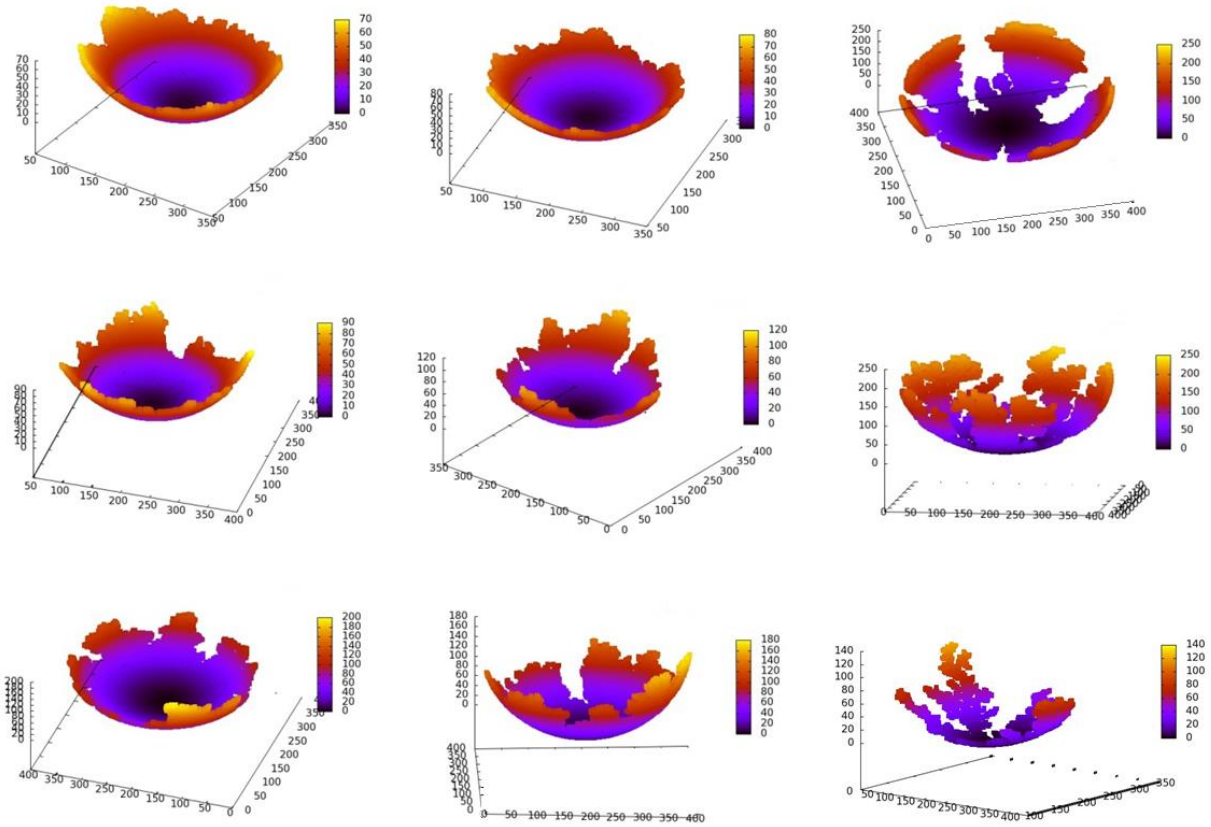

Figure 8.8. Clusters prepared with the cellular automaton model, representing nine different shapes for various reaction conditions. On the left to right P_{surf} = 0.01, 0.1 and 1, from the top to the bottom P_{agr} = 0.01, 0.1 and 1.

Taking into account all collected information, and an important role of the cell geometry, hydrophilic/hydrophobic character of anion and extremely high resistivity of the gold precursor solution in toluene, a reduction reaction of TOA($AuCl_4$) at a three-phase junction can be proposed:

$$TOA(AuCl_4)_{(org)} + 3\bar{e}_{(electrode)} \rightarrow Au^0_{(s)} + 4\ Cl^-_{(org)} + TOA^+_{(org)} \qquad \textbf{(8.1)}$$

Although both anion Cl^- and cation TOA^+ can be expelled into the aqueous phase:

$$4\ Cl^-_{(org)} + TOA^+_{(org)} \rightarrow 4\ Cl^-_{(aq)} + TOA^+_{(aq)} \qquad \textbf{(8.2)}$$

it is more probable that the TOA^+ stays in the organic phase and the hydrophilic chloride anions are replaced by the more hydrophobic hexafluorophosphate from the aqueous phase

$$Cl^-_{(org)} + PF_6^-{}_{(aq)} \rightarrow Cl^-_{(aq)} + PF_6^-{}_{(org)} \quad \textbf{(8.3)}$$

The last conclusion is in agreement with the test prepared with different anions (section 8.1 and Figure 8.4). For more hydrophilic anions in aqueous electrolyte the deposition process was less efficient, and for chloride ions does not occur at all.

8.3. Characterization

After general understanding of the system and explanation of the mechanism of the reaction, in this part properties of gold deposit are described. For a more detailed characterization of electrogenerated AuNPs electrochemical and spectroscopic measurements as well as microscopic analysis were used.

8.3.1. Voltammetry

Cyclic voltammetry profile is widely used as a basic method to get information about the surface of gold structures [24,424–426]. Measurements are performed in acidic solution with a scan rate 50 mV s^{-1}. Voltammogram (— Figure 8.9a) obtained for AuNPs deposited on ITO electrode presents characteristic features of gold with the oxidation region above 1 V which corresponds to gold oxide formation and its dissolution (re-reduction) at ~0.9 V [24,424,425]. In the forward scan in the region 1 – 1.6 V there are two oxidation peaks which can be attributed to two oxidation reactions [426]:

$$Au + H_2O \rightarrow Au\text{–}OH + H^+ + e^- \quad \textbf{(8.4)}$$

$$Au\text{–}OH \rightarrow AuO + H^+ + e^- \quad \textbf{(8.5)}$$

For a reference measurement a bare ITO electrode was used (— Figure 8.9b).

It can be also calculated by integration of a cathodic peak area at 0.9 V how much of the charge (Q_c) was involved in the reduction of AuO layer. If one assumes that the entire

surface of gold deposit was involved in the reaction, the value of the surface coverage Γ for gold can be estimated from the equation 8.6:

$$\Gamma = Q_c/nFA \qquad \textbf{(8.6)}$$

where n is the number of electrons exchanged (n = 1) and A is a surface area (A = 0.1 cm^2). A surface coverage of gold Γ = 1.06 10^{-9} mol cm^{-2}, which is comparable or slightly larger than some results presented in the literature [427,428]. In the "double-layer" region, below ~0.7 V a slight increase of a current density for an electrode modified with AuNPs in comparison with bare ITO is visible resulting from the nanoparticulate nature of the electrode [428].

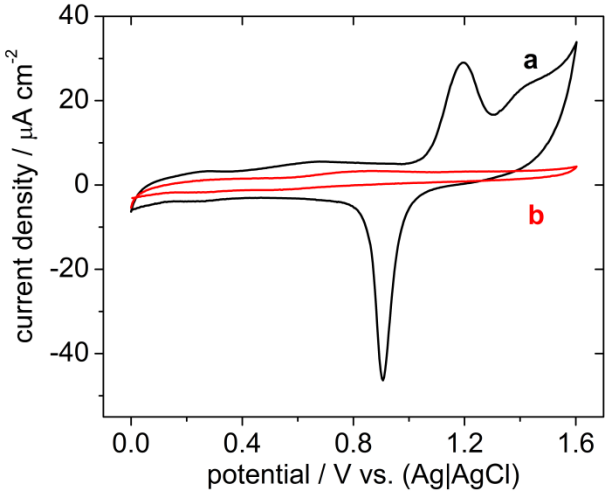

Figure 8.9. Cyclic voltammograms of gold particles electrodeposited on ITO electrode (a – black curve) and bare ITO electrode as a reference (b – red curve) obtained with deoxygenated 0.1 M aqueous H_2SO_4. Scan rate 0.05 V s^{-1}.

8.3.2. Optical, SEM and AFM imaging

Scanning electron microscopy (SEM) is a very powerful tool for imaging nanometer- and micrometer-size structures. Images in Figure 8.10 present gold deposits obtained for different growth times: 500 – 2500 s. One can see from pictures on the right, with higher magnification, that there is no significant difference in size but the density is clearly dependent on deposition time. Electrogenerated gold particles are multifarious with no substantial aggregates, and rather evenly distributed on the electrode surface. Another feature visible on both optical (Figure 8.10_A) and SEM (Figure 8.10_B-G) images is a sharp edge which might be the place where the deposition starts. However the width of the stripe is rather

significant and equals to at least a few hundred (300-400) of micrometers for time of growth 10 s, up to several hundred (800-900) micrometers for 2500 s. A possible reason is an emulsion formation as described in the previous section. Its presence does not allow to obtain infinitely narrow deposit, *e.g.* a single line with nanoparticles as was shown before [429–431]. The limit of the deposit thickness was reported to be in the order of ten of micrometers [429–431]. The average diameter of nanoparticles equals 150 ± 40 nm (Figure 8.11).

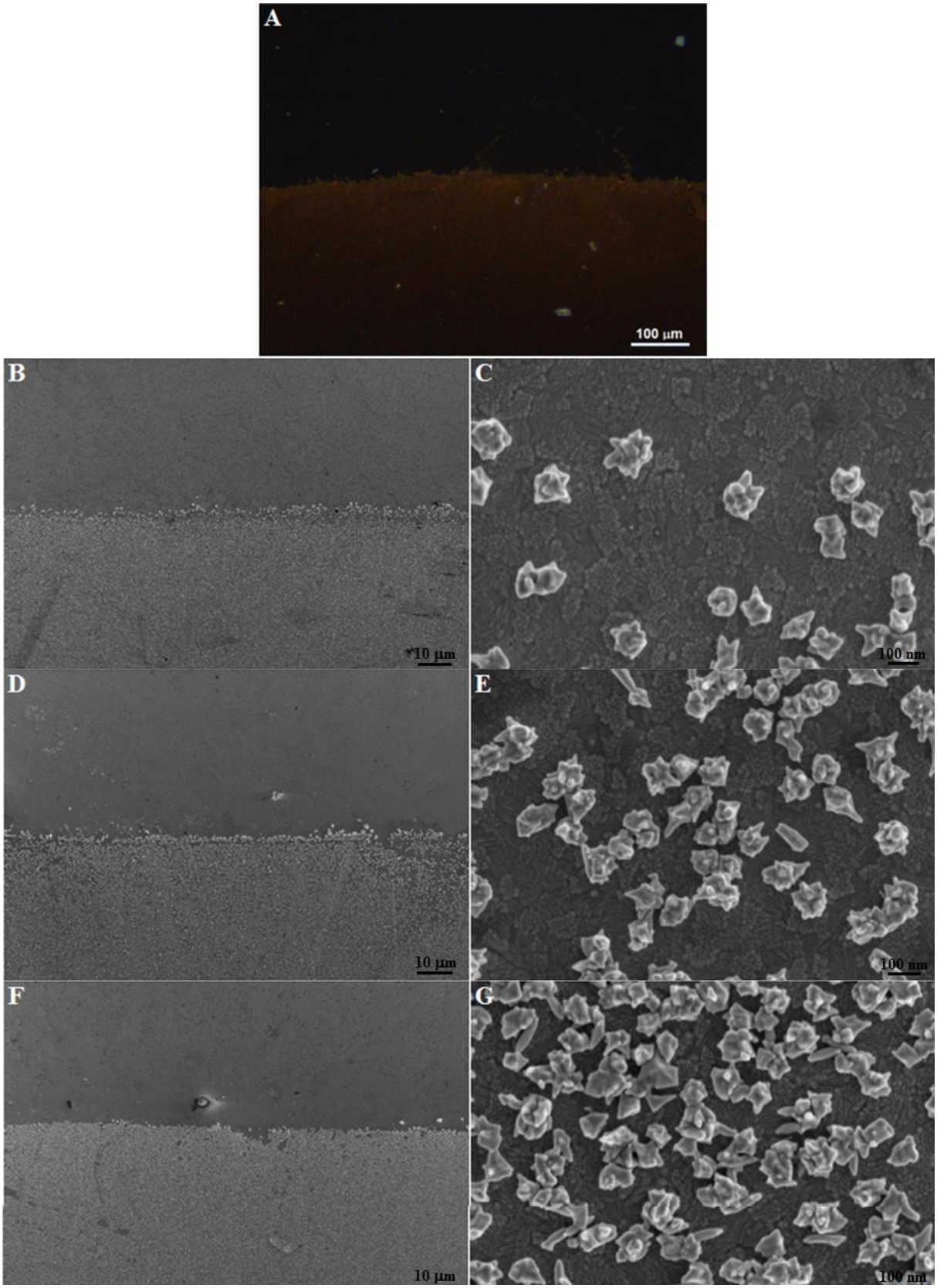

Figure 8.10. Optical (A) and SEM (B-G) images of gold deposits on ITO electrode obtained by double-potential-step CA with the first potential step at −0.7 V for 50 ms and the second one shifted to 0 V for (B-C) 500, (D-E) 1500, and (F-G) 2500 s.

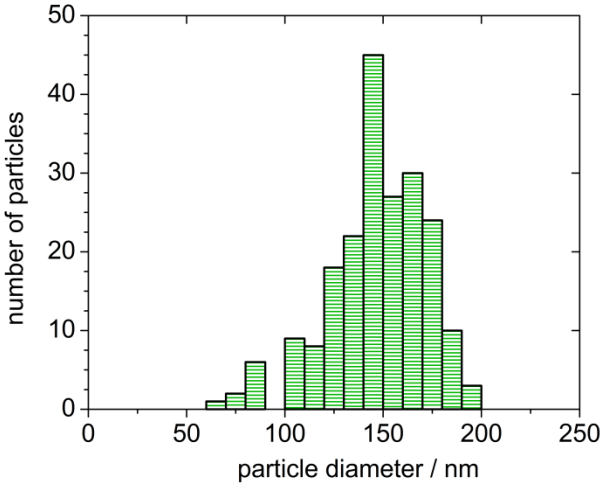

Figure 8.11. Size distribution of gold particles obtained by double-potential-step CA at the three-phase junction. The potential program consists of two steps: −0.7 V for 50 ms followed by 0 V for 2500 s.

It appeared that for the time range 10 – 500 s, the shape of particles changes with time, from rather round and small structures for short times to more and more developed and multifarious for longer times (Figure 8.12_A). After 500 s the diameter of generated gold particles does not change, only the density increases (Figure 8.10 and 8.12_A). The maximum value of the particle diameter (200 nm) is a consequence of the presence of the emulsion. It can be assumed that each particle is formed in a droplet of the emulsion and its size is limited by the droplet size. Let assume that the approximate volume of a gold particle can be calculated from equation $V_{AuNP} = {}^4/_3\pi(½d)^3$, which describes the volume of a sphere. Taking into account that the average diameter d = 150 nm, V_{AuNP} = 1.77 10^{-3} μm^3. Then using the value of gold density ρ = 19.3 g/cm^3, one can estimate the mass of single gold particle, m = 3.14 10^{-14} g. From equation $n = m/M$, (for gold M = 196.97 g/mol) the amount of the substance n = 1.76 10^{-16} mol. In performed experiments, the concentration of the precursor c that was used equals 10^{-3} mol/dm^3, so finally the volume ($V_{drop} = n/c$) of the droplet is estimated to be ~170 fL, that gives the radius of a single droplet ($V_{drop} = {}^4/_3\pi r^3$), r = 3.5 μm. This value corresponds well to the micrometer-size domains observed with optical microscope (Figure 8.6). These results show that the assumption about a single gold particle formation in a single droplet was a good approximation, and might be the reason for a maximum value of particles diameter.

A diameter and density distribution can be described as a function of the distance from the sharp edge of the stripe (Figure 8.12_B). Particles found in the middle of the stripe are smaller of ~35% compared to those close to the edge (Figure 8.12_B (■)). The density of the

deposit decreases with the distance from the edge in a similar matter like the size of the particles (Figure 8.12_B (●)). The size/density relation with a distance in Figure 8.12 can be related to all samples.

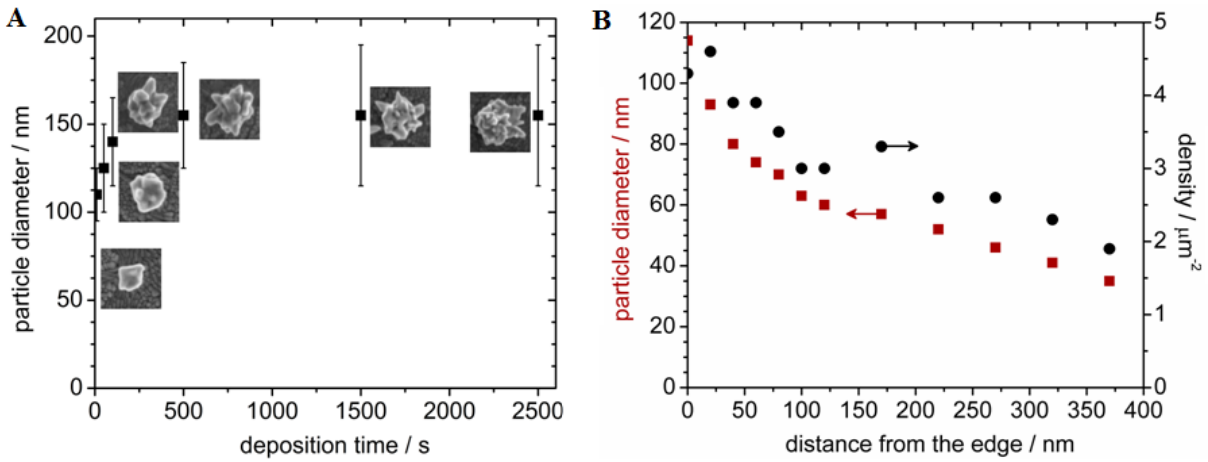

Figure 8.12. Diameter of gold particles as a function of growth time (A), for times between 10 and 2500 s and SEM images (for all side of a square is *ca.* 200nm) of related gold particles; (B) size (■) and density (●) as a function of distance measured from the edge of the stripe.

From AFM images shown in the Figure 8.13, recorded for two areas 25 × 25 μm and 5 × 5 μm, it was possible to estimate the average height of AuNPs. Similarly like for size distribution based in SEM imaging, also in this case an automated procedure written for the free software ImageJ was used. The obtained value equals 105 ± 40 nm (Figure 8.14).

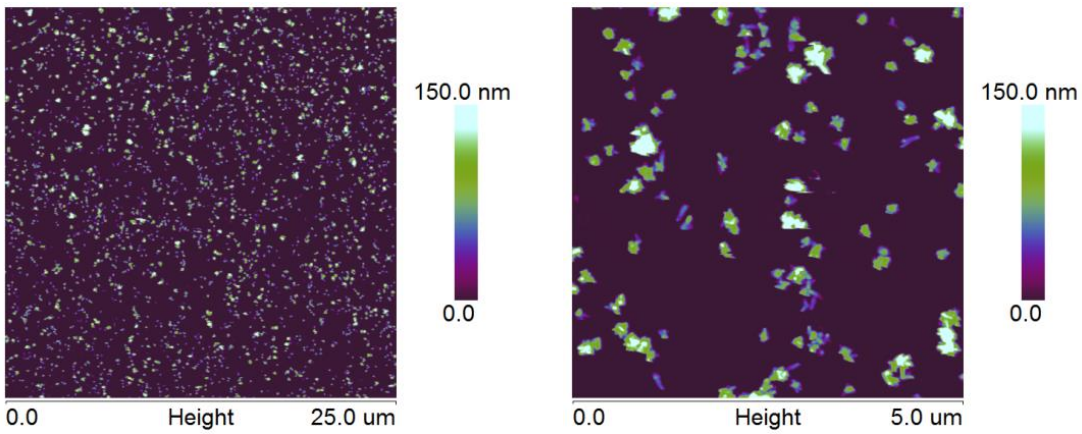

Figure 8.13. AFM images of gold deposit on ITO electrode obtained by double-potential-step CA: E_1 = −0.7 V for 50 ms and E_2 = 0 V for 1500 s (the same spot with two magnifications).

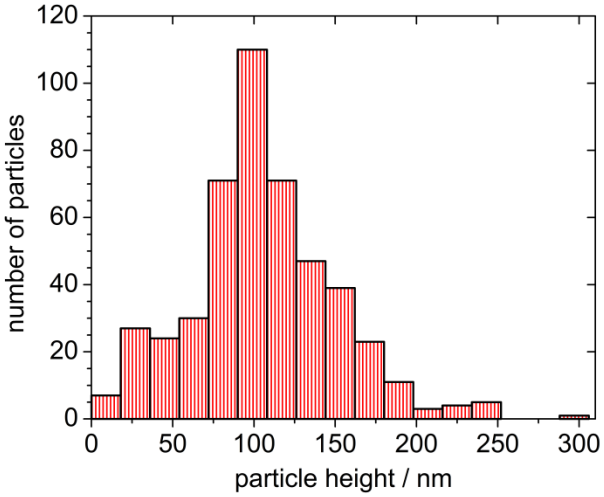

Figure 8.14. Height distribution of gold particles obtained by double-potential-step CA at the three-phase junction. The potential program consists of two steps: −0.7 V for 50 ms followed by 0 V for 1500 s.

8.3.3. Auger Electron Spectroscopy

High resolution AES (MNN transition) was performed to confirm the presence of metallic Au on the electrode surface. At first, two spectra were recorded for two distant spots (P1 and P2 on SEM images) and compared with a high resolution elemental Au reference spectrum (Figure 8.15 top). Comparison of these spectra does not reveal any distinct difference in the position and shape of the main Au peak. A good agreement between all three spectra indicates that metallic gold particles are electrodeposited on the electrode surface. In order to discuss a qualitative distribution of gold signal across the sample, a signal along a ~1.1 μm line was collected. This plot clearly shows a significant increase of the signal intensity of Au in the areas where gold is present what is confirmed with SEM image (Figure 8.15 bottom).

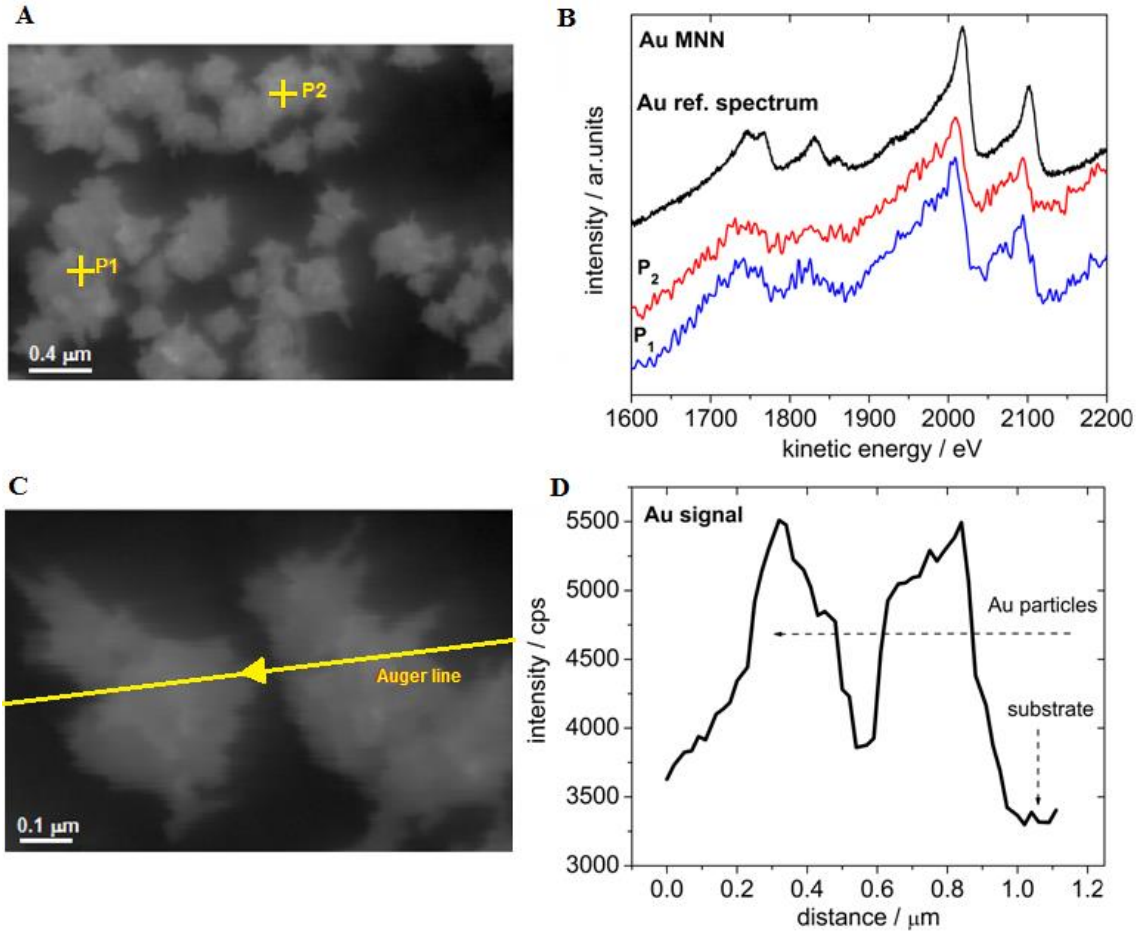

Figure 8.15. SEM image of Au particles deposited on ITO substrate (A) and high energy resolution Auger Au MNN spectra recorded at points P1 and P2 and at Au reference (B); SEM image of two areas with gold deposit (C) and Auger line analysis recorded across this area (D).

8.3.4. UV-vis spectroscopy

Spectroscopic measurements in a visible range are very useful for determining the presence of metallic nanoparticles and their average size. They are also used to estimate the homogeneity of the deposit and its sensitivity for changes of the closest surrounding. This information can be gathered by investigating the wavelength of a peak position, a full width at a half maximum (fwhm) and by recording spectra in different media [37,41,48,432–435]. The first measurement was performed in air and the result is presented in the Figure 8.16_A. Estimated fwhm equals ~100 nm. This indicates comparable or lower size distribution when compared to other flower-like gold particles [432–434]. The position of a maximum in absorption spectrum is connected with a size of nanostructure, as described by Mie's [41] and Gun's [48] theories. However, their calculations are relevant only to round [41] and elongated [48] nanoparticles. For this reason, the size of multifarious and rather irregularly shaped electrodeposited particles

cannot be easily deduced. Nonetheless, the value of 554 nm (Figure 8.16a) is in agreement with some previous reports about similar AuNPs [432–434,436].

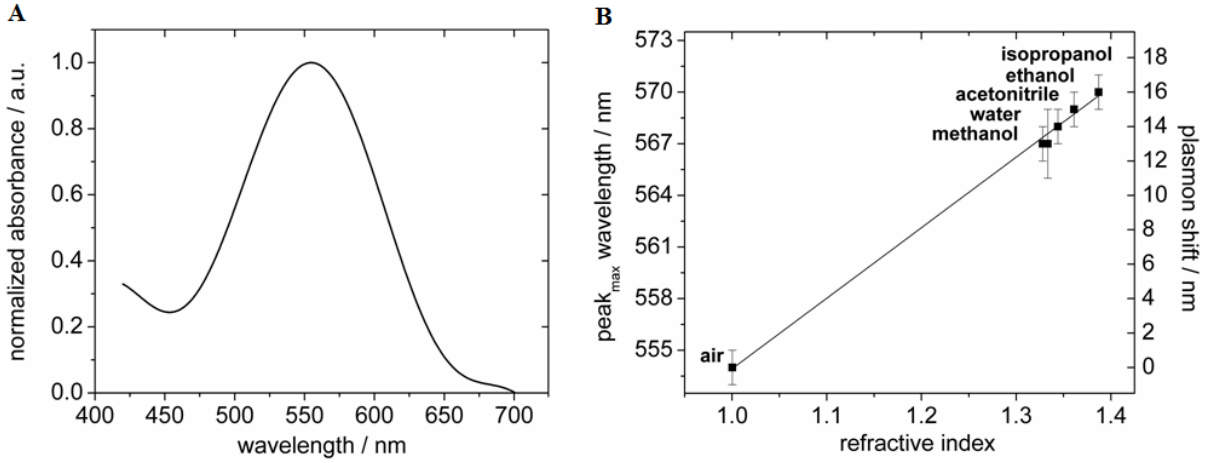

Figure 8.16. UV-visible absorption spectrum of AuNPs electrodeposited on ITO performed in air (A); maximum peak values plotted as a function of refractive index prepared for different solvents (B).

Measurements in various solvents with different refractive indexes *n* allowed to estimate the sensitivity of a surface decorated with gold nanoparticles on changes of the closest surrounding. This feature reveals whether investigated materials can find an application in biosensing [37]. The first parameter that definitely influences a bulk refractive index sensitivity *m* is the morphology of metallic nanostructures, however high homogeneity, geometry and very low size distribution are also of crucial importance. This is the reason why the best results, up to 1000 nm/RIU (nanometer of peak shift per refractive index unit), are obtained with well-defined structures prepared with electron beam lithography (EBL) [37]. From measurements in air (n = 1.0003), methanol (1.328), water (1.3334), acetonitrile (1.344), ethanol (1.361) and isopropanol (1.387), using simple relation $\Delta\lambda = m\Delta n$, it was calculated that for electrodeposited gold nanoparticles, m = 41 nm/RIU (Figure 8.16b). This value is comparable with results obtained for round gold nanoparticles [437]. The possible reason for such a low value might be rather irregular shape of particles and their random arrangement with respect to a laser beam direction. Although they can be described as multifarious or flower-like particles which are potentially highly sensitive, they are not so regularly deposited like structures with EBL technique. This is probably the main explanation for rather low sensitivity.

In conclusion, it was shown with electrochemical, microscopic and spectroscopic characterization that AuNPs can be electrodeposited at an

electrode|toluene(TOA($AuCl_4$))|aqueous electrolyte three phase junction. The arrangement of an electrochemical cell influences the stripe shape of the deposit. Electrogenerated gold particles are stable and well-adhered to the surface. AuNPs are multifarious with an average diameter of 150 nm and height of 105 nm. Although the general mechanism of gold formation at a three-phase junction in not clear, some conclusions based on computer modeling and long-term observations were made. Most probably the emulsion formation is responsible for the size dependence in time and its maximum value ~200 nm. However, it was assumed that a single particle is formed in a single droplet, what simplifies calculations. The presence of the emulsion also influences the thickness of the deposit and prevents obtaining a stripe with a thickness of several hundreds of nanometers or single micrometers. Applications of the obtained surfaces modified with gold nanoparticles are presented in the next chapters.

9. Catalytic properties of gold nanoparticles

Gold is well-known for its catalytic and bioelectrocatalytic activity (Chapter 1.3.3). AuNPs electrodeposited at a three-phase junction were investigated as a catalyst in the reaction of glucose electrooxidation and dioxygen reduction. In both cases multifarious particles are compared with bare ITO electrode and polycrystalline flat Au electrode.

9.1. Glucose electrooxidation

Glucose oxidation was chosen as the first reaction to study a catalytic behavior of gold particles. Glucose is a simple monosaccharide, which plays an important role as a source of energy that is necessary for every organism existence and takes part in a cellular respiration [438–441]. This carbohydrate is created in the photosynthetic organisms from carbon dioxygen and water, accompanied by the energy of light [442]. Gold catalysts are used either as glucose detectors [26,443–447] or in (bio)fuel cells [447–451], while in the second case, enzymes are usually involved [447,449–451]. Electrogenerated gold particles without any additional modification were engaged in non-enzymatic reaction and compared with other gold structures in terms of electrocatalytic activity [24,26,424,425,443–446,448,452–458].

All experiments were performed in an alkaline solution with a scan rate 0.02 V s^{-1}. At first, a bare ITO was used in a reference measurement. One can see that ITO does not exhibit any activity (Figure 9.1 a — black curve). When responses from the flat gold electrode (Figure 9.1 b — red curve) and ITO with electrodeposited AuNPs (Figure 9.1 c — blue curve) are compared it is clear that in the second case, recorded current density is much higher. For a peak at 0.11 V it is 20 times higher, at 0.26 V it is slightly smaller, ~7 times.

Except higher current density, there is also a significant difference in peak positions. For multifarious gold particles, in the forward scan, there are two characteristic regions. The first one, with a peak at -0.31 V, is assigned to the oxidation of glucose to gluconolactone [424,452,455]. When the potential is positively shifted further, there is a second peak at 0.26 V which is attributed to the oxidation of gluconolactone to gluconic acid and is connected with gold hydroxide formation [24,424,452]. Scanning the potential above 0.4 V results in gold oxides formation and this step limits catalytic activity of gold nanostructures by decreasing the amount of active sites [424,452]. The presence of a strong oxidation peak at 0.11 V in the backward scan which corresponds to further oxidation of glucose is explained by the presence of available active sites. This process is possible due to the reduction of gold oxides that

allows to restore active gold surface [424,452]. For a flat gold electrode recorded cyclic voltammogram differs in the range between -0.5 and -0.1 V. There is no signal which can indicate glucose oxidation. This behavior is explained by the poor catalytic activity of smooth gold substrates towards glucose electrooxidation and limited amount of active sites [443,444,456].

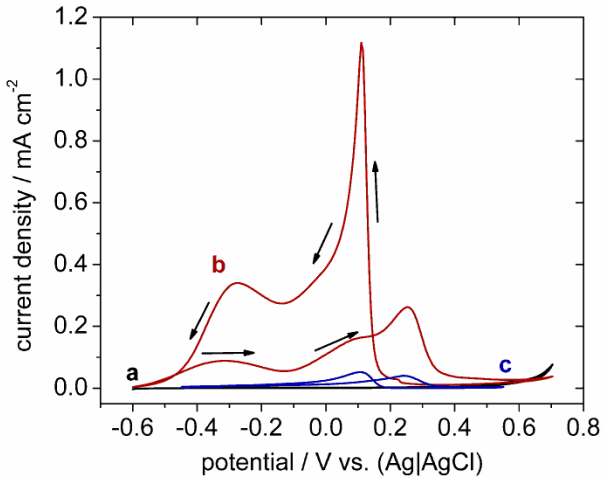

Figure 9.1. Cyclic voltammograms of: a bare ITO electrode (a — black), ITO|Au (b — red) and flat gold electrode (c — blue). All results obtained with 0.01 M glucose solution in 0.1 M aqueous NaOH. Scan rate 0.02 V s^{-1}.

To summarize shortly, multifarious gold nanoparticles perform much better catalytic behavior when compared with the polycrystalline flat gold electrode and obtained results are comparable [425,454] or improved [446,453,457] than others shown in some previous reports.

9.2. Dioxygen reduction

In the second part of this chapter, electrodeposited AuNPs are investigated as a catalyst in dioxygen reduction reaction (oxygen reduction reaction – ORR). This reaction plays a key role in fuel or biofuel cells [433,450,459–461], as well as metal-air batteries and electrochemical oxygen sensors [461–463]. (Bio)fuel cells are important in terms of new, efficient materials for energy conversion which are strongly needed nowadays. In these devices dioxygen is utilized as an oxidant that is a compound which is reduced on the cathode. It is crucial to create materials which catalyze this reaction in the most efficient way. Electrodeposited gold particles were investigated in this respect.

All experiments were performed in oxygenated 0.1 M McIlvaine buffer at pH 4.8 and at a scan rate 0.002 V s^{-1}. At first, bare ITO electrode was utilized as a working electrode and from cyclic voltammogram the onset potential was estimated to be -0.23 V, while for flat gold

electrode it is positively shifted to -0.05 V (Figure 9.2). For electrodeposited gold nanoparticles, recorded current was 3.5 times higher than for bare ITO electrode, and the onset potential was estimated to be ~0.03 V. Moreover, the value of the capacitance for bare ITO was determined as 0.01 mF cm^{-2}, while for ITO_Au it is much higher, 0.33 mF cm^{-2}, due to extended active surface area [370]. It is visible that the efficiency of this reaction is improved in the presence of AuNPs in comparison with bare ITO and flat gold electrodes [464,465].

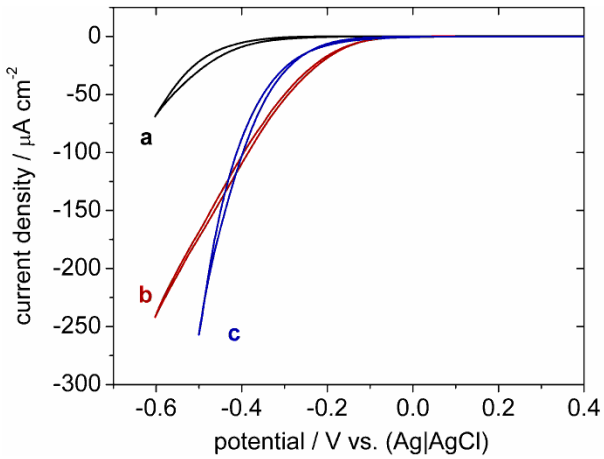

Figure 9.2. Cyclic voltammograms of a bare ITO electrode (a — black), ITO|Au (b — red) and flat gold electrode (c — blue). All results obtained with 0.1 M McIlvaine buffer at pH 4.8. Scan rate 0.002 V s^{-1}

Measurements performed with SECM allowed to determine products of ORR in McIlvaine buffer at pH 4.8. In aqueous electrolyte they are strongly influenced by the pH, which also determines the pathway of the reaction [466,467]. In this case, it was investigated whether bare gold nanoparticles catalyze the following two- (equation 9.1_a-b) or four-electron (equation 9.2) ORR [466]:

$$O_2 + 2e^- + 2H^+ \rightarrow H_2O_2 \qquad \textbf{(9.1 a)}$$

$$H_2O_2 + 2e^- + 2H^+ \rightarrow 2H_2O \qquad \textbf{(9.1 b)}$$

$$O_2 + 4e^- + 4H^+ \rightarrow 2H_2O \qquad \textbf{(9.2)}$$

Experiments were carried out in a four-electrode electrochemical cell with two working electrodes, Pt SECM tip and ITO_Au or bare ITO, as well as Pt wire and Ag|AgCl electrode as a counter and reference electrodes, respectively. Pt tip was adjusted 30 μm (*z* position) above electrode surface and its *x* and *y* positions were controlled by stepper motors. Potential values of 0.8 and -0.35 V were applied to Pt tip and ITO electrode, respectively. The first

value is due to H_2O_2 oxidation on Pt electrode, while the second correspond to ORR on ITO [466]. In this experiment, products of ORR are not determined in a direct way [466]. Instead, H_2O_2 which might be an intermediate of ORR (equation 9.1a) is detected on Pt tip (top reaction in Figure 9.3_A). Two different situations are observed on voltammograms recorded for bare ITO (Figure 9.3_B-a) and gold particles electrodeposited on ITO (Figure 9.3_B-b). When anodic scans above 0.6 V (with a peak at ~0.8 V) are compared one can see, that in the presence of gold recorded current is higher than for bare ITO electrode. This is the region assigned to H_2O_2 oxidation [468]. Nonetheless, it has to be emphasized that the difference in current, in this region, is relatively low.

This situation is vizualized on 3D maps in Figure 9.4. H_2O_2 oxidation current is plotted in *z* axis for an area of 1400 μm × 1400 μm (*x* and *y* axes) or 500 μm × 500 μm. Measurements were performed above the stripe of gold nanoparticles (Figure 9.4_A) and bare ITO electrode (Figure 9.4_B). One can see a significant difference between the region without nanoparticles (blue color) and when the Pt tip was scanned through the stripe (yellow-red color). For bare ITO electrode the map shows homogeneous but much less active surface.

Results obtained with SECM are in agreement with voltammograms in Figure 9.2. First of all, electrodeposited AuNPs significantly increase catalytic activity with respect to bare ITO electrode. Additionally one can see that in described conditions H_2O_2 is produced (reaction 9.1a).

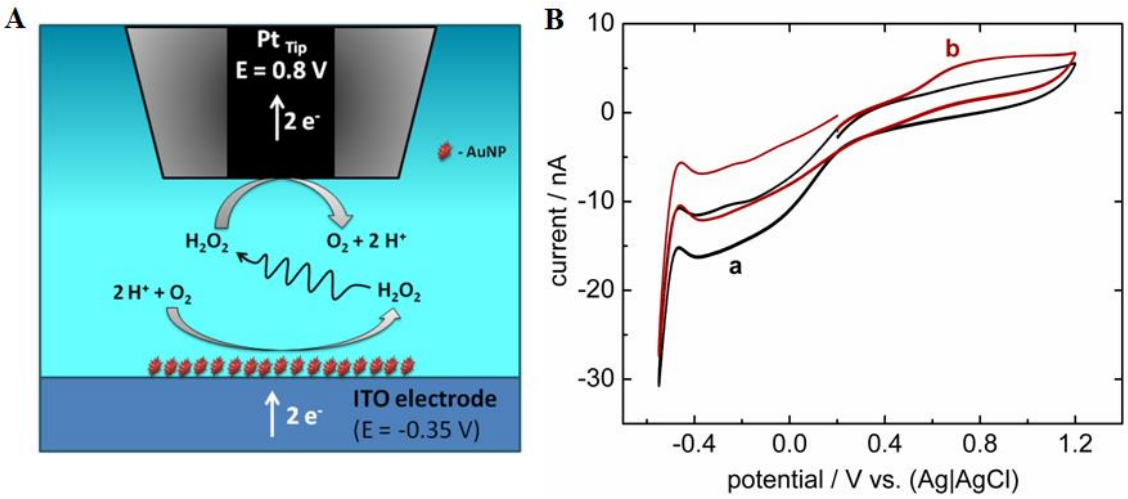

Figure 9.3. (A) Illustration of SECM setup together with the reactions scheme, (B) CV recorded at Pt SECM tip electrode above (a) ITO electrode and (b) AuNPs with a constant potential (-0.35 V) applied to ITO electrode in 0.1 M McIlvaine solution at pH 4.8 under aerobic conditions and scan rate 100 mV s^{-1}.

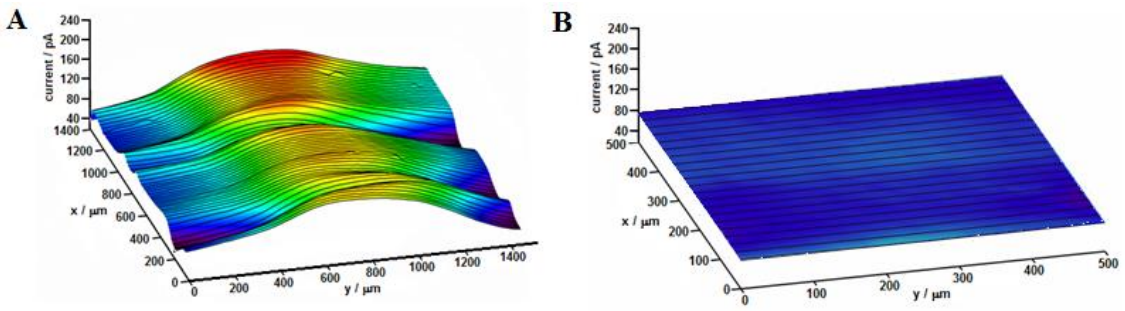

Figure 9.4. SECM image of H_2O_2 oxidation at Pt microelectrode (25 µm in diameter) in 0.1 McIlvaine solution at pH 4.8. H_2O_2 was generated by oxygen reduction at (A) AuNPs stripe at ITO electrode or (B) bare ITO electrode. Scanning velocity = 62.5 µm s^{-1}.

Afterwards, ITO and ITO with gold particles were modified with bilirubin oxidase (BOx). Namely, each surface was immersed into 1 mg cm^{-3} BOx in 0.1 M McIlvaine buffer (pH 4.8) solution for 2 h at *ca.* 5°C, then it was gently washed in 0.1 M McIlvaine buffer (pH 4.8). Recorded voltammograms (Figure 9.5) show a significant onset potential shift, up to ~0.6 V for both electrodes when compared with non-enzymatic conditions. It is a direct consequence of BOx presence and is in agreement with previous reports [84,373,460,461]. This value corresponds to the redox potential of T_1 center of BOx [469,470], which is engaged in a direct electron transfer from the electrode surface to the active sites [471]. The second copper center, which consists of three copper atoms (trinuclear copper cluster – TCN), is responsible for dioxygen binding and its reduction. The only difference between two investigated electrodes is in current density. The one recorded for electrodes with gold is 1.3 higher than without AuNPs. There is no shift of the onset potential, what might be explained by the fact that for bioelectrocatalytic reaction, the whole process is controlled by the presence of an enzyme. Higher current density in case of gold particles might be due to more developed active surface area, since AuNPs serve additional binding sites for the enzyme but they do not influence the efficiency of the bioelectrocatalytic process.

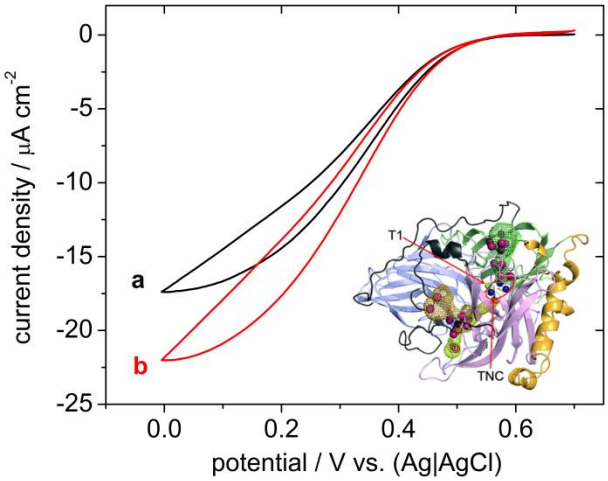

Figure 9.5. Cyclic voltammograms of a bare ITO electrode (a — black) and ITO|Au (b — red) with additionally adsorbed BOx. All results obtained with 0.1 M McIlvaine buffer at pH 4.8. Scan rate 0.002 V s^{-1}. Inset schematic illustration of BOx [471].

To summarize, it was shown that multifarious electrodeposited gold nanoparticles provide favourable conditions for glucose electrooxidation, as well as catalytic and mediatorless bioelectrocatalytic dioxygen reduction. For the first group of experiments, a catalytic activity of AuNPs over flat gold electrode was presented. Bare ITO does not reveal any catalytic activity towards glucose oxidation. The situation is similar for dioxygen reduction reaction. The onset potential is positively shifted from -0.23 V for bare ITO, to -0.05 V for flat gold electrode, up to 0.03 V for multifarious gold particles. Measurements carried out with SECM allowed to determine H_2O_2 as an intermediate of a two-electron dioxygen reduction reaction. Finally, for experiments performed with BOx, one can see, that the reaction is controlled by the presence of an enzyme and measured onset potential for all surfaces is constant and in agreement with previous reports [84,373,460,461].

10. Indium tin oxide and gold nanoparticles hybrid material

In this chapter, indium tin oxide (ITO) nanoparticles widely used in optoelectronics [347,349,351,353,375,472] and electrochemistry [370,373] are introduced as a support for AuNPs. At first, a deposition protocol of ITO nanoparticles at an ITO electrode (ITO|ITO_{NP}) is presented. Afterwards, various surfaces are characterized with SEM and AFM imaging. In the next part of this chapter, it is shown that both bare ITO electrode as well as ITO|ITO_{NP} can be used as a substrate for AuNPs electrodeposition. Differently modified electrodes are characterized with SEM and TEM and compared with results presented in the chapter 8. Finally, all kinds of surfaces are applied as a (bio)catalyst in glucose oxidation and dioxygen reduction reactions.

10.1. Layer by layer deposition of ITO nanoparticles

10.1.1. Deposition protocol

ITO electrode surface was modified with ITO_{NP} by a subsequent immersion and withdrawal of ITO slice in the 3wt.% suspension of ITO_{NP} in methanol (Figure 10.1) [370,373]. Next, the modified substrate was immersed in ethanol in order to remove an excess of ITO_{NP} which were not stable and well-adhered. After each step, ITO slide was left for drying for a couple of minutes. Alternative immersion and withdrawal in the suspension of ITO_{NP} could be repeated up to 10 times, since for thicker deposit nanoparticulate layer was not stable anymore [373]. To facilitate the description, each double step of immersion and withdrawal in both ITO_{NP} suspension in methanol and then in clean ethanol is alternatively called – one layer, 1L. Although as it is shown in the next sections of this chapter, this method of ITO_{NP} deposition allows for increasing electrode surface area in a less ordered way rather than obtaining single layer of nanoparticles.

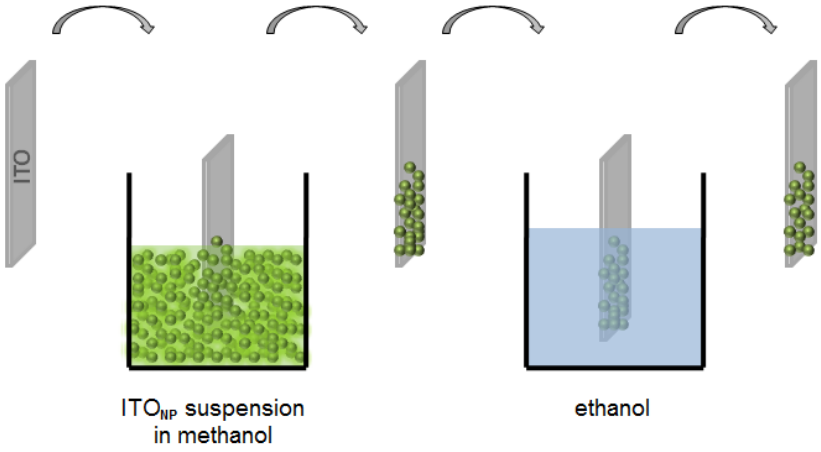

Figure 10.1. Schematic illustration of ITO nanoparticles deposition at an ITO electrode.

10.1.2. SEM and AFM characterization

ITO_{NP} deposit even only after a single immersion and withdrawal step is visible with a naked eye and has a bright green color. After a couple of immersion and withdrawal steps, an ITO electrode becomes less and less transparent. To analyze the morphology of the deposit in a more detailed way, SEM images were performed. In Figure 10.2_A one can see slightly rough surface of a bare ITO surface. Depending on the provider its roughness is usually not bigger than 0.01 μm. Figure 10.2_B shows ITO substrate after a single immersion and withdrawal step (ITO^{1L}) and as it is clearly visible, electrode surface is inhomogeneously covered with ITO_{NP}. Only for three (ITO^{3L}) to ten (ITO^{10L}) withdrawal and immersion steps (Figure 10.2_C-D) substrate is entirely covered with densely packed ITO nanoparticulate film.

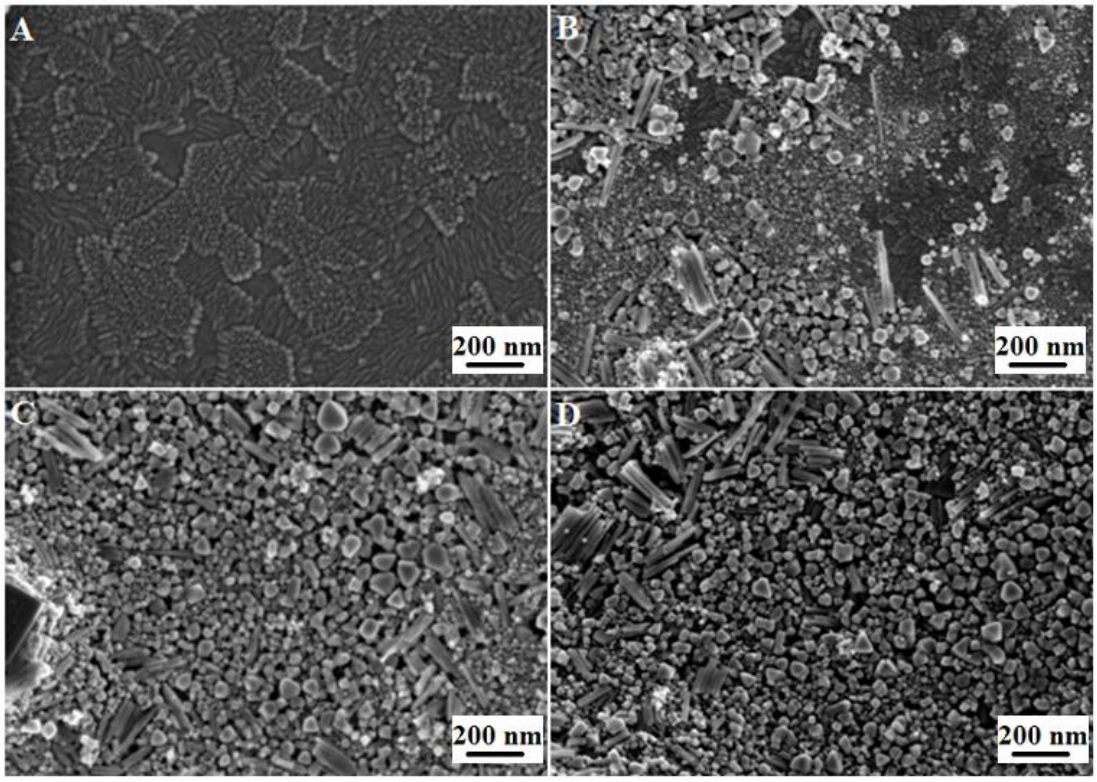

Figure 10.2. SEM images of (A) bare ITO electrode and ITO coated with (B) one (ITO^{1L}), (C) three (ITO^{3L}) and (D) ten (ITO^{10L}) ITO_{NP} layers (all scale bars equals 200 nm).

Although SEM images for ITO^{3L} and ITO^{10L} look very similar there is a significant difference in thickness of the deposit between them. It was estimated from a cross section profile in AFM analysis that the average thickness of ITO^{3L} is ~250 nm (Figure 10.3), while for ITO^{10L} it is ~810 nm. It can be deduced that a single immersion and withdrawal sequence results in average thickness deposit of ~80 nm, what is *ca.* 3 times more than the diameter of an ITO nanoparticle. This is in agreement with earlier report [370].

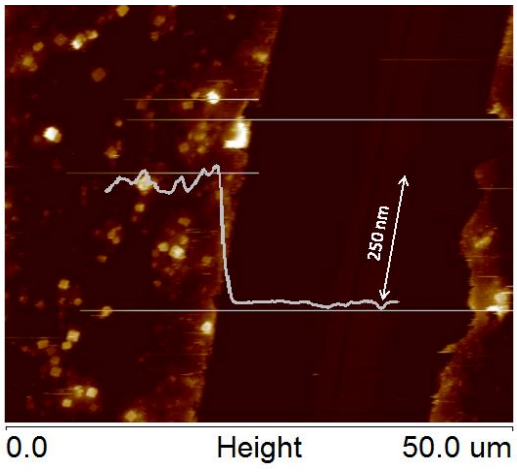

Figure 10.3. AFM image and cross section profile of $ITO|ITO_{NP}^{3L}$.

10.2. Electrodeposition of gold nanoparticles on ITO nanoparticulate film

10.2.1. (Electro)deposition protocol

Although materials based on gold supported on metal oxides are widely explored [76], to the best of our knowledge, nobody reported a hybrid materials which consists of both gold and ITO nanoparticles. The protocol of the preparation is presented in the Figure 10.4. At first, ITO_{NP} were deposited by simple immersion and withdrawal steps in the suspension of ITO_{NP}. After cleaning and drying, substrates were used as a working electrode for electrogeneration at a three-phase junction using conditions described in Chapter 8.

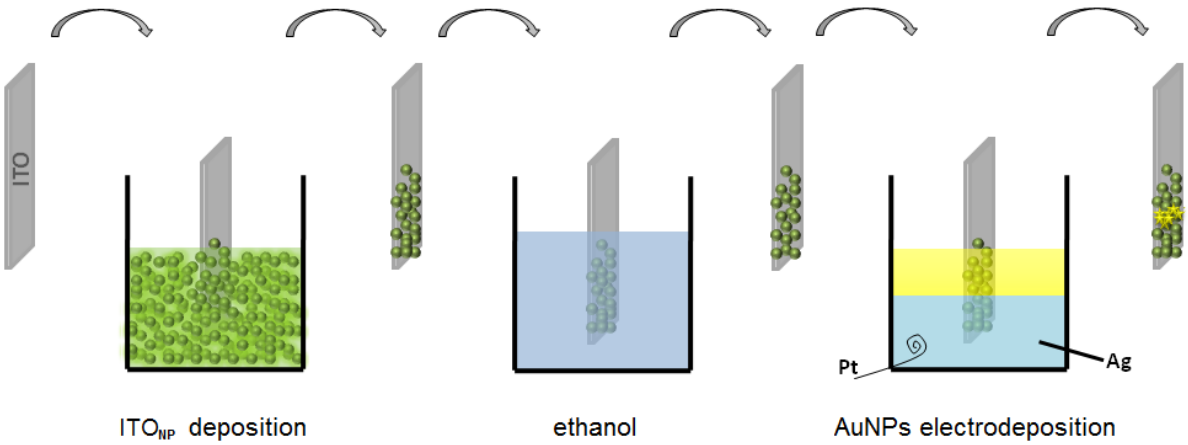

Figure 10.4. Schematic illustration of AuNPs electrodeposition at an ITO| ITO_{NP} electrode; Pt – platinum wire, and Ag – silver wire.

10.2.2. Electrochemical and microscopic characterization

Similarly as described in chapter 8, due to the presence of gold, all prepared substrates were first investigated with cyclic voltammetry. Voltammograms (— red and — blue in Figure 8.7a) obtained for AuNPs deposited on bare ITO electrode and ITO_{NP}^{3L} show characteristic features of gold with the oxidation region in the potential range 1-1.6 V which corresponds to gold oxide formation and its dissolution (re-reduction) at ~0.9 V [24,424,425]. In a reference measurement bare ITO (— black) and ITO^{3L} (— green) were used. Corresponding surfaces (with the same thickness of ITO_{NP}) with and without AuNPs reveal a significant difference in capacitive current which is in agreement with the predictions that ITO nanoparticles should provide an additional extended active surface area [370].

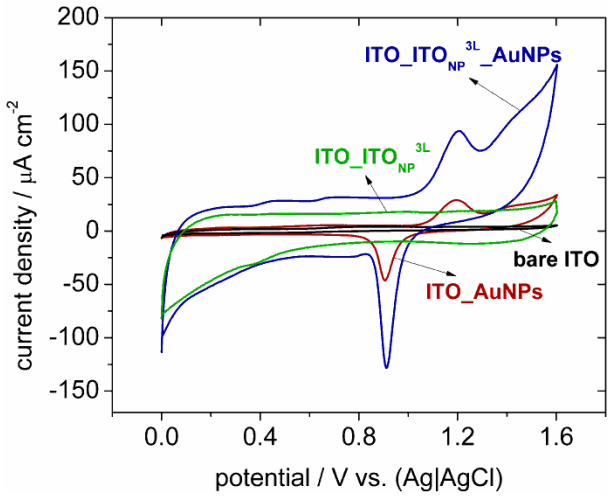

Figure 10.5. Cyclic voltammograms of: ITO electrode as a reference (bare ITO), gold particles electrodeposited on ITO electrode (ITO_AuNPs), ITO after three immersion and withdrawal steps in ITO_{NP} suspension (ITO|ITO^{3L}) and gold particles deposited on ITO|ITO^{3L} (ITO|ITO^{3L}|AuNPs) obtained with deoxygenated 0.1 M aqueous H_2SO_4. Scan rate 0.05 V s^{-1}.

Although, the presence of gold was confirmed with CV measurements, further investigations were necessary to compare gold deposit in the absence and presence of ITO_{NP}. First of all, SEM images were recorded to depict morphological properties of AuNPs. In Figure 10.6_A are displayed SEM images obtained with two different detectors in order to clearly distinguish between gold and ITO material. Image presented in Figure 10.6_A was obtained with InLens detector. This detector collects low-energy secondary electrons and allows to record high-quality images with high resolution [393]. However when two materials have similar features, like in this case, it might be hard to distinguish between them. With ESB (energy selective backscattered) detector it is possible to display high compositional contrast, as it is shown with the SEM image in Figure 10.6_B. This detector collects high-energy backscattered electrons and provides a high contrast between elements with different chemical composition [393]. Figure 10.6_A presents round ITO nanoparticles and flower-like bigger Au particles and Figure 10.6_B clearly shows ITO in a dark grey color, while gold is bright grey–white.

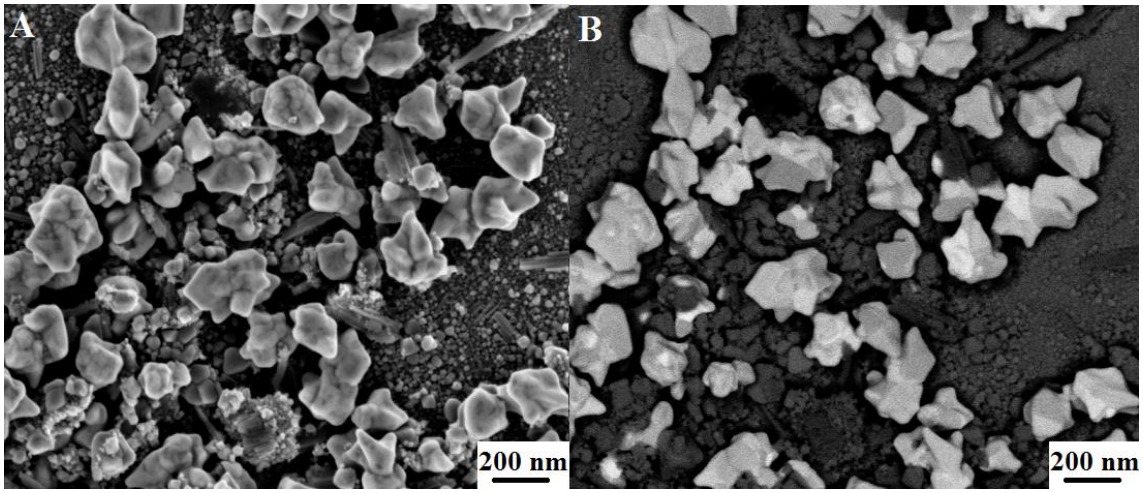

Figure 10.6. SEM images of ITO|ITO^{3L} with electrodeposited AuNPs obtained with InLens (on the left) and EBS (on the right) detectors.

From described measurements it is undeniable that stably deposited gold particles are present on the top of ITO porous film. Nonetheless, it was interesting and important for further discussion to know what is inside this 3D densely packed scaffold. Using FIB (focused ion beam) cross sections method combined with SEM imaging, a thin slice of a substrate with ITO_{NP}|Au deposit was isolated (Figure 10.7). In FIB technique a finely focused beam of ions is utilized while in SEM it is a beam of electrons [473].

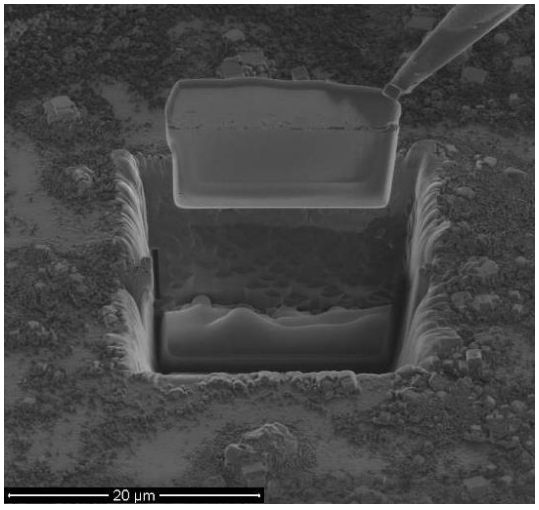

Figure 10.7. FIB image of a cross-section cut from the sample with deposited ITO nanoparticles and electrodeposited AuNPs.

TEM in a scanning mode (STEM) with XEDS (X-ray Energy Dispersive Spectroscopy) and HAADF (High Angle Annular Dark Field) analysis techniques were used

to define a localization of AuNPs and ITO_{NP} in a probe. Figure 10.8_A shows an example of Au particle surrounded with ITO nanoparticles obtained with HAADF detector and XEDS compositional map of the same region (Figure 10.8_B), which confirms the presence of gold inside the porous material. Additionally, Figure 10.8_C presents the same region but with a higher magnification for a better view of a size ratio of both kinds of particles.

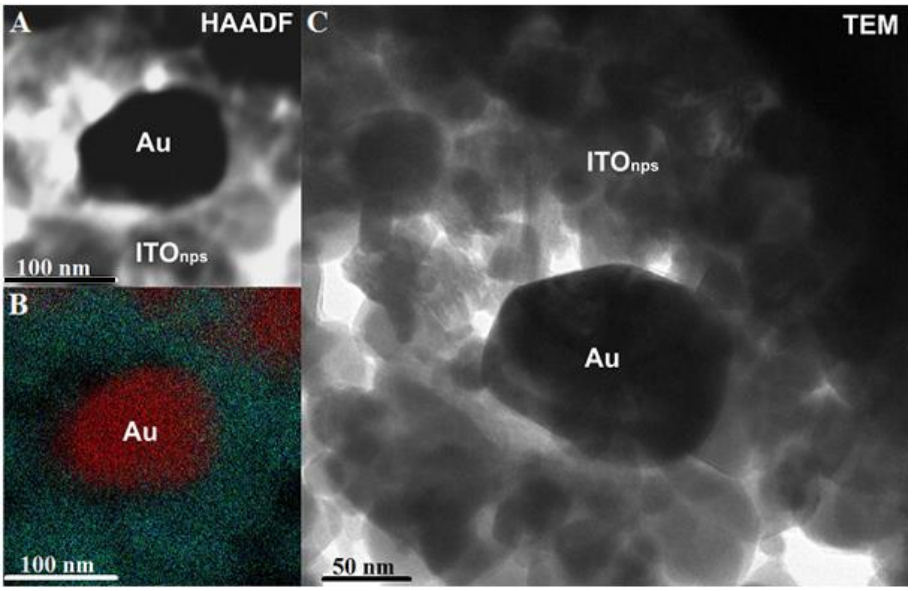

Figure 10.8. STEM mode images of ITO electrode coated with ITO_{NP} and AuNPs: the image of analyzed area obtained with HAADF detector (A, C) and XEDS elemental distribution maps of Au (red colour) and In–Sn (turquoise colour) (B).

Additionally, Figure 10.9 clearly shows that gold particles are present in various regions of ITO_{NP} scaffold. Top images (A-C) were performed inside a densely packed area where multifarious gold particles are surrounded with ITO nanoparticles. Here, XEDS maps show in one image only gold in red (Figure 10.9_B) and in the second, gold in red together with In and Sn in turquoise (Figure 10.9_C). Finally, analogous analysis was performed for a place in a direct contact with ITO electrode surface (Figure 10.9_D-F). This is a clear evidence that both liquid phases (aqueous electrolyte and gold precursor in toluene) have to penetrate entirely a porous ITO_{NP} structure which, together with ITO electrode, is electrochemically active and provides extended surface for gold electrodeposition.

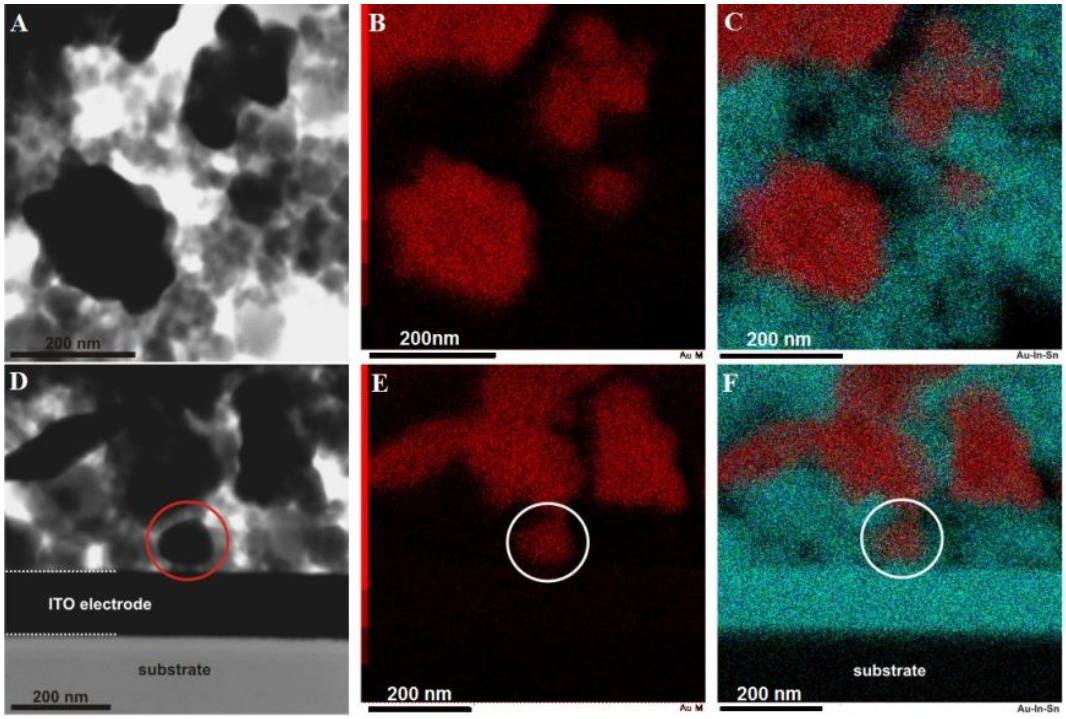

Figure 10.9. STEM mode images of ITO electrode coated with ITO_{NP} film and Au particles of two different spots (A-C and D-F): (A, D) images obtained with HAADF detector, and XEDS distribution maps of chemical composition of Au alone in red (B, E), and of Au (red) together with In–Sn (turquoise) (C, F).

10.3. Catalytic properties of the hybrid material

With a reference to Chapter 9, where catalytic activity of electrodeposited AuNPs on bare ITO electrode at a three-phase junction were described, in this section ITO_{NP} and ITO_{NP}|AuNPs modified electrodes are presented.

10.3.1. Glucose electrooxidation

All experiments were performed in the same conditions, as it was mentioned before, namely, in an alkaline solution at a scan rate 0.02 V s^{-1}. In Figure 10.10_A in comparison with Figure 9.1 there is additionally included a plot for ITO electrode prepared with ten immersion and withdrawal steps in ITO_{NP} suspension (ITO|ITO^{10L} — red) and for ITO after one immersion and withdrawal step together with electrodeposited AuNPs (ITO|ITO^{1L}|Au — pink). It can be assumed that ITO_{NP} similarly like ITO electrode do not provide any catalytic activity towards glucose electrooxidation. However when ITO|ITO^{10L} is compared with bare

ITO electrode, an increase of capacitive current is noticeable, in agreement with previous observation (Figure 10.5).

In the case of gold modified electrodes only a single immersion and withdrawal step in ITO_{NP} suspension before gold deposition result in at least 1.9 times higher current density. For two oxidation peaks in the forward scan, there is 2.8 and 3.3 times increase at 0.26 V and -0.31 V, respectively. In a backward scan a slight shift of oxidation peak from 0.11 to 0.13 V and 1.9 times current density increase are visible. In Figure 10.10_B the most efficiently working electrode is shown, it consists of an ITO nanoparticulate layer with a maximum thickness (10L) and gold particles. When obtained results are compared with other reports, recorded current density is twice [24,452,458], five times [425] and as much as ten times higher [445].

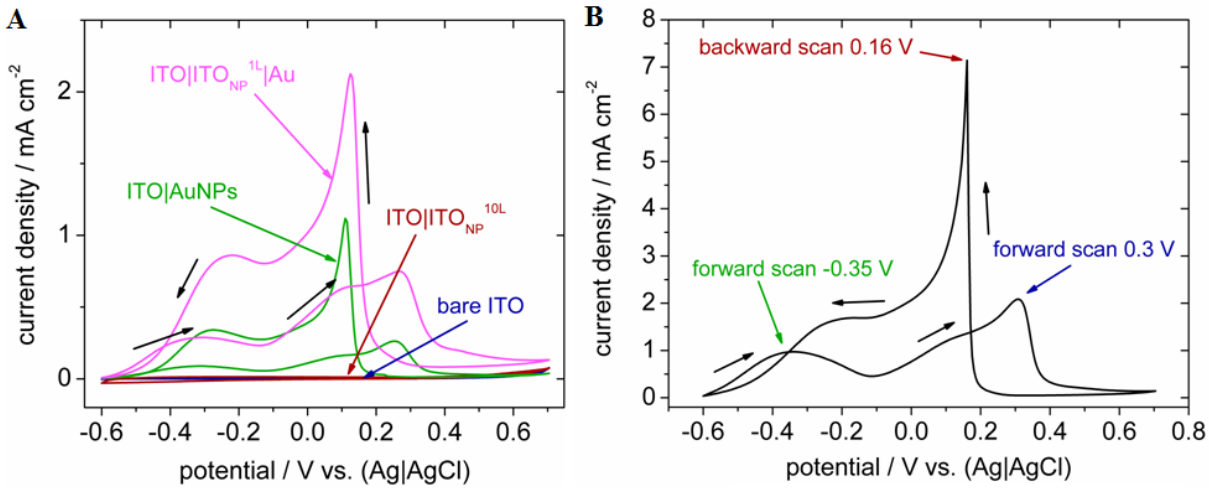

Figure 10.10. Cyclic voltammograms of: A) bare ITO electrode (— blue), ITO|ITO^{10L} (— red), ITO|Au (— green), ITO|ITO^{1L}|Au (— pink); B) ITO|ITO^{10L}|Au (— black). All results obtained with 0.01 M glucose solution in 0.1 M aqueous NaOH. Scan rate 0.02 V s^{-1}.

Important characteristics were provided when the number of immersion and withdrawal steps was plotted versus peak current density for all three oxidation peaks (Figure 10.11). It clearly shows linear dependence in all cases. This indicates that the entire hybrid material is electroactive and this result is in agreement with conclusions drawn from STEM images (Figure 10.8 and 10.9) that the whole volume of the film provides a scaffold for gold particles generation. All presented results are based on experiments performed 3-5 times for each kind of electrode. It was calculated that the peak current density varied 15, 7 and 10 % for the peak at -0.35, 0.3 and 0.16 V, respectively, suggesting that the protocols used to modify electrodes allow to prepare reproducible surfaces.

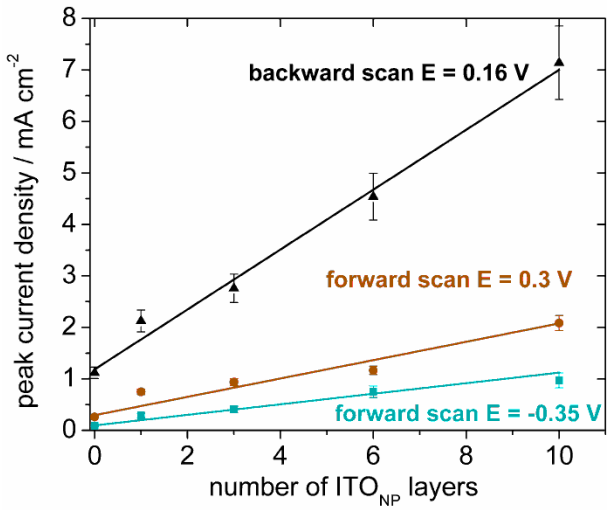

Figure 10.11. Peak current density in the function of immersion and withdrawal steps prepared for three oxidation peaks: −0.35 V (■) and 0.3 V (●) in forward scan, and 0.16 V (▲) in backward scan. All results obtained with 0.01 M glucose solution in 0.1 M aqueous NaOH. Scan rate 0.02 V s^{-1}.

10.3.2. Dioxygen reduction

Similarly like for glucose electrooxidation reaction, ITO_{NP} and/or AuNPs modified electrodes were investigated in ORR and compared with results obtained in Chapter 9. All experiments were performed in oxygenated 0.1 M McIlvaine buffer at pH 4.8 and at a scan rate 0.002 V s^{-1}. At first, all surfaces modified with different number of immersion and withdrawal steps in ITO_{NP} suspension (1-10) were investigated with respect to a bare ITO (Figure 10.12_A). One can see that the current density grows in an ordered manner, as confirmed in Figure 10.12_D, where the number of immersion and withdrawal steps is plotted versus peak current density (■). Obtained linear dependence is in agreement with previous report [373]. It was also estimated that the onset potential changes very slightly with a thickness of ITO nanoparticulate film, ~5 mV per layer, what was not shown before.

Analogous experiments were performed with electrodeposited gold particles on all kinds of substrates (Figure 10.12_B). From the first observations one can see, that the onset potential is shifted according to electrodes without gold by ~0.25 V (Figure 10.12_B-C). For electrodes without AuNPs, the difference in current density between bare ITO and ITO^{10L} equals 182 μA cm^{-2}. For Au modified electrodes this value is much higher, 619 μA cm^{-2}. In both cases, these values were measured at -0.6 V. This relation is noticeable in Figure

10.12_D, where the slope of fitted linear function is ~3.3 times higher for substrates with gold, than without gold.

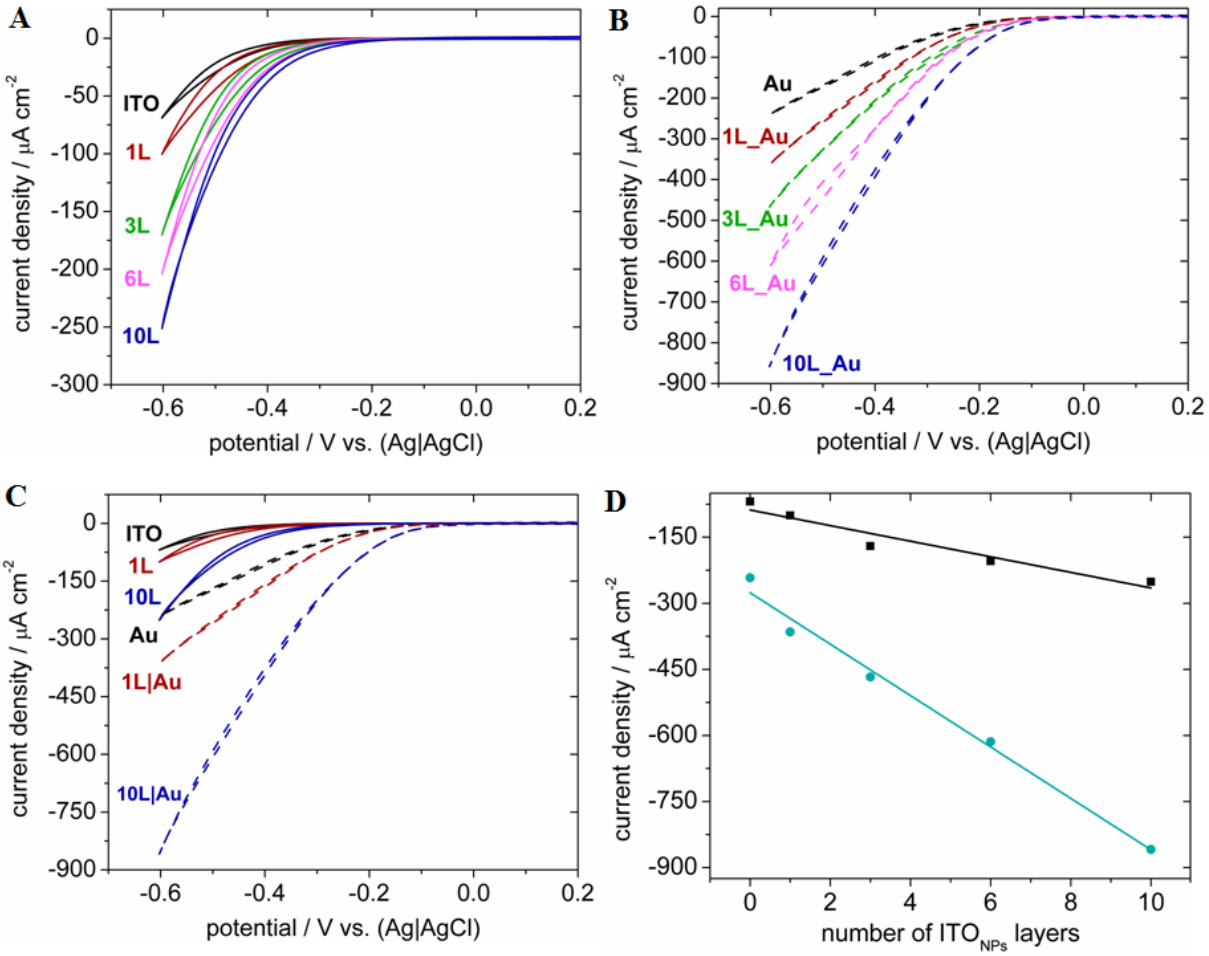

Figure 10.12. Cyclic voltammograms of ITO electrodes coated with different number of immersion and withdrawal steps (0L – bare ITO, 1L, 3L, 6L and 10L) A) without (—) and B) with (- - -) electrodeposited gold particles. C) Comparison of selected electrodes with 0L, 1L and 10L ITO_{NP} without (—) and with (- - -) electrodeposited gold particles. D) Peak current density as a function of immersion and withdrawal steps prepared for samples without (■) and with (●) electrogenerated gold particles, both measured at −0.6 V. All results obtained with 0.1 M McIlvaine buffer at pH 4.8. Scan rate 0.002 V s^{-1}.

SECM analysis was also employed to investigate the pathway of ORR performed with electrode coated with ITO_{NP} or ITO_{NP}|AuNPs. Similarly as described in Chapter 9, experiments were recorded in a four-electrode electrochemical cell with two working electrodes, Pt SECM tip and ITO_Au or bare ITO, as well as Pt wire and Ag|AgCl electrode as a counter and reference electrodes, respectively. Pt tip was adjusted 30 µm (*z* position) above electrode surface and its *x* and *y* positions were controlled by stepper motors. Potential values of 0.8 and -0.35 V were applied to Pt tip and ITO electrode, respectively. The first

value is due to H_2O_2 oxidation on Pt electrode, while the second correspond to O_2 reduction on ITO [466]. As it was shown in chapter 9, monitoring of H_2O_2 oxidation at Pt tip (top reaction in Figure 10.13_A), allows to determine whether this compound is one of the product of ORR (bottom reaction in Figure 10.13_A). It is visible (Figure 10.13_B) that in the region attributed to H_2O_2 oxidation (0.5 – 1 V), in the presence of gold there is an increase of current density, however again (as described in chapter 9) it is not significant. Nonetheless, this shows that H_2O_2 is formed during ORR.

Perspicuous 3D maps of both experiments are presented in Figure 10.14. In the case of electrodeposited gold on ITO nanoparticulate film, crossing from the region without gold into Au stripe results in a rapid oxidation current increase. This is in agreement with results obtained for gold deposited at a bare ITO (Figure 9.4). ITO nanoparticles reveal homogenous behavior with a constant current across entire scanned area, similarly like bare ITO.

Concluding this part, one can see that catalytic activity varies between electrodes modified with ITO_{NP} and/or Au. However, the pathway of dioxygen reduction reaction is similar and H_2O_2 is present as an intermediate in the two-electron reaction.

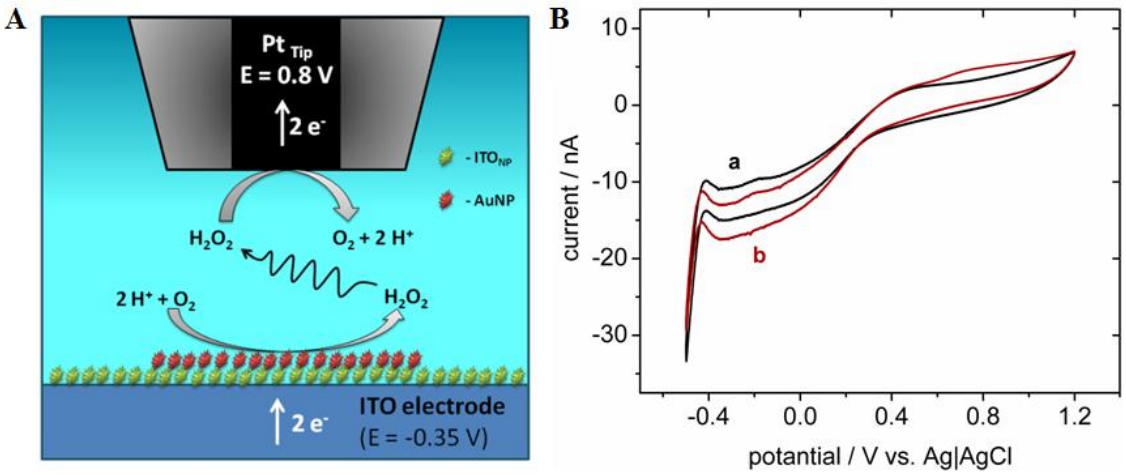

Figure 10.13. (A) Schematic illustration of dioxygen reduced on ITO_Au electrode and H_2O_2 oxidized on Pt SECM tip placed above, (B) CV recorded at Pt SECM tip electrode above (a) ITO electrode and (b) AuNPs with a constant potential (-0.35 V) applied to ITO electrode in 0.1 M McIlvaine solution at pH 4.8 under aerobic conditions and scan rate 100 mV s^{-1}.

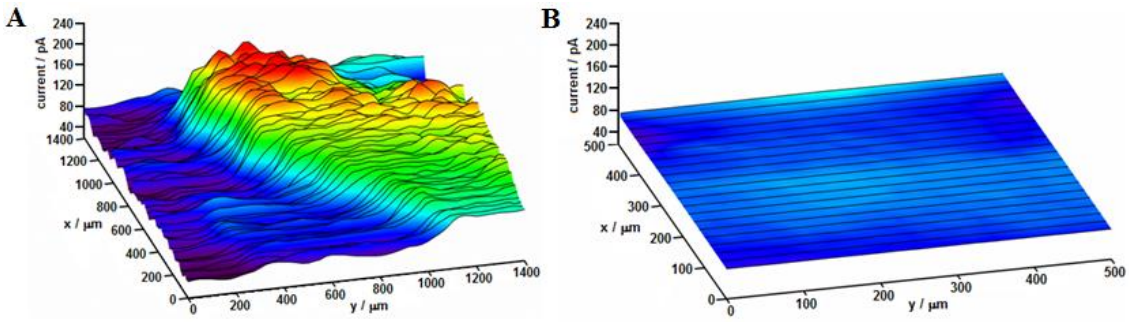

Figure 10.14. SECM image of H_2O_2 oxidation at Pt microelectrode (25 µm in diameter) in 0.1 McIlvaine solution at pH 4.8. H_2O_2 was generated by oxygen reduction at ITO|ITO^{3L} electrode (A) with and (B) without AuNPs stripe. Scanning velocity = 62.5 µm s^{-1}.

10.3.3. Mediatorless bioeletrocatalysis with immobilized enzyme

All surfaces presented in previous sections were further modified with bilirubin oxidase (BOx), by immersing each substrate into 1 mg cm^{-3} BOx in 0.1 M McIlvaine buffer (pH 4.8) solution for 2 h at *ca.* 5°C, and subsequent washing. Figure 10.15_A clearly indicates a similar dependence between number of immersion and withdrawal steps and recorded current density, like for electrodes not modified with an enzyme [373]. This linear relation is shown in Figure 10.15_D (■). Additionally it was calculated that the differences in current density between ITO and ITO|ITO^{10L}, as well as corresponding ITO|BOx and ITO|ITO^{10L}|BOx are various. Without the enzyme, the current density increases 3.3 times after addition of ITO^{10L} while with BOx the growth is more rapid and equals 5.4 times.

When surfaces with electrodeposited gold are taken into account there are two important conclusions (Figure 10.15_B). First of all, the value of the onset potential does not change at all, for any kind of electrode and this is consistent with reports from the literature [84,373,460,461]. This means that mediatorless bioelectrocatalytic reaction is controlled by the presence of an enzyme [469,470] and determined by a direct electron transfer, as it was described in the chapter 9. ITO and gold nanoparticles provide an extended active surface area for BOx immobilization but they do not influence ORR. Second conclusion concerns current density increase, while the difference between ITO|ITO$_{NP}^{10L}$ and ITO|ITO^{10L}|Au equals ~3.3 times, for ITO|ITO^{10L}|BOx and ITO|ITO^{10L}|Au|BOx it is only ~2 times (Figure 10.12_C and 10.15_C). It means that in non-enzymatic reaction, appearance of gold on the electrode surface influences more its catalytic activity, than in the presence of BOx, when gold provides only new binding sites.

Concluding, for non-enzymatic reaction changes that result from modification with ITO_{NP} and AuNPs are more visible than for enzymatic one, in terms of current density and relative shift of the onset potential. However, it is indisputable that BOx definitely facilitates dioxygen reduction reaction and significantly positively shifts the onset potential, up to ~0.6 V, which is constant for all kinds of electrodes.

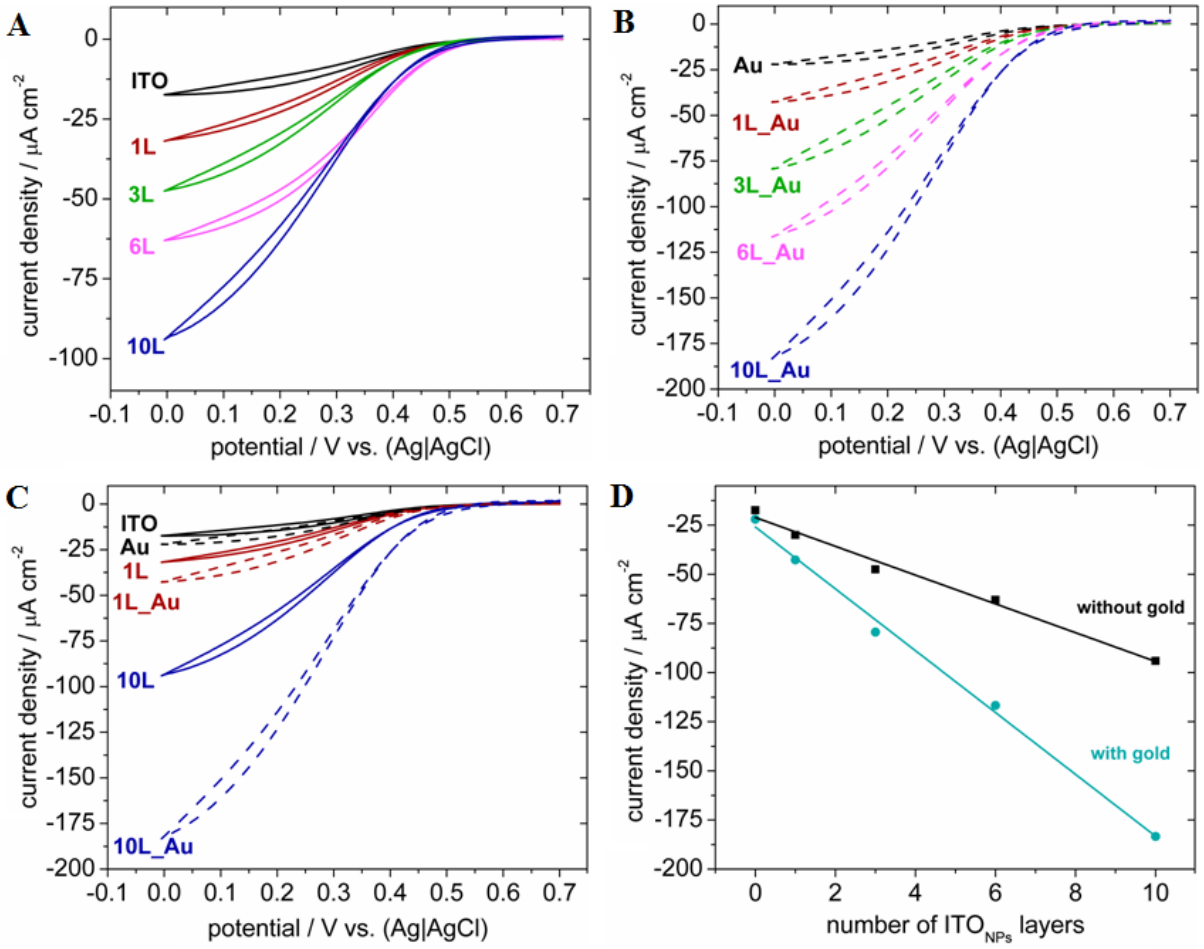

Figure 10.15. Cyclic voltammograms of ITO electrodes coated with different number of immersion and withdrawal steps (0L – bare ITO, 1L, 3L, 6L and 10L) A) without (—) and B) with (- - -) electrodeposited gold particles. C) Comparison of selected electrodes with 0L, 1L and 10L ITO_{NP} without (—) and with (- - -) electrodeposited gold particles. D) Peak current density as a function of immersion and withdrawal steps prepared for samples without (■) and with (●) electrogenerated gold particles, both measured at 0 V. All electrodes with additionally adsorbed BOx. All results obtained with 0.1 M McIlvaine buffer at pH 4.8. Scan rate 0.002 V s^{-1}.

In summary, deposition of ITO_{NP} allowed to obtain a densely packed 3D electroactive porous material for AuNPs electrodeposition. Surfaces prepared with up to ten immersion and withdrawal steps were stable and for the first time successfully used as working electrodes for

gold electrodeposition, creating a novel hybrid material. The presence of gold in the whole volume of ITO nanoparticulate film was confirmed with SEM and STEM-HAADF combination imaging and XEDS elemental mapping. All surfaces were successfully tested in catalytic reaction of glucose electroxidation as well as catalytic and mediatorless bioelectrocatalytic ORR. The best results in both cases were obtained for electrodes modified with both ITO_{NP} and AuNPs, in terms of recorded onset potential and current density.

11. Graphene oxide and reduced graphene oxide based composites

Graphene has attracted a great scientific interest in recent years (chapter 4). One of the indirect way for its production is based on graphene oxide (GO chemical reduction) [174,175,177,186]. In this chapter, a characterization of GO as well as preparation methods and properties of reduced GO (rGO) are presented. The main goal was to find favourable conditions for efficient reduction of GO *via* non-covalent functionalization [194,201–212]. This method takes advantage of strong π-π stacking interactions between various aromatic molecules and GO lattice. All composites were characterized with electrochemical, spectroscopic and microscopic techniques. Additionally, selected hybrid materials were further functionalized to develop sensing platforms.

11.1. Graphene oxide and reduced graphene oxide

Graphene oxide contains a significant number of oxygen containing functional groups (Figure 11.1_A) [174]. Due to their presence, hexagonal carbon lattice is distorted and results in insulating character of GO compared with highly conductive pristine graphene. The first goal was to find an efficient method for GO reduction in mild conditions, to restore its sp^2 carbon structure (Figure 11.1_B). Until now, one of the best results among chemical methods are obtained with hydrazine. Therefore reduced GO (rGO) obtained with hydrazine is used as a reference sample.

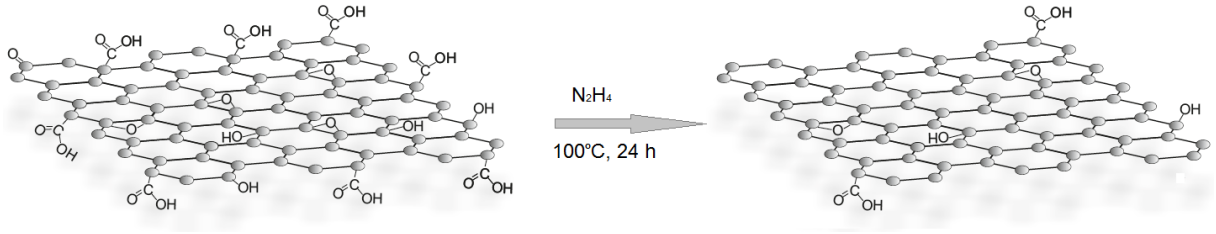

Figure 11.1. Schematic illustration of GO and rGO structures.

Cyclic voltammetry (CV) was used as a prime measurement to examine a conductive nature of investigated materials. At first, 50 μL of GO aqueous solution was deposited on a bare ITO electrode by drop casting and left for drying. In the next step, GO was reduced with hydrazine (reaction was kept in 100°C for 24 h) [175,177]. Since rGO is not soluble in water

anymore, it was suspended in THF. Similarly like for GO, 50 μL of THF solution of rGO was deposited on an electrode surface and left for evaporation. CV was recorded in 5 mM $Ru(NH_3)_6^{3+}$ in 0.1 M KCl aqueous solution, at a scan rate = 50 mV s^{-1}. This redox couple is known to be very sensitive towards electronic states of the electrode and is rather not influenced by impurities or surface oxides [474,475]. Current density recorded for rGO slightly exceeds the one for bare ITO (Figure 11.2 black and blue). This may indicate that rGO facilitates electron transfer, however the electron transfer rate for both is similar [475]. GO (Figure 11.2 red) exhibits insulating character with much higher potential peaks separation. Obtained results are in agreement with predictions and previous reports [174,186].

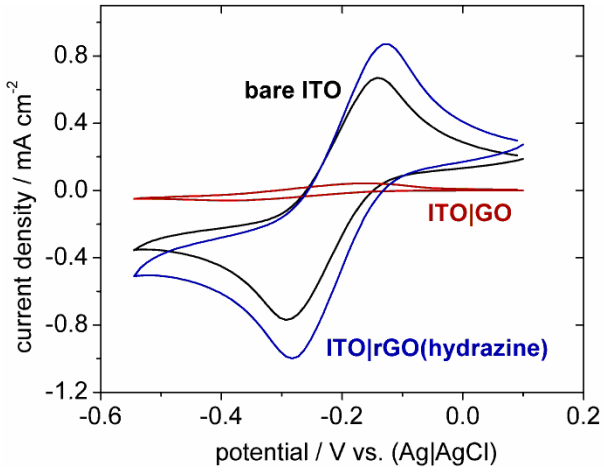

Figure 11.2. Cyclic voltammograms of: a bare ITO (black), ITO|GO (red) and ITO|rGO (GO reduced using hydrazine) (blue) prepared in 5 mM $Ru(NH_3)_6^{3+}$ in 0.1 M KCl aqueous solution; scan rate = 50 mV s^{-1}.

High resolution XPS is a strong analytical tool which allows to investigate the chemical composition of the materials as well as chemical and electronic states of elements that are present in the sample. C1s core level spectrum of GO nanosheets can be deconvoluted into four peaks (Figure 11.2_A). Bands with a binding energy of 283.8 and 284.7 eV are assigned to sp^2-hybridized carbon and C-H/C-C species [203,216,476–478]. The strongest band at 286.6 eV corresponds to C-O and 287.9 eV is attributed to C=O [216,477,478]. After the reduction with hydrazine, there is a visible change in the spectrum (Figure 11.2_B). The band at 283.9 eV due to sp^2-hybridized carbon atoms becomes predominant, what might be the consequence of partial restoration of the graphitic network. Three other bands at 284.7, 286.9 and 288.1 eV are assigned to C-C/C-H, C-O and C=O species, respectively. Estimated value of C/O ratio for GO is 1.98 and for rGO it increased to 7.08. Although a successful reduction of oxygen

species is observed, it is clearly visible that even in the case of hydrazine, chemical reduction does not provide 100% efficiency of carbon lattice restoration [174,175,177,186].

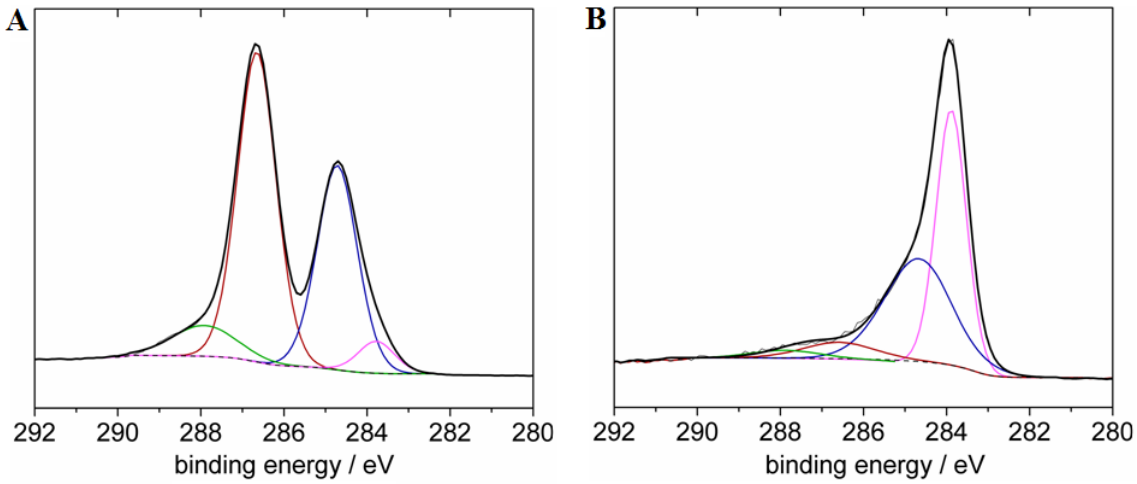

Figure 11.3. C1s core-level XPS spectra of (A) GO and (B) rGO reduced with hydrazine.

Preliminary electrochemical characterization of GO and GO reduced with hydrazine shows their insulating and conductive character, respectively. Moreover XPS analysis confirms reduction of oxygen-containing functional group in the latter case. However, because of hazardous character of hydrazine it was important to find more environmentally friendly and less toxic reducing agents which provide reaction in milder conditions. Aromatic molecules were chosen as suitable candidates, because, except reduction, a simultaneous functionalization should be possible.

11.2. Reduced graphene oxide composites with dopamine and its derivatives

Dopamine was tested as a first aromatic molecule. It is an important compound in every animal organism, involved in functioning nervous system where it plays a role of neurotransmitter [479–481]. However, outside the brain it is also a very important chemical messenger [479,480,482,483]. Moreover environmentally friendly and biocompatible dopamine can be easily funtionalized through amide group. It is a good reducing agent and strongly interacts with metal oxides and graphene [337,409,484]. Additionally, carbon-based materials provide sensitive detection of dopamine and its derivatives [264,485,486].

In the first step, two solutions: 1mL of both GO and 10 mM dopamine aqueous solution were mixed and a precipitation of dark brown flakes was immediately visible (Figure 11.4_A). After the centrifugation at 14000 rpm for 20 min the precipitant was entirely

separated (Figure 11.4_B) from the solution, which was removed. Finally, the precipitant that left was dried and suspended in THF.

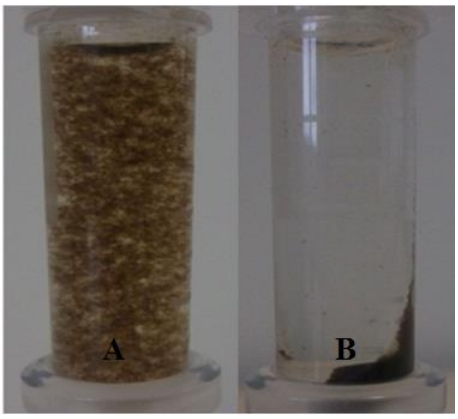

Figure 11.4. Optical images of (A) precipitant in water immediately after mixing GO with dopamine and (B) after centrifugation.

However more intentional was using azide- or alkynyl-terminated dopamine, to enable further functionalization of rGO-based composite. All materials were prepared in analogous way as it is described for dopamine.

11.2.1. Characterization

Similarly like for GO reduced with hydrazine, GO reduced with azide-dopamine (rGO|DA-N_3) and alkynyl-dopamine (rGO|DA≡) were characterized with CV and XPS. Additionally, UV-vis absorption measurements and SEM images were performed. Figure 11.5 shows SEM images of both rGO composites deposited on ITO substrate by drop casting. It was estimated that the thickness of the deposit equals ~240-300 nm and the results obtained with this simple method are very reproducible. Such prepared electrodes were used for electrochemical measurements. For XPS, ITO was changed for Si wafer to avoid a significant contribution of oxygen present in ITO in high resolution XPS spectra.

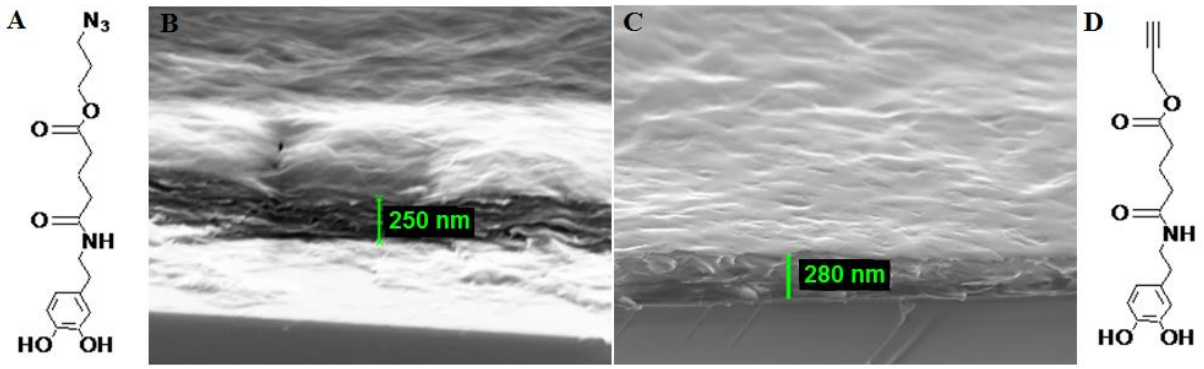

Figure 11.5. SEM images of (B) rGO|DA-N_3 and (C) rGO|DA≡ drop-casted on ITO surface; model of DA-N_3 (A) and rGO|DA≡ (D).

At first C1s core level spectrum of rGO|DA-N_3 can be compared with GO and rGO reduced with hydrazine (Figure 11.3_B and Figure 11.6_A). Two most intensive bands at 283.7 and 284.9 eV are attributed to sp^2 hybridized carbon and C-C/C-H, while 286.8 and 287.9 are assigned to C-O and C=O species, respectively. One can see a strong similarity with GO reduced by hydrazine, where band due to sp^2 hybridized carbon is predominant and those assigned to oxygen-containing functional group greatly decrease. This confirms efficient reduction and reconstitution of graphitic network. However the presence of dopamine and probably slightly less efficient reduction results in lower C/O ratio = 4.75. Incorporation of azide terminated dopamine is confirmed by the presence of a band at 400 eV (Figure 10.6_C). It can be deconvoluted into three peaks at 398.9, 400.3 and 403.7 eV which correspond to NH_2 and NH-C=O species as well as nitrogen atoms of azide group $\underline{N}$=N=$\underline{N}$ and N=$\underline{N}$=N, respectively [38,487,488]. The results are in agreement with the chemical composition of azide dopamine.

High resolution spectra of C1s core-level measured for rGO|DA≡ consist of five bands at 283.6, 284.7, 285.6, 286.8 and 287.9 eV (Figure 10.6_B). While four of them were previously described, there is additional band at 285.6 eV due to C-N species [489]. Although peak at 283.6 eV corresponding to sp^2-hydridized carbon atoms is very intensive, calculated C/O ratio is slightly lower than for azide dopamine and equals 3.54.

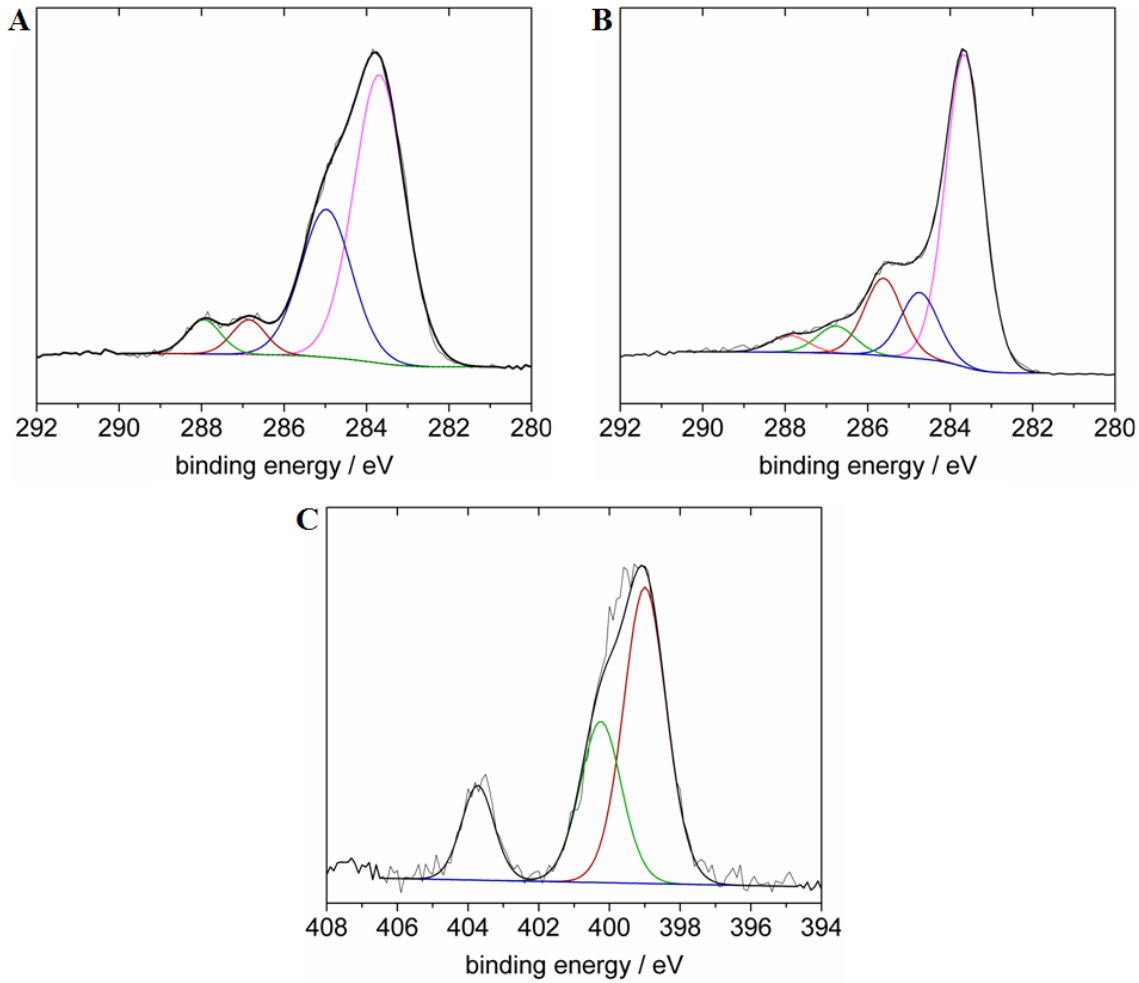

Figure 11.6. C1s core-level XPS spectra of (A) rGO|DA-N_3 and (B) rGO|DA≡; (C) N1s high resolution XPS spectra of rGO|DA-N_3.

CV was recorded in 5 mM $Ru(NH_3)_6^{3+}$ in 0.1 M KCl aqueous solution, at a scan rate 50 mV s^{-1}. Voltammogram obtained for rGO|DA-N_3 (pink) presented in Figure 11.7 shows comparable current density like rGO, while for rGO|DA≡ (green) it is slightly lower. For both composites electron transfer rate is a little bit lower than for bare ITO and rGO, however still much higher than GO, which confirms their improved conductivity behavior after reduction with dopamine derivatives.

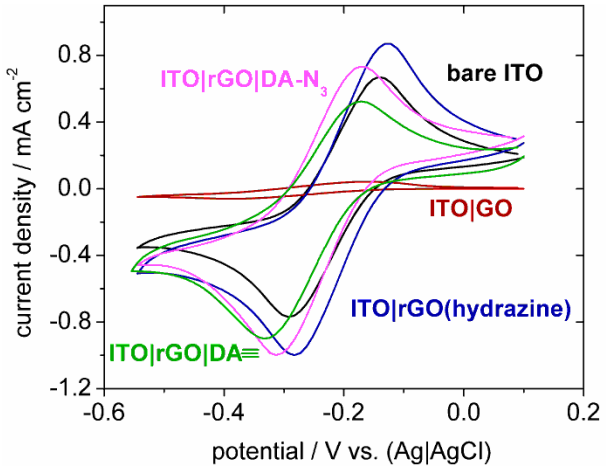

Figure 11.7. Cyclic voltammograms of: a bare ITO (black), ITO|GO (red), ITO|rGO (GO reduced using hydrazine) (blue), ITO|rGO|DA-N_3 (pink) and ITO|rGO|DA≡ (green) prepared in 5 mM $Ru(NH_3)_6^{3+}$ in 0.1 M KCl aqueous solution; scan rate = 50 mV s^{-1}.

UV-vis spectroscopy is another technique used to characterize GO and rGO-composites. Black curve in Figure 11.6 represents aqueous solution of GO with a main peak at 228 nm assigned to π-π* transition in the C-C bonds of the aromatic network and a shoulder at 299 nm due to n-π* transition of C=O bonds in carboxylic functional groups [181,203,216]. For both reduced forms main peak is red shifted in a similar manner. Moreover, in the region above 400 nm there is very strong intensity increase which might be explained by the restoration of electronic conjugation of graphitic lattice [181,203,216].

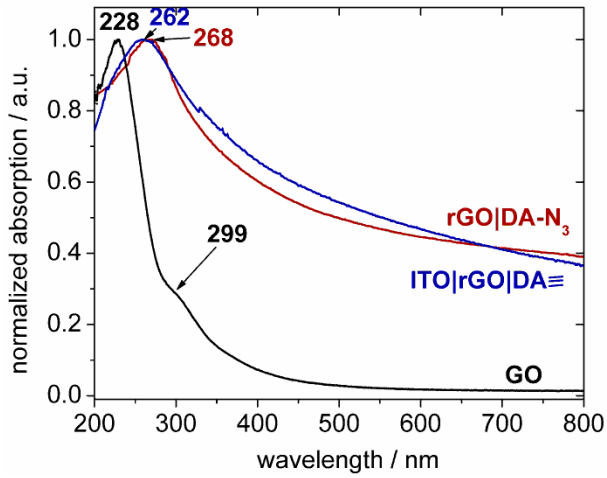

Figure 11.8. (A) UV vis spectra of GO (black), rGO|DA-N_3 (red) and rGO|DA≡ (blue).

11.2.2. Modification

In the next step both rGO-based composites were functionalized through dopamine derivatives functional groups to check their stability and reactivity but also to test their potential applications as a sensing platform.

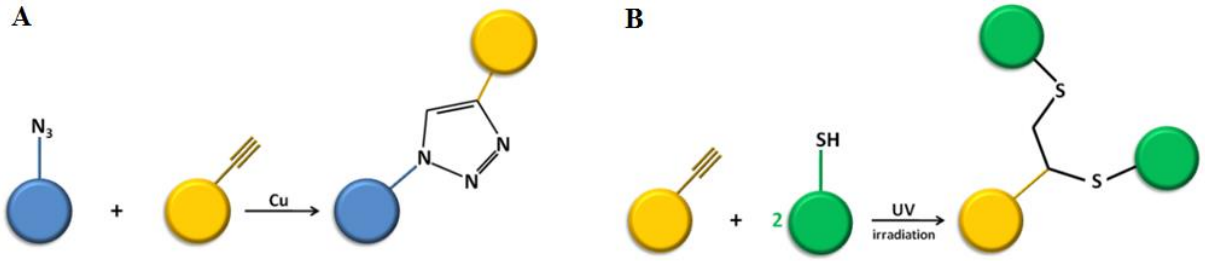

Figure 11.9. Schematic illustration of (A) "click" (Huisgen 1,3-dipolar cycloaddition) and (B) "thiol-yne" reactions.

Chemical compounds with an azide group are widely used in one of a "click" reactions, Huisgen 1,3-dipolar cycloaddition [490]. This is a copper catalyzed reaction between azide- and alkynyl-terminated compounds, where triazole ring is formed (Figure 11.9_A) [38,478,490,491]. Like all "click' reactions it is characterized by high yield and specificity. At first, rGO|DA-N_3 was modified with ferrocene (Fc) derivative, ethynylferrocene (EFc).

Successful "click" of ferrocene with dopamine moieties was confirmed by XPS measurements. High resolution N1s core-level spectrum (Figure 11.10_A) shows that previously presented peak (Figure 11.6_C) at 403.7 eV attributed to nitrogen atom (N=N=N) in azide group disappeared. Bands at 400.7 and 402.3 eV correspond to nitrogen atoms of triazole ring, C-N and N=N species, respectively [38,478,488]. The incorporation of ferrocene is revealed by Fe2p spectrum with two bands at 712.1 and 724.9 eV, attributed to $Fe2p_{3/2}$ and $Fe2p_{1/2}$, respectively (Figure 11.10_B) [491,492].

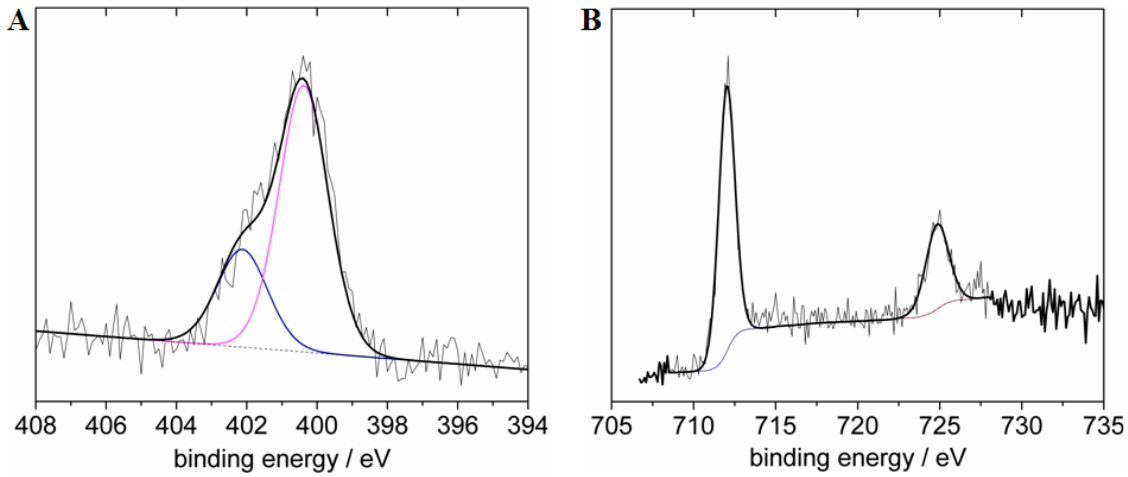

Figure 11.10. (A) N1s and (B) Fe2p high resolution XPS spectra of rGO|DA-N_3|Fe.

Another advantage of employing Fc as a testing molecule is its easy electrochemical detection [491,493–495]. It undergoes one-electron oxidation at relatively low potential. Here it was investigated at different scan rates 10-200 mV s^{-1} (Figure 11.11). One can see no peak potential shift for each measurement, only current density growth. This shows that Fc is stably bound at the electrode surface. Anodic and cathodic peaks current density plotted versus scan rate show linear dependence which confirms surface controlled electron transfer. Surface coverage Γ of Fc moieties can be calculated by integrating the anodic peak area. Using equation 8.6, and values of n = 1 and A = 0.2 cm^2, Γ equals 4.09 × 10^{14} molecules cm^{-2}, which is comparable [37,491,496] or higher [38,409,493] than other reports using "click" chemistry for modifying electrode surface.

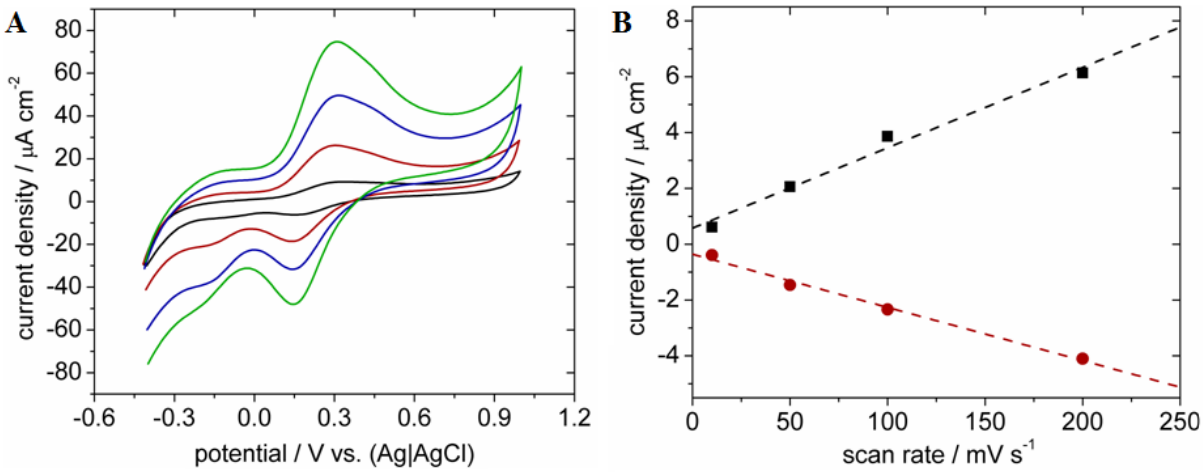

Figure 11.11. (A) Cyclic voltammograms of ITO|rGO|DA-N_3 after "clicking" EFc in 0.1 M KCl at different scan rates 10 – 200 mV s^{-1}, and (B) anodic and cathodic peak current density plotted versus scan rate.

Another possibility for functionalization is “thiol-yne” reaction, also from the family of “click” reactions [496,497]. It takes place between alkyne and thiolated molecules under UV irradiation (Figure 11.9_B). It allows for efficient surface modification with high density of functional groups. Composite which consists of rGO and alkyne dopamine was suitable for functionalization with thiolated molecules, here perfluorodecanethiol (HS-PF). Photochemical reaction was performed at a lamp power of 100 mW cm^{-2}, at 365 nm for 30 min, under nitrogen.

XPS survey spectrum of the final product reveals strong signal from fluorine with high contribution of 14.4 % (Figure 11.12_A). The incorporation of HS-PF in rGO-DA≡ (rGO|DA-S-PF) is also confirmed by changes in C1s spectrum and presence of S2p band. C1s core-level spectrum is deconvoluted into six bands (Figure 11.12_B). Peaks at 283.9 and 284.5 eV are due to sp^2-hybridized carbon atoms and C-C/C-H species. Relatively strong contribution at 285.8 eV corresponds to C-S/C-N/C-O, while 287.8 eV is due to C=O. The presence of CF_3 and CF_2 functionalities appeared at 290.7 and 293.1 eV, respectively [476]. S2p core-level spectrum can be deconvoluted into bands at 162.9 ($S2p_{3/2}$) and 164.1 eV ($S2p_{1/2}$), which are assigned to S-C bonds and another two at higher energies 167.4 ($S2p_{3/2}$) and 168.6 eV ($S2p_{1/2}$) due to oxidized sulfur-containing species (Figure 11.12_C) [498,499]. For both sulfur doublet pairs peak separation equals 1.2 eV and the intensity ratio $S2p_{3/2}$/ $S2p_{1/2}$ is *ca.* 2 [498,499].

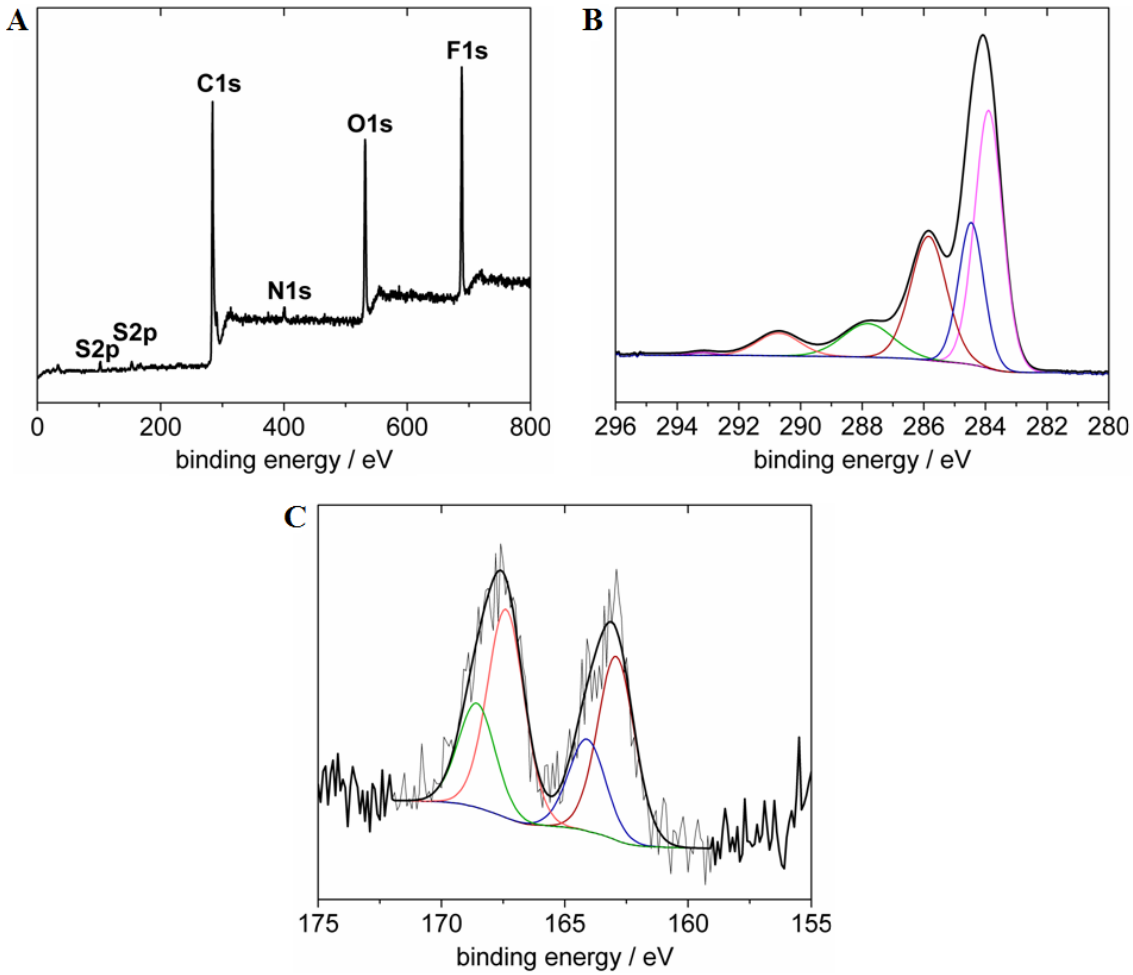

Figure 11.12. (A) XPS survey spectrum of rGO|DA-S-PF deposited on Si wafer, (B) C1s and (Sp2) core-level XPS spectra of rGO|DA-S-PF.

Contact angle measurements of ITO|rGO|DA≡ performed before and after "thiol-yne" reaction with HS-PF show clear changes (Figure 11.13). Alkynyl-terminated surface is highly hydrophilic with a contact angle of 44°. Linked HS-PF changes properties into more hydrophobic with contact angle ~83°. Although relative difference between both substrates is similar as reported before and contact angle after "thiol-yne" reaction increases of ~40-50°, the surface presented here is still less hydrophobic of ~25° [496]. This might be influenced by the nature of a primary surface used in both cases, here it is ITO, while in previous report it is a more hydrophobic boron-doped diamond [478,496].

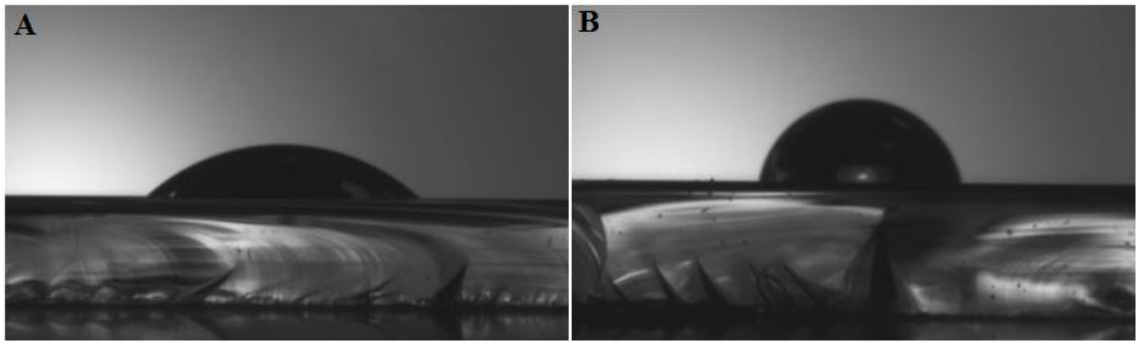

Figure 11.13. Optical images taken during contact angle measurements of ITO|rGO|DA-≡ (A) before and (B) after the reaction with perfluorodecanethiol.

11.3. Reduced graphene oxide composites with tetrathiafulvalene and its derivatives

Tetrathiafulvalene (TTF) (Figure 11.14) is a strong electron donor molecule. Due to its multi-stable oxidation states (TTF^0, $TTF^{\bullet+}$, TTF^{2+}), TTF was employed in electrochemically controlled-mechanically interlocked molecular structures such as pseudorotaxanes, rotaxanes or catenanes [38,410,500–504]. These structures found applications in building logic gates or (electrochemical) switches [500–503]. Addition of TTF into aqueous solution of GO not only allows for non-covalent functionalization but also simultaneous reduction of GO. Moreover it shows promises for creating new molecular switches. Additionally TTF might influence electronic properties of rGO, what was reported before with graphene [205].

Similarly like with dopamine, 1 mL of 10 mM solution of TTF and GO were mixed and sonicated for 3 h. After this time a precipitation of dark brown flakes was visible (Figure 11.14_A). After the centrifugation at 14000 rpm for 20 min the precipitant was separated (Figure 11.14_B) from the solution, which was removed. Afterwards, the precipitant was dried and suspended in THF.

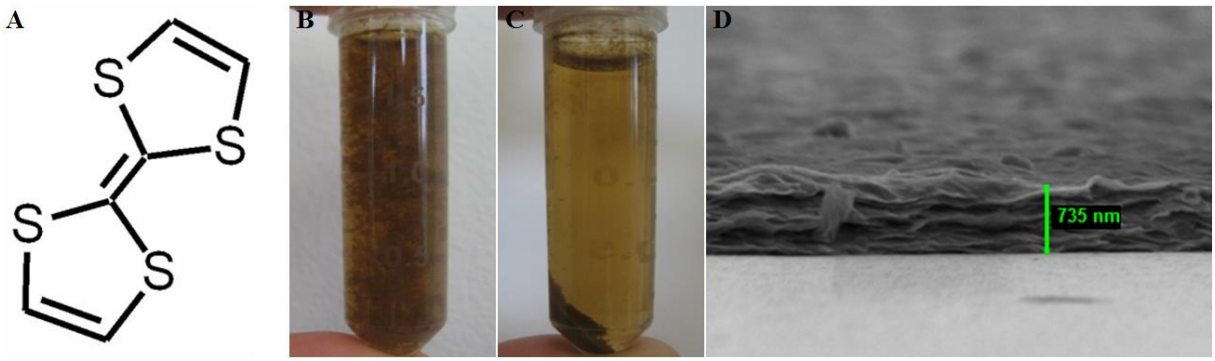

Figure 11.14. Optical images of (A) precipitant in water immediately after mixing GO with TTF and (B) after centrifugation, (C) SEM image SEM images of rGO|TTF drop casted on ITO surface, with TTF chemical structure on the left.

11.3.1. Characterization

Figure 11.14_C shows SEM images of TTF|rGO composite deposited on ITO substrate by drop casting. It was estimated that the thickness equals ~735 nm, which is *ca.* 3 times more than for dopamine-based rGO composites. Such prepared electrodes were used for electrochemical measurements, while for XPS analysis, ITO was replaced by Si wafer.

At first, CV was performed for TTF deposited on ITO electrode without redox probe in the solution. Two redox waves due to multi-stable oxidation states of TTF are visible (Figure 11.15_A black). In anodic scan, there are two oxidation peaks at 0.56 and 1.03 V while in cathodic scan two corresponding reduction peaks at 0.34 and 0.73 V (vs. Ag|AgCl). Voltammogram obtained for rGO|TTF exhibits similar signature, however a significant potential shift towards negative potential is observed. Each peak current density in both forward and backward scan changes of *ca.* 0.29-0.39 V. This shift may suggest intermolecular charge transfer interactions between TTF and rGO, where TTF plays a role of electron donor and rGO electron acceptor [205,230]. When TTF is integrated into graphene composite its oxidation is facilitated. Additionally the amount of TTF moieties on the surface can be estimated by peak integration. According to equation 8.6 (n = 1 and A = 0.2 cm^2), surface coverage Γ of TTF in rGO|TTF composite equals 8.9 × 10^{14} molecules cm^{-2} which is much higher than TTF doped graphene [205] but in the same order of magnitude like other composites prepared in the similar approach (10^{14} ÷ 10^{15} molecules cm^{-2}).

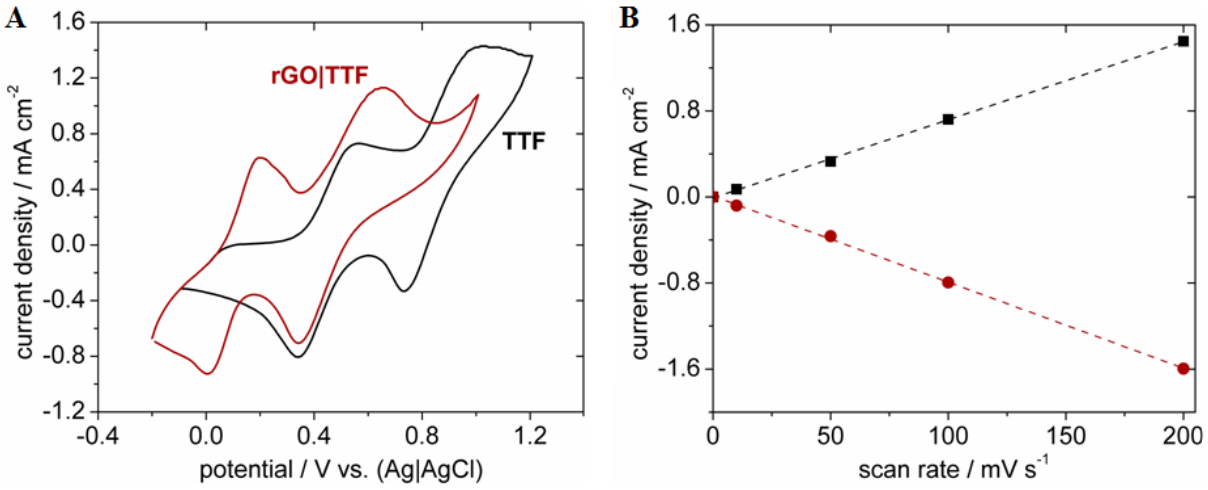

Figure 11.15. (A) Cyclic voltammograms of acetonitrile solution of TTF (black) and ITO interface modified with rGO|TTF nanosheets by drop casting (red), both in 0.1 M KCl, scan rate 100 mV s^{-1}. (B) Anodic (■) and cathodic (▲) peak current plotted in the function of scan rate.

XPS was used to investigate how effectively, in comparison with dopamine and its derivatives, TTF can reduce GO. C1s core level spectrum can be deconvoluted into five bands. Peak at 283.9 eV assigned to sp^2-hybridized carbon atoms became predominant similarly like in dopamine case. This shows that TTF also takes part, at least in partial, restoration of honeycomb carbon network. Bands at 284.9, 285.9, 287.2 and 288.5 correspond to C-C/C-H, C-O/C-S, C=O/C=S and C=O, respectively. Presence of TTF molecules in the composite are also confirmed by the appearance of a band due to S2p. It can be deconvoluted into two intensive bands at 163.5 and 164.6 eV, and a very weak one at 166 eV. The first two are attributed to sulfur doublet $S2p_{3/2}$ and $S2p_{1/2}$, respectively with a peak separation 1.1 eV [205]. Small contribution with the highest binding energy is due C=S bonds of TTF cations [205].

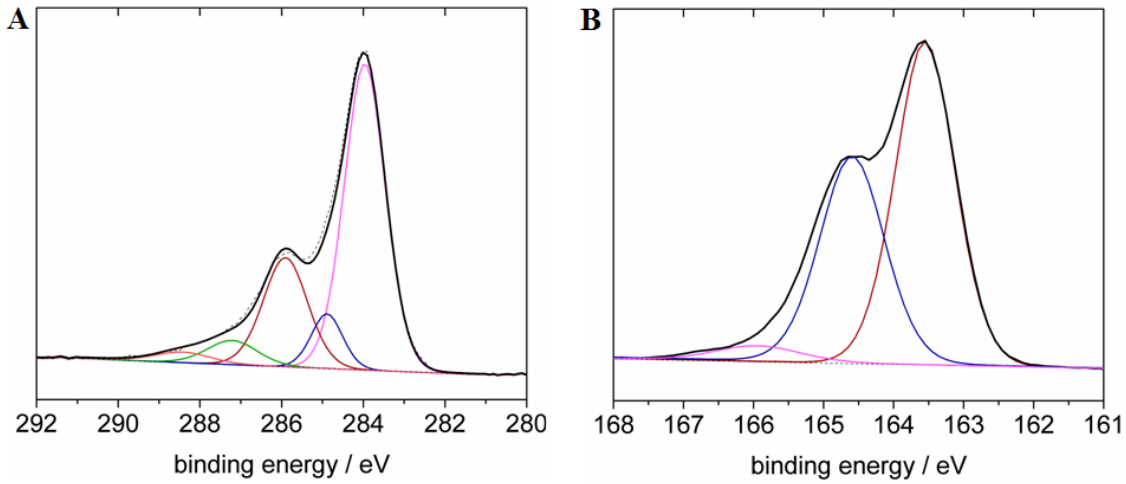

Figure 11.16. High resolution XPS (A) C1s and (B) S2p core-level spectra of rGO|TTF.

One of the main issues that makes rGO|TTF so different from rGO|dopamine is the perspective for preparing chemical switches. Controlled releasing and reintegrating of TTF molecules from the composite show promises for reusable sensing surfaces. While in dopamine case, once intercalated molecules cannot be triggered, for TTF there are at least two strategies for release.

In the first method, a chemical oxidation of TTF to TTF^{2+} by $Fe(ClO_4)$ allows to remove it from graphene network. Two strategies were used, at first ITO with deposited rGO|TTF was immersed in aqueous solution of $Fe(ClO_4)$ and left for 30 min. In the second experiments composite was directly added to the $Fe(ClO_4)$ and reaction was performed in the solution without solid substrate. Both approaches give the same results which are confirmed by CV performed after oxidation (Figure 11.17_A-b). However it is visible that this process is not 100% efficient. Although recorded current density significantly decreases, a double-wave

of TTF signature is still evident. Surface coverage calculations reveal that the amount of TTF molecules is 14 times lower after oxidation with $Fe(ClO_4)$. This attempt confirms that rGO composite serves appropriate environment for releasing of TTF molecules, similarly like other known controlled interlocked molecular structures [505,506].

However, there was a space for more effective chemically triggered release. In the next approach, an electron deficient cyclophane cyclobis(paraquat-*p*-phenylene) ($CBPQT^{4+}$) was employed [38,507]. It is well-known to form strong host-guest complex with TTF molecules (Figure 11.17_B inset) which can be utilized in pseudo-rotaxanes systems for tunable structures [38,507]. RGO|TTF composite was treated in analogous way like with $Fe(ClO_4)$. In Figure 11.17_A-c one can see a voltammogram with no signal from TTF molecules. This confirms that interaction between this electron-rich and electron-deficient molecules are strong enough to release TTF from a stable rGO|TTF composite. Interestingly, this host-guest couple can be also detected with UV-vis spectroscopy. TTF itself shows strong absorption band at 446 nm with a narrow fwhm. In contrast, $CBPQT^{4+}$ is not detectable under these experimental conditions. When the complex is formed an intensive and broad band at 855 nm is visible due to the strong charge-transfer between both species [38]. This method is very useful for analysis of more complex modified rGO|TTF composites, which are presented in the next section of this chapter.

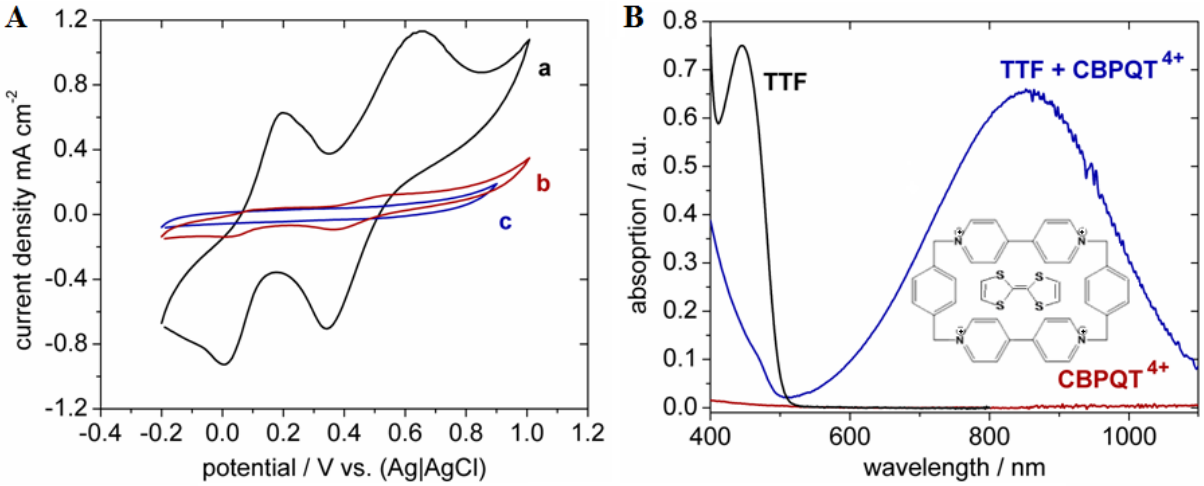

Figure 11.17. (A) CV of ITO|rGO|TTF before (a black) and after treatment with 2 mM aqueous solutions of (b red) $Fe(ClO_4)$ and (c blue) $CBPQT^{4+}$; 0.1 M KCl, scan rate 100 mV s^{-1}. (B) UV-vis spectra of TTF (black), $CBPQT^{4+}$ (red) and TTF-$CBPQT^{4+}$ complex (blue) (inset: $CBPQT^{4+}$ molecule scheme).

11.3.2. Modification

In order to check the stability and activity of rGO-based composites, TTF molecules were exchanged with TTF-N_3 for the same reason why DA was changed for DA-N_3. At first, XPS analysis of the new material was performed. The incorporation of azide-terminated TTF was confirmed by the appearance of N1s and S2p bands. The first one can be deconvoluted into three peaks 400.4, 401.9 and 405.5 eV. Two latter ones are due to electron-rich outer nitrogen atoms (N=N=N) and electron-deficient inner central nitrogen (N=N=N). A band with the lowest binding energy might correspond to partially decomposed azide moieties by destructive XPS irradiation as was shown before [508]. S2p shows very similar signature like for TTF, $S2p_{3/2}$ and $S2p_{1/2}$ doublet is present at 163.8 and 164.9 eV. Very small contribution at 167.6 eV is assigned to C=S bonds of higher oxidation states of TTF.

The presence of azide species was utilized for "click" reactions (Figure 11.9_A). The second compound that was employed was alkynyl-terminated mannose (in the following description a short name "mannose" is used). Mannose is a sugar monomer that belongs to the group of aldohexoses. It is involved in many important processes in human metabolisms [509–511]. It mainly interacts with saccharides, proteins or lipids in enzymatic reactions (so called glycosylation processes) in which fundamental biopolymers are formed [509,510]. Interfaces coated with carbohydrates may enable the study of some protein folding or cell-cell interactions. They also show promises for preparing sensor for glycan-protein interactions [509,510]. Any disorder in glycosylation processes may results in serious health problems line weakened immune system [511]. In this part, preliminary studies about perspective mannose-modified stable surface are shown. At first, "click" reaction was confirmed with XPS measurements. Figure 11.18_C presents N1s core level spectrum which, most of all, shows the formation of a triazole ring by disappearance of the band at 405.5 eV characteristic of the azide group. Two bands that are present at 400.6 and 402.3 eV are assigned to N=N and N-C species of triazole ring, respectively.

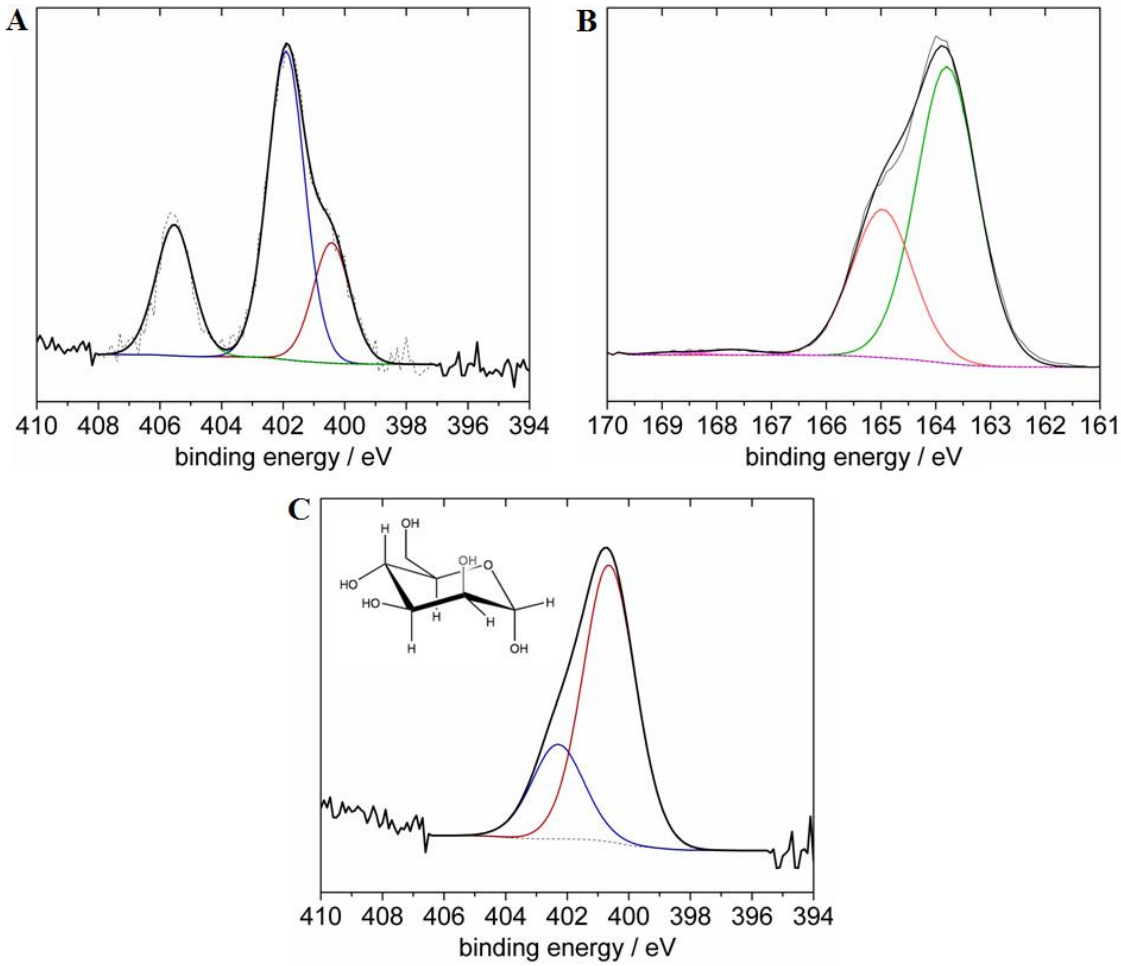

Figure 11.18. (A) N1s and (B) S2p core-level XPS spectra of rGO|TTF-N_3 and (C) N1s core-level XPS spectra of rGO|TTF-mannose (inset: mannose molecule structure).

It is shown in the previous section that TTF can be released from rGO-based composite. This gives promises for preparing reusable glycan-modified sensor. To investigate chemical triggering of TTF-mannose pair, both oxidation in $Fe(ClO_4)$ aqueous solution and complex formation with aqueous solution of $CBPQT^{4+}$ were tested. At first ITO|rGO|TTF-mannose surface was immersed in $Fe(ClO_4)$ for 1 min and then withdrawn. Afterwards UV-vis spectrum of the solution was recorded. This protocol was repeated until UV-vis spectrum did not change what means than no TTF-mannose could be released anymore. Analogous experiment was prepared with $CBPQT^{4+}$. For this compound instead of monitoring band at 446 nm due to TTF what was used in the case of $Fe(ClO_4)$, a broad band at 855 nm from TTF-$CBPQT^{4+}$ host-guest complex was analyzed. Measurement was completed when no further change in absorption spectrum was recorded.

Described experiments proved that TTF-mannose can be released from rGO-based composite. However, the amount of mannose itself was not determined. To solve this

problem, solutions used for UV-vis measurements (after each immersing step) were utilized in a so called colorimetric Molisch test. 60 μL of each solution was added individually to the mixture of 60 μL of 5 wt % aqueous phenolic solution and 900 μL of concentrated H_2SO_4. In a strong acidic solution mannose is dehydrated to aldehyde and condenses with two molecules of phenol creating red- or purple-colored compound. Due to this process, the presence of mannose is visible at 486 nm in the UV-vis spectrum (Figure 11.19_A). The amount of mannose was recalculated using a calibration curve (Figure 11.19_B) and its release was finally plotted versus time as shown in Figure 11.19_C. The assumption that TTF-mannose pair is released with $CBPQT^{4+}$ with efficiency close to 100% was assumed from CV measurements where no signal from TTF after this treatment was recorded. When these results were analyzed together with calibration curve, it was estimated that after 1 h *ca.* 2.2×10^{15} molecules cm^{-2} of mannose were released together with TTF. For $Fe(ClO_4)$ this amount was lower of *ca.* 35%, what is also in agreement with previously shown CV results.

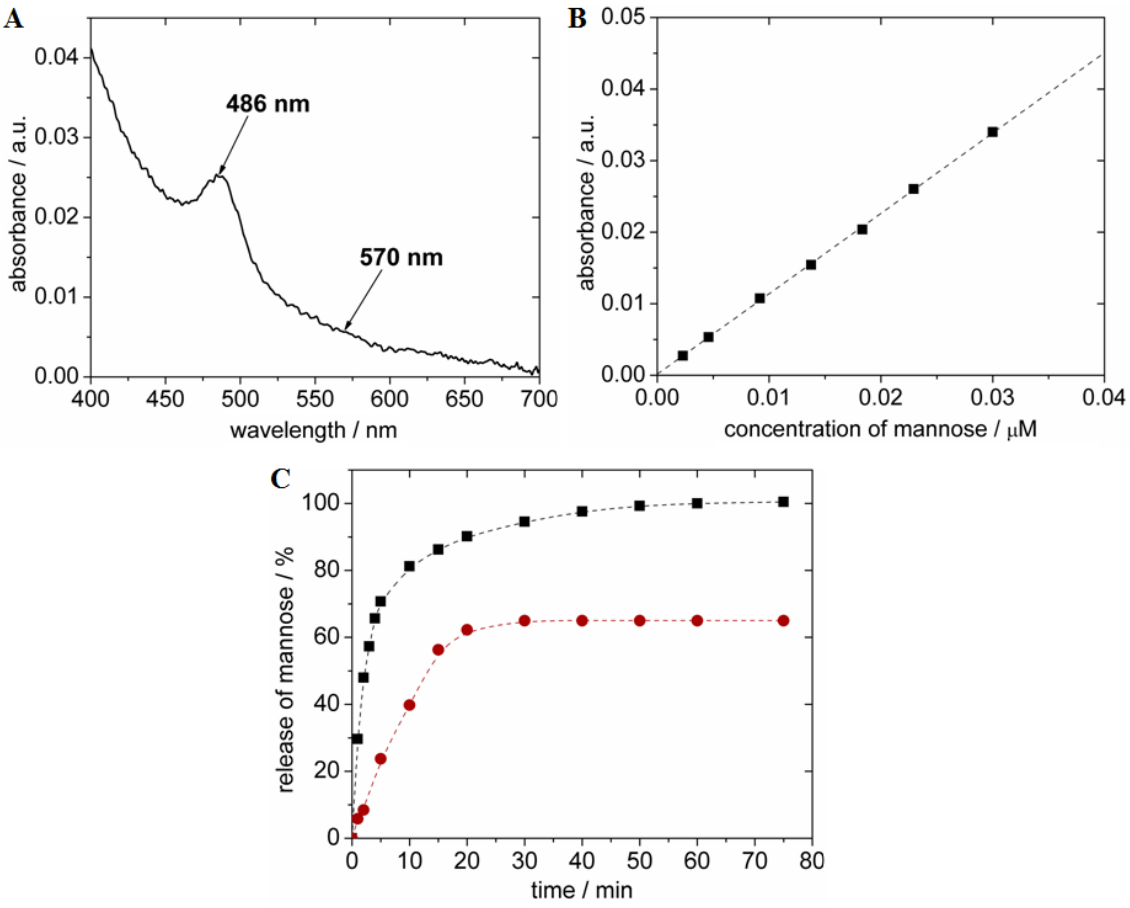

Figure 11.19. (A) absorbance spectrum of dye formed in condensation reaction from mannose and phenol molecules, (B) calibration curve of absorbance peak plotted versus concentration of mannose, (C) time-dependent release of TTF-mannose using 2 mM solution of $CBPQT^{4+}$ (■) and 2 mM of $Fe(ClO_4)$ (●).

These experiments proved that rGO|TTF composites are good candidates for preparing stable and efficient biosensors. Detailed investigations that are presented in this section confirmed that TTF simultaneously reduces GO and is incorporated into the composite. What is more, the properties of this compound were successfully used for its releasing without any damage of the carbon network.

To conclude this chapter, a new approach of one step simultaneous reduction and functionalization of GO with DA, TTF and their derivatives is presented. This simple method performed in mild conditions in ultrasound bath, at pH ~7 and at room temperature was utilized to prepare stable rGO-based composites. The efficiency of this method was confirmed by CV and XPS analysis. Additionally the activity of the materials with azide and alkynyl moieties was investigated with "click" and "thiol-yne" reactions. Obtained results show that all composites are suitable for preparing biosensing platforms at will. Moreover, although both kinds of materials with DA and TTF are stable, the latter one can be released on demand from the composite, essential to design reusable surfaces.

12. Surface-enhanced Raman spectroscopy

In this chapter an application of electrochemically deposited AuNPs as a platform for surface-enhanced Raman spectroscopy (SERS) is presented and discussed. In order to characterize the ability of multifarious NPs to enhance Raman scattering and calculate enhancement factor (EF) various dyes as model compounds were engaged. Afterwards, two biomolecules, alanine and choline, were immobilized on AuNPs and their spectrum was performed and compared with normal Raman spectra.

12.1. Preliminary experiments with dyes

AuNPs are well-known and widely used as a platform for SERS [89,95,97,108,111]. However, their ability to enhance Raman scattering strongly depends on their size, shape and a distance from each other [42,512]. It is important to investigate the efficiency of such surfaces with properly selected dyes.

In the case of AuNPs electrodeposited at a three-phase junction, four dyes were selected: malachite green isothiocyanate (MGITC), rhodamine 6G (R6G), porphycene (PP) and 1,4-mercaptobenzoic acid (MBA). Each of these molecules absorbs the light in a different range of wavelength which can influence the way how they are enhanced. In order to calculate EF, both SERS and normal Raman (NR) spectra have to be carried out. One can estimate EF using the following equation:

$$EF = \frac{I_{SERS} N_{NR}}{I_{NR} N_{SERS}} \qquad \textbf{(12.1)}$$

where I_{SERS} and I_{NR} are intensities of SERS and NR spectrum respectively measured in certain mode position, while N_{SERS} and N_{NR} are corresponding numbers of molecules that were probed.

12.1.1. Malachite green isothiocyanate

As a first model molecule MGITC was investigated. At the beginning its absorption spectrum was measured with UV-vis spectrophotometer and is shown in the Figure 12.1 together with its chemical structure.

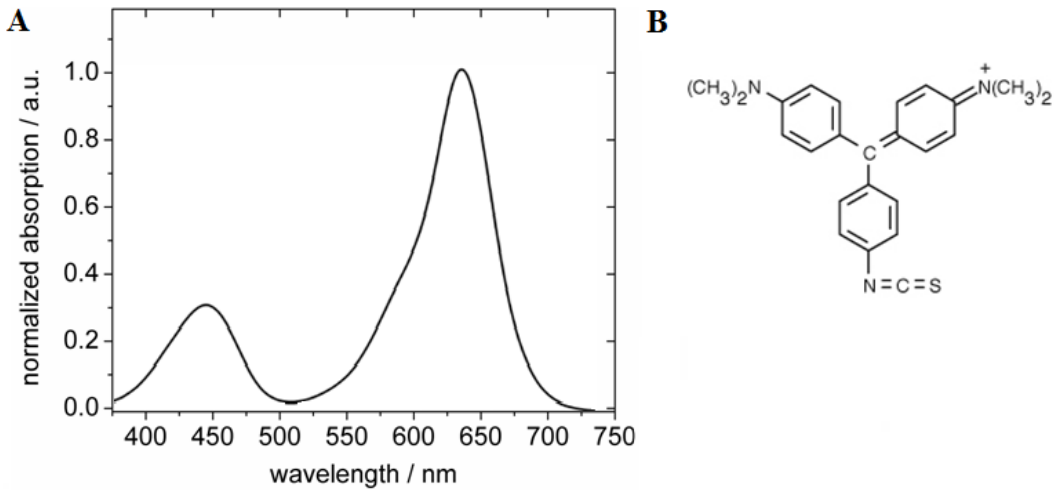

Figure 12.1. UV-vis spectrum (A) and chemical structure (B) of malachite green isothiocyanate [513].

SERS signal was collected from a sample of the electrodeposited Au particles left in 10^{-6} M MGITC aqueous solution for 24 h, then rinsed with pure water, and dried at room temperature. Figure 12.2 shows (a) a normal Raman spectrum of MGITC and (b) SERS spectrum of MGITC adsorbed on AuNPs. The most prominent bands at 417 with a shoulder at 426, 1072, 1172 and 1584 cm^{-1} are attributed to benzene ring deformation, out-of-plane C-H bending, in-plane C-H bending and in-plane ring stretching, respectively [512–514]. 1365 and 1613 cm^{-1} modes are due to phenyl-N stretching. In-plane benzene deformation and bending appear at 525, 728 and 912 cm^{-1}. Finally, 1295 cm^{-1} is assigned to C-C/C-C-H stretching modes, while 1444 cm^{-1} comes from methyl group rocking and bending [512–514].

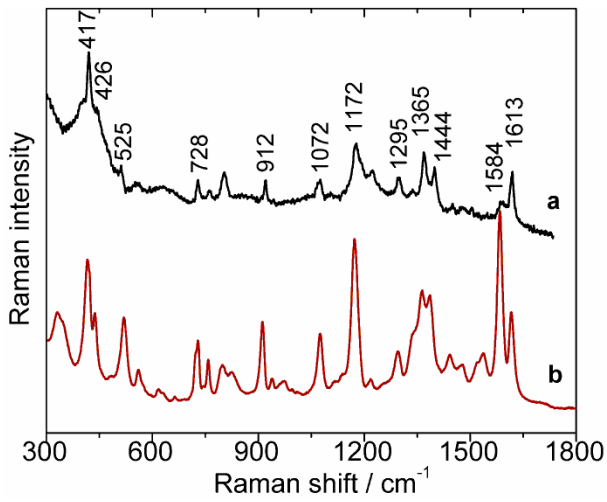

Figure 12.2. Normal Raman (a) and SERS (b) spectra of malachite green isothiocyanate.

Stability, homogeneity and reproducibility are very important properties of SERS platforms. To investigate these features, SERS spectra were recorded on different spots across one sample (Figure 12.3), as well as on several different separately prepared samples of gold deposit (Figure 12.4). On basis of these measurements the standard deviation for spectra collected from a hundred spots on one sample was calculated to be ~12%, while for four different samples it is ~15%.

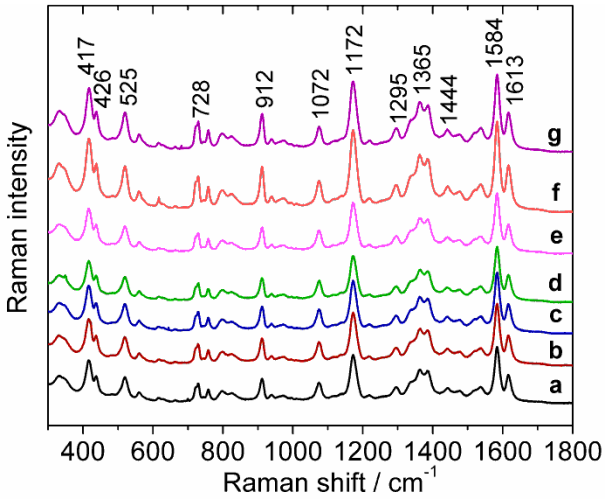

Figure 12.3. SERS spectra of MGITC collected from seven (a-g) random spots across one sample.

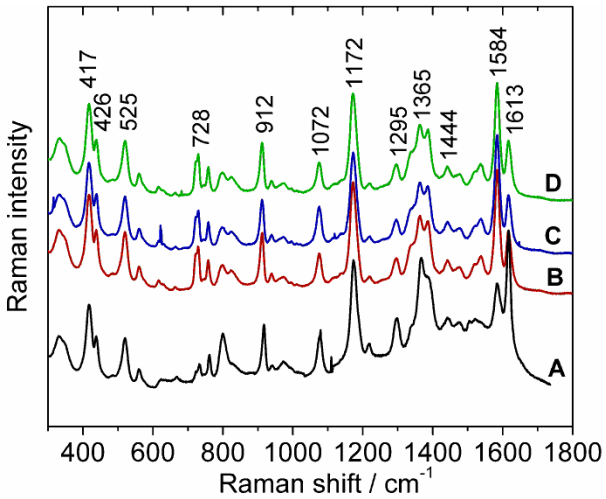

Figure 12.4. SERS spectra of MGITC collected from four (A-D) different samples.

In order to calculate EF (equation 12.1), the numbers of molecules for NR and SERS have to be estimated. NR spectra were collected from a cell containing pure MGITC, which molecular weight M equals 485.98 g mol^{-1} and density c_{NR} is 1.014 g cm^{-3}. The volume V_{NR} that is illuminated during this measurement equals 22 μm^3. Using the following equation:

$$N_{NR} = \frac{V_{NR} c_{NR} N_A}{M} \qquad \textbf{(12.2)}$$

where N_A is Avogadro constant = 6.02214129(27) × 10^{23} mol^{-1}, N_{NR} = 2.7 × 10^{12} molecules. SERS measurements were recorded by dipping a surface into diluted solution of MGTIC. The crucial factor was to ensure less than a monolayer coverage, otherwise the EF is overestimated. Using the concentration of 10^{-6} mol L^{-1} of MGTIC and the laser beam of ~5 μm in diameter so the irradiated area ~19.6 μm^2 yields N_{SERS} = 4.2 × 10^6 molecules. Collecting all the information together, EF is in the order of 10^6.

12.1.2. Rhodamine 6G, 1,4–mercaptobenzoic acid and porphycene

Although EF gives information about efficiency of SERS substrates, this value is strongly dependent on investigated molecules. It is interesting to compare together three dyes R6G, MBA and PC since they absorb the light in different ranges (Figure 12.5) and they bind to the gold surface in different ways, either by thiol group (MBA) [515–517] or nitrogen atoms (lone pair) (R6G and PC) [515,518] (Figure 12.6). Both of these features can influence the efficiency of Raman scattering enhancement by electrodeposited AuNPs.

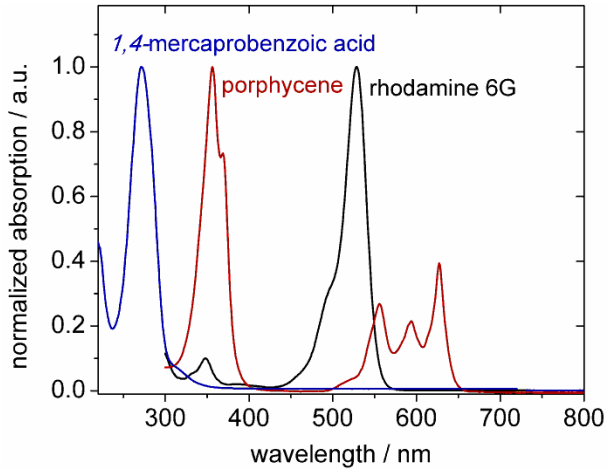

Figure 12.5. UV-vis spectra of rhodamine 6G (black), 1,4–mercaptobenzoic acid (blue) and porphycene (red).

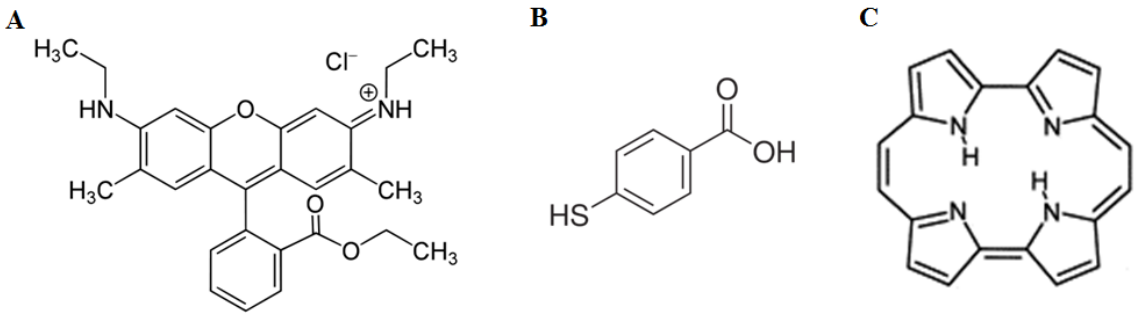

Figure 12.6. Schemes of rhodamine 6G (A), 1,4–mercaptobenzoic acid (B) and porphycene molecules (C).

In order to prepare a broader view of the capabilities of AuNPs-SERS-platforms (Au-3P, a three-phase junction), they were compared with two other substrates. The first one, round AuNPs (diameter 12 ± 5 nm) prepared with thermal annealing of thin gold film on ITO surface (Au_therm), and the second one, 2 nm thick gold film (Au_film).

At first, results obtained for R6G are shown in Figure 12.7. Above 1300 cm^{-1}: 1313, 1365, 1509, 1576 and 1653 cm^{-1} bands correspond to aromatic stretching vibrations [519–521]. Two bands at 1128 and 1186 cm^{-1} are assigned to C-H in-plane bending, while 1077 cm^{-1} is due to C-H out-of-plane bending [519–521]. The band at 776 cm^{-1} is attributed to out-of-plane bending motions of H atoms of the xanthenes skeleton and 613 cm^{-1} is due to C-C-C ring in-plane bending [519–521]. When Raman spectrum is compared with SERS performed on Au_3P a strong relation is clear. The only region that is changed is between 1120-1190 cm^{-1}, two bands at 1128 and 1186 cm^{-1} disappeared and a new relatively intensive band at 1154 cm^{-1} is visible. This region corresponds to C-H in-plane bending [519–521]. When both described spectra are compared with SERS recorded on Au_therm or Au-film (with 10 times magnification), one can barely notice a weak signal around 1359 and 1578 cm^{-1} or no signal, respectively. These two bands may be due to aromatic stretching vibrations as well as carbon contaminations.

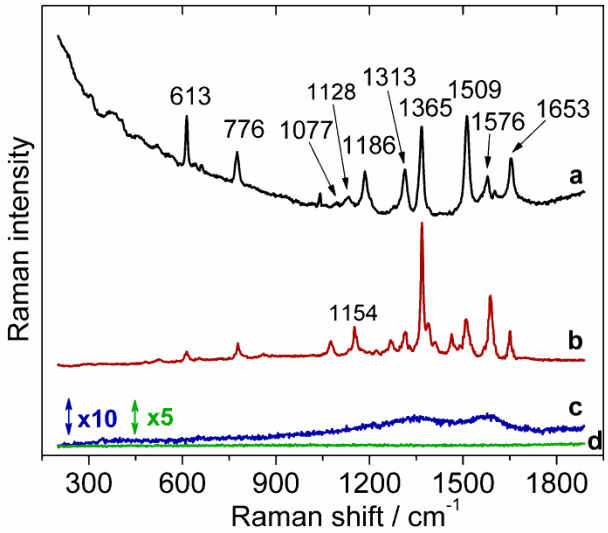

Figure 12.7. Normal Raman (a) and SERS (b-d) spectra of rhodamine 6G (b – Au_3P, c – Au_therm, d – Au_film).

The next molecule, 1,4–mercaptobenzoic acid (MBA), although typically used to investigate silver surfaces, can be also engaged to test gold platforms. Raman spectrum (Figure 12.8 a) contains two predominant bands at 1077 and 1596 cm^{-1}, that are usually used to identify the presence of MBA [522–524]. The first one can be assigned to C-C stretching (a ring breathing mode) together with C-S stretching, while the second one is due to the ring axial deformation mode. C-H bending modes are visible at 1179 and 1453 cm^{-1}. While 522, 799 and 1701 cm^{-1} can be attributed to C=O vibrations in –COOH group [523,524]. Similarly like for R6G there is a very good correlation between Raman and SERS spectrum for Au_3P, only a band at 1596 is slightly shifted to 1588 cm^{-1} (Figure 12.8 b), and no response from Au_therm and Au_film (Figure 12.8 c-d), even after 10 times magnification. This again clearly indicates a superiority of multifarious gold particles over round ones in terms of Raman scattering enhancement.

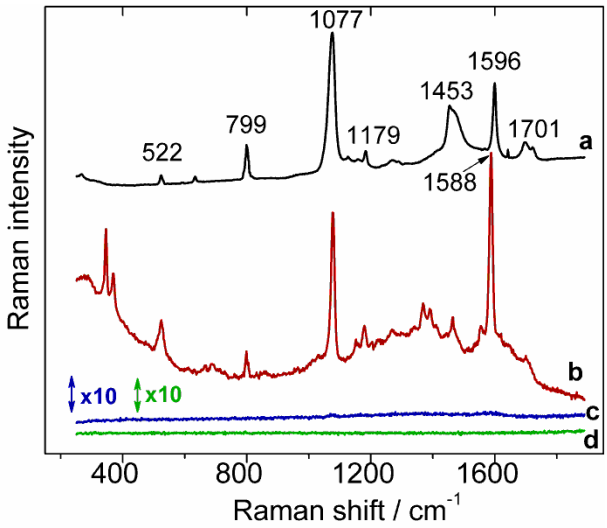

Figure 12.8. Normal Raman (a) and SERS (b-d) spectra of *1,4*–mercaptobenzoic acid (b – Au_3P, c – Au_therm, d – Au_film).

The last example of a dye that was employed in SERS measurements is porphycene (PC). Contrary to R6G and MBA, PC is not so intensively investigated with Raman spectroscopy. There are only few examples in which Raman spectra of PC are presented and described together with some theoretical modeling and simulations. It has to be emphasized that analysis of SERS spectrum of PC is very general and sketchy. It is shown here just to highlight even more the application character of electrodeposited AuNPs for various chemical compounds. For PC, the recorded SERS spectrum is compared only with other reports from the literature [525–527], not with its NR spectrum. This is the consequence of a very strong fluorescence of PC observed for measurements performed with the laser 633 nm, which greatly hinders collecting its spectrum (Figure 12.9). Bands at 665, 965, 990, 1539 and 1561 cm^{-1} are assigned to in-plate skeleton deformation modes [525–527]. There is also a contribution from in-plane N-H bending at 1255, 1471 and 1607 cm^{-1}. Out-of-plane C-H bending modes are visible at 710 cm^{-1} and in-plane C-H bending modes are at 1066 and 1392 cm^{-1}, while bands at 1202 and 1333 cm^{-1} are attributed to in-plane *meso*-CH and phenylene bending modes, respectively [525].

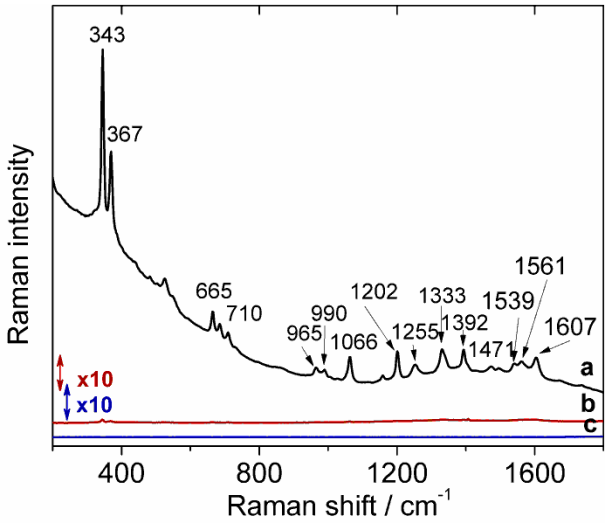

Figure 12.9. SERS (a-c) spectra of porphycene (a – Au_3P, b – Au_therm, c – Au_film).

To summarize Raman and SERS measurements performed with Au_3P, Au_therm and Au_film, all results are collected in a Table 12.1. One can find the intensity of SERS spectra obtained on all surfaces (two samples of every kind) for R6G, MBA and PC, as well as calculated EF. The highest enhancement of the signal was obtained for R6G deposited on Au_3P. For Au_therm particles the intensity is at least three orders of magnitude lower than Au_3P. In the case of R6G there is no enhancement on Au_therm at all. Finally, for all investigated molecules one can see that no signal was recorded on gold film, in agreement with the principle that only rough or nanoparticulate metallic surface can be used as SERS substrates. In the case of PC only SERS intensity is presented since, as it was mentioned above, NR spectrum of this compound could not be obtained due to its strong fluorescence.

Table 12.1. Intensities of selected SERS bands (cps – counts per second) and EF obtained for MBA, R6G and PC on Au_3P, Au_therm and Au_film.

	***R6G* (*1588 cm^{-1}*)**		***MBA* (*613 cm^{-1}*)**		***PC* (*343 cm^{-1}*)**
sample	I_{SERS} [cps]	EF	I_{SERS} [cps]	EF	I_{SERS} [cps]
Au_3P (*1*)	9	$4.6 \cdot 10^7$	230	$1.4 \cdot 10^7$	11400
Au_3P (*2*)	8	$4.1 \cdot 10^7$	130	$7.8 \cdot 10^6$	8500
Au_therm (*1*)	0	0	0.15	$8.9 \cdot 10^3$	18
Au_therm (*2*)	0	0	-	-	0
Au_film (*1*)	0	0	0	0	0
Au_film (*2*)	0	0	0	0	0

12.2. Biomolecules sensing

SERS found an application not only as an imaging technique [95] but also for biomedical sensing, mostly due to extremely high specificity and sensitivity [89,97,108]. In this section two biomolecules are presented and investigated as an example of biological compounds. This can give an answer whether electrogenerated AuNPs can be utilized as a biomedical sensor or detector.

12.2.1. L-alanine

L-alanine (inset Figure 12.10) is one of amino acids, a component of a large group of proteins. It is an aliphatic nonpolar amino acid, and because of four different functional groups bound to an α-carbon atom, it is optically active [528]. L-alanine is used as a simple model of molecular dynamics in proteins [528,529] or as a biosignature for future extraterrestrial planetary exploration [530].

For SERS measurements, alanine was immobilized on gold platform by simple adsorption of 10^{-5} M aqueous solution. In order to perform a normal Raman spectrum, a measurement with 0.5 M alanine water solution was prepared.

According to experimental results found in the literature as well as in agreement with some calculations and modeling [528–530] I have made the following assumption about the attribution of normal Raman and SERS modes (Figure 12.10). Bands at 284, 534, 774, 852 and 1410 cm^{-1} are assigned to C-COO^{-} asymmetric stretching mode. Additionally 534, 852 and 1410 cm^{-1} are coupled with C-C and 284 cm^{-1} with CH_2 stretching modes. Very intensive bands observed at 1307 as well as 1361 and 1484 cm^{-1} are due to NH bending and CH_3 deformation, respectively. Other deformation modes of methyl group appear at 398, 923, 1464 and 1502 cm^{-1}. Bands at 398, 1464 and 1503 cm^{-1} are also attributed to CN and NH modes, while 1238 cm^{-1} is due to CH deformation mode. Amine group stretching vibrations can be assigned to 1115, 1149, 1502 and 1598 cm^{-1} [528–530].

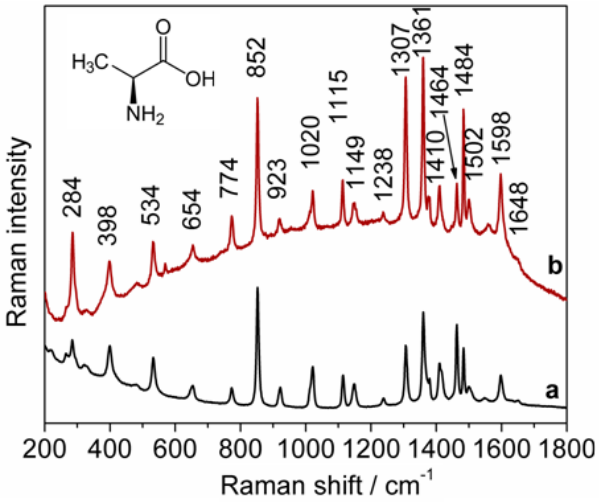

Figure 12.10. Normal Raman (a) and SERS (b) spectra of L-alanine; inset: schematic illustration of L-alanine.

12.2.2. Choline

Next investigated biomolecule is choline (inset Figure 12.11), a precursor for acetylocholine, a very important neurotransmitter [531]. Choline can be also found in a cell membrane as a part of phospholipids [532,533]. An inappropriate level of this compound in the body may mainly influence a proper functioning of neurological system and liver [531]. In contrast with alanine, which is produced in the body in a sufficient amount and does not need to be provided with diet, choline daily intake is well-defined and should be restricted [534].

For SERS measurements, choline was immobilized on gold platform by simple adsorption of 10^{-5} M aqueous solution. For reference spectrum, normal Raman experiment was recorded with 0.5 M choline water solution. Obtained results (Figure 12.11) are in agreement with previous reports [532,533,535,536]. The most intensive bands at 715 and 1445 cm^{-1} can be assigned to symmetric headgroup ($CN^{+}(CH_3)_3$) stretching mode and CH bending modes including CH_2 scissor and CH_3 deformation vibrations, respectively [536]. 863 cm^{-1} and 873 cm^{-1} modes are attributed to symmetric N-$(CH_3)_3$, while 951 cm^{-1} is due to asymmetric stretching vibrations of C-N bonds. Both 1133 and 1268 cm^{-1} correspond to weak CH_3 rocking vibrations, while 1043/1053 and 1334/1348 cm^{-1} are assigned to CH and C-C stretching modes [532,533,535].

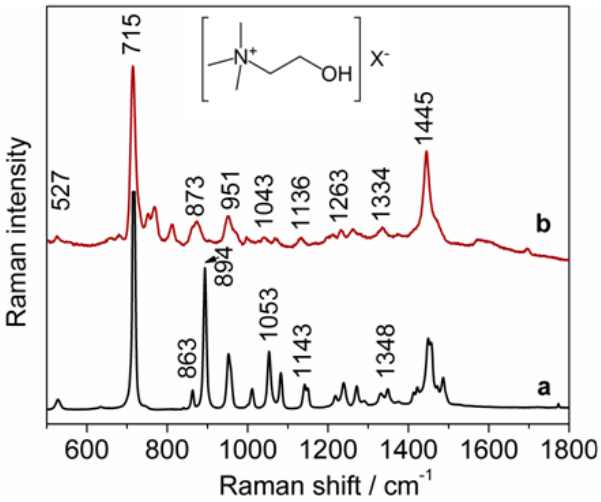

Figure 12.11. Normal Raman (a) and SERS (b) spectra of choline.

To conclude, stable and well-adhered gold nanoparticles with flower-like shapes obtained by electrodeposition at a three-phase junction are efficiently employed as a SERS platform with enhancement factor up to 10^7. For the future detection applications the homogeneity needs to be improved. However, it was already proved that such-prepared surfaces show promises for biosensing. It was also noted that multifarious particles provide much greater enhancement of Raman scattering than spherical gold nanoparticles.

13. Fluorescence microscopy

13.1. Introduction

In this chapter, fluorescence of the Fenna-Matthews-Olson (FMO) complex, deposited on various substrates, is introduced and described. First, the measurements performed separately in the presence of AuNPs electrodeposited at the three-phase junction (ITO|AuNPs) or a thin layer of reduced graphene oxide (rGO) are presented. Afterwards, the fluorescence of the FMO is performed on ITO|AuNPs covered with a thin layer of rGO. To the best of our knowledge, fluorescent properties of the FMO were not investigated before in the presence of metallic nanoparticles or graphene-based materials.

The FMO is a photosynthetic pigment-protein complex (PPC), which appears in green sulfur bacteria [537–542]. It is the first water soluble protein with chlorophyll, whose high-resolution crystal structure (resolution of 1.9 Å) was elucidated. The FMO consists of three monomers (Figure 13.1_A) and each of them contains seven/eight Bacteriochlorophyll-*a* (Bchl-*a*) molecules [537,540,542]. This complex belongs to the family of light-harvesting antenna proteins which extremely efficiently transfer the excitation energy from chlorosomes to reaction centers (> 99%) (Figure 13.1_B) [537,538]. Such a process is controlled by the scaffold and geometry of the protein. Since FMO is the simplest and well-explored PPC, information about its structure as well as absorption and fluorescence spectra may lead to understanding of the process of adjustment of the energy sites by the protein and photon conversion.

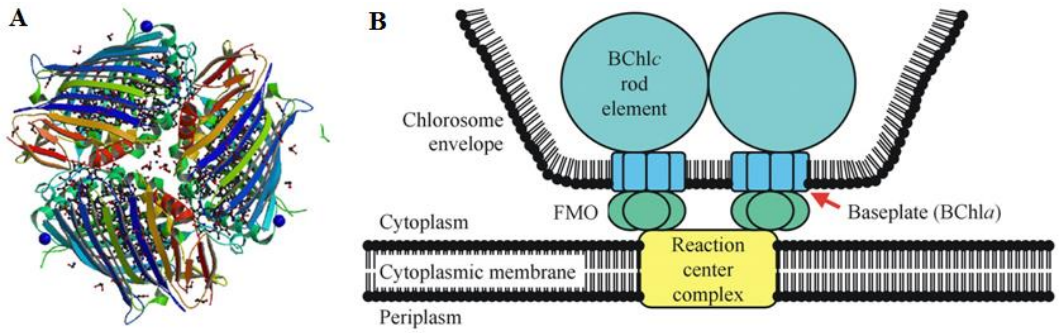

Figure 13.1. (A) The Fenna-Matthews-Olson protein from *Prosthecochloris aestuarii* and (B) the schematic representation of the location of the FMO protein in the photosynthetic apparatus of green sulfur bacteria according to the most recent models [537,538].

The characteristic fluorescence of gold nanoparticles depends on their morphology and the closest surrounding *e.g.* capping agents and matrices [54–65] (Chapter 1.3). It is also well-known that the fluorescence of investigated (bio)molecules is affected in the close proximity

of metallic nanoparticles by their strong electromagnetic field [53,66]. Depending on the distance between the probe and AuNPs the fluorescence may be quenched or enhanced. Recently, graphene and GO are also intensively explored as optical biosensors [212,236–246] (Chapter 4.3). Graphene-based materials are thoroughly studied as promising and more sensitive substitutes for metallic surfaces. This chapter is devoted to combined measurements of FMO fluorescence in the presence of both AuNPs and rGO.

13.2. Preparation protocol and SEM characterization

Gold nanoparticles were deposited at the ITO|aqueous electrolyte|gold precursor solution in toluene three phase junction using double-pulse chronoamperometry as described in Chapter 8. GO was reduced with hydrazine as described in Chapter 11. First, a thin film of rGO was deposited with a spin coater on a bare ITO. Namely, 10 μL of rGO in THF was drop casted on ITO surface and spin coated at the speed of 2000 rpm for 30 sec. This step was repeated twice to provide better coverage of ITO by rGO. SEM image shown in figure 13.2_A presents the boundary between bare ITO (bright grey) and ITO covered with rGO (dark grey). SEM image with a higher magnification is not shown, since the contrast is too low and both areas are not distinguishable anymore. Then, the same procedure was used to cover ITO|AuNPs with rGO. SEM images (Figure 13.2_B-D) show relatively high homogeneity of rGO film, however there are also areas that are not fully covered (Figure 13.2_B). This simple coating method requires a compromise between small thickness of rGO layer and homogenous coverage.

In the next step, FMO was diluted in 2% polyvinyl alcohol in 1:5 ratio. The droplet of 5 μL of this solution was deposited on the surface and pressed with a cover glass (for measurements with oil immersion objective using a wide-field microscope) or spin coated (for confocal microscope measurements).

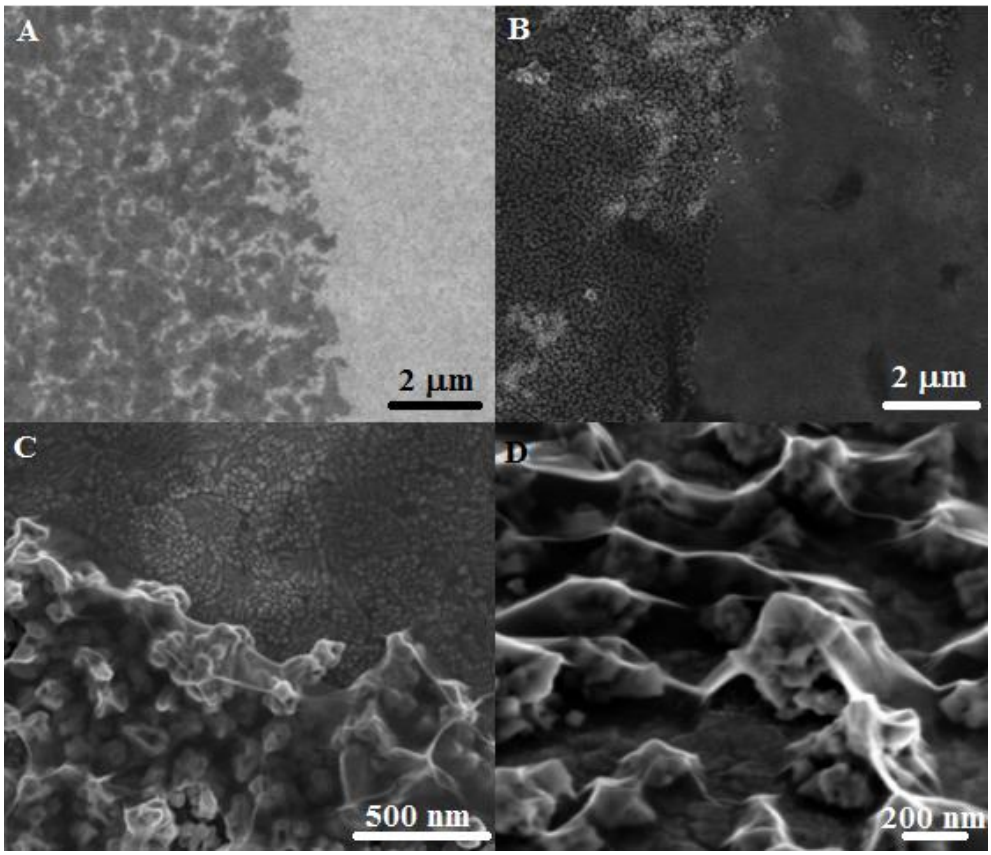

Figure 13.2. SEM images of (A) a bare ITO and (B-D) ITO|AuNPs coated with rGO.

13.3. Wide-field fluorescence microscopy

First measurements were carried out with a wide-field microscope. At first, areas with a visible boundary between a bare ITO and ITO covered with AuNPs were selected (Figure 13.3). Images of each area were recorded in transmission and emission modes. In figure 13.3, one can see two different areas of the same sample together with calculated profile lines for each image. Dark areas on images captured in transmission mode present ITO covered with AuNPs (Figure 13.3 A, E), while bright regions show a bare ITO electrode. In emission mode it is the opposite. In order to define a correlation between the images acquired in both transmission and fluorescence modes, Pearson's correlation coefficient was calculated. More precisely, for the intensity of either transmitted light and fluorescence light, anticorrelation is determined. For the first pair of images anticorrelation equals -0.826, for the second it is -0.615. These values show a good correlation between images recorded in both modes. Except for the differences, which result from the characteristics of the samples, anticorrelation might be disturbed by the slight shift of both images during quantitative analysis. Analogous experiments were carried out for the FMO deposited on ITO|AuNPs|rGO. In this case, dark

regions visible in images acquired in transmission mode (bright - in emission mode) represent ITO covered with both AuNPs and rGO, and bright areas in transmission mode (dark – in emission mode) represent ITO|rGO. Anticorrelation coefficients calculated for analysis performed on both cross lines equal to -0.649 and -0.865, respectively.

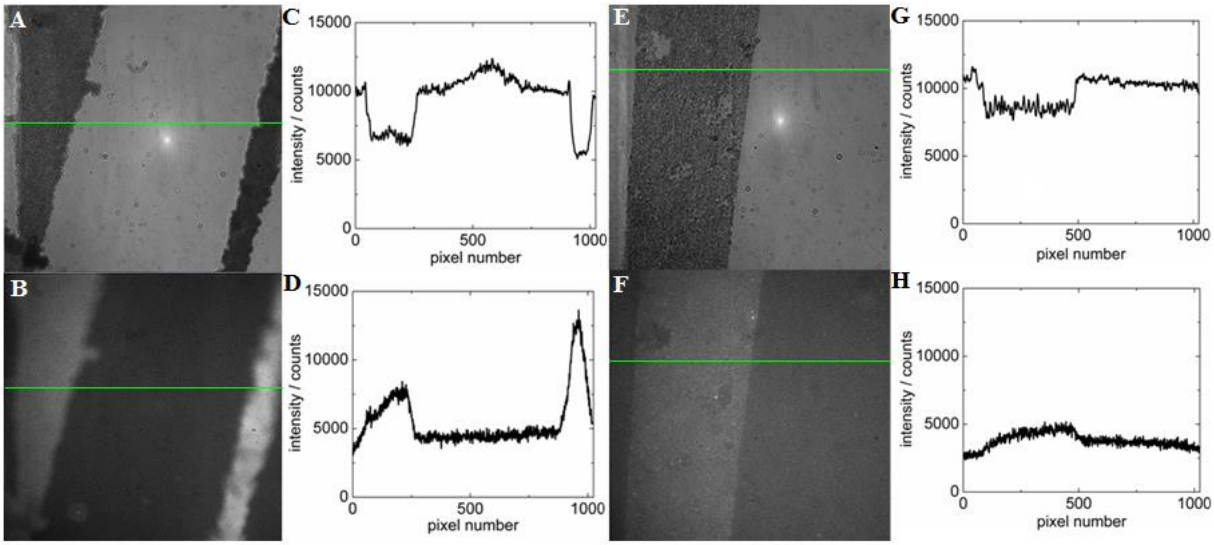

Figure 13.3. Optical images in (A, E) transmission and (B, F) emission modes recorded with a wide-field microscope for FMO deposited on ITO|AuNPs and corresponding (C, G, D, H), profile lines marked as green lines.

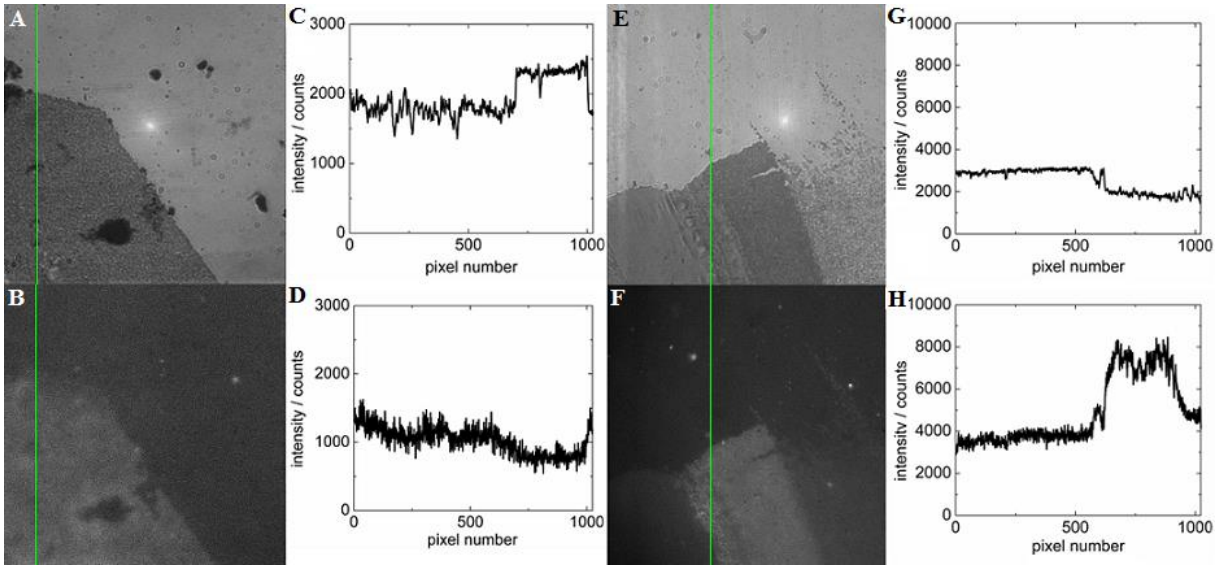

Figure 13.4. Optical images in (A, E) transmission and (B, F) emission modes recorded with a wide-field microscope for FMO deposited on ITO|AuNPrGO and corresponding (C, G and D, H) profile lines marked as green lines.

Images acquired with the wide-field microscope allowed to calculate enhancement factors (EF) of fluorescence intensity of the FMO at various substrates. At first, ITO electrode with AuNPs was investigated. Two circles (10 pixels in diameter) were marked, the first one on the area covered with AuNPs (dark region in transmission mode and corresponding bright area in emission mode) and the second one close to this place, however on bare ITO (bright region in transmission mode and corresponding dark area in emission mode). This step was repeated for hundred pairs of circles (Figure 13.5_A) and for each circle the average intensity per pixel was estimated. Fluorescence enhancement factor (EF) was calculated for AuNPs with respect to a bare ITO by dividing the average fluorescence intensity measured on ITO_AuNPs by the one measured on a bare ITO. Analogous analysis was performed for ITO covered with both AuNPs and rGO (Figure 13.5_B). In this case, the area covered with both materials was examined, and afterwards ITO covered only with rGO. The fluorescence EF was calculated for AuNPs|rGO with respect to rGO. In both cases average, minimum and maximum EFs were calculated (Table 13.1). Obtained values are higher for uncovered gold, compared to AuNPs|rGO, of *ca*. 15% in average. This is in agreement with intensity profile lines presented in Figures 13.3 and 13.4.

Calculated correlation lines and enhancement factors reveal that the fluorescence intensity of the FMO depends on the utilized substrate. In the investigated system, the distance of the FMO molecules from AuNPs and/or rGO is not fully controlled. For this reason, it cannot be considered in terms of distance-dependent properties. For AuNPs, recorded values are the highest but at the same time, intensity distribution is the largest. This shows that FMO fluorescence is influenced by multifarious nanoparticles which are not fully ordered and may create some aggregates, which most likely enhance fluorescence even stronger than single nanoparticles. This is different for surfaces covered with rGO. The presence of rGO results in quenching of fluorescence. For ITO covered only with rGO, fluorescence intensity is even lower than for a bare ITO. The presence of AuNPs covered with rGO, partially reduces the quenching effect. It was reported that graphene effectively quenches fluorescence of the fluorophore due to the charge transfer [543,544]. In these preliminary experiments this conclusion was also confirmed.

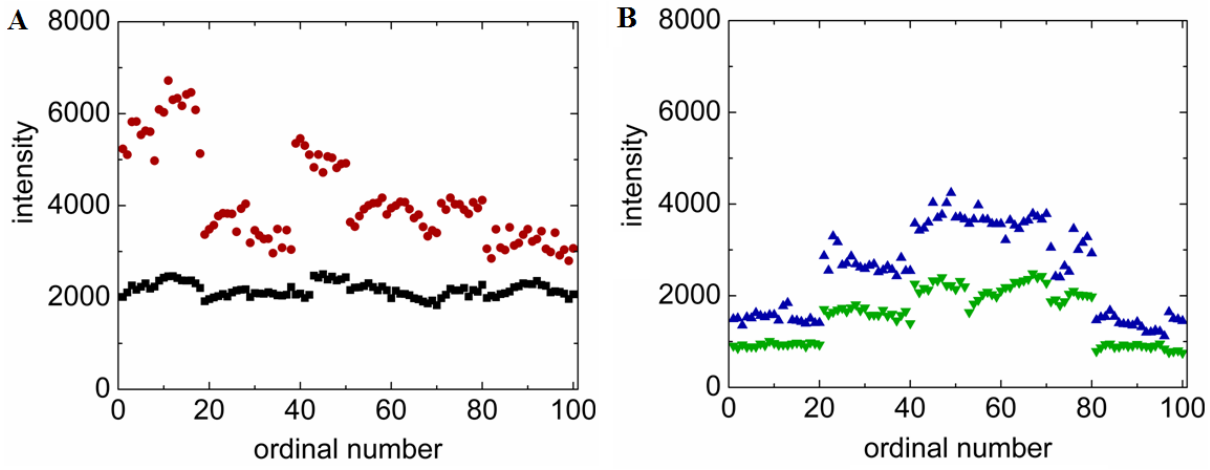

Figure 13.5. Comparison of average fluorescence intensity values calculated for (A) a bare ITO (■), ITO|AuNPs (●), (B) ITO|rGO (▼) and ITO|AuNPs|rGO (▲).

Table 13.1. Enhancement factors of fluorescence intensity of FMO for ITO electrode covered with AuNPs and rGO.

	average EF	EF_{min}	EF_{max}
ITO|AuNPs	1.91	1.36	2.73
ITO|AuNPs|rGO	1.64	1.24	2.18

13.4. Confocal microscopy

Fluorescence spectra of the FMO were measured using a confocal microscope (excitation at 590 nm). Ten spectra were recorded on different spots of each type of the sample (Figure 13.6). There are two main effects that need to be considered: shifts in fluorescence maximum wavelength and changes in the intensity. One can see that only for the FMO deposited on gold nanoparticles covered with rGO the shifts of a peak maximum are, except for one value, rather negligible (2 ± 2 nm). However, for the FMO deposited on other substrates, relatively large variations are visible.

There might be two main origins of these fluctuations. The first reason could concern inhomogeneous coverage with AuNPs. This problem is discussed in Chapters 8 and 12. It is shown that electrodeposited nanoparticles have limited sensitivity as a platform used in LSPR and SERS measurements due to heterogeneity. Nonetheless, they are still very promising and superior over spherical AuNPs or gold nanoislands. The second reason of intensity variations may have to do with the complexity of the FMO protein. As it is described in the introduction of this chapter, each monomer of FMO complex contains seven/eight Bchl-*a* molecules.

Calculation of the excited-state dynamics in FMO were used to discuss site energies and electronic coupling of seven/eight Bchl-*a* molecules [540,542]. Determined site energies of Bchl-*a* pigments in the FMO complex vary in the range between 780.2 and 824.4 nm depending on the Bchl-*a* molecule and measurement method [542]. These calculations were made separately for each pigment molecule in a monomer or a trimer. Here in this work, the entire complex is investigated at once. Maximum fluorescence intensity variations cannot be directly assigned to different energy sites. Nonetheless, deposited FMO complexes might be randomly oriented towards surface in various spots of one sample. For this reason recorded spectra might differ among each other and maximum fluorescence intensity deviations are observed. In order to confirm this statement, better control over complex arrangement is required.

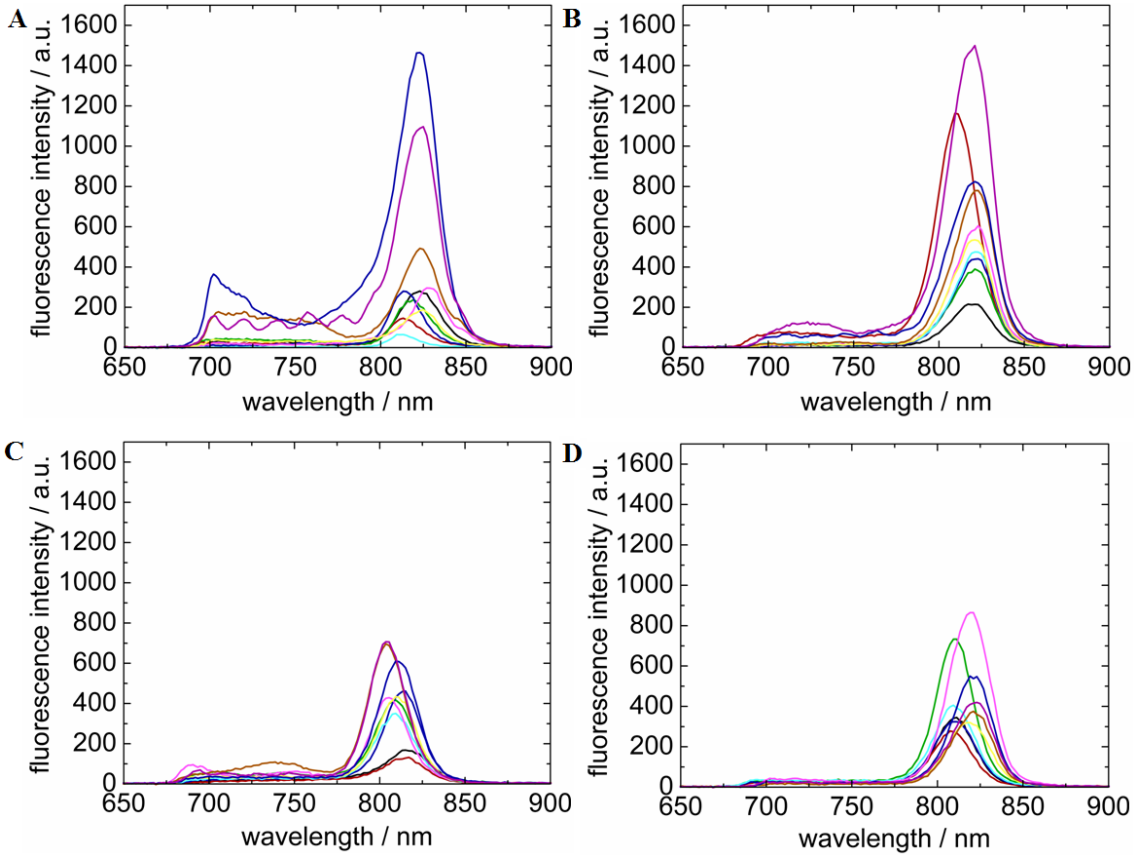

Figure 13.6. Fluorescence spectra of FMO measured on (A) ITO|AuNPs, (B) ITO|AuNPs|rGO, (C) ITO and (D) ITO|rGO, for ten different spots across one sample of each kind.

In order to understand the influence of a particular substrate upon the dynamics of the excited state in the FMO protein, fluorescence transients were measured at the same spots where fluorescence spectra were recorded. Average fluorescence transients presented in figure

13.7 were calculated by averaging curves obtained for measurements carried out in ten spots on each sample. The coefficient of determination R^2 equals to 0.99 ± 0.01. All curves show bi-exponential characteristics. It was reported before that the FMO pigment-protein excitation dynamics simulated with classical molecular dynamics method show a decay time described with mono-exponential function, in a subpicosecond range [540]. However, this was fitted separately for every pigment molecule and shows direct energy transfer for each pair of Bchl-*a* molecules in the FMO complex [540]. In this work, as it was mentioned before, the entire FMO complex is analyzed at once and fluorescence decay is attributed to the whole protein with all pigments. Bi-exponential characteristic presented here reveals the presence of two processes, relatively short one at a time ranging between 80 and 100 ps, and the second one longer (0.9 – 1.2 ns) by approximately one order of magnitude. At this stage of experiments it cannot be clearly identified what kind of processes these are. In was reported that bi-exponential characteristic is attributed to shorter- and longer-lifetime components, which comes from adsorbed and free/unadsorbed chlorophyll species [545]. It was also shown that bi-exponential behavior might be assigned to chlorophyll species located very close to the surface, which are affected by the substrate (τ_1) and species which are in a focal plane of a laser spot but too far to be influenced by the substrate (τ_2) [546]. In table 13.2 there are values of both characteristic times τ_1 and τ_2 calculated for FMO deposited on all kinds of surfaces. One can see that for a bare ITO and ITO covered with rGO, both values are comparable and characterized with the longest τ_2 (> 1.15 ns). For AuNPs both values are lower, and additionally the first process is the shortest among others. Interestingly, for AuNPs covered with rGO the first component of a decay time is the longest and the second is the shortest among all recorded curves. Although these results cannot be simply explained, they show that not only fluorescence intensity but also FMO complex lifetime is influenced by both materials. However, when they are both present on the surface, characteristic times change slightly, but not in a simple manner, when compared to AuNPs and rGO alone. This might be the result of AuNPs and rGO interactions in terms of charge transfer or other non-radiative processes. The reason for bi-exponential characteristics of fluorescence transients of the FMO in the presence of all kinds of substrates but slight differences in the value of decay times might have various origins. First of all, this may result from the radiative recombination properties of the FMO which do not change significantly on different substrates. Another possibility are characteristic times which are too short for precise measurements, especially τ_1 which is close to the temporal resolution of the setup. For these reasons, the influence of

different materials on fluorescence transients of the FMO cannot be clearly defined and further studies are necessary.

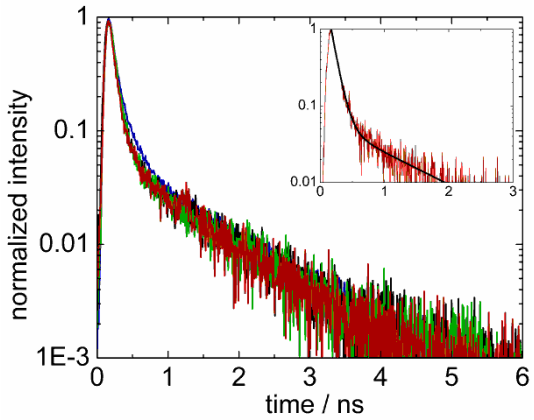

Figure 13.7. Fluorescence decay time obtained for FMO deposited on a bare ITO (black —), ITO|AuNPs (red —), (B) ITO|rGO (green —) and ITO|AuNPs|rGO (blue —).

Table 13.2. Average characteristic times τ_1 and τ_2, calculated from fitted bi-exponential function.

characteristic time [ns]	ITO	ITO|AuNPs	ITO|rGO	ITO|AuNPs|rGO
τ_1	0.095	0.084	0.092	0.099
τ_2	1.161	1.023	1.148	0.928

To summarize this chapter, it was shown that electrodeposited multifarious AuNPs and/or rGO can be used as platforms for optical applications. They are both well-known for their distance-dependent quenching/enhancement properties towards fluorescent (bio)molecules. Preliminary measurements presented in this chapter show that their influence on the FMO pigment-protein is complex and not easily explainable. It can be concluded that the highest enhancement of fluorescence intensity was observed on gold. The presence of graphene caused a decrease of the fluorescence intensity, probably due to more complicated non-radiative effects. For the future experiments, a better control over FMO distance from the surface would be required. Additionally, more homogeneous deposit of AuNPs and rGO might be of importance. It would be also very interesting to compare such prepared rGO thin film with a pristine CVD graphene. Described substrates and their influence on fluorescence properties of pigment-protein complexes might be more precisely investigated with another photosynthetic protein. In this case, especially longer decay times and fluorescence spectrum

of the protein beyond the range of the fluorescence of an ITO are of great importance. Nonetheless, obtained results are very promising and further researches may result in valuable information about photosynthetic complexes.

Summary and conclusions

This thesis is devoted to deposition, modification and application of two nanomaterials: gold nanoparticles and graphene-based structures.

It was demonstrated that gold nanoparticles can be successfully electrodeposited at the electrode|aqueous electrolyte|toluene solution of gold precursor three-phase junction. In this way, it is possible to obtain stable, well-adhered and multifarious AuNPs. This setup can be considered as an alternative to a single phase system which has several drawbacks, like deposition of less stable and spherical gold nanoparticles. The average diameter (~150 nm) and height (~105 nm) of flower-like AuNPs were determined on the basis of SEM and AFM images. Electrochemical and microscopic measurements indicated that the shape and size of the entire deposit are controlled by the presence of a three phase junction as well as the emulsion formation. It was also concluded that the droplets of the emulsion determines the size of nanoparticles, smaller than *ca.* 200 nm. Results obtained by the cellular automaton model indicated that their growth is controlled partially by the aggregation and partially by the reaction.

AuNPs obtained at the three phase junction exhibit catalytic activity towards glucose oxidation and dioxygen reduction, comparable with other reported electrodes. Additionally, when surfaces were further modified with bilirubin oxidase, bioelectrocatalysis of dioxygen reduction was observed. ITO surfaces were further extended with ITO nanoparticulate (ITO_{NP}) film of different thicknesses. This step allowed to develop electrochemically active porous structure for gold nanoparticles electrodeposition. The presence of gold at the ITO_{NP} film surface as well as inside this 3D scaffold was confirmed with SEM, STEM-HAADF combination imaging and XEDS elemental mapping. All surfaces were investigated in terms of catalytic activity towards glucose oxidation and dioxygen reduction. The best results were obtained for surfaces modified with both materials, the thickest ITO_{NP} film further modified with gold nanoparticles.

Multifarious AuNPs were also applied as SERS platforms. They exhibit enhancement of Raman scattering with selected dyes and biomolecules. Calculated enhancement factor is in the range 10^6 – 10^7, that is comparable with other electrochemically deposited gold nanostructures. Reproducibility and repeatability of SERS results were confirmed with the value of the calculated standard deviation for spectra collected from a hundred spots on one sample (<12 %) and for four different samples (<15 %). Nonetheless, it appeared that for biosensing applications the homogeneity of the coverage with AuNPs needs to be improved.

A new approach of a one-pot simultaneous reduction and functionalization of GO with selected aromatic molecules was presented. The efficiency of a carbon lattice restoration using dopamine, tetrathiafulvalene (TTF) and their derivatives is confirmed with CV and XPS analysis. Additionally, the activity of these composites was studied with "click" and "thiol-yne" reactions. Obtained results show that all composites are suitable for preparing biosensing platforms at will. Although both kinds of materials, rGO with dopamine or tetrathiafulvalene, are stable, the latter one (TTF) can be released on demand from the composite, which might be important in reusable surfaces.

It was also shown that electrodeposited multifarious AuNPs and/or rGO can be used as platforms for fluorescence microscopy. They are both well-known for their distance-dependent quenching/enhancement properties towards fluorescent (bio)molecules. Preliminary measurements show that their influence on the FMO pigment-protein is complex and not easily explainable. It can be concluded, that the highest enhancement of fluorescence intensity is obtained on gold nanoparticles. The presence of graphene caused a decrease of this process, probably due to more complicated non-radiative effects. For the future experiments, a better control over FMO distance from the surface would be required. Additionally more homogeneous deposit of AuNPs and rGO might be of great importance. However, obtained results are very promising and further researches may result in valuable information about photosynthetic complexes.

Electrochemical method presented in this thesis allows to obtain multifarious and stable gold nanoparticles. Protocol used for reduction of graphene oxide can be easily applied for preparing various graphene-based composites. Properties of both materials make them very promising in (bio)sensing and it might be interesting to explore them precisely in the future.

References

(1) Higby, G. J. *Gold Bulletin* **1982**, *15*, 130–140.
(2) Maclagan, N. F. *British Journal of Experimental Pathology* **1946**, *27*, 369–377.
(3) Faraday, M. *Philosophical Transactions of the Royal Society of London* **1857**, *147*, 145–181.
(4) Turkevich, J.; Stevenson, P. C.; Hillier, J. *Discussions of the Faraday Society* **1951**, 55–75.
(5) Frens, G. *Kolloid-Zeitschrift & Zeitschrift fur Polymere* **1972**, *250*, 736–741.
(6) Frens, G. *Nature Physical Science* **1973**, *241*, 20–22.
(7) Brust, M.; Walker, M.; Bethell, D.; Schiffrin, D. J.; Whyman, R. *Chemical Communications* **1994**, 801–802.
(8) Cheng, Y.; Schiffrin, D. J. *Journal of the Chemical Society, Faraday Transactions* **1996**, *92*, 3865–3871.
(9) Foss, C. A.; Hornyak, G. L.; Stockert, J. A.; Martin, C. R. *Journal of Physical Chemistry* **1994**, *98*, 2963–2971.
(10) Hulteen, J. C.; Patrissi, C. J.; Miner, D. L.; Crosthwait, E. R.; Oberhauser, E. B.; Martin, C. R. *Journal of Physical Chemistry B* **1997**, *101*, 7727–7731.
(11) Zhao, P.; Li, N.; Astruc, D. *Coordination Chemistry Reviews* **2013**, *257*, 638–665.
(12) Calandra, P.; Calogero, G.; Sinopoli, A.; Gucciardi, P. G. *International Journal of Photoenergy* **2010**, *2010*, 1–15.
(13) Selvakannan, P. R.; Mandal, S.; Pasricha, R.; Adyanthaya, S. D.; Sastry, M. *Chemical Communications* **2002**, 1334–1335.
(14) Knake, R.; Fahmi, A. W.; Tofail, S. A. M.; Clohessy, J.; Mihov, M.; Cunnane, V. J. *Langmuir* **2005**, *21*, 1001–1008.
(15) Lepková, K.; Clohessy, J.; Cunnane, V. J. *Journal of Physics: Condensed Matter* **2007**, *19*, 375106.
(16) Lepková, K.; Clohessy, J.; Cunnane, V. J. *Electrochimica Acta* **2008**, *53*, 6273–6277.
(17) Campbell, A. I.; Dryfe, R. A. W.; Haw, M. D. *Analytical Sciences: The International Journal of the Japan Society for Analytical Chemistry* **2009**, *25*, 307–310.
(18) Luo, K.; Schroeder, S. L. M.; Dryfe, R. A. W. *Chemistry of Materials* **2009**, *21*, 4172–4183.
(19) Swami, A.; Kumar, A.; D'Costa, M.; Pasricha, R.; Sastry, M. *Journal of Materials Chemistry* **2004**, *14*, 2696–2702.
(20) Rao, C. N. R.; Kalyanikutty, K. P. *Accounts of Chemical Research* **2008**, *41*, 489–499.
(21) Martin, C. R. *Science* **1994**, *266*, 1961–1966.
(22) Horikoshi, T.; Itoh, M.; Kurihara, M.; Kubo, K.; Nishihara, H. *Journal of Electroanalytical Chemistry* **1999**, *473*, 113–116.
(23) Luo, X.-L.; Xu, J.-J.; Du, Y.; Chen, H.-Y. *Analytical Biochemistry* **2004**, *334*, 284–289.
(24) Celebanska, A.; Lesniewski, A.; Paszewski, M.; Jonsson-Niedziolka, M.; Niedziolka-Jonsson, J.; Opallo, M. *Electrochemistry Communications* **2011**, *13*, 1170–1173.
(25) Dai, X.; Compton, R. G. *Analytical Sciences: The International Journal of the Japan Society for Analytical Chemistry* **2006**, *22*, 567–570.
(26) Ma, Y.; Di, J.; Yan, X.; Zhao, M.; Lu, Z.; Tu, Y. *Biosensors & Bioelectronics* **2009**, *24*, 1480–1483.
(27) Sakai, N.; Fujiwara, Y.; Arai, M.; Yu, K.; Tatsuma, T. *Journal of Electroanalytical Chemistry* **2009**, *628*, 7–15.
(28) Sheridan, E.; Hjelm, J.; Forster, R. J. *Journal of Electroanalytical Chemistry* **2007**, *608*, 1–7.
(29) Komsiyska, L.; Staikov, G. *Electrochimica Acta* **2008**, *54*, 168–172.
(30) Oyama, T.; Okajima, T.; Ohsaka, T. *Journal of The Electrochemical Society* **2007**, *154*, D322.
(31) Hu, M.; Chen, J.; Li, Z.-Y.; Au, L.; Hartland, G. V; Li, X.; Marquez, M.; Xia, Y. *Chemical Society Reviews* **2006**, *35*, 1084–1094.
(32) Ghosh, S. K.; Pal, T. *Chemical Reviews* **2007**, *107*, 4797–4862.
(33) Maalouli, N.; Barras, A.; Siriwardena, A.; Bouazaoui, M.; Boukherroub, R.; Szunerits, S. *The Analyst* **2013**, *138*, 805–812.
(34) Touahir, L.; Niedziółka-Jönsson, J.; Galopin, E.; Boukherroub, R.; Gouget-Laemmel, A. C.; Solomon, I.; Petukhov, M.; Chazalviel, J.-N.; Ozanam, F.; Szunerits, S. *Langmuir* **2010**, *26*, 6058–6065.
(35) Willets, K. A.; Van Duyne, R. P. *Annual Review of Physical Chemistry* **2007**, *58*, 267–297.
(36) Petryayeva, E.; Krull, U. J. *Analytica Chimica Acta* **2011**, *706*, 8–24.
(37) Szunerits, S.; Boukherroub, R. *Chemical Communications* **2012**, *48*, 8999–9010.
(38) Barka-Bouaifel, F.; Niedziółka-Jönsson, J.; Castel, X.; Saison, O.; Akjouj, A.; Pennec, Y.; Djafari-Rouhani, B.; Woisel, P.; Lyskawa, J.; Sambe, L.; Cooke, G.; Bezzi, N.; Boukherroub, R.; Szunerits, S. *Journal of Materials Chemistry* **2011**, *21*, 3006–3013.
(39) Spadavecchia, J.; Barras, A.; Lyskawa, J.; Woisel, P.; Laure, W.; Pradier, C.; Boukherroub, R.; Szunerits, S. *Analytical Chemistry* **2013**, *85*, 3288–3296.

(40) Niedziółka-Jönsson, J.; Barka, F.; Castel, X.; Pisarek, M.; Bezzi, N.; Boukherroub, R.; Szunerits, S. *Langmuir* **2010**, *26*, 4266–4273.
(41) Mie, G. *Annalen der Physik* **1908**.
(42) Kelly, K. L.; Coronado, E.; Zhao, L. L.; Schatz, G. C. *Journal of Physical Chemistry B* **2003**, *107*, 668–677.
(43) Huang, X.; El-Sayed, M. A. *Journal of Advanced Research* **2010**, *1*, 13–28.
(44) Daniel, M.-C.; Astruc, D. *Chemical Reviews* **2004**, *104*, 293–346.
(45) Loo, C.; Lin, A.; Hirsch, L.; Lee, M.-H.; Barton, J.; Halas, N.; West, J.; Drezek, R. *Technology in Cancer Research & Treatment* **2004**, *3*, 33–40.
(46) Tam, F.; Moran, C.; Halas, N. *Journal of Physical Chemistry B* **2004**, *108*, 17290–17294.
(47) Sharma, V.; Park, K.; Srinivasarao, M. *Materials Science and Engineering: R* **2009**, *65*, 1–38.
(48) Gans, R. *Annalen der Physik* **1912**, *342*, 881–900.
(49) Purcell, E. M.; Pennypacker, C. R. *The Astrophysical Journal* **1973**, *186*, 705–714.
(50) Yurkin, M. A.; Hoekstra, A. G. *Journal of Quantitative Spectroscopy and Radiative Transfer* **2007**, *106*, 558–589.
(51) Mooradian, A. *Physical Review Letters* **1969**, *22*, 5–7.
(52) Huang, X.; Jain, P. K.; El-Sayed, I. H.; El-Sayed, M. A. *Nanomedicine* **2007**, *2*, 681–693.
(53) Eustis, S.; El-Sayed, M. A. *Chemical Society Reviews* **2006**, *35*, 209–217.
(54) Goldys, E. M.; Sobhan, M. A. *Advanced Functional Materials* **2012**, *22*, 1906–1913.
(55) He, H.; Xie, C.; Ren, J. *Analytical Chemistry* **2008**, *80*, 5951–5957.
(56) Abdelhalim, M. A. K.; M. Mady, M. *Journal of Nanomedicine & Nanotechnology* **2012**, *03*.
(57) Huang, C.-C.; Yang, Z.; Lee, K.-H.; Chang, H.-T. *Angewandte Chemie International Edition* **2007**, *46*, 6824–6828.
(58) Zheng, J.; Zhang, C.; Dickson, R. *Physical Review Letters* **2004**, *93*, 077402.
(59) Lin, C.-A. J.; Yang, T.-Y.; Lee, C.-H.; Huang, S. H.; Sperling, R. A.; Zanella, M.; Li, J. K.; Shen, J.-L.; Wang, H.-H.; Yeh, H.-I.; Parak, W. J.; Chang, W. H. *ACS Nano* **2009**, *3*, 395–401.
(60) Wang, G.; Huang, T.; Murray, R. W.; Menard, L.; Nuzzo, R. G. *Journal of the American Chemical Society* **2005**, *127*, 812–813.
(61) Huang, T.; Murray, R. W. *Journal of Physical Chemistry B* **2001**, *105*, 12498–12502.
(62) Link, S.; Beeby, A.; FitzGerald, S.; El-Sayed, M. A.; Schaaff, T. G.; Whetten, R. L. *Journal of Physical Chemistry B* **2002**, *106*, 3410–3415.
(63) Eustis, S.; El-Sayed, M. *Journal of Physical Chemistry B* **2005**, *109*, 16350–16356.
(64) Mohamed, M. B.; Volkov, V.; Link, S.; El-sayed, M. A. *Chemical Physics Letters* **2000**, *317*, 517–523.
(65) Li, C.-Z.; Male, K. B.; Hrapovic, S.; Luong, J. H. T. *Chemical Communications* **2005**, 3924–3926.
(66) Lakowicz, J. R. *Principles of Fluorescence Spectroscopy*; Third Edit.; Springer, 2006; pp. 278–317, 841–859.
(67) Haruta, M.; Kobayashi, T.; Sano, H.; Yamada, N. *Chemistry Letters* **1987**, *16*, 405–408.
(68) Haruta, M.; Yamada, N.; Kobayashi, T.; Iijima, S. *Journal of Catalysis* **1989**, *115*, 301–309.
(69) Hutchings, G. J. *Journal of Catalysis* **1985**, *96*, 292–295.
(70) Bond, G. C.; Sermon, P. A. *Gold Bulletin* **1973**, *6*, 102–105.
(71) Haruta, M. *Catalysis Today* **1997**, *36*, 153–166.
(72) Ma, Z.; Dai, S. *Nano Research* **2010**, *4*, 3–32.
(73) Bond, G. C.; Thompson, D. T. *Catalysis Reviews: Science and Engineering* **1999**, *41*, 319–388.
(74) Meyer, R.; Lemire, C. *Gold Bulletin* **2004**, *37*, 72–124.
(75) Chen, M.; Goodman, D. W. *Chemical Society Reviews* **2008**, *37*, 1860–1870.
(76) Gong, J. *Chemical Reviews* **2012**, *112*, 2987–3054.
(77) Hashmi, A. S. K.; Hutchings, G. J. *Angewandte Chemie International Edition* **2006**, *45*, 7896–7936.
(78) Zaera, F. *Chemical Society Reviews* **2012**, *2*, 2746–2762.
(79) Hashmi, A. S. K. *Gold Bulletin* **2004**, *37*, 51–65.
(80) Hutchings, G. J. *Catalysis Today* **2005**, *100*, 55–61.
(81) Corma, A.; Garcia, H. *Chemical Society Reviews* **2008**, *37*, 2096–2126.
(82) Bharathi, S.; Nogami, M. *The Analyst* **2001**, *126*, 1919–1922.
(83) Hutchings, G. J.; Brust, M.; Schmidbaur, H. *Chemical Society Reviews* **2008**, *37*, 1759–1765.
(84) Murata, K.; Kajiya, K.; Nakamura, N.; Ohno, H. *Energy & Environmental Science* **2009**, *2*, 1280–1285.
(85) Gutiérrez-Sánchez, C.; Pita, M.; Vaz-Domínguez, C.; Shleev, S.; De Lacey, A. L. *Journal of the American Chemical Society* **2012**, *134*, 17212–17220.
(86) Jia, J.; Wang, B.; Wu, A.; Cheng, G.; Li, Z.; Dong, S. *Analytical Chemistry* **2002**, *74*, 2217–2223.
(87) Zhou, M.; Dong, S. *Accounts of Chemical Research* **2011**, *44*, 1232–1243.
(88) Coquet, R.; Howard, K. L.; Willock, D. J. *Chemical Society Reviews* **2008**, *37*, 2046–2076.
(89) Saha, K.; Agasti, S. S.; Kim, C.; Li, X.; Rotello, V. M. *Chemical Reviews* **2012**, *112*, 2739–2779.

(90) Jones, M. R.; Macfarlane, R. J.; Lee, B.; Zhang, J.; Young, K. L.; Senesi, A. J.; Mirkin, C. A. *Nature Materials* **2010**, *9*, 913–917.
(91) Gronbeck, H.; Curioni, A.; Andreoni, W. *Journal of the American Chemical Society* **2000**, *122*, 3839–3842.
(92) Radhakumary, C.; Sreenivasan, K. *Analytical Chemistry* **2011**, *83*, 2829–2833.
(93) Boisselier, E.; Astruc, D. *Chemical Society Reviews* **2009**, *38*, 1759–1782.
(94) Yeh, Y.-C.; Creran, B.; Rotello, V. M. *Nanoscale* **2012**, *4*, 1871–1880.
(95) Mieszawska, A. J.; Mulder, W. J. M.; Fayad, Z. A.; Cormode, D. P. *Molecular Pharmaceutics* **2013**, *10*, 831–847.
(96) Murphy, C. J.; Gole, A. M.; Stone, J. W.; Sisco, P. N.; Alkilany, A. M.; Goldsmith, E. C.; Baxter, S. C. *Accounts of Chemical Research* **2008**, *41*, 1721–1730.
(97) Dykman, L.; Khlebtsov, N. *Chemical Society Reviews* **2012**, *41*, 2256–2282.
(98) Sperling, R. A.; Gil, P. R.; Zhang, F.; Zanella, M.; Parak, W. J. *Chemical Society Reviews* **2008**, *37*, 1896–1908.
(99) Leuvering, J. H. W.; Thal, P. J. H. M.; Waart, M. V. D.; Schuurs, A. H. W. M. *Fresenius' Zeitschrift fur Analytische Chemie* **1980**, *301*, 132.
(100) Mirkin, C. A.; Letsinger, R. L.; Mucic, R. C.; Storhoff, J. J. *Letters to Nature* **1996**, *382*, 607–609.
(101) Shiigi, H.; Tokonami, S.; Yakabe, H.; Nagaoka, T. *Journal of the American Chemical Society* **2005**, *127*, 3280–3281.
(102) Wilson, R. *Chemical Society Reviews* **2008**, *37*, 2028–2045.
(103) Sönnichsen, C.; Reinhard, B. M.; Liphardt, J.; Alivisatos, A. P. *Nature Biotechnology* **2005**, *23*, 741–745.
(104) Sugunan, A.; Thanachayanont, C.; Dutta, J.; Hilborn, J. G. *Science and Technology of Advanced Materials* **2005**, *6*, 335–340.
(105) Lee, S.; Cha, E.-J.; Park, K.; Lee, S.-Y.; Hong, J.-K.; Sun, I.-C.; Kim, S. Y.; Choi, K.; Kwon, I. C.; Kim, K.; Ahn, C.-H. *Angewandte Chemie International Edition* **2008**, *47*, 2804–2807.
(106) Wang, X.; Guo, X. *Analyst* **2009**, *134*, 1348–1354.
(107) Liu, J.; Lee, J. H.; Lu, Y. *Analytical Chemistry* **2007**, *79*, 4120–4125.
(108) Sharma, B.; Frontiera, R. R.; Henry, A.-I.; Ringe, E.; Van Duyne, R. P. *Materials Today* **2012**, *15*, 16–25.
(109) Etchegoin, P. G.; Meyer, M.; Blackie, E.; Ru, E. C. Le *Analytical Chemistry* **2007**, *79*, 8411–8415.
(110) El-Ansary, A.; Faddah, L. M. *Nanotechnology, Science and Applications* **2010**, *3*, 65–76.
(111) Drescher, D.; Kneipp, J. *Chemical Society Reviews* **2012**, *41*, 5780–5799.
(112) Hudson, S. D.; Chumanov, G. *Analytical and Bioanalytical Chemistry* **2009**, *394*, 679–686.
(113) Guo, S.; Wang, E. *Analytica Chimica Acta* **2007**, *598*, 181–192.
(114) Castañeda, M. T.; Alegret, S.; Merkoçi, a. *Electroanalysis* **2007**, *19*, 743–753.
(115) Emerich, D. F.; Thanos, C. G. *Biomolecular Engineering* **2006**, *23*, 171–184.
(116) Chou, L. Y. T.; Ming, K.; Chan, W. C. W. *Chemical Society Reviews* **2011**, *40*, 233–245.
(117) Kingsley, J. D.; Dou, H.; Morehead, J.; Rabinow, B.; Gendelman, H. E.; Destache, C. J. *Journal of Neuroimmune Pharmacology* **2006**, *1*, 340–350.
(118) Reymond, F.; Fermın, D.; Lee, H. J.; Girault, H. H. *Electrochimica Acta* **2000**, *45*, 2647–2662.
(119) Scholz, F. *Annual Reports Section "C" (Physical Chemistry)* **2006**, *102*, 43–70.
(120) Olaya, A. J.; Ge, P.; Girault, H. H. *Electrochemistry Communications* **2012**, *19*, 101–104.
(121) Sinha, A.; Mollah, A. K.; Hardt, S.; Ganguly, R. *Soft Matter* **2013**, *9*, 5438–5447.
(122) Sefer, B.; Gulaboski, R.; Mir, V. *Journal of Solid State Electrochemistry* **2012**, *16*, 2373–2381.
(123) Li, X.; Yao, K.; Lu, W.; Wang, J. *CrystEngComm* **2013**, *15*, 1289–1292.
(124) Shi, C.; Anson, F. C. *Analytical Chemistry* **1998**, *70*, 3114–3118.
(125) Adamiak, W.; Opallo, M. *Journal of Electroanalytical Chemistry* **2010**, *643*, 82–88.
(126) Komorsky-Lovric, S.; Riedl, K.; Gulaboski, R.; Mirceski, V.; Scholz, F. *Langmuir* **2002**, *18*, 8000–8005.
(127) Bouchard, G.; Galland, A.; Carrupt, P.-A.; Gulaboski, R.; Mirceski, V.; Scholz, F.; Girault, H. H. *Physical Chemistry Chemical Physics* **2003**, *5*, 3748–3751.
(128) Mirceski, V.; Gulaboski, R.; Scholz, F. *Electrochemistry Communications* **2002**, *4*, 814–819.
(129) Gulaboski, R.; Scholz, F. *Journal of Physical Chemistry B* **2003**, *107*, 5650–5657.
(130) Davies, T. J.; Garner, A. C.; Davies, S. G.; Compton, R. G. *Journal of Electroanalytical Chemistry* **2004**, *570*, 171–185.
(131) Wadhawan, J. D.; Wain, A. J.; Compton, R. G. *A European Journal of Chemical Physics and Physical Chemistry* **2003**, *4*, 1211–1215.
(132) Marken, F.; Blythe, A.; Compton, R. G.; Bull, S. D.; Davies, S. G.; Road, S. P. *Chemical Communications* **1999**, 1823–1824.
(133) Aoki, K.; Tasakorn, P.; Chen, J. *Journal of Electroanalytical Chemistry* **2003**, *542*, 51–60.

(134) Scholz, F.; Komorsky-Lovric, S.; Lovric, M. *Electrochemistry Communications* **2000**, *2*, 112–118.
(135) Davies, T. J.; Wilkins, S. J.; Compton, R. G. *Journal of Electroanalytical Chemistry* **2006**, *586*, 260–275.
(136) Marken, F.; Webster, R. D.; Bull, S. D.; Davies, S. G. *Journal of Electroanalytical Chemistry* **1997**, *437*, 209–218.
(137) Lovric, M. *Electrochemistry Communications* **1999**, *1*, 207–212.
(138) Wadhawan, J. D.; Evans, R. G.; Banks, C. E.; Wilkins, S. J.; France, R. R.; Oldham, N. J.; Fairbanks, A. J.; Wood, B.; Walton, D. J. *Journal of Physical Chemistry B* **2002**, *106*, 9619–9632.
(139) Rayner, D.; Fietkau, N.; Streeter, I.; Marken, F.; Buckley, B. R.; Page, P. C. B.; Campo, J.; Mas, R.; Mun, F. X.; Compton, R. G. *Journal of Physical Chemistry C* **2007**, *111*, 9992–10002.
(140) Gergely, A.; Inzelt, G. *Electrochemistry Communications* **2001**, *3*, 753–757.
(141) Scholz, F.; Gulaboski, R. *A European Journal of Chemical Physics and Physical Chemistry* **2005**, *6*, 16–28.
(142) Bak, E.; Donten, M.; Stojek, Z. *Electrochemistry Communications* **2005**, *7*, 483–489.
(143) Bak, E.; Donten, M. L.; Donten, M.; Stojek, Z. *Electrochemistry Communications* **2005**, *7*, 1098–1104.
(144) Bak, E.; Donten, M.; Stojek, Z. *Journal of Electroanalytical Chemistry* **2007**, *600*, 45–53.
(145) Niedziolka, J.; Opallo, M. *Electrochemistry Communications* **2008**, *10*, 1445–1447.
(146) Niedziolka-Jonsson, J.; Jonsson-Niedziolka, M.; Nogala, W.; Palys, B. *Electrochimica Acta* **2011**, *56*, 3311–3316.
(147) MacDonald, S. M.; Watkins, J. D.; Gu, Y.; Yunus, K.; Fisher, A. C.; Shul, G.; Opallo, M.; Marken, F. *Electrochemistry Communications* **2007**, *9*, 2105–2110.
(148) Watkins, J. D.; MacDonald, S. M.; Fordred, P. S.; Bull, S. D.; Gu, Y.; Yunus, K.; Fisher, A. C.; Bulman-Page, P. C.; Marken, F. *Electrochimica Acta* **2009**, *54*, 6908–6912.
(149) MacDonald, S. M.; Watkins, J. D.; Bull, S. D.; Davies, I. R.; Gu, Y.; Yunus, K.; Fisher, A. C.; Page, P. C. B.; Chan, Y.; Elliott, C.; Marken, F. *Journal of Physical Organic Chemistry* **2009**, *22*, 52–58.
(150) Saczek-Maj, M.; Opallo, M. *Electroanalysis* **2002**, *14*, 1060–1066.
(151) Opallo, M.; Saczek-Maj, M. *Electrochemistry Communications* **2001**, *3*, 306–311.
(152) Geim, A.; Novoselov, K. S. *Nature Materials* **2007**, *6*, 183–191.
(153) Novoselov, K. S.; Geim, A.; Morozov, S. V.; Jiang, D.; Zhang, Y.; Dubonos, S. V.; Grigorieva, I. V.; Firsov, A. A. *Science* **2004**, *306*, 666–669.
(154) Wallace, P. R. *Physical Review* **1947**, *71*, 622–634.
(155) Semenoff, G. W. *Physical Review Letters* **1984**, *55*, 2449–2452.
(156) Mouras, S.; Hamm, A.; Djurado, D.; Cousseins, J.-C. *Revue de Chimie Minérale* **1987**, *24*, 572–582.
(157) Fradkin, E. *Physical Review B* **1986**, *33*, 3263–3268.
(158) Shioyama, H. *Journal of Materials Science Letters* **2001**, *20*, 499–500.
(159) Novoselov, K. S.; Geim, A. K.; Morozov, S. V; Jiang, D.; Katsnelson, M. I.; Grigorieva, I. V; Dubonos, S. V; Firsov, A. A. *Nature* **2005**, *438*, 197–200.
(160) Ohta, T.; Bostwick, A.; McChesney, J.; Seyller, T.; Horn, K.; Rotenberg, E. *Physical Review Letters* **2007**, *98*, 206802.
(161) Sutter, P. *Nature Materials* **2009**, *8*, 171–172.
(162) Berger, C.; Song, Z.; Li, T.; Li, X.; Ogbazghi, A. Y.; Feng, R.; Dai, Z.; Marchenkov, A. N.; Conrad, E. H.; First, P. N.; de Heer, W. A. *Journal of Physical Chemistry B* **2004**, *108*, 19912–19916.
(163) Lin, Y.; Dimitrakopoulos, C.; Jenkins, K. A.; Farmer, D. B.; Chiu, H.; Grill, A.; Avouris, P. *Science* **2010**, *327*, 662.
(164) Kim, K. S.; Zhao, Y.; Jang, H.; Lee, S. Y.; Kim, J. M.; Kim, K. S.; Ahn, J.-H.; Kim, P.; Choi, J.-Y.; Hong, B. H. *Nature* **2009**, *457*, 706–710.
(165) Bae, S.; Kim, H.; Lee, Y.; Xu, X.; Park, J.-S.; Zheng, Y.; Balakrishnan, J.; Lei, T.; Kim, H. R.; Song, Y. Il; Kim, Y.-J.; Kim, K. S.; Ozyilmaz, B.; Ahn, J.-H.; Hong, B. H.; Iijima, S. *Nature Nanotechnology* **2010**, *5*, 574–578.
(166) Mattevi, C.; Kim, H.; Chhowalla, M. *Journal of Materials Chemistry* **2011**, *21*, 3324–3334.
(167) Losurdo, M.; Giangregorio, M. M.; Capezzuto, P.; Bruno, G. *Physical Chemistry Chemical Physics* **2011**, *13*, 20836–20843.
(168) Liu, L.; Zhou, H.; Cheng, R.; Chen, Y.; Lin, Y.-C.; Qu, Y.; Bai, J.; Ivanov, I. A.; Liu, G.; Huang, Y.; Duan, X. *Journal of Materials Chemistry* **2012**, *22*, 1498–1503.
(169) Han, S.-J.; Jenkins, K. a; Valdes Garcia, A.; Franklin, A. D.; Bol, A. A.; Haensch, W. *Nano Letters* **2011**, *11*, 3690–3693.
(170) Han, T.-H.; Lee, Y.; Choi, M.-R.; Woo, S.-H.; Bae, S.-H.; Hong, B. H.; Ahn, J.-H.; Lee, T.-W. *Nature Photonics* **2012**, *6*, 105–110.
(171) Wei, D.; Xie, L.; Lee, K. K.; Hu, Z.; Tan, S.; Chen, W.; Sow, C. H.; Chen, K.; Liu, Y.; Wee, A. T. S. *Nature Communications* **2013**, *4*, 1374.

(172) Bao, Q.; Zhang, H.; Wang, B.; Ni, Z.; Haley, C.; Xuan, Y.; Wang, Y. *Nature Photonics* **2011**, *5*, 411–415.
(173) Novoselov, K. S.; Fal'ko, V. I.; Colombo, L.; Gellert, P. R.; Schwab, M. G.; Kim, K. *Nature* **2012**, *490*, 192–200.
(174) Gao, W.; Alemany, L. B.; Ci, L.; Ajayan, P. M. *Nature Chemistry* **2009**, *1*, 403–408.
(175) Gao, X.; Jang, J.; Nagase, S. *Journal of Physical Chemistry C* **2010**, *114*, 832–842.
(176) Fernandez-Merino, M. J.; Guardia, L.; Paredes, J. I.; Villar-Rodil, S.; Solis-Fernandez, P.; Martinez-Alonso, A.; Tascon, J. M. D. *Journal of Physical Chemistry C* **2010**, *114*, 6426–6432.
(177) Stankovich, S.; Dikin, D. A.; Piner, R. D.; Kohlhaas, K. A.; Kleinhammes, A.; Jia, Y.; Wu, Y.; Nguyen, S. T.; Ruoff, R. S. *Carbon* **2007**, *45*, 1558–1565.
(178) Shin, H.-J.; Kim, K. K.; Benayad, A.; Yoon, S.-M.; Park, H. K.; Jung, I.-S.; Jin, M. H.; Jeong, H.-K.; Kim, J. M.; Choi, J.-Y.; Lee, Y. H. *Advanced Functional Materials* **2009**, *19*, 1987–1992.
(179) Wang, G.; Yang, J.; Park, J.; Gou, X.; Wang, B.; Liu, H.; Yao, J. *Journal of Physical Chemistry C* **2008**, *112*, 8192–8195.
(180) Ambrosi, A.; Chua, C. K.; Bonanni, A.; Pumera, M. *Chemistry of Materials* **2012**, *24*, 2292–2298.
(181) Zhang, J.; Yang, H.; Shen, G.; Cheng, P.; Zhang, J.; Guo, S. *Chemical Communications* **2010**, *46*, 1112–1114.
(182) Fan, X.; Peng, W.; Li, Y.; Li, X.; Wang, S.; Zhang, G.; Zhang, F. *Advanced Materials* **2008**, *20*, 4490–4493.
(183) Park, S.; An, J.; Piner, R. D.; Jung, I.; Yang, D.; Velamakanni, A.; Nguyen, S. T.; Ruoff, R. S. *Chemistry of Materials* **2008**, *20*, 6592–6594.
(184) Dreyer, D. R.; Murali, S.; Zhu, Y.; Ruoff, R. S.; Bielawski, C. W. *Journal of Materials Chemistry* **2011**, *21*, 3443–3447.
(185) Su, C.-Y.; Xu, Y.; Zhang, W.; Zhao, J.; Liu, A.; Tang, X.; Tsai, C.-H.; Huang, Y.; Li, L.-J. *ACS Nano* **2010**, *4*, 5285–5292.
(186) Zhu, C.; Guo, S.; Fang, Y.; Dong, S. *ACS Nano* **2010**, *4*, 2429–2437.
(187) Moon, I. K.; Lee, J.; Ruoff, R. S.; Lee, H. *Nature Communications* **2010**, *1:73*, 1–6.
(188) McAllister, M. J.; Li, J.-L.; Adamson, D. H.; Schniepp, H. C.; Abdala, A. A.; Liu, J.; Herrera-Alonso, M.; Milius, D. L.; Car, R.; Prud'homme, R. K.; Aksay, I. A. *Chemistry of Materials* **2007**, *19*, 4396–4404.
(189) Acik, M.; Lee, G.; Mattevi, C.; Pirkle, A.; Wallace, R. M.; Chhowalla, M.; Cho, K.; Chabal, Y. *Journal of Physical Chemistry C* **2011**, *115*, 19761–19781.
(190) Dubin, S.; Gilje, S.; Wang, K.; Tung, V. C.; Cha, K.; Hall, A. S.; Farrar, J.; Varshneya, R.; Yang, Y.; Kaner, R. B. *ACS Nano* **2010**, *4*, 3845–3852.
(191) Chua, C. K.; Pumera, M. *Chemical Society Reviews* **2013**, *42*, 3222–3233.
(192) Liu, L.-H.; Yan, M. *Journal of Materials Chemistry* **2011**, *21*, 3273–3276.
(193) Lomeda, J. R.; Doyle, C. D.; Kosynkin, D. V; Hwang, W.-F.; Tour, J. M. *Journal of the American Chemical Society* **2008**, *130*, 16201–16206.
(194) Wang, H.-X.; Zhou, K.-G.; Xie, Y.-L.; Zeng, J.; Chai, N.-N.; Li, J.; Zhang, H.-L. *Chemical Communications* **2011**, *47*, 5747–5749.
(195) Avinash, M. B.; Subrahmanyam, K. S.; Sundarayya, Y.; Govindaraju, T. *Nanoscale* **2010**, *2*, 1762–1766.
(196) Liu, Z.-B.; Xu, Y.-F.; Zhang, X.-Y.; Zhang, X.-L.; Chen, Y.-S.; Tian, J.-G. *Journal of Physical Chemistry B* **2009**, *113*, 9681–9686.
(197) Veca, L. M.; Lu, F.; Meziani, M. J.; Cao, L.; Zhang, P.; Qi, G.; Qu, L.; Shrestha, M.; Sun, Y.-P. *Chemical Communications* **2009**, 2565–2567.
(198) Yang, H.; Shan, C.; Li, F.; Han, D.; Zhang, Q.; Niu, L. *Chemical Communications* **2009**, 3880–3882.
(199) Yang, H.; Li, F.; Shan, C.; Han, D.; Zhang, Q.; Niu, L.; Ivaska, A. *Journal of Materials Chemistry* **2009**, *19*, 4632–4638.
(200) Burress, J. W.; Gadipelli, S.; Ford, J.; Simmons, J. M.; Zhou, W.; Yildirim, T. *Angewandte Chemie International Edition* **2010**, *49*, 8902–8904.
(201) Lee, D.-W.; Kim, T.; Lee, M. *Chemical Communications* **2011**, *47*, 8259–8261.
(202) Chen, Q.; Wei, W.; Lin, J.-M. *Biosensors & Bioelectronics* **2011**, *26*, 4497–4502.
(203) Xu, L. Q.; Yang, W. J.; Neoh, K.-G.; Kang, E.-T.; Fu, G. D. *Macromolecules* **2010**, *43*, 8336–8339.
(204) Varghese, N.; Ghosh, A.; Voggu, R.; Ghosh, S.; Rao, C. N. R. *Journal of Physical Chemistry C* **2009**, *113*, 16855–16859.
(205) Choudhury, D.; Das, B.; Sarma, D. D.; Rao, C. N. R. *Chemical Physics Letters* **2010**, *497*, 66–69.
(206) Dong, X.; Shi, Y.; Zhao, Y.; Chen, D.; Ye, J.; Yao, Y.; Gao, F.; Ni, Z.; Yu, T.; Shen, Z.; Huang, Y.; Chen, P.; Li, L.-J. *Physical Review Letters* **2009**, *102*, 135501.
(207) Yang, G.; Zhang, G.; Sheng, P.; Sun, F.; Xu, W.; Zhang, D. *Journal of Materials Chemistry* **2012**, *22*, 4391–4395.

(208) He, S.; Song, B.; Li, D.; Zhu, C.; Qi, W.; Wen, Y.; Wang, L.; Song, S.; Fang, H.; Fan, C. *Advanced Functional Materials* **2010**, *20*, 453–459.
(209) Bi, S.; Zhao, T.; Luo, B. *Chemical Communications* **2012**, *48*, 106–108.
(210) Morales-Narváez, E.; Merkoçi, A. *Advanced Materials* **2012**, *24*, 3298–3308.
(211) Yang, X.; Zhang, X.; Liu, Z.; Ma, Y.; Huang, Y.; Chen, Y. *Journal of Physical Chemistry C* **2008**, *112*, 17554–17558.
(212) Wang, Y.; Li, Z.; Hu, D.; Lin, C.-T.; Li, J.; Lin, Y. *Journal of the American Chemical Society* **2010**, *132*, 9274–9276.
(213) Georgakilas, V.; Otyepka, M.; Bourlinos, A. B.; Chandra, V.; Kim, N.; Kemp, K. C.; Hobza, P.; Zboril, R.; Kim, K. S. *Chemical Reviews* **2012**, *112*, 6156–6214.
(214) Shao, Y.; Wang, J.; Engelhard, M.; Wang, C.; Lin, Y. *Journal of Materials Chemistry* **2010**, *20*, 743–748.
(215) Zhou, M.; Wang, Y.; Zhai, Y.; Zhai, J.; Ren, W.; Wang, F.; Dong, S. *Chemistry A European Journal* **2009**, *15*, 6116–6120.
(216) Fellahi, O.; Das, M. R.; Coffinier, Y.; Szunerits, S.; Hadjersi, T.; Maamache, M.; Boukherroub, R. *Nanoscale* **2011**, *3*, 4662–4669.
(217) Williams, G.; Seger, B.; Kamat, P. V *ACS Nano* **2008**, *2*, 1487–1491.
(218) Huang, L.; Liu, Y.; Ji, L.-C.; Xie, Y.-Q.; Wang, T.; Shi, W.-Z. *Carbon* **2011**, *49*, 2431–2436.
(219) Cote, L. J.; Cruz-Silva, R.; Huang, J. *Journal of the American Chemical Society* **2009**, *131*, 11027–11032.
(220) Matsumoto, Y.; Koinuma, M.; Kim, S. Y.; Watanabe, Y.; Taniguchi, T.; Hatakeyama, K.; Tateishi, H.; Ida, S. *ACS Applied Materials & Interfaces* **2010**, *2*, 3461–3466.
(221) Pumera, M. *Energy & Environmental Science* **2011**, *4*, 668–674.
(222) Sun, Y.; Wu, Q.; Shi, G. *Energy & Environmental Science* **2011**, *4*, 1113–1132.
(223) Chen, D.; Zhang, H.; Liu, Y.; Li, J. *Energy & Environmental Science* **2013**, *6*, 1362–1387.
(224) Xu, C.; Xu, B.; Gu, Y.; Xiong, Z.; Sun, J.; Zhao, X. S. *Energy & Environmental Science* **2013**, *6*, 1388–1414.
(225) Guo, S.; Wen, D.; Zhai, Y.; Dong, S.; Wang, E. *ACS Nano* **2010**, *4*, 3959–3968.
(226) Imran Jafri, R.; Rajalakshmi, N.; Ramaprabhu, S. *Journal of Materials Chemistry* **2010**, *20*, 7114–7117.
(227) Wu, X.; Zeng, X. C. *Nano Letters* **2009**, *9*, 250–256.
(228) Wang, D.; Kou, R.; Choi, D.; Yang, Z.; Nie, Z.; Li, J.; Saraf, L. V; Hu, D.; Zhang, J.; Graff, G. L.; Liu, J.; Pope, M. a; Aksay, I. a *ACS Nano* **2010**, *4*, 1587–1595.
(229) Huang, X.; Qi, X.; Boey, F.; Zhang, H. *Chemical Society Reviews* **2012**, *41*, 666–686.
(230) Tang, Q.; Zhou, Z.; Chen, Z. *Nanoscale* **2013**, *5*, 4541–4583.
(231) Zhang, Q.; Uchaker, E.; Candelaria, S. L.; Cao, G. *Chemical Society Reviews* **2013**, *42*, 3127–3171.
(232) Yan, J.; Wei, T.; Shao, B.; Fan, Z.; Qian, W.; Zhang, M.; Wei, F. *Carbon* **2010**, *48*, 487–493.
(233) Wang, H.; Casalongue, H. S.; Liang, Y.; Dai, H. *Journal of the American Chemical Society* **2010**, *132*, 7472–7477.
(234) Wu, Z.-S.; Wang, D.-W.; Ren, W.; Zhao, J.; Zhou, G.; Li, F.; Cheng, H.-M. *Advanced Functional Materials* **2010**, *20*, 3595–3602.
(235) Chang, K.; Hu, C.; Chou, C.; Cheng, C.; Uni, V.; Road, U. V; December, R. V; Re, V.; Recei, M.; February, V. *Chemistry of Materials* **2007**, *19*, 2112–2119.
(236) Li, F.; Huang, Y.; Yang, Q.; Zhong, Z.; Li, D.; Wang, L.; Song, S.; Fan, C. *Nanoscale* **2010**, *2*, 1021–1026.
(237) Balapanuru, J.; Yang, J.-X.; Xiao, S.; Bao, Q.; Jahan, M.; Polavarapu, L.; Wei, J.; Xu, Q.-H.; Loh, K. P. *Angewandte Chemie International Edition* **2010**, *49*, 6549–6553.
(238) Tang, Z.; Wu, H.; Cort, J. R.; Buchko, G. W.; Zhang, Y.; Shao, Y.; Aksay, I. A.; Liu, J.; Lin, Y. *Small* **2010**, *6*, 1205–1209.
(239) Yi, J. W.; Park, J.; Singh, N. J.; Lee, I. J.; Kim, K. S.; Kim, B. H. *Bioorganic & Medicinal Chemistry Letters* **2011**, *21*, 704–706.
(240) Lu, C.; Yang, H.; Zhu, C.; Chen, X.; Chen, G. *Angewandte Chemie International Edition* **2009**, *121*, 4879–4881.
(241) Chang, H.; Tang, L.; Wang, Y.; Jiang, J.; Li, J. *Analytical Chemistry* **2010**, *82*, 2341–2346.
(242) Wang, X.; Wang, C.; Qu, K.; Song, Y.; Ren, J.; Miyoshi, D.; Sugimoto, N.; Qu, X. *Advanced Functional Materials* **2010**, *20*, 3967–3971.
(243) Wen, Y.; Xing, F.; He, S.; Song, S.; Wang, L.; Long, Y.; Li, D.; Fan, C. *Chemical Communications* **2010**, *46*, 2596–2598.
(244) Zhao, X.; Kong, R.; Zhang, X.; Meng, H.; Liu, W.; Tan, W.; Shen, G.; Yu, R. *Analytical Chemistry* **2011**, *83*, 5062–5066.

(245) Jung, J. H.; Cheon, D. S.; Liu, F.; Lee, K. B.; Seo, T. S. *Angewandte Chemie International Edition* **2010**, *49*, 5708–5711.
(246) Liu, F.; Choi, J. Y.; Seo, T. S. *Biosensors & Bioelectronics* **2010**, *25*, 2361–2365.
(247) Szunerits, S.; Maalouli, N.; Wijaya, E.; Vilcot, J.-P.; Boukherroub, R. *Analytical and Bioanalytical Chemistry* **2013**, *405*, 1435–1443.
(248) Wijaya, E.; Maalouli, N.; Boukherroub, R.; Szunerits, S.; Vilcot, J.-P. *Proceedings of the SPIE* **2012**, *8424*, 84240R–7.
(249) Zhang, J.; Sun, Y.; Xu, B.; Zhang, H.; Gao, Y.; Zhang, H.; Song, D. *Biosensors & Bioelectronics* **2013**, *45*, 230–236.
(250) Wu, L.; Chu, H. S.; Koh, W. S.; Li, E. P. *Optics Express* **2010**, *18*, 14395–14400.
(251) Subramanian, P.; Lesniewski, A.; Kaminska, I.; Vlandas, A.; Vasilescu, A.; Niedziolka-Jonsson, J.; Pichonat, E.; Happy, H.; Boukherroub, R.; Szunerits, S. *Biosensors & Bioelectronics* **2013**, *50*, 239–243.
(252) Lu, G.; Li, H.; Liusman, C.; Yin, Z.; Wu, S.; Zhang, H. *Chemical Science* **2011**, *2*, 1817–1821.
(253) Ren, W.; Fang, Y.; Wang, E. *ACS Nano* **2011**, *5*, 6425–6433.
(254) Zhang, Y.; Liu, S.; Wang, L.; Qin, X.; Tian, J.; Lu, W.; Chang, G.; Sun, X. *RSC Advances* **2012**, *2*, 538–545.
(255) Xu, W.; Mao, N.; Zhang, J. *Small* **2013**, *9*, 1206–1224.
(256) Liu, X.; Cao, L.; Song, W.; Ai, K.; Lu, L. *ACS Applied Materials & Interfaces* **2011**, *3*, 2944–2952.
(257) Zhou, K.; Zhu, Y.; Yang, X.; Luo, J.; Li, C.; Luan, S. *Electrochimica Acta* **2010**, *55*, 3055–3060.
(258) Zeng, Q.; Cheng, J.; Tang, L.; Liu, X.; Liu, Y.; Li, J.; Jiang, J. *Advanced Functional Materials* **2010**, *20*, 3366–3372.
(259) Alwarappan, S.; Liu, C.; Kumar, A.; Li, C.-Z. *Journal of Physical Chemistry C* **2010**, *114*, 12920–12924.
(260) Wang, Y.; Shao, Y.; Matson, D. W.; Li, J.; Lin, Y. *ACS Nano* **2010**, *4*, 1790–1798.
(261) Zhou, M.; Zhai, Y.; Dong, S. *Analytical Chemistry* **2009**, *81*, 5603–5613.
(262) Zhang, J.; Lei, J.; Pan, R.; Xue, Y.; Ju, H. *Biosensors & Bioelectronics* **2010**, *26*, 371–376.
(263) Huang, K.-J.; Niu, D.-J.; Sun, J.-Y.; Han, C.-H.; Wu, Z.-W.; Li, Y.-L.; Xiong, X.-Q. *Colloids and Surfaces B: Biointerfaces* **2011**, *82Huang, K*, 543–549.
(264) Wang, Y.; Li, Y.; Tang, L.; Lu, J.; Li, J. *Electrochemistry Communications* **2009**, *11*, 889–892.
(265) Hou, S.; Kasner, M. L.; Su, S.; Patel, K.; Cuellari, R. *Journal of Physical Chemistry C* **2010**, *114*, 14915–14921.
(266) Choi, B. G.; Park, H.; Park, T. J.; Yang, M. H.; Kim, J. S.; Jang, S.; Heo, N. S.; Lee, S. Y.; Kong, J.; Hong, W. H. *ACS Nano* **2010**, *4*, 2910–2918.
(267) Shan, C.; Yang, H.; Han, D.; Zhang, Q.; Ivaska, A.; Niu, L. *Biosensors & Bioelectronics* **2010**, *25*, 1070–1074.
(268) Zhong, Z.; Wu, W.; Wang, D.; Wang, D.; Shan, J.; Qing, Y.; Zhang, Z. *Biosensors & Bioelectronics* **2010**, *25*, 2379–2383.
(269) Li, F.; Chai, J.; Yang, H.; Han, D.; Niu, L. *Talanta* **2010**, *81*, 1063–1068.
(270) Tan, L.; Zhou, K.-G.; Zhang, Y.-H.; Wang, H.-X.; Wang, X.-D.; Guo, Y.-F.; Zhang, H.-L. *Electrochemistry Communications* **2010**, *12*, 557–560.
(271) Zhang, H.; Grüner, G.; Zhao, Y. *Journal of Materials Chemistry B* **2013**, *1*, 2542–2567.
(272) Hu, X.; Zhou, Q. *Chemical Reviews* **2013**, *113*, 3815–3835.
(273) Mao, H. Y.; Laurent, S.; Chen, W.; Akhavan, O.; Imani, M.; Ashkarran, A. A.; Mahmoudi, M. *Chemical Reviews* **2013**, *113*, 3407–3424.
(274) Feng, L.; Wu, L.; Qu, X. *Advanced Materials* **2013**, *25*, 168–186.
(275) Sreeprasad, T. S.; Maliyekkal, M. S.; Deepti, K.; Chaudhari, K.; Xavier, P. L.; Pradeep, T. *ACS Applied Materials & Interfaces* **2011**, *3*, 2643–2654.
(276) Akhavan, O.; Ghaderi, E. *Carbon* **2012**, *50*, 1853–1860.
(277) Mejías Carpio, I. E.; Santos, C. M.; Wei, X.; Rodrigues, D. F. *Nanoscale* **2012**, *4*, 4746–4756.
(278) Wang, H.; Zhang, Q.; Chu, X.; Chen, T.; Ge, J.; Yu, R. *Angewandte Chemie International Edition* **2011**, *50*, 7065–7069.
(279) Wang, Y.; Zhen, S. J.; Zhang, Y.; Li, Y. F.; Huang, C. Z. *Journal of Physical Chemistry C* **2011**, *115*, 12815–12821.
(280) Hong, H.; Yang, K.; Zhang, Y.; Engle, J. W.; Feng, L.; Yang, Y.; Nayal, T. R.; Goel, S.; Bean, J.; Theuer, C. P.; Barnhart, T. E.; Liu, Z.; Cai, W. *ACS Nano* **2012**, *6*, 2361–2370.
(281) Peng, J.; Gao, W.; Gupta, B. K.; Liu, Z.; Romero-Aburto, R.; Ge, L.; Song, L.; Alemany, L. B.; Zhan, X.; Gao, G.; Vithayathil, S. A.; Kaipparettu, B. A.; Marti, A. A.; Hayashi, T.; Zhu, J.-J.; Ajayan, P. M. *Nano Letters* **2012**, *12*, 844–849.
(282) Sreejith, S.; Ma, X.; Zhao, Y. *Journal of the American Chemical Society* **2012**, *134*, 17346–17349.

(283) Liu, K.; Zhang, J.-J.; Cheng, F.-F.; Zheng, T.-T.; Wang, C.; Zhu, J.-J. *Journal of Materials Chemistry* **2011**, *21*, 12034–12040.
(284) Lu, C.-H.; Zhu, C.-L.; Li, J.; Liu, J.-J.; Chen, X.; Yang, H.-H. *Chemical Communications* **2010**, *46*, 3116–3118.
(285) Feng, L.; Zhang, S.; Liu, Z. *Nanoscale* **2011**, *3*, 1252–1257.
(286) Zhang, L.; Lu, Z.; Zhao, Q.; Huang, J.; Shen, H.; Zhang, Z. *Small* **2011**, *7*, 460–464.
(287) Liu, C.-L.; Wu, H.-T.; Hsiao, Y.-H.; Lai, C.-W.; Shih, C.-W.; Peng, Y.-K.; Tang, K.-C.; Chang, H.-W.; Chien, Y.-C.; Hsiao, J.-K.; Cheng, J.-T.; Chou, P.-T. *Angewandte Chemie International Edition* **2011**, *50*, 7056–7060.
(288) Liu, Z.; Robinson, J. T.; Tabakman, S. M.; Yang, K.; Dai, H. *Materials Today* **2011**, *14*, 316–323.
(289) Mayorov, A. S.; Gorbachev, R. V.; Morozov, S. V.; Britnell, L.; Jalil, R.; Ponomarenko, L. A.; Blake, P.; Novoselov, K. S.; Watanabe, K.; Taniguchi, T.; Geim, A. K. *Nano Letters* **2011**, *11*, 2396–2399.
(290) Balandin, A. A. *Nature Materials* **2011**, *10*, 569–581.
(291) Kuzmenko, A. B.; van Heumen, E.; Carbone, F.; van der Marel, D. *Physical Review Letters* **2008**, *100*, 117401.
(292) Nair, R. R.; Blake, P.; Grigorenko, A. N.; Novoselov, K. S.; Booth, T. J.; Stauber, T.; Peres, N. M. R.; Geim, A. K. *Science* **2008**, *320*, 1308.
(293) Lee, C.; Wei, X.; Kysar, J. W.; Hone, J. *Science* **2008**, *321*, 385–388.
(294) Petersen, K. E. *Proceedings of the IEEE* **1982**, *70*, 420–457.
(295) Yajima, S.; Hayashi, J.; Omori, M.; Okamura, K. *Nature* **1976**, *261*, 683–685.
(296) Wei, X.; Wang, M.-S.; Bando, Y.; Golberg, D. *Advanced Materials* **2010**, *22*, 4895–4899.
(297) Yu, M. *Science* **2000**, *287*, 637–640.
(298) Treacy, M. M. J.; Ebbesen, T. W.; Gibson, J. M. *Nature* **1996**, *381*, 678–680.
(299) Kosynkin, D. V; Higginbotham, A. L.; Sinitskii, A.; Lomeda, J. R.; Dimiev, A.; Price, B. K.; Tour, J. M. *Nature* **2009**, *458*, 872–876.
(300) Jiao, L.; Zhang, L.; Wang, X.; Diankov, G.; Dai, H. *Nature* **2009**, *458*, 877–880.
(301) Mohammadi, S.; Kolahdouz, Z.; Darbari, S.; Mohajerzadeh, S.; Masoumi, N. *Carbon* **2013**, *52*, 451–463.
(302) Kosynkin, D. V; Lu, W.; Sinitskii, A.; Pera, G.; Sun, Z.; Tour, J. M. *ACS Nano* **2011**, *5*, 968–974.
(303) Xie, L.; Wang, H.; Jin, C.; Wang, X.; Jiao, L.; Kazu, S.; Dai, H. *Journal of the American Chemical Society* **2011**, *133*, 10394–10397.
(304) Brodie, B. C. *Philosophical Transactions of the Royal Society of London* **1859**, *149*, 249–259.
(305) Staudenmaier, L. *Berichte der Deutschen Chemischen Gesellschaft* **1898**, *32*, 1481–1487.
(306) Hummers, W. S.; Offeman, R. E. *Journal of the American Chemical Society* **1958**, *80*, 1339.
(307) Dreyer, D. R.; Park, S.; Bielawski, C. W.; Ruoff, R. S. *Chemical Society Reviews* **2010**, *39*, 228–240.
(308) He, Q.; Wu, S.; Yin, Z.; Zhang, H. *Chemical Science* **2012**, *3*, 1764–1772.
(309) Ang, P. K.; Chen, W.; Wee, A. T. S.; Loh, K. P. *Journal of the American Chemical Society* **2008**, *130*, 14392–14393.
(310) Dua, V.; Surwade, S. P.; Ammu, S.; Agnihotra, S. R.; Jain, S.; Roberts, K. E.; Park, S.; Ruoff, R. S.; Manohar, S. K. *Angewandte Chemie International Edition* **2010**, *49*, 2154–2157.
(311) Yu, K.; Wang, P.; Lu, G.; Chen, K.-H.; Bo, Z.; Chen, J. *Journal of Physical Chemistry Letters* **2011**, *2*, 537–542.
(312) Lu, G.; Ocola, L. E.; Chen, J. *Applied Physics Letters* **2009**, *94*, 083111.
(313) Lu, G.; Yu, K.; Ocola, L. E.; Chen, J. *Chemical Communications* **2011**, *47*, 7761–7763.
(314) Johnson, J. L.; Behnam, A.; Pearton, S. J.; Ural, A. *Advanced Materials* **2010**, *22*, 4877–4880.
(315) Cuong, T. V.; Pham, V. H.; Chung, J. S.; Shin, E. W.; Yoo, D. H.; Hahn, S. H.; Huh, J. S.; Rue, G. H.; Kim, E. J.; Hur, S. H.; Kohl, P. A. *Materials Letters* **2010**, *64*, 2479–2482.
(316) Robinson, J. T.; Perkins, F. K.; Snow, E. S.; Wei, Z.; Sheehan, P. E. *Nano Letters* **2008**, *8*, 3137–3140.
(317) Dong, X.; Shi, Y.; Huang, W.; Chen, P.; Li, L.-J. *Advanced Materials* **2010**, *22*, 1649–1653.
(318) Choi, B. G.; Park, H.; Yang, M. H.; Jung, Y. M.; Lee, S. Y.; Hong, W. H.; Park, T. J. *Nanoscale* **2010**, *2*, 2692–2697.
(319) Yin, Z.; He, Q.; Huang, X.; Zhang, J.; Wu, S.; Chen, P.; Lu, G.; Zhang, Q.; Yan, Q.; Zhang, H. *Nanoscale* **2012**, *4*, 293–297.
(320) Huang, Y.; Dong, X.; Shi, Y.; Li, C. M.; Li, L.-J.; Chen, P. *Nanoscale* **2010**, *2*, 1485–1488.
(321) Mao, S.; Lu, G.; Yu, K.; Bo, Z.; Chen, J. *Advanced Materials* **2010**, *22*, 3521–3526.
(322) Yang, M.; Gong, S. *Chemical Communications* **2010**, *46*, 5796–5798.
(323) Ohno, Y.; Maehashi, K.; Matsumoto, K. *Journal of the American Chemical Society* **2010**, *132*, 18012–18013.
(324) Mao, S.; Yu, K.; Lu, G.; Chen, J. *Nano Research* **2011**, *4*, 921–930.
(325) He, Q.; Wu, S.; Gao, S.; Cao, X.; Yin, Z.; Li, H.; Chen, P.; Zhang, H. *ACS Nano* **2011**, *5*, 5038–5044.

(326) Huang, Y.; Dong, X.; Liu, Y.; Li, L.-J.; Chen, P. *Journal of Materials Chemistry* **2011**, *21*, 12358–12362.
(327) He, Q.; Sudibya, H. G.; Yin, Z.; Wu, S.; Li, H.; Boey, F.; Huang, W.; Chen, P.; Zhang, H. *ACS Nano* **2010**, *4*, 3201–3208.
(328) Cao, L.; Liu, Y.; Zhang, B.; Lu, L. *ACS Applied Materials & Interfaces* **2010**, *2*, 2339–2346.
(329) Chen, W.; Cai, S.; Ren, Q.-Q.; Wen, W.; Zhao, Y.-D. *The Analyst* **2012**, *137*, 49–58.
(330) Wu, H.; Wang, J.; Kang, X.; Wang, C.; Wang, D.; Liu, J.; Aksay, I. A.; Lin, Y. *Talanta* **2009**, *80*, 403–406.
(331) Du, D.; Zou, Z.; Shin, Y.; Wang, J.; Wu, H.; Engelhard, M. H.; Liu, J.; Aksay, I. A.; Lin, Y. *Analytical Chemistry* **2010**, *82*, 2989–2995.
(332) Du, D.; Wang, L.; Shao, Y.; Wang, J.; Engelhard, M. H.; Lin, Y. *Analytical Chemistry* **2011**, *83*, 746–752.
(333) Yang, M.; Javadi, A.; Li, H.; Gong, S. *Biosensors & Bioelectronics* **2010**, *26*, 560–565.
(334) Guo, Y.; Jia, X.; Zhang, S. *Chemical Communications* **2011**, *47*, 725–727.
(335) Xie, X.; Zhao, K.; Xu, X.; Zhao, W.; Liu, S.; Zhu, Z.; Li, M.; Shi, Z.; Shao, Y. *Journal of Physical Chemistry C* **2010**, *114*, 14243–14250.
(336) Wang, Z.; Zhang, J.; Chen, P.; Zhou, X.; Yang, Y.; Wu, S.; Niu, L.; Han, Y.; Wang, L.; Boey, F.; Zhang, Q.; Liedberg, B.; Zhang, H. *Biosensors & Bioelectronics* **2011**, *26*, 3881–3886.
(337) Shang, N. G.; Papakonstantinou, P.; McMullan, M.; Chu, M.; Stamboulis, A.; Potenza, A.; Dhesi, S. S.; Marchetto, H. *Advanced Functional Materials* **2008**, *18*, 3506–3514.
(338) Marín, S.; Merkoçi, A. *Electroanalysis* **2012**, *24*, 459–469.
(339) Pan, R.; Pan, S.; Zhou, J.; Wu, Y. *Applied Surface Science* **2009**, *255*, 3642–3647.
(340) Edwards, P. P.; Porch, A.; Jones, M. O.; Morgan, D. V.; Perks, R. M. *Dalton Transactions* **2004**, 2995–3002.
(341) Ding, Z.; An, C.; Li, Q.; Hou, Z.; Wang, J.; Qi, H.; Qi, F. *Journal of Nanomaterials* **2010**, *2010*, 1–5.
(342) Tao, P.; Viswanath, A.; Schadler, L. S.; Benicewicz, B. C.; Siegel, R. W. *ACS Applied Materials & Interfaces* **2011**, *3*, 3638–3645.
(343) Liu, H.; Zeng, X.; Kong, X.; Bian, S.; Chen, J. *Applied Surface Science* **2012**, *258*, 8564–8569.
(344) Song, J. E.; Kim, Y. H.; Kang, Y. S. *Current Applied Physics* **2006**, *6*, 791–795.
(345) Usui, H.; Sasaki, T.; Koshizaki, N. *Journal of Physical Chemistry B* **2006**, *110*, 12890–12895.
(346) Lany, S.; Zakutayev, A.; Mason, T. O.; Wager, J. F.; Poeppelmeier, K. R.; Perkins, J. D.; Berry, J. J.; Ginley, D. S.; Zunger, A. *Physical Review Letters* **2012**, *108*, 016802(5).
(347) Heusing, S.; de Oliveira, P. W.; Kraker, E.; Haase, a.; Palfinger, C.; Veith, M. *Thin Solid Films* **2009**, *518*, 1164–1169.
(348) Jung, B. O.; Kim, D. C.; Kong, B. H.; Lee, J. H.; Lee, J. Y.; Cho, H. K. *Electrochemical and Solid-State Letters* **2011**, *14*, H446–H449.
(349) Deng, D.; Chen, F. *Journal of Materials Science: Materials in Electronics* **2013**, *24*, 2072–2076.
(350) Sytchkova, A.; Zola, D.; Bailey, L. R.; Mackenzie, B.; Proudfoot, G.; Tian, M.; Ulyashin, A. *Materials Science and Engineering: B* **2013**, *178*, 586–592.
(351) Chou, T.-H.; Cheng, K.-Y.; Hsieh, C.-W.; Takaya, Y. *Journal of Micromechanics and Microengineering* **2012**, *22*, 045009.
(352) Nakajima, R.; Yamada, Y.; Komatsu, T.; Murashiro, K.; Saji, T.; Hoshino, K. *RSC Advances* **2012**, *2*, 4377–4381.
(353) Betz, U.; Kharrazi Olsson, M.; Marthy, J.; Escolá, M. F.; Atamny, F. *Surface and Coatings Technology* **2006**, *200*, 5751–5759.
(354) Hsu, S.-Y.; Lee, M.-C.; Lee, K.-L.; Wei, P.-K. *Applied Physics Letters* **2008**, *92*, 013303.
(355) Choi, S.; Nam, K. M.; Park, B. K.; Seo, W. S.; Park, J. T. *Chemistry of Materials* **2008**, *20*, 2609–2611.
(356) Sun, Z.; He, J.; Kumbhar, A.; Fang, J. *Langmuir* **2010**, *26*, 4246–4250.
(357) Kanehara, M.; Koike, H.; Yoshinaga, T.; Teranishi, T. *Journal of the American Chemical Society* **2009**, *131*, 17736–17737.
(358) Dabaghi, H. H.; Ganjkhanlou, Y.; Kazemzad, M.; Moghaddam, A. B. *Micro & Nano Letters* **2011**, *6*, 4294–4233.
(359) Lu, J.; Minami, K.; Takami, S.; Shibata, M.; Kaneko, Y.; Adschiri, T. *ACS Applied Materials & Interfaces* **2012**, *4*, 351–354.
(360) Gilstrap, R. A.; Capozzi, C. J.; Carson, C. G.; Gerhardt, R. A.; Summers, C. J. *Advanced Materials* **2008**, *20*, 4163–4166.
(361) Chou, T. P. *Journal of Nanophotonics* **2008**, *2*, 023511.
(362) Liu, S.; Ding, W.; Chai, W. *Materials Letters* **2011**, *65*, 1272–1275.
(363) Sasaki, T.; Endo, Y.; Nakaya, M.; Kanie, K.; Nagatomi, A.; Tanoue, K.; Nakamura, R.; Muramatsu, A. *Journal of Materials Chemistry* **2010**, *20*, 8153–8157.

(364) Ba, J.; Feldhoff, A.; Fattakhova Rohlfing, D.; Wark, M.; Antonietti, M.; Niederberger, M. *Small* **2007**, *3*, 310–317.
(365) Lee, I.; Lee, S.-Y. *Journal of Physical Chemistry C* **2009**, *113*, 17372–17377.
(366) Senthilkumar, V.; Senthil, K.; Vickraman, P. *Materials Research Bulletin* **2012**, *47*, 1051–1056.
(367) Wang, H.; Xu, X.; Zhang, J.; Li, C. *Journal of Materials Science & Technology* **2010**, *26*, 1037–1040.
(368) Rietveld, H. M. *Journal of Applied Crystallography* **1969**, *2*, 65–71.
(369) Popa, N. C. *Journal of Applied Crystallography* **1998**, *31*, 176–180.
(370) Niedziolka, J.; Szot, K.; Marken, F.; Opallo, M. *Electroanalysis* **2007**, *19*, 155–160.
(371) Ebert, D.; Bhushan, B. *Langmuir* **2012**, *28*, 11391–11399.
(372) Zhou, C.; Li, J.; Chen, S.; Wu, J.; Heier, K. R.; Cheng, H. *Journal of Physical Chemistry C* **2008**, *112*, 14015–14020.
(373) Rozniecka, E.; Jonsson-Niedziolka, M.; Sobczak, J. W.; Opallo, M. *Electrochimica Acta* **2011**, *56*, 8739–8745.
(374) Xu, X.; Wei, W.; Huang, M.; Yao, L.; Liu, S. *Chemical Communications* **2012**, *48*, 7802–7804.
(375) Cirpan, A.; Karasz, F. E. *Journal of Applied Polymer Science* **2006**, *99*, 3125–3129.
(376) Wolz, A.; Zils, S.; Ruch, D.; Kotov, N.; Roth, C.; Michel, M. *Advanced Energy Materials* **2012**, *2*, 569–574.
(377) Peng, C. Q.; Thio, Y. S.; Gerhardt, R. A. *Nanotechnology* **2008**, *19*, 505603.
(378) Fan, Y.; Chen, X.; Kong, J.; Tung, C.; Gao, Z. *Angewandte Chemie International Edition* **2007**, *119*, 2097–2100.
(379) Kangasniemi, K. H.; Condit, D. A.; Jarvi, T. D. *Journal of The Electrochemical Society* **2004**, *151*, E125–E132.
(380) Bard, A. J.; Faulkner, L. R. *Electrochemical Methods, Fundamentals and Applications*; Second Edi.; John Wiley & Sons, Inc., 2001.
(381) Sandmann, G.; Dietz, H.; Plieth, W. *Journal of Electroanalytical Chemistry* **2000**, *491*, 78–86.
(382) Ueda, M.; Dietz, H.; Anders, A.; Kneppe, H.; Meixner, A.; Plieth, W. *Electrochimica Acta* **2002**, *48*, 377–386.
(383) Safavi, A.; Maleki, N.; Farjami, E. *Electroanalysis* **2009**, *21*, 1533–1538.
(384) Sun, P.; Laforge, O.; Mirkin, M. V *Physical Chemistry Chemical Physics* **2007**, *9*, 802–823.
(385) Wittstock, G.; Burchardt, M.; Pust, S. E.; Shen, Y.; Zhao, C. *Angewandte Chemie International Edition* **2007**, *46*, 1584–1617.
(386) Geisse, N. A. *Materials Today* **2009**, *12*, 40–45.
(387) Giessibl, F. J. *Reviews of Modern Physics* **2003**, *75*, 949–983.
(388) Cappella, B.; Dietler, G. *Surface Science Reports* **1999**, *34*, 1–104.
(389) Casero, E.; Vázquez, L.; Parra-Alfambra, A. M.; Lorenzo, E. *The Analyst* **2010**, *135*, 1878–1903.
(390) http://www.wittstock.chemie.uni-oldenburg.de/en/research/methods/afm.html.
(391) Zhou, W.; Wang, Z. L. *Scanning Microscopy for Nanotechnology*; Zhou, W.; Wang, Z. L., Eds.; Springer New York: New York, NY, 2006; pp. 1–40.
(392) Smith, K. C. A.; Oatley, C. W. *British Journal of Applied Physics* **1955**, *6*, 391–399.
(393) Reimer, L. *Scanning Electron Microscopy: Physics of Image Formation and Microanalysis*; 2010; pp. 207–233.
(394) Reimer, L.; Kohl, H. *Transmission Electron Microscopy*; Fifth Edit.; Springer, 2008; pp. 1–10, 419–425.
(395) Kisielowski, C.; Freitag, B.; Bischoff, M.; van Lin, H.; Lazar, S.; Knippels, G.; Tiemeijer, P.; van der Stam, M.; von Harrach, S.; Stekelenburg, M.; Haider, M.; Uhlemann, S.; Müller, H.; Hartel, P.; Kabius, B.; Miller, D.; Petrov, I.; Olson, E. A.; Donchev, T.; Kenik, E. A.; Lupini, A. R.; Bentley, J.; Pennycook, S. J.; Anderson, I. M.; Minor, A. M.; Schmid, A. K.; Duden, T.; Radmilovic, V.; Ramasse, Q. M.; Watanabe, M.; Erni, R.; Stach, E. A.; Denes, P.; Dahmen, U. *Microscopy and Microanalysis* **2008**, *14*, 469–477.
(396) O'Keefe, M. A.; Allard, L. F.; Blom, D. A. *Journal of Electron Microscopy* **2005**, *54*, 169–180.
(397) http://en.wikipedia.org/wiki/Transmission_electron_microscopy.
(398) Szczepaniak, W. *Metody instrumentalne w analizie chemicznej*; Wydawnictwo Naukowe PWN: Warszawa, 1996; pp. 64–97, 370–375.
(399) Kęcki, Z. *Podstawy spektroskopii molekularnej*; Wydawnictwo Naukowe PWN, 1998.
(400) Pellicer, A.; Bravo, M. D. C. *Seminars in Fetal & Neonatal Medicine* **2011**, *16*, 42–49.
(401) http://www.research.a-star.edu.sg/research/6304.
(402) Edmund Optics Ltd http://www.edmundoptics.jp/technical-resources-center/microscopy/fluorescence-microscopy-in-line-illumination-with-imaging-filters/.
(403) Krajnik, B.; Piątkowski, D.; Maćkowski, S.; Gagoś, M.; Tomaszewska, E.; Grobelny, J. *LAB Laboratoria, Aparatura, Badania* **2011**, 6–8.
(404) Turner, N.; Schreifels, J. *Analytical Chemistry* **2000**, *72*, 99R–110R.

(405) http://www.chem.queensu.ca/people/faculty/horton/research.html.
(406) Kwok, D. Y.; Neumann, A. W. U. *Advances in Colloid and Interface Science* **1999**, *81*, 167–249.
(407) Urbańska, N.; Pietraszkiewicz, M.; Waluk, J. *Journal of Porphyrins and Phthalocyanines* **2007**, *11*, 596–600.
(408) Vogel, E.; Köcher, M.; Schmickler, H.; Lex, J. *Angewandte Chemie International Edition* **1986**, *25*, 257–259.
(409) Watson, M. A.; Lyskawa, J.; Zobrist, C.; Fournier, D.; Jimenez, M.; Traisnel, M.; Gengembre, L.; Woisel, P. *Langmuir* **2010**, *26*, 15920–15924.
(410) Asakawa, M.; Dehaen, W.; Gerrit, L.; Menzer, S.; Nouwen, J.; Raymo, M.; Stoddart, J. F.; Williams, D. J. *Journal of Organic Chemistry* **1996**, *3263*, 9591–9595.
(411) Roy, B.; Mukhopadhyay, B. *Tetrahedron Letters* **2007**, *48*, 3783–3787.
(412) Yeoh, K. K.; Butters, T. D.; Wilkinson, B. L.; Fairbanks, A. J. *Carbohydrate Research* **2009**, *344*, 586–591.
(413) Garín, J.; Orduna, J.; Uriel, S.; Moore, A. J.; Bryce, M. R.; Wegener, S.; Yufit, D. S.; Howard, J. A. K. *Synthesis* **1994**, *1994*, 489–493.
(414) Das, M. R.; Sarma, R. K.; Saikia, R.; Kale, V. S.; Shelke, M. V; Sengupta, P. *Colloids and Surfaces B: Biointerfaces* **2011**, *83*, 16–22.
(415) Palomar-Pardavé, M.; Scharifker, B. R.; Arce, E. M.; Romero-Romo, M. *Electrochimica Acta* **2005**, *50*, 4736–4745.
(416) Brülle, T.; Ju, W.; Niedermayr, P.; Denisenko, A.; Paschos, O.; Schneider, O.; Stimming, U. *Molecules* **2011**, *16*, 10059–10077.
(417) Shul, G.; Adamiak, W.; Opallo, M. *Electrochemistry Communications* **2008**, *10*, 1201–1204.
(418) Sada, E.; Kito, S.; Ito, Y. *Journal of Chemical and Engineering Data* **1975**, *20*, 373–375.
(419) Poulson, S.; Harrington, R.; Drever, J. *Talanta* **1999**, *48*, 633–641.
(420) Witten, T. A.; Sander, L. M. *Physical Review Letters* **1981**, *47*, 1400–1403.
(421) Eden, M. In *In Proceedings of Fourth Berkeley Symposium on Mathematics, Statistics, and Probability*; 1961; pp. 223–239.
(422) Ferreira Jr., S. C.; Alves, S. G. *Journal of Statistical Mechanics* **2006**, P11007.
(423) Chopard, B.; Droz, M. *Cellular Automata Modeling Of Physical Systems*; 1999.
(424) Burke, L. D.; Nugent, P. F. *Gold Bulletin* **1997**, *30*, 43–53.
(425) Wang, J.; Gong, J.; Xiong, Y.; Yang, J.; Gao, Y.; Liu, Y.; Lu, X.; Tang, Z. *Chemical Communications* **2011**, *47*, 6894–6896.
(426) Rouya, E.; Cattarin, S.; Reed, M. L.; Kelly, R. G.; Zangari, G. *Journal of The Electrochemical Society* **2012**, *159*, K97–K102.
(427) Lai, L.-J.; Yang, Y.-W.; Lin, Y.-K.; Huang, L.-L.; Hsieh, Y.-H. *Colloids and Surfaces B: Biointerfaces* **2009**, *68*, 130–135.
(428) Huang, M.; Shen, Y.; Cheng, W.; Shao, Y.; Sun, X.; Liu, B.; Dong, S. *Analytica Chimica Acta* **2005**, *535*, 15–22.
(429) Chen, J.; Sato, M. *Journal of Electroanalytical Chemistry* **2004**, *572*, 153–159.
(430) Aoki, K.; Li, M.; Chen, J.; Nishiumi, T. *Electrochemistry Communications* **2009**, *11*, 239−241.
(431) Takhistov, P.; Paul, S. *Food Biophysics* **2006**, *1*, 57–73.
(432) Xu, S.; Yong, L.; Wu, P. *ACS Applied Materials & Interfaces* **2013**, *5*, 654–662.
(433) Jena, B. K.; Raj, C. R. *Langmuir* **2007**, *23*, 4064–4070.
(434) Li, H.; Yang, Y.; Wang, Y.; Li, W.; Bi, L.; Wu, L. *Chemical Communications* **2010**, *46*, 3750–3752.
(435) Haiss, W.; Thanh, N. T. K.; Aveyard, J.; Fernig, D. G. *Analytical Chemistry* **2007**, *79*, 4215–4221.
(436) Yang, Z.; Lin, Z. H.; Tang, C.-Y.; Chang, H.-T. *Nanotechnology* **2007**, *18*, 255606.
(437) Chen, H.; Kou, X.; Yang, Z.; Ni, W.; Wang, J. *Langmuir* **2008**, *24*, 5233–5237.
(438) Tao, Z.; Raffel, R. A.; Souid, A.-K.; Goodisman, J. *Biophysical Journal* **2009**, *96*, 2977–2988.
(439) Zimmermann, S.; Zarse, K.; Schulz, T. J.; Siems, K.; Müller-Kuhrt, L.; Birringer, M.; Ristow, M. *Hormone and Metabolic Research* **2008**, *40*, 29–37.
(440) Ruklisha, M.; Ionina, R. *Process Biochemistry* **2000**, *35*, 841–848.
(441) Fairclough, S. H.; Houston, K. *Biological Psychology* **2004**, *66*, 177–190.
(442) Calvin, M. *Angewandte Chemie International Edition* **1962**, *1*, 65–75.
(443) Jena, B. K.; Raj, C. R. *Chemistry A European Journal* **2006**, *12*, 2702–2708.
(444) Cho, S.; Kang, C. *Electroanalysis* **2007**, *19*, 2315–2320.
(445) Seo, B.; Kim, J. *Electroanalysis* **2010**, *22*, 939–945.
(446) Li, Y.; Song, Y.-Y.; Yang, C.; Xia, X.-H. *Electrochemistry Communications* **2007**, *9*, 981–988.
(447) Yehezkeli, O.; Tel-Vered, R.; Raichlin, S.; Willner, I. *ACS Nano* **2011**, *5*, 2385–2391.
(448) Chaudhuri, S. K.; Lovley, D. R. *Nature Biotechnology* **2003**, *21*, 1229–1232.
(449) Falk, M.; Blum, Z.; Shleev, S. *Electrochimica Acta* **2012**, *82*, 191–202.

(450) Boland, S.; Leech, D. *The Analyst* **2012**, *137*, 113–117.
(451) Habrioux, A.; Sibert, E.; Servat, K.; Vogel, W.; Kokoh, K. B.; Alonso-Vante, N. *Journal of Physical Chemistry B* **2007**, *111*, 10329–10333.
(452) Pasta, M.; La Mantia, F.; Cui, Y. *Electrochimica Acta* **2010**, *55*, 5561–5568.
(453) Habrioux, A.; Servat, K.; Girardeau, T.; Guérin, P.; Napporn, T. W.; Kokoh, K. B. *Current Applied Physics* **2011**, *11*, 1149–1152.
(454) Tominaga, M.; Shimazoe, T.; Nagashima, M.; Kusuda, H.; Kubo, A.; Kuwahara, Y.; Taniguchi, I. *Journal of Electroanalytical Chemistry* **2006**, *590*, 37–46.
(455) Beden, B.; Largeaud, F.; Kokoh, K. B.; Lamy, C. *Electrochimica Acta* **1996**, *41*, 701–709.
(456) Cho, S.; Shin, H.; Kang, C. *Electrochimica Acta* **2006**, *51*, 3781–3786.
(457) Tominaga, M.; Shimazoe, T.; Nagashima, M.; Taniguchi, I. *Electrochemistry Communications* **2005**, *7*, 189–193.
(458) Pasta, M.; Ruffo, R.; Falletta, E.; Mari, C. M.; Pina, C. Della *Gold Bulletin* **2010**, *43*, 57–64.
(459) Liu, Y.; Du, Y.; Li, C. M. *Electroanalysis* **2013**, *25*, 815–831.
(460) Wang, X.; Falk, M.; Ortiz, R.; Matsumura, H.; Bobacka, J.; Ludwig, R.; Bergelin, M.; Gorton, L.; Shleev, S. *Biosensors & Bioelectronics* **2012**, *31*, 219–225.
(461) Opallo, M.; Bilewicz, R. *Advances in Physical Chemistry* **2011**, *2011*, 1–21.
(462) Kowalczk, I.; Read, J.; Salomon, M. *Pure and Applied Chemistry* **2007**, *79*, 851–860.
(463) Vaddiraju, S.; Tomazos, I.; Burgess, D. J.; Jain, F. C.; Papadimitrakopoulos, F. *Biosensors & Bioelectronics* **2010**, *25*, 1553–1565.
(464) Alexeyeva, N.; Laaksonen, T.; Kontturi, K.; Mirkhalaf, F.; Schiffrin, D. J.; Tammeveski, K. *Electrochemistry Communications* **2006**, *8*, 1475–1480.
(465) El-Deab, M. S.; Okajima, T.; Ohsaka, T. *Journal of The Electrochemical Society* **2003**, *150*, A851–A857.
(466) Shen, Y.; Träuble, M.; Wittstock, G. *Analytical Chemistry* **2008**, *80*, 750–759.
(467) Yeager, E. *Electrochimica Acta* **1984**, *29*, 1527–1537.
(468) Imokawa, T.; Williams, K.-J.; Denuault, G. *Analytical Chemistry* **2006**, *78*, 265–271.
(469) Ramírez, P.; Mano, N.; Andreu, R.; Ruzgas, T.; Heller, A.; Gorton, L.; Shleev, S. *Biochimica & Biophysica Acta* **2008**, *1777*, 1364–1369.
(470) Nogala, W.; Celebanska, A.; Szot, K.; Wittstock, G.; Opallo, M. *Electrochimica Acta* **2010**, *55*, 5719–5724.
(471) Cracknell, J. A.; McNamara, T. P.; Lowe, E. D.; Blanford, C. F. *Dalton Transactionss* **2011**, *40*, 6668–6675.
(472) Baierl, D.; Fabel, B.; Lugli, P.; Scarpa, G. *Organic Electronics* **2011**, *12*, 1669–1673.
(473) Giannuzzi, L. A.; Stevie, F. A. *Introduction to Focused Ion Beams, Instrumentation, Theory, Techniques and Practice*; 2005; pp. 133–142.
(474) McCreery, R. L. *Chemical Reviews* **2008**, *108*, 2646–2687.
(475) Tang, L.; Wang, Y.; Li, Y.; Feng, H.; Lu, J.; Li, J. *Advanced Functional Materials* **2009**, *19*, 2782–2789.
(476) Shirasaki, T.; Moguet, F.; Lozano, L.; Tressaud, A.; Nanse, G.; Papirer, E. *Carbon* **1999**, *37*, 1891–1900.
(477) Tien, H.-W.; Huang, Y.-L.; Yang, S.-Y.; Wang, J.-Y.; Ma, C.-C. M. *Carbon* **2011**, *49*, 1550–1560.
(478) Szunerits, S.; Niedziolka, J.; Boukherroub, R.; Woisel, P.; Siriwardena, A. *Analytical Chemistry* **2010**, *82*, 8203–8210.
(479) Schultz, W. *Annual Review of Neuroscience* **2007**, *30*, 259–288.
(480) Missale, C.; Nash, S. R.; Robinson, S. W.; Jaber, M.; Caron, M. G. *Physiological Reviews* **1998**, *78*, 189–225.
(481) Christine, C. W.; Aminoff, M. J. *The American Journal of Medicine* **2004**, *117*, 412–419.
(482) Basu, S.; Dasgupta, P. S. *Journal of Neuroimmunology* **2000**, *102*, 113–124.
(483) Rubí, B.; Maechler, P. *Endocrinology* **2010**, *151*, 5570–5581.
(484) Lee, H.; Dellatore, S. M.; Miller, W. M.; Messersmith, P. B. *Science* **2007**, *318*, 426–430.
(485) Guo, Z.; Seol, M.-L.; Kim, M.-S.; Ahn, J.-H.; Choi, Y.-K.; Liu, J.-H.; Huang, X.-J. *The Analyst* **2013**, *138*, 2683–2690.
(486) Sansuk, S.; Bitziou, E.; Joseph, M. B.; Covington, J. A.; Boutelle, M. G.; Unwin, P. R.; Macpherson, J. V *Analytical Chemistry* **2013**, *85*, 163–169.
(487) Collman, J. P.; Devaraj, N. K.; Eberspacher, T. P. A.; Chidsey, C. E. D. *Langmuir* **2006**, *22*, 2457–2464.
(488) Qin, G.; Santos, C.; Zhang, W.; Li, Y.; Kumar, A.; Erasquin, U. J.; Liu, K.; Muradov, P.; Trautner, B. W.; Cai, C. *Journal of the American Chemical Society* **2010**, *132*, 16432–16441.
(489) Lee, S.; Bharathy, P. V.; Elangovan, T.; Kim, D.; Kim, J. In *Nanocomposites: New Trends and Developments*; Ebrahimi, F., Ed.; 2012; pp. 447–451.
(490) Kolb, H. C.; Finn, M. G.; Sharpless, K. B. *Angewandte Chemie International Edition* **2001**, *40*, 2004–2021.

(491) Das, M. R.; Wang, M.; Szunerits, S.; Gengembre, L.; Boukherroub, R. *Chemical Communications* **2009**, 2753–2755.
(492) Grosvenor, A. P.; Kobe, B. A.; Biesinger, M. C.; McIntyre, N. S. *Surface and Interface Analysis* **2004**, *36*, 1564–1574.
(493) Collman, J. P.; Devaraj, N. K.; Chidsey, C. E. D. *Langmuir* **2004**, *20*, 1051–1053.
(494) Lenhard, J. R.; Royce, W. *Journal of the American Chemistry Society* **1978**, *100*, 7870–7875.
(495) Gagne, R. R.; Koval, C. A.; Lisensky, G. C. *Inorganic Chemistry* **1980**, *19*, 2854–2855.
(496) Meziane, D.; Barras, A.; Kromka, A.; Houdkova, J.; Boukherroub, R.; Szunerits, S. *Analytical Chemistry* **2012**, *84*, 194–200.
(497) Fairbanks, B. D.; Scott, T. F.; Kloxin, C. J.; Anseth, K. S.; Bowman, C. N. *Macromolecules* **2009**, *42*, 211–217.
(498) Smart, R. S. C.; Skinner, W. M.; Gerson, A. R. *Surface and Interface Analysis* **1999**, *28*, 101–105.
(499) Urban, N. R.; Ernst, K.; Bernasconi, S. *Goechimica et Cosmochimica Acta* **1999**, *63*, 837–853.
(500) Zhu, Z.; Fahrenbach, A. C.; Li, H.; Barnes, J. C.; Liu, Z.; Dyar, S. M.; Zhang, H.; Lei, J.; Carmieli, R.; Sarjeant, A. A.; Stern, C. L.; Wasielewski, M. R.; Stoddart, J. F. *Journal of the American Chemical Society* **2012**, *134*, 11709–11720.
(501) Zhao, Y.-L.; Dichtel, W. R.; Trabolsi, A.; Saha, S.; Aprahamian, I.; Stoddart, J. F. *Journal of the American Chemical Society* **2008**, *130*, 11294–11296.
(502) Balzani, V.; Credi, A.; Mattersteig, G.; Matthews, O. A.; Raymo, F. M.; Stoddart, J. F.; Venturi, M.; White, A. J. P.; Williams, D. J. *Journal of Organic Chemistry* **2000**, *65*, 1924–1936.
(503) Yasuda, T.; Tanabe, K.; Tsuji, T.; Coti, K. K.; Aprahamian, I.; Stoddart, J. F.; Kato, T. *Chemical Communications* **2010**, *46*, 1224–126.
(504) Nielsen, M. B.; Lomholt, C.; Becher, J. *Chemical Society Reviews* **2000**, *29*, 153–164.
(505) Fukuzumi, S.; Ohkubo, K.; Kawashima, Y.; Kim, D. S.; Park, J. S.; Jana, A.; Lynch, V. M.; Kim, D.; Sessler, J. L. *Journal of the American Chemical Society* **2011**, *133*, 15938–15941.
(506) Frei, M.; Diederich, F. *Helvetica Chimica Acta* **2006**, *89*, 2040–2057.
(507) Olea Ulloa, C.; Ponce Vargas, M.; Guajardo Maturana, R.; Muñoz-Castro, A. *Polyhedron* **2013**, *54*, 119–122.
(508) Darlatt, E.; Traulsen, C. H.-H.; Poppenberg, J.; Richter, S.; Kühn, J.; Schalley, C. A.; Unger, W. E. S. *Journal of Electron Spectroscopy and Related Phenomena* **2012**, *185*, 85–89.
(509) Varki, A. *Essensials of Glycobiology*; 2002; pp. 41–68.
(510) Alton, G.; Hasilik, M.; Niehues, R.; Panneerselvam, K.; Etchison, J. R.; Fana, F.; Freeze, H. H. *Glycobiology* **1998**, *8*, 285–295.
(511) Freeze, H. H.; Eklund, E. A.; Ng, B. G.; Patterson, M. C. *Lancet Neurology* **2012**, *11*, 453–466.
(512) Li, M.; Cushing, S. K.; Zhang, J.; Lankford, J.; Aguilar, Z. P.; Ma, D.; Wu, N. *Nanotechnology* **2012**, *23*, 115501.
(513) Domke, K. F.; Zhang, D.; Pettinger, B. *Journal of the American Chemical Society* **2006**, *128*, 14721–14727.
(514) Lueck, H. B.; Daniel, D. C.; Mchale, J. L. *Journal of Raman Spectroscopy* **1993**, *24*, 363–370.
(515) Chu, C.; Na, J.-S.; Parsons, G. N. *Journal of the American Chemical Society* **2007**, *129*, 2287–2296.
(516) Häkkinen, H. *Nature Chemistry* **2012**, *4*, 443–455.
(517) Gro, H.; Curioni, A.; Andreoni, W. *Journal of the American Chemical Society* **2000**, *122*, 3839–3842.
(518) Mollenhauer, D.; Floß, J.; Reissig, H.; Voloshina, E.; Paulus, B. *Journal of Computational Chemistry* **2011**, *32*, 1839–1845.
(519) Kim, N. H.; Kim, K. *Journal of Raman Spectroscopy* **2005**, *36*, 623–628.
(520) Pristinski, D.; Tan, S.; Erol, M.; Du, H.; Sukhishvili, S. *Journal of Raman Spectroscopy* **2006**, *37*, 762–770.
(521) He, X. N.; Gao, Y.; Mahjouri-Samani, M.; Black, P. N.; Allen, J.; Mitchell, M.; Xiong, W.; Zhou, Y. S.; Jiang, L.; Lu, Y. F. *Nanotechnology* **2012**, *23*, 205702.
(522) Yu, Y.; Handa, S.; Yajima, T.; Futamata, M. *Chemical Physics Letters* **2013**, *560*, 49–54.
(523) Michota, A.; Bukowska, J. *Journal of Raman Spectroscopy* **2003**, *34*, 21–25.
(524) Kudelski, A. *Journal of Raman Spectroscopy* **2009**, *40*, 2037–2043.
(525) Gawinkowski, S.; Walewski, Ł.; Vdovin, A.; Slenczka, A.; Rols, S.; Johnson, M. R.; Lesyng, B.; Waluk, J. *Physical Chemistry Chemical Physics* **2012**, *14*, 5489–5503.
(526) Gulam, R. M.; Matsushita, T.; Neya, S.; Funasaki, N.; Teraoka, J. *Chemical Physics Letters* **2002**, *357*, 126–130.
(527) Gulam, R. M.; Teraoka, J. *Spectrochimica Acta Part A: Molecular and Biomolecular Spectroscopy* **2010**, *76*, 207–212.
(528) Williams, R. W.; Schlücker, S.; Hudson, B. S. *Chemical Physics* **2008**, *343*, 1–18.

(529) Lima, J. A.; Freire, P. T. C.; Melo, F. E. A.; Mendes Filho, J.; De Sousa, G. P.; Lima, R. J. C.; Façanha Filho, P. F.; Bordallo, H. N. *Journal of Raman Spectroscopy* **2010**, *41*, 808–813.
(530) Osterrothová, K.; Jehlička, J. *Spectrochimica Acta Part A: Molecular and Biomolecular Spectroscopy* **2011**, *83*, 288–296.
(531) Cohen, E.; Wurtman, R. *Science* **1976**, *191*, 561–562.
(532) Lentz, B. R.; Wu, J. R.; Zheng, L.; Prevrátil, J. *Biophysical Journal* **1996**, *71*, 3302–3310.
(533) Wong, P. T. T. *Annual Review of Biophysics & Bioengineering* **1984**, *13*, 1–24.
(534) Zeisel, S. H.; Da Costa, K.-A. *Nutrition Reviews* **2009**, *67*, 615–623.
(535) Siek, M.; Kaminska, A.; Kelm, A.; Rolinski, T.; Holyst, R.; Opallo, M.; Niedziolka-Jonsson, J. *Electrochimica Acta* **2013**, *89*, 284–291.
(536) Swain, R. J.; Kemp, S. J.; Goldstraw, P.; Tetley, T. D.; Stevens, M. M. *Biophysical Journal* **2008**, *95*, 5978–5987.
(537) Cogdell, R. J.; Gardiner, A. T.; Cronin, L. *Philosophical Transactions of The Royal Society A: Mathematical, Physical, and Engineering Sciences* **2012**, *370*, 3819–3826.
(538) Müh, F.; Madjet, M. E.-A.; Adolphs, J.; Abdurahman, A.; Rabenstein, B.; Ishikita, H.; Knapp, E.-W.; Renger, T. *Proceedings of the National Academy of Sciences of the United States of America* **2007**, *104*, 16862–16867.
(539) Tronrud, D. E.; Wen, J.; Gay, L.; Blankenship, R. E. *Photosynthesis Research* **2009**, *100*, 79–87.
(540) Olbrich, C.; Jansen, T. L. C.; Liebers, J.; Aghtar, M.; Strümpfer, J.; Schulten, K.; Knoester, J.; Kleinekathöfer, U. *Journal of Physical Chemistry B* **2011**, *115*, 8609–8621.
(541) Adolphs, J.; Renger, T. *Biophysical Journal* **2006**, *91*, 2778–2797.
(542) Milder, M. T. W.; Brüggemann, B.; van Grondelle, R.; Herek, J. L. *Photosynthesis Research* **2010**, *104*, 257–274.
(543) Kasry, A.; Ardakani, A. A.; Tulevski, G. S.; Menges, B.; Copel, M.; Vyklicky, L. *Journal of Physical Chemistry C* **2012**, *116*, 2858–2862.
(544) Gaudreau, L.; Tielrooij, K. J.; Prawiroatmodjo, G. E. D. K.; Osmond, J.; García de Abajo, F. J.; Koppens, F. H. L. *Nano Letters* **2013**, *13*, 2030–2035.
(545) Kathiravan, A.; Chandramohan, M.; Renganathan, R.; Sekar, S. *Spectrochimica Acta Part A: Molecular and Biomolecular Spectroscopy* **2009**, *71*, 1783–1787.
(546) Olejnik, M.; Krajnik, B.; Kowalska, D.; Lin, G.; Mackowski, S. *Journal of Physics: Condensed Matter* **2013**, *25*, 194103.

Published papers

Results presented in this thesis have been published in the following papers:

1. **I. Kaminska**, M. Opallo, A. Łaszcz, A. Czerwinski and J. Niedziolka-Jonsson, "*(Bio)electrocatalysis at tin-doped indium oxide nanoparticulate film decorated with gold*", ***Electrochimica Acta***, 106 (2013) 165-171.

2. **I. Kaminska**, W. Qi, A. Barras, J. Sobczak, J. Niedziolka-Jonsson, P. Woisel, J. Lyskawa, W. Laure, M. Opallo, M. Li, R. Boukherroub and S. Szunerits, "*Thiol-yne click reaction on alkynyl-dopamine modified reduced graphene oxide (rGO)*", ***Chemistry – A European Journal***, 19 (2013) 8673-8678.

3. **I. Kaminska**, M. Jönsson-Niedziolka, A. Kaminska, M. Pisarek, R. Holyst, M. Opallo and J. Niedziolka-Jönsson, *"Electrodeposition of Well-Adhered Multifarious Au-Particles at a Solid|Toluene|Aqueous Electrolyte Three-Phase Junction"*, ***The Journal of Physical Chemistry C***, 116 (2012) 22476-22485.

4. **I. Kaminska**, A. Barras, Y. Coffinier, W. Lisowski, J. Niedziółka-Jönsson, P. Woisel, J. Lyskawa, M. Opallo, A. Siriwardena, R. Boukherroub, and S. Szunerits, *"Preparation of a responsive carbohydrate-coated biointerface based on graphene/azido-terminated tetrathiafulvalene nanohybird material"*, ***ACS Applied Materials and Interfaces***, 4 (2012) 5386-5393.

5. **I. Kaminska**, M. R. Das, Y. Coffinier, J. Niedziolka-Jonsson, J. Sobczak, P. Woisel, J. Lyskawa, M. Opallo, R. Boukherroub, and S. Szunerits, *"Reduction and Functionalization of Graphene Oxide Sheets Using Biomimetic Dopamine Derivatives in One Step"*, ***ACS Applied Materials and Interfaces***, 4 (2012) 1016-1020.

6. **I. Kaminska**, M. R. Das, Y. Coffinier, J. Niedziolka-Jonsson, P. Woisel, M. Opallo, S. Szunerits and R. Boukherroub, *"Preparation of graphene/tetrathiafulvalene nanocomposite switchable surfaces"*, ***Chemical Communications***, 48 (2012) 1221-1223.

7. **I. Kaminska**, A. Roguska, J. Niedziołka-Jonsson, M. Opallo, *"Electrodeposition of gold nanoparticles at a solid|ionic liquid|aqueous electrolyte three-phase junction"*, ***Electrochemistry Communications***, 12 (2010) 1742-1745.

Other papers published during PhD studies:

1. Q. Wang, **I. Kaminska**, J. Niedziolka-Jonsson, M. Opallo, M. Li, R. Boukherroub, S. Szunerits, "Sensitive sugar detection using 4-aminophenylboronic acid modified graphene", ***Biosensors and Bioelectronics***, 50 (2013) 331–337.

2. P. Subramanian, A. Lesniewski, **I. Kaminska**, A. Vlandas, A. Vasilescu, J. Niedziolka-Jonsson, E. Pichonat, H. Happy, R. Boukherroub, S. Szunerits, "Lysozyme detection on aptamer functionalized graphene-coated SPR interfaces", ***Biosensors and Bioelectronics***, 50 (2013) 239-243.